frontiers | Research Topics

Statistical model-based computational biomechanics: Applications in joints and internal organs

Edited by
Emmanuel A. Audenaert, Tinashe E. M. Mutsvangwa, Bhushan Borotikar and Shireen Y. Elhabian

Published in
Frontiers in Bioengineering and Biotechnology

ISSN 1664-8714
ISBN 978-2-8325-2893-8
DOI 10.3389/978-2-8325-2893-8

About Frontiers

Frontiers is more than just an open access publisher of scholarly articles: it is a pioneering approach to the world of academia, radically improving the way scholarly research is managed. The grand vision of Frontiers is a world where all people have an equal opportunity to seek, share and generate knowledge. Frontiers provides immediate and permanent online open access to all its publications, but this alone is not enough to realize our grand goals.

Frontiers journal series

The Frontiers journal series is a multi-tier and interdisciplinary set of open-access, online journals, promising a paradigm shift from the current review, selection and dissemination processes in academic publishing. All Frontiers journals are driven by researchers for researchers; therefore, they constitute a service to the scholarly community. At the same time, the *Frontiers journal series* operates on a revolutionary invention, the tiered publishing system, initially addressing specific communities of scholars, and gradually climbing up to broader public understanding, thus serving the interests of the lay society, too.

Dedication to quality

Each Frontiers article is a landmark of the highest quality, thanks to genuinely collaborative interactions between authors and review editors, who include some of the world's best academicians. Research must be certified by peers before entering a stream of knowledge that may eventually reach the public - and shape society; therefore, Frontiers only applies the most rigorous and unbiased reviews. Frontiers revolutionizes research publishing by freely delivering the most outstanding research, evaluated with no bias from both the academic and social point of view. By applying the most advanced information technologies, Frontiers is catapulting scholarly publishing into a new generation.

What are Frontiers Research Topics?

Frontiers Research Topics are very popular trademarks of the *Frontiers journals series*: they are collections of at least ten articles, all centered on a particular subject. With their unique mix of varied contributions from Original Research to Review Articles, Frontiers Research Topics unify the most influential researchers, the latest key findings and historical advances in a hot research area.

Find out more on how to host your own Frontiers Research Topic or contribute to one as an author by contacting the Frontiers editorial office: frontiersin.org/about/contact

Statistical model-based computational biomechanics: Applications in joints and internal organs

Topic editors

Emmanuel A. Audenaert — Ghent University, Belgium
Tinashe E. M. Mutsvangwa — University of Cape Town, South Africa
Bhushan Borotikar — Symbiosis International University, India
Shireen Y. Elhabian — The University of Utah, United States

Citation

Audenaert, E. A., Mutsvangwa, T. E. M., Borotikar, B., Elhabian, S. Y., eds. (2023). *Statistical model-based computational biomechanics: Applications in joints and internal organs*. Lausanne: Frontiers Media SA. doi: 10.3389/978-2-8325-2893-8

Table of contents

frontiers | Frontiers in Bioengineering and Biotechnology

TYPE Editorial
PUBLISHED 13 June 2023
DOI 10.3389/fbioe.2023.1232464

OPEN ACCESS

EDITED AND REVIEWED BY
Markus O. Heller,
University of Southampton,
United Kingdom

*CORRESPONDENCE
Bhushan Borotikar,
bhushan.borotikar@scmia.edu.in

RECEIVED 31 May 2023
ACCEPTED 08 June 2023
PUBLISHED 13 June 2023

CITATION
Borotikar B, Mutsvangwa TEM, Elhabian SY and Audenaert EA (2023), Editorial: Statistical model-based computational biomechanics: applications in joints and internal organs. *Front. Bioeng. Biotechnol.* 11:1232464. doi: 10.3389/fbioe.2023.1232464

Editorial: Statistical model-based computational biomechanics: applications in joints and internal organs

Bhushan Borotikar[1,2,3]*, Tinashe E. M. Mutsvangwa[2,3], Shireen Y. Elhabian[4,5] and Emmanuel A. Audenaert[6,7,8,9]

[1]Symbiosis Centre for Medical Image Analysis, Symbiosis International University, Pune, India, [2]Department of Human Biology, Division of Biomedical Engineering, University of Cape Town, Cape Town, South Africa, [3]IMT Atlantique, Brest, France, [4]Kahlert School of Computing, University of Utah, Salt Lake City, UT, United States, [5]Scientific Computing and Imaging Institute, University of Utah, Salt Lake City, UT, United States, [6]Department of Orthopedic Surgery and Traumatology, Ghent University Hospital, Ghent, Belgium, [7]Department of Human Structure and Repair, Ghent University, Ghent, Belgium, [8]Department of Electromechanics, InViLab Research Group, University of Antwerp, Antwerp, Belgium, [9]Department of Trauma and Orthopedics, NHS Foundation Trust, Addenbrooke's Hospital, Cambridge University Hospitals, Cambridge, United Kingdom

KEYWORDS

computational morphometrics, osteoarthritis, foot and ankle, cerebral palsy, particle-based shape modeling, spatiotemporal modeling, automated mitral valve assessment, multi-organ statistical shape modeling

Editorial on the Research Topic
Statistical model-based computational biomechanics: applications in joints and internal organs

As the era of big data continues to unfold, data-driven statistical models are increasingly being applied to the study of anatomical structures, including bones, joints, and internal organs (Cootes et al., 1995; Golland et al., 2000). Statistical model-based computational biomechanics has shown immense potential in the study of joints and internal organs, shedding light on the relationships between mechanical properties, tissue structure, and function (Blanc et al., 2012). Despite their potential, these tools are not widely used in clinical applications related to joints and internal organs due to technical challenges, including handling high-dimensional data, representing nonlinear tissue behavior, addressing data heterogeneity, achieving improved generalizability for better clinical utility, and modeling anatomically valid multi-objects (joints). This Research Topic highlights state-of-the-art statistical model-based approaches used as tools in clinical applications. In this editorial, we discuss recent advances in statistical model-based computational biomechanics and their applications in studying joints and internal organs. We highlight the potential of these methods to revolutionize the diagnosis and treatment of musculoskeletal disorders and promote personalized medicine.

Bartsoen et al. proposed a workflow that combines statistical and deep learning methods to optimize implant position in Total Knee Arthroplasty (TKA) planning. This approach achieved improved results in pre-operative planning and emphasized the importance of non-invasive extraction of subject-specific ligament strains to

reduce uncertainty in ligament-balanced planning. In a separate study, Van Oevelen et al. used a principal polynomial autoencoder model to nonlinearly encode cartilage wear patterns in a dataset of osteoarthritis (OA) images. They converted 3D joint space width data into 2D pixel images and compared healthy and OA cases using this approach. The study presented a novel concept of converting anatomically corresponding distance maps into pixel images for neural-based learning. The study also reconstructed a healthy virtual twin using a statistical shape model (SSM) to predict pre-morbid bone geometries of the femur and tibia bones. Using the healthy SSM-derived geometries for comparisons, the study identified four dominant orthogonal wear components (posteromedial, anteromedial, bicompartmental, and lateral) in OA that are highly correlated with relative limb geometry. Another work by Van Oevelen et al. focused on enhancing subject-specificity in computational musculoskeletal modeling by predicting various soft tissue structures around the knee, including cartilage layer, ligament anatomies, meniscal anatomy, and patellar tendon anatomy. The accuracy of these predictions was validated against manual measures, but the impact on the performance of the musculoskeletal model remains unknown.

Peterson et al. focused on developing SSMs of subtalar, talonavicular, and calcaneocuboid joints using CT scans. The study brings an interesting perspective of characterizing asymptomatic joint-level morphology and alignment differences using multi-level models, providing insights into 3D joint characteristics such as joint coverage, convergence index, and joint space distance. Another study by the same group (Khan et al.) introduced theoretical and technical problems of scalability, anatomical inconsistencies, and entangled shape statistics for multi-organ models. The study used particle-based shape modeling (PSM) and proposed a novel correspondence-point optimization of multi-organ anatomies to tackle these limitations. The study disentangles the shared space among organs, allowing for the modeling of intra-organ shape and inter-organ pose variabilities. The authors also elaborated on quantitative evaluation metrics for assessing the generality, specificity, and compactness of these multi-organ models. These two studies have improved the clinical applicability of SSMs from single-organ understanding to multi-organ understanding. A study by Cheng et al. reported differences in shape characteristics of ankle bones between healthy children and children with ankle equinus deformity due to cerebral palsy (CP). The study compared SSMs of healthy and CP cohorts and reported volumetric differences in mean shapes and subject-level differences in specific bone regions of interest. However, no precise deformation pattern could be observed for any of the three ankle bones studied.

Computational assessment of cardiovascular organs presents an increased level of technical complexity in terms of the spatiotemporal and non-linear dynamic behavior of the tissues. While large deformation models have been proposed and used in literature, they are limited to single object assessment. Lopes et al. developed an automated approach for evaluating the mitral valve apparatus in the context of transcatheter mitral valve replacement (TMVR) for mitral valve disease. They used retrospective cardiac CT scans from 50 patients to create an SSM of the left heart chambers during end-diastole. This model was then extended to other phases of the cardiac cycle to capture the dynamic changes of the mitral valve. The researchers employed anatomical landmarks to fit the model to specific cases and assess the mitral valve during end-diastolic and end-systolic phases for TMVR planning. The automated assessment was compared to manual assessment and showed an error rate of less than 5% for various mitral valve measurements. The study suggests that automated methods can improve consistency and reduce inter-observer variability, while also saving time in pre-interventional assessments. Modeling the non-linear and time-dependent shape changes of heart tissue was further refined in a study by Iyer et al. They developed a multi-organ SSM using the PSM approach to detect and extract shared boundaries between two organs. They introduced a novel technique incorporating shared boundaries within PSM for modeling multi-organ anatomies. The study included a toy dataset of parameterized shapes and a clinical dataset of biventricular heart models, specifically modeling the right ventricle, left ventricle wall, and interventricular septum. The illustrations demonstrated that the integrity of shared boundaries between multiple organs was preserved, and pathological changes could be effectively detected using this approach. Another interesting study by Adams et al. presented a spatiotemporal SSM to assess non-linear dynamic anatomies such as left atrium shape changes over the cardiac cycle. They combined an entropy-based correspondence optimization with non-linear regression—called regularized principal component polynomial regression. A 4D left atrium data was used to illustrate the model's ability to capture underlying time dependency compared to baseline methods. The resulting SSMs have inter and intra-subject correspondence to capture a statistically significant time dependency and are agnostic to the consistency of temporal sequences across subjects.

In conclusion, data-driven statistical models have emerged as a powerful tool for evaluating anatomies, offering valuable insights into the complex relationships between morphology, function, and pathology. However, their implementation requires addressing various mathematical challenges. This special Research Topic highlights many methodological advancements in investigating the dynamic, non-linear, time-dependent, age- and gender-relevant, and subject-specific nature of joints and internal organs of the human body. While doing so, the articles published here cover a variety of topics ranging from TMVR and TKA planning, knee OA and ankle equinus due to CP, cartilage and ligament abnormalities, and cardiovascular diseases. Future research should be focused on validating the models for their clinical use, developing models that combine bone and soft tissue structures, and mechanical characterization of multi-organ deformations.

Through the development of innovative mathematical approaches presented here and the refinement of existing techniques, our understanding of the human body can be expanded, leading to improved healthcare outcomes.

Author contributions

BB participated in the review process, drafted and edited the editorial. EA coordinated the Research Topic, participated in the review process, and critically revised the manuscript. TM and SE participated in the review process and critically revised the editorial. All authors contributed to the article and approved the submitted version.

Conflict of interest

The authors declare that the research was conducted in the absence of any commercial or financial relationships that could be construed as a potential conflict of interest.

Publisher's note

References

Blanc, R., Seiler, C., Székely, G., Nolte, L.-P., and Reyes, M. (2012). Statistical model based shape prediction from a combination of direct observations and various surrogates: application to orthopaedic research. *Med. Image Anal.* 16 (6), 1156–1166.

Cootes, T. F., Cooper, D., Taylor, C. J., and Graham, J. (1995). Active shape models—their training and application. *Comput. Vis. Image Underst.* 61 (1), 38–59.

Golland, P., Eric, W., and Grimson, L. (2000). "Fixed topology skeletons," in Proceedings IEEE Conference on Computer Vision and Pattern Recognition (CVPR) 1, 10–17.

frontiers | Frontiers in Bioengineering and Biotechnology

TYPE Original Research
PUBLISHED 11 October 2022
DOI 10.3389/fbioe.2022.937326

OPEN ACCESS

EDITED BY
Emmanuel A. Audenaert,
Ghent University, Belgium

REVIEWED BY
Liang Wang,
Southeast University, China
Hiroshi Yamada,
Kyushu Institute of Technology, Japan

*CORRESPONDENCE
Jungsil Kim,
jungsilkim@scnu.ac.kr

SPECIALTY SECTION
This article was submitted to Biomechanics, a section of the journal Frontiers in Bioengineering and Biotechnology

RECEIVED 06 May 2022
ACCEPTED 29 August 2022
PUBLISHED 11 October 2022

CITATION
Ryu D, Baek S and Kim J (2022), Region-dependent mechanical characterization of porcine thoracic aorta with a one-to-many correspondence method to create virtual datasets using uniaxial tensile tests.
Front. Bioeng. Biotechnol. 10:937326.
doi: 10.3389/fbioe.2022.937326

Region-dependent mechanical characterization of porcine thoracic aorta with a one-to-many correspondence method to create virtual datasets using uniaxial tensile tests

Dongman Ryu[1,2], Seungik Baek[2] and Jungsil Kim[3,4]*

[1]Medical Research Institute, Pusan National University, Busan, South Korea, [2]Department of Mechanical Engineering, Michigan State University, East Lansing, MI, United States, [3]Department of Convergent Biosystems Engineering, Sunchon National University, Suncheon, South Korea, [4]Institute of Human Harmonized Robotics, Sunchon National University, Suncheon, South Korea

The simulation of the cardiovascular system and *in silico* clinical trials have garnered attention in the biomedical engineering field. Physics-based modeling is essential to associate with physical and clinical features. In physics-based constitutive modeling, the identification of the parameters and estimation of their ranges based on appropriate experiments are required. Uniaxial tests are commonly used in the field of vascular mechanics, but they have limitations in fully characterizing the regional mechanical behavior of the aorta. Therefore, this study is aimed at identifying a method to integrate constitutive models with experimental data to elucidate regional aortic behavior. To create a virtual two-dimensional dataset, a pair of uniaxial experimental datasets in the longitudinal and circumferential directions was combined using a one-to-many correspondence method such as bootstrap aggregation. The proposed approach is subsequently applied to three constitutive models, i.e., the Fung model, Holzapfel model, and constrained mixture model, to estimate the material parameters based on the four test regions of the porcine thoracic aorta. Finally, the regional difference in the mechanical behavior of the aorta, the correlation between the experimental characteristics and model parameters, and the inter-correlation of the material parameters are confirmed. This integrative approach will enhance the prediction capability of the model with respect to the regions of the aorta.

KEYWORDS

virtual dataset, regional variation, arterial stiffness, Fung model, holzapfel model, constrained mixture model, statistical correlations, bootstrapping

Introduction

Recently, the simulation of the cardiovascular system and *in silico* clinical trials have garnered attention in biomedical engineering. Virtual patient cohorts and digital twins are emerging as promising strategies in precision medicine, although they are not yet fully established for clinical applications (Niederer et al., 2020; Chakshu et al., 2021). In physics-based modeling, a virtual model comprises two layers, where one layer includes a set of clinical features, and the other includes a set of model parameters. It is important to associate the model with physical or clinical features. Inadequate anatomical, physiological, and functional parameters of the heart and vasculature hinder the further development of cardiovascular devices and novel treatments (Hose et al., 2019).

The constitutive model represents the behavior of materials in the form of relationship between strain and stress. To establish physics-based modeling, an essential step is to identify the constitutive parameters and estimate their ranges based on appropriate experiments such as the tensile test of flat segments or the extension-inflation test of cylindrical segments. The mechanical properties of the blood vessel are generally determined by using a specific constitutive model. Blood vessels exhibit hyperelastic and anisotropic properties. It is well known that elastin dominates the initial linear behavior in the low-stiffness regime, whereas collagen is recruited in the high-stiffness regime (Harkness et al., 1957). To identify the anisotropic behavior of blood vessels, pairs of experimental datasets in two loading directions for the same sample are required. Biaxial testing is more reliable in determining the material parameters in the constitutive models, while uniaxial testing is advantageous in investigating the regional variation in the heterogeneous properties of the blood vessel. We previously demonstrated that the posterior side of the porcine thoracic aorta is significantly stiffer than the anterior side in the extension-inflation test, and that the longitudinal difference in the aortic mechanical properties is dependent on the circumferential region (Kim and Baek, 2011; Kim et al., 2013). Therefore, the uniaxial tensile test must be revisited in terms of the spatial description of arterial heterogeneity and its potential application to *in silico* studies of the virtual aorta.

To elucidate the regional variation of blood vessels, this study was conducted to identify a new approach to integrate a constitutive model and uniaxial test data. To this end, uniaxial tensile tests were performed on the eight sets of aortic segments in consideration of the test regions and loading directions. For an integrated prediction tool based on experimental data, we propose a three-step approach to describe the regional and nonlinear anisotropic mechanical behavior, as well as the relationship between the physical characteristics (arterial stiffness) and constitutive model parameters. First, each virtual two-dimensional (2D) dataset is constructed using a pair of uniaxial tests in the longitudinal and circumferential loading directions for the same sample, followed by the estimation of a set of anisotropic constitutive model parameters. Consequently, a number of virtual datasets are generated *via* bootstrap aggregation, which can be used to improve the predictive performance of the model. Second, the data populated using the models allows the analysis of their regional variabilities and differences in the mechanical behavior of the aorta through various statistical tools. Finally, the correlations between the arterial physical characteristics and model parameters, as well as the correlations among the model parameters are determined. The proposed approach is evaluated using three constitutive models: the Fung model, Holzapfel model, and constrained mixture model (CMM).

Methods

To investigate the regional variations in the mechanical behavior and material parameters of the aorta, the thoracic aorta was segmented into eight sets according to the circumferential direction (i.e., anterior vs. posterior), longitudinal direction (i.e., proximal vs. distal), and loading directions (i.e., circumferential vs. longitudinal) in the experiment (Figure 1), as follows:

1) circumferential specimen of the anterior side of proximal descending thoracic aorta (PAC)
2) longitudinal specimen of the anterior side of proximal descending thoracic aorta (PAL)
3) circumferential specimen of the anterior side of distal descending thoracic aorta (DAC)
4) longitudinal specimen of the anterior side of distal descending thoracic aorta (DAL)
5) circumferential specimen of the posterior side of proximal descending thoracic aorta (PPC)
6) longitudinal specimen of the posterior side of proximal descending thoracic aorta (PPL)
7) circumferential specimen of the posterior side of distal descending thoracic aorta (DPC)
8) longitudinal specimen of the posterior side of distal descending thoracic aorta (DPL).

Sample and uniaxial tensile test

Eight fresh descending thoracic aortas from approximately 6-month-old pigs were obtained from a local slaughterhouse. They were immediately used after their loose connective tissues were removed from the adventitia. The aorta was cut in the order of circumferential and longitudinal directions with a width of 6 mm along the aortic tree. The total number of aortic segments used in

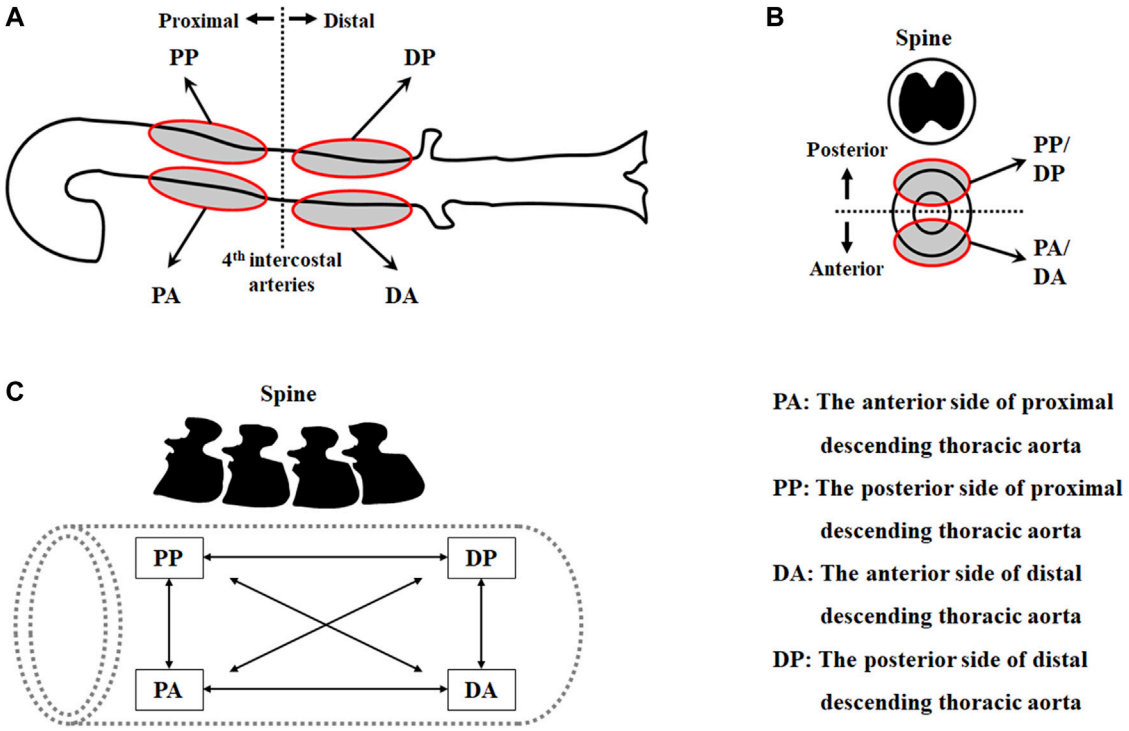

FIGURE 1
Test regions of the thoracic aorta in **(A)** the longitudinal direction and **(B)** the circumferential direction, and **(C)** pairs of datasets in two loading directions.

this study was 35, 29, 26, 28, 25, 25, 28, and 28 for the PAC, PAL, DAC, DAL, PPC, PPL, DPC, and DPL, respectively. The thickness of the sample was measured twice at three different points using a Vernier caliper. The ends of the sample were attached to sandpaper with cyanoacrylate to avoid slipping during the experiments. Two microspheres with a 10 mm gap were attached to the center of the sample. Subsequently, the sample was mounted on the experimental device at a length of 20 mm between the clamps of the device, which was originally developed for the extension-inflation test (Kim and Baek, 2011) but was modified for the uniaxial tensile test. Before commencing the tensile test, the distance between two clamps was adjusted to flatten the sample in the absence of bending, which was confirmed by the microspheres attached to the sample. The sample was maintained in the moist state and then stretched at a speed of 2.9 mm/s until rupture. During the test, the axial force exerted on the sample was measured continuously at a sampling rate of 100 Hz with a 50 N load cell. The images of the sample were also taken using a CCD camera, and the position of the microspheres were tracked through the post imaging process with custom-written Matlab codes and were used to determine the stretch.

Calculation of slope in stress–stretch curve

The experimental data up to fiber breakage points in which the stress–stretch curve deviated from the high-stiffness regime was used for analysis. Two distinct regimes were observed in the stress–stretch curve: A moderate gradient slope (low-stiffness) regime and a steep gradient slope (high-stiffness) regime. To quantitatively characterize the nonlinear behavior of the aortic tissues, the slope of the tangent to the stress–stretch curve was determined. The slope was determined in two steps for each regime to represent the stiffness of the aortic tissue. Since the stress-stretch curve can be approximated as a piecewise linear function, the optimal range of each linear fit before and after transition was first determined based on the coefficient of determination (R^2). The first point of the stress-stretch curve served as a starting point for the optimal range in the low-stiffness regime, and the last point of the curve was used as an endpoint in the high-stiffness regime. Next, the fitting equation to describe the stress-stretch curve was defined and the derivative of the fitting equation was determined at one point within the optimal range for each regime.

Constitutive models for hyperelasticity

Stress tensor and incompressibility

A majority of constitutive models consider the elastic behavior of blood vessels to be hyperelastic. Aortic tissues are typically characterized by the hyperelastic strain energy function. The aortic wall is assumed to be an incompressible material, i.e., $J^2 = \det \mathbf{C} = 1$, where J is the Jacobian, and $\mathbf{C}$ is the right Cauchy–Green deformation tensor. The Cauchy stress tensor, $\mathbf{T}$, which describes the true stress state in the material configuration, can be defined by the hyperelastic strain energy as follows:

$$\mathbf{T} = -p\mathbf{I} + 2\mathbf{F}\frac{\partial W}{\partial \mathbf{C}}\mathbf{F}^T, \tag{1}$$

where p is the Lagrange multiplier that can be determined by the boundary conditions, $\mathbf{F}$ the deformation gradient, and W the strain energy function. For the uniaxial test, the deformation gradient of the incompressible material is expressed as

$$\mathbf{F} = \begin{bmatrix} \lambda & 0 & 0 \\ 0 & \lambda^{-\frac{1}{2}} & 0 \\ 0 & 0 & \lambda^{-\frac{1}{2}} \end{bmatrix}, \tag{2}$$

assuming that stress is applied along the loading direction (Martins et al., 2006; Annaidh et al., 2012; de Rooij and Kuhl, 2016), where λ is the stretch ratio.

Fung model

Chuong and Fung (Chuong and Fung, 1983; Zulliger et al., 2004) proposed a strain energy function to describe the mechanical behavior of an artery under internal pressure or stretching. They considered the anisotropic property and nonlinearity of the artery, and the mechanical behavior is described through the strain energy function W.

$$W = \frac{c_1}{2}\left[\exp(Q) - 1\right] \tag{3}$$

where

$$Q = b_1E_{11}^2 + b_2E_{22}^2 + b_3E_{33}^2 + 2b_4E_{11}E_{22} + 2b_5E_{11}E_{33} + 2b_6E_{22}E_{33} \tag{4}$$

$$\mathbf{E} = \frac{1}{2}(\mathbf{C} - \mathbf{I}), \tag{5}$$

where $\mathbf{E}$ is the Green–Lagrange strain tensor, c_1 is an elastic constant, and b_1–b_6 are parameters describing the contribution of the principal strains. The uniaxial stress–stretch relationship for the Fung model, based on Eqs 3, 5, is expressed as (by solving for the Lagrange multiplier p using the free boundary condition in each uniaxial loading direction):

$$\mathrm{T}_1 = \frac{1}{2}c_1\lambda^2\left[\exp\left(Q'\right)\right]\left[b_1(\lambda^2 - 1) + b_4(\lambda^{-1} - 1) + b_5(\lambda^{-1} - 1)\right] - p' \tag{6}$$

where

$$Q' = \frac{1}{4}b_1(\lambda^2 - 1)^2 + \frac{1}{4}b_2(\lambda^{-1} - 1)^2 + \frac{1}{4}b_3(\lambda^{-1} - 1)^2 + \frac{1}{2}b_4(\lambda^2 - 1)(\lambda^{-1} - 1) + \frac{1}{2}b_5(\lambda^{-1} - 1)(\lambda^2 - 1) + \frac{1}{2}b_6(\lambda^{-1} - 1)^2, \tag{7}$$

$$p' = \frac{1}{2}c_1\lambda^{-1}\left[\exp\left(Q'\right)\right]\left[b_3(\lambda^{-1} - 1) + b_5(\lambda^2 - 1) + b_6(\lambda^{-1} - 1)\right], \tag{8}$$

$$\mathrm{T}_2 = \frac{1}{2}c_1\lambda^2\left[\exp\left(Q''\right)\right]\left[b_2(\lambda^2 - 1) + b_4(\lambda^{-1} - 1) + b_6(\lambda^{-1} - 1)\right] - p'' \tag{9}$$

where

$$Q'' = \frac{1}{4}b_1(\lambda^{-1} - 1)^2 + \frac{1}{4}b_2(\lambda^2 - 1)^2 + \frac{1}{4}b_3(\lambda^{-1} - 1)^2 + \frac{1}{2}b_4(\lambda^{-1} - 1)(\lambda^2 - 1) + \frac{1}{2}b_5(\lambda^{-1} - 1)^2 + \frac{1}{2}b_6(\lambda^2 - 1)(\lambda^{-1} - 1), \tag{10}$$

$$p'' = \frac{1}{2}c_1\lambda^{-1}\left[\exp\left(Q''\right)\right]\left[b_3(\lambda^{-1} - 1) + b_5(\lambda^{-1} - 1) + b_6(\lambda^2 - 1)\right]. \tag{11}$$

Holzapfel model

Holzapfel et al. (Holzapfel et al., 2000) proposed a strain energy function that includes two families of collagen fibers. They assumed that each layer of the arterial wall demonstrated similar mechanical characteristics (Schroeder et al., 2018). In this model, the strain energy function is divided into two: W_{iso} associated with isotropic deformations and W_{aniso} associated with anisotropic deformations. The neo-Hookean model is used in the isotropic response component, as follows (Ogden, 1997):

$$W_{iso} = \frac{c}{2}(I_1 - 3), \tag{12}$$

where $c > 0$ is a stress-like material parameter. The strain energy function associated with anisotropic deformation is proposed to be an exponential function, as follows:

$$W_{aniso} = \frac{k_1}{2k_2}\sum_{i=4,6}\{\exp\left[k_2(I_i - 1)^2\right] - 1\}, \tag{13}$$

where $k_1 > 0$ is a stress-like material parameter, and $k_2 > 0$ is a dimensionless parameter. The fiber direction can be described as a model parameter using I_4 and I_6. The uniaxial stress–stretch relationship in each loading direction for the Holzapfel model based on Eq. 12 and Eq. 13 is expressed as follows:

$$\mathrm{T}_1 = -c\lambda^{-1} + c\lambda^2 + \sum_{i=4,6} 2k_1\left(I_i' - 1\right)\left\{\exp\left(k_2\left(I_i' - 1\right)^2\right)\right\}\lambda^2\cos^2\gamma, \tag{14}$$

where

$$I_4' = I_6' = \lambda^2 \cos^2\gamma + \lambda^{-1}\sin^2\gamma, \tag{15}$$

$$T_2 = -c\lambda^{-1} + c\lambda^2 + \sum_{i=4,6} 2k_1\left(I_i'' - 1\right)\left\{\exp\left(k_2\left(I_i'' - 1\right)^2\right)\right\}\lambda^2\sin^2\gamma, \tag{16}$$

where

$$I_4'' = I_6'' = \lambda^{-1}\cos^2\gamma + \lambda^2\sin^2\gamma. \tag{17}$$

In Eqs 14–17, γ is the angle of fiber orientation measured from the longitudinal direction.

CMM

The CMM proposed by Humphrey and Rajagopal (2002) presents general concepts for the modeling of biological tissues. The basic principle of the model is that living tissues have a preferred state. When the preferred state is changed, the rates of production and removal and the natural configurations of multiple constituents can be changed to restore them to the preferred state. Typically, the CMM is utilized in the computational simulation of vascular growth and remodeling; however, in this study, the CMM is presented as a constitutive model that describes the arterial mechanical behavior. In addition, in the CMM, the tissue is considered to be a homogenized mixture and the deformation of the mixture as a whole is constrained by incompressibility. In the model, the stored energy functions are given by

$$W = \rho^e\Psi^e\left(\boldsymbol{C}_n^e\right) + \sum_{k=1}\rho^k\Psi^k\left(\lambda_n^k\right), \tag{18}$$

where

$$\Psi^e\left(\boldsymbol{C}_n^e\right) = \frac{c_1}{2}\left\{C_{n[11]}^e + C_{n[22]}^e + \frac{1}{C_{n[11]}^e C_{n[22]}^e - C_{n[12]}^e 2}\right\}, \tag{19}$$

$$\Psi^k\left(\lambda_n^k\right) = \frac{c_2^k}{4c_3^k}\left\{\exp\left[c_3^k\left(\lambda_n^k 2 - 1\right)^2\right] - 1\right\} \tag{20}$$

for elastin and collagen fiber families, respectively. Here, ρ^e and ρ^k are the density of elastin and collagen fiber $k = 1, \ldots, 4$, and c_1, c_2^k, and c_3^k are intrinsic material parameters. $C_{n[ij]}^e$ is a component of $\mathbf{C}_n^e = [\mathbf{F}_n^e]^T\mathbf{F}_n^e$. In CMM, orientations of collagen fiber families are assumed to be symmetric with respect to the axial direction. The stretches of the kth collagen fiber families from their natural configurations to the current configuration are calculated as described by Zeinali-Davarani et al. (2011) and Seyedsalehi et al. (2015) as follows:

$$\lambda_n^k = G_h^c\lambda^k, \tag{21}$$

where

$$\lambda^k = \sqrt{\mathbf{F}\mathbf{M}^k \cdot \mathbf{F}\mathbf{M}^k}, \tag{22}$$

$$\mathbf{M}^k = \frac{\mathbf{F}^{-1}\mathbf{m}^k}{|\mathbf{F}^{-1}\mathbf{m}^k|}, \tag{23}$$

where G_h^c is the pre-stretch of the collagen, and λ^k is the stretch of the fiber from the reference to the current configuration. The unit vector $\mathbf{M}^k$ in the reference configuration that corresponds to $\mathbf{m}^k$ is given by Eq. 23, and the $\mathbf{m}^k$ is the unit vector in the direction of the k-th collagen fiber. The angle between $\mathbf{m}^k$ and the first principal direction is denoted by α^k. The homeostatic stretch tensor of elastin, $\mathbf{G}^e$, which is the mapping from the reference configuration to the current configuration, is written as

$$\mathbf{G}^e = \mathrm{diag}\{G_1, G_2\}, \tag{24}$$

where G_1 and G_2 are the elastin pre-stretches in the circumferential and longitudinal directions, respectively. The deformation gradient of the elastin mapping from its natural state to the current configuration is $\mathbf{F}_n^e = \mathbf{F}\mathbf{G}^e$.

The uniaxial stress–stretch relationship in each loading direction is expressed as

$$T_1 = -c_1G_1^{-1}\lambda^{-1} + c_1G_1^2\lambda^2 + \lambda^2\sum_{k=1}^{2}c_2^{(k)}\left(\left(\lambda_n^{(k)}\right)^2 - 1\right) \times \left\{\exp\left[c_3^{(k)}\left(\left(\lambda_n^{(k)}\right)^2 - 1\right)^2\right]\right\}\left(\frac{G_h^c}{\lambda_n^k}\right)^2\lambda^2\cos^2\alpha, \tag{25}$$

$$T_2 = -c_1G_2^{-1}\lambda^{-1} + c_1G_2^2\lambda^2 + \lambda^2\sum_{k=1}^{2}c_2^{(k)}\left(\left(\lambda_n^{(k)}\right)^2 - 1\right) \times \left\{\exp\left[c_3^{(k)}\left(\left(\lambda_n^{(k)}\right)^2 - 1\right)^2\right]\right\}\left(\frac{G_h^c}{\lambda_n^k}\right)^2\lambda^2\sin^2\alpha, \tag{26}$$

where α is the angle of fiber orientation from the axial direction.

Calculation of material parameters

The biaxial tensile or inflation test can be used to investigate the anisotropic behavior of the aorta; however, it is limited to the characterization of spatially heterogeneous material parameters in local regions. The uniaxial tensile test allows the intrinsic material characteristics in the local regions of the blood vessel to be estimated. However, it is difficult to estimate all parameters simultaneously, particularly when numerous parameters are involved. Thus, a novel data-oriented approach, i.e., the bootstrap approach, was employed in this study. More specifically, cross-mapping involving one circumferential-to-many longitudinal mapping (or vice versa) was performed to generate a virtual biaxial dataset using custom-written Matlab codes. For a virtual dataset, a set of material parameters in the region of interest was estimated individually for each loading direction. They were then integrated to determine the common range of the material parameters for the biaxial behavior in a given region. However, a single set of material parameters for the biaxial behavior may result in a large error, if the ranges of the material parameters for each loading direction are too wide or the common ranges are too narrow such as in transition. To minimize the error, the error tolerance for the iterative

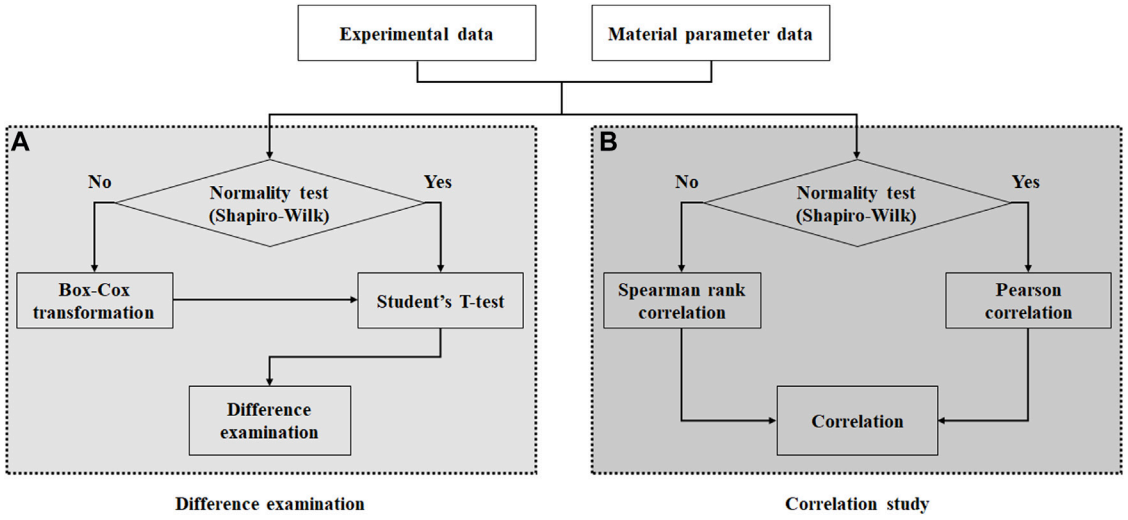

FIGURE 2
Flow chart showing procedures for **(A)** difference examination and **(B)** correlation study.

solution in the Matlab codes was adjusted based on the goodness of the curve fit.

Statistical analyses

In this study, two separate statistical analyses were performed. Analysis of variance was used to identify regional differences in the experimental results, followed by the Bonferroni correction as a post-hoc test. Additionally, the Student's t-test was performed to examine the significance of the regional differences as well as the relationship between the material parameters and experimental results.

To determine the appropriate method for performing the Student's t-test and correlation study, the following procedures were performed: 1) The normal distribution of the calculated material parameters and stiffness as well as the experimental data were examined using the Shapiro–Wilk test, as shown in Figure 2. 2) In the normality test, a significant difference was determined based on the p-value of 0.05. 3) The Student's t-test was conducted to examine the differences between the material parameters based on the test regions. 4) If the normality test of the data fails, then the data can be transformed to the normally distributed data *via* Box–Cox transformations with an optimal Lambda using MATLAB codes, followed by the Student's t-test. In addition, Pearson and Spearman rank correlation studies were conducted between the estimated material parameters and experimental data, as well as a correlation study among material parameters based on the test regions. Once the correlation coefficients (r) were calculated, the relationship strengthened in the positive and negative directions as the correlation coefficients approached +1 and −1, respectively. In addition, no correlation was observed when the correlation coefficient was 0 or the p-value was 0.05 or more. The SPSS software was used for the statistical analysis.

Results

Stress–stretch response

The overall stress–stretch responses were nonlinear with pronounced regional differences (Figures 3, 4). In terms of the anisotropy of the blood vessel, the circumferential specimens were stiffer than the longitudinal specimens. In addition, the transition of the circumferential specimens from the low- to high-stiffness regimes was greater than that of the longitudinal specimens.

The slopes of the stress-stretch curves for aortic tissues represent the stiffness of the aortas, which depend on the test region, the loading direction, and the regime of nonlinear behavior. The slope of the distal posterior region (DPC and DPL) was the greatest in both regimes for each loading direction. Significant difference between the anterior and posterior sides was found in the high-

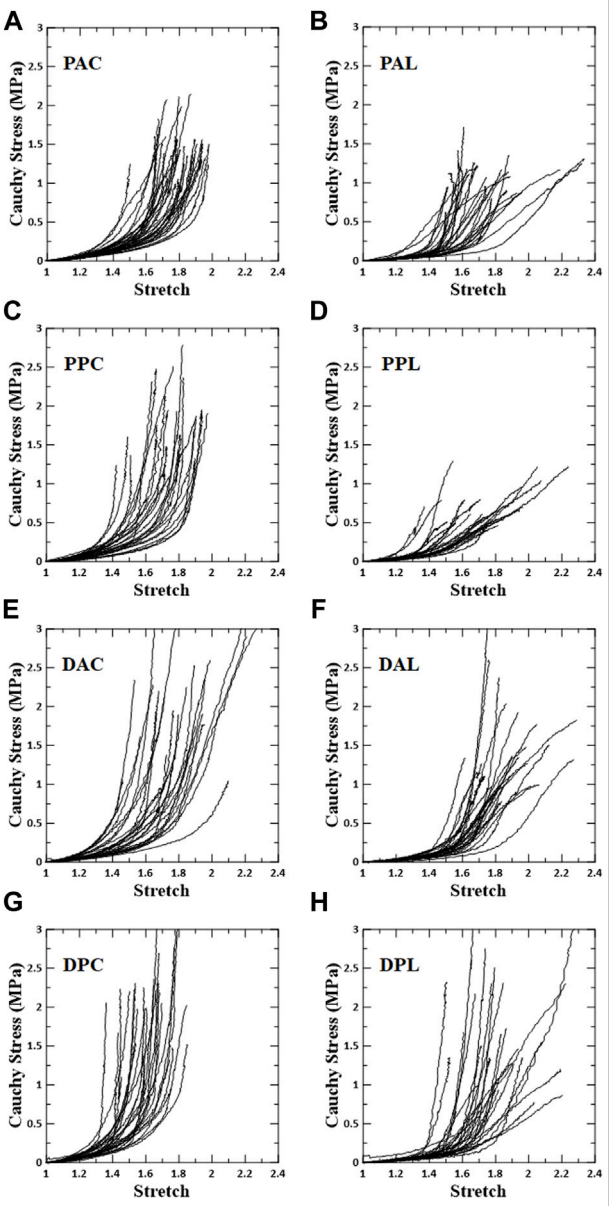

FIGURE 3
Stress–stretch response for each test region. Left column shows circumferential specimens [**(A)** PAC, **(C)** PPC, **(E)** DAC, and **(G)** DPC], and right column shows longitudinal specimens [**(B)** PAL, **(D)** PPL, **(F)** DAL, and **(H)** DPL].

stiffness regime (DPC vs. DAC, and PPL vs. PAL). Significant difference between the proximal and distal regions was found at the posterior side, but only in the longitudinal specimens of both regimes (PPL vs. DPL). In addition, the interaction between the circumferential and longitudinal regions was significant for the circumferential specimens (PAC vs. DPC) in both regimes and for the longitudinal specimens (PPL vs. DPL) in the high-stiffness regime.

Material parameters

The representative fitting results for each constitutive model along with the experimental data are shown in Figure 5. The results indicate that the fitting method used in this study is reliable.

Figures 6–8 show the Box–Whisker plots for the distribution of the estimated material parameters for three constitutive models based on the experimental data. Material parameters were calculated by sequentially applying pairs of experimental datasets for the circumferential and longitudinal specimens and were estimated without constraints. Subsequently, curve fitting was performed for 9,456 cases [{PAC–PAL (35 × 29 = 1,015 cases), PPC–PPL (25 × 25 = 625 cases), DAC–DAL (26 × 28 = 728 cases), DPC–DPL (28 × 28 = 784 cases)} × three constitutive models]. The minimum, maximum, first quartile (1Q), third quartile (3Q), and median of the estimated material parameters for all three models are listed in the Supplementary Appendix S1.

The values of the material parameters, c_1, b_1, b_2, b_3, b_4, b_5, and b_6, were obtained using the Fung model, as shown in Figure 6. The material parameters of c_1 on the DA specimens indicated the widest interquartile ranges (IQRs) and the highest median value of 0.3012. The values of b_1 and b_2 for the DP specimens were the most widely distributed in the IQR, with the highest median values of 2.4510 and 1.1120, respectively. Additionally, material parameters b_3 and b_5 indicated a wide IQR, with slight differences in the median over all test regions. The means ± standard deviations of all median values for parameters b_3 and b_5 were 1.2538 ± 0.1706 and 0.9191 ± 0.1705, respectively. The median values of b_4 and b_6 were relatively low compared with those of the other parameters. In particular, the material parameters of b_4 on the DP specimens and b_6 in the PP region were approximately zero.

The values of material parameters c, k_1, k_2, and γ obtained using the Holzapfel model are shown in Figure 7. In the regional comparison, the material parameter c of the PP specimens exhibited the highest median value of 0.0581. Meanwhile, the material parameter k_2 of the DP specimens indicated the widest IQR, with the highest median value of 3.3020. Material parameters k_1 and γ indicated only slight differences over all the test regions.

The values of material parameters c_1, c_2^1, c_2^2, c_3^1, c_3^2, G_1, G_2, G_h, and α for the CMM are shown in Figure 8. In the regional comparison, the values of c_1 for all test regions were low, and the median values were less than 0.0003. The material

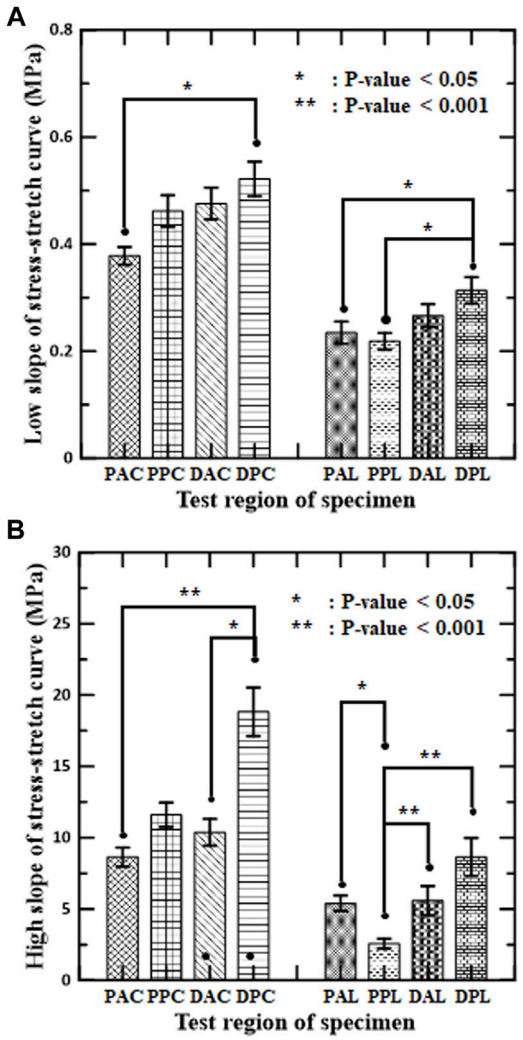

FIGURE 4
Mean and standard error of mean for slopes of stress–stretch curves of aortic tissues in **(A)** low-stiffness regimes and **(B)** high-stiffness regimes for circumferential and longitudinal specimens, respectively.

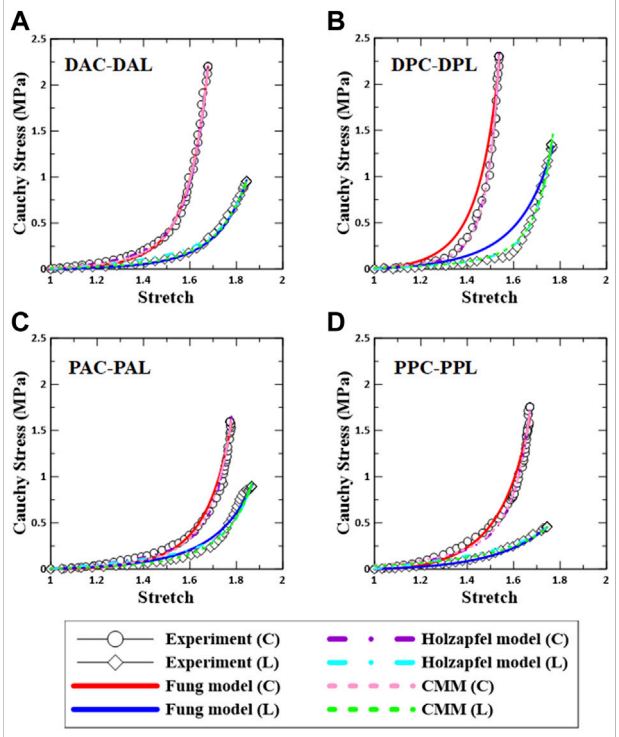

FIGURE 5
Comparison between experimental data and constitutive models based on regional aortic specimens. **(A)** DAC–DAL, **(B)** DPC–DPL, **(C)** PAC–PAL, and **(D)** PPC–PPL. C: circumferential specimen; L: longitudinal specimen.

parameter c_2^1 of the PA and DA specimens indicated wider IQR distributions with higher mean values compared with those of the other specimens. The material parameter c_2^2 of the DA specimens indicated the narrowest IQR, with the lowest median value of 0.2755, whereas c_3^1 of the DA specimens indicated the widest IQR. Meanwhile, the median value of c_2^2 of the DP specimens was the highest and indicated the widest IQR, whereas that of c_3^2 of the DP specimens was the lowest. The values of G_1 and G_2 did not differ significantly among all test regions. The material parameter G_h of the PP specimens indicated the widest IQR, with the highest median value of 1.3390. The mean value of α of the PA specimens was slightly lower than those of the others.

Significant difference of the material parameters

The Student's t-test for the estimated material parameters was performed to determine the difference among all test regions. It was discovered that material parameters c_1 and b_6 in the Fung model, k_2 and γ in the Holzapfel model, and c_2^2, G_h, and α in the CMM indicated significant differences between proximal and distal regions (PA vs. DA and PP vs. DP), anterior and posterior regions (PA vs. PP and DA vs. DP), and their interactions (PA vs. DP and PP vs. DA) simultaneously. The Student's t-test shows that the material parameters of the constitutive models depended on the regions of the aortic tissue.

Statistical correlations

The estimated material parameters were used sequentially for the correlation study. Spearman rank correlation coefficients (r) were computed to quantify the correlation degree between the

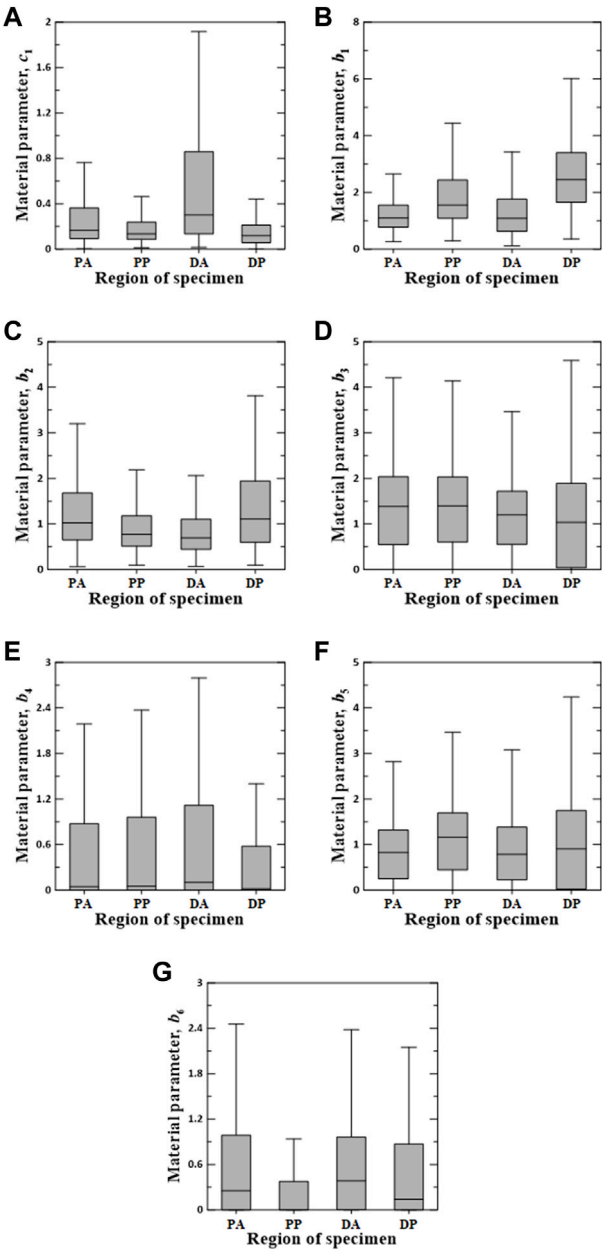

FIGURE 6
Random value distribution of material parameters estimated using Fung model for PA, PP, DA, and DP specimens. **(A)** c_1, **(B)** b_1, **(C)** b_2, **(D)** b_3, **(E)** b_4, **(F)** b_5, and **(G)** b_6.

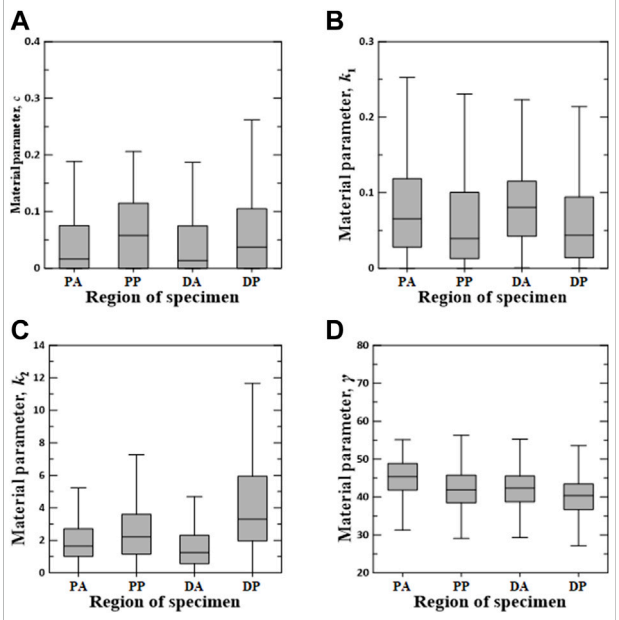

FIGURE 7
Random value distribution of material parameters estimated using Holzapfel model for PA, PP, DA, and DP specimens. **(A)** c, **(B)** k_1, **(C)** k_2, and **(D)** γ.

regional experimental data (i.e., slopes of stress-stretch curves) and material parameters or among the material parameters. Only cases exhibiting a correlation in all test regions are reported, as shown in Figures 9–11. To understand the general trend from the correlation study, the average values of the correlation coefficients over the four test regions (PA, PP, DA, and DP) were obtained.

In the correlation study between the parameters of Fung model and experimental results, b_1 (r = 0.665 on average) indicated the strongest correlation with the slope in the high-stiffness regime, hereinafter known as the high slope, in the circumferential specimens, followed by b_5 (0.408) (Figure 9A). Meanwhile, b_2 showed the strong correlation with both high slope (0.617) and low slope (0.310) in the longitudinal specimens.

In the correlation study among the material parameters of the Fung model, c_1 indicated the strongest correlation with b_1 (−0.578), followed by b_2 (−0.492) (Figure 9B). Next, b_1 and b_2 indicated a strong correlation with b_5 (0.458) and b_6 (0.364), respectively.

For the correlation study between the parameters of Holzapfel model and experimental results, γ indicated the strongest correlation with the high slope (0.583) and low slope (0.380) in the longitudinal specimens (Figure 10A). Meanwhile, k_2 (0.485) showed the strong correlation with the high slope in the circumferential specimens.

In the correlation study among the material parameters of the Holzapfel model, c indicated the strongest correlation with k_1 (−0.759), followed by k_2 (0.459) (Figure 10B). In addition, k_1 was negatively correlated with k_2 (-0.539).

In the correlation study between the parameters of CMM and experimental results, α showed the strongest negative correlation with the high slope (−0. 580) and low slope (−0.377) in the longitudinal specimens (Figure 11A). Meanwhile, G_h (0.376) had the strong positive correlation with the high slope in the

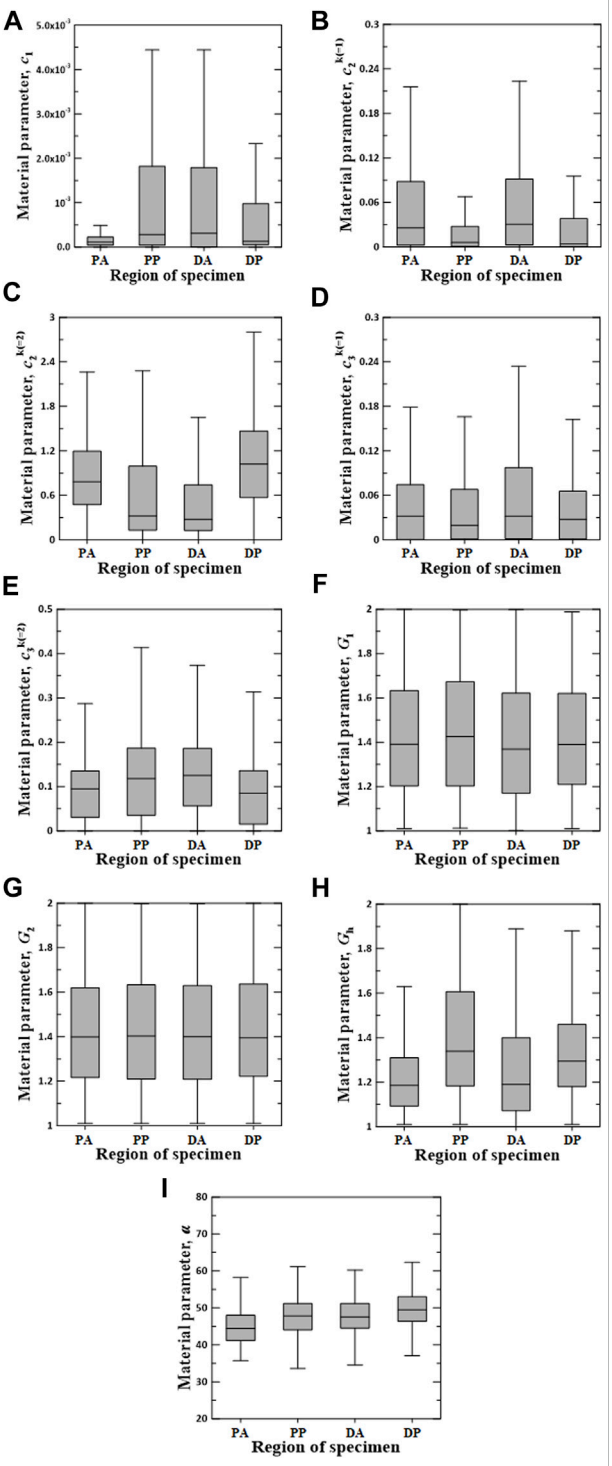

FIGURE 8
Random value distribution of material parameters estimated using CMM for PA, PP, DA, and DP specimens. **(A)** c_1, **(B)** c_2^1, **(C)** c_2^2, **(D)** c_3^1, **(E)** c_3^2, **(F)** G_1, **(G)** G_2, **(H)** G_h, and **(I)** α.

circumferential specimens, followed by c_2^1 (−0.307) with the negative coefficient.

In the correlation study among the material parameters of the CMM, c_2^2 indicated the strongest correlation with G_h (−0.410) (Figure 11B). In the correlation analysis between c_2^1 and G_h, the absolute values of the coefficients were the highest, but PP indicated a positive correlation, whereas PA, DA, and DP indicated a negative correlation. The combinations of positive and negative coefficients indicated non-uniform correlations over the test region.

Discussion

In this study, first of all, a virtual 2D regional dataset is generated by experimental data from uniaxial tensile tests to overcome the limitations of conventional experimental setups to characterize the anisotropic behavior of the artery. We use cross-mapping to determine the material parameters by applying experimental data in both loading directions. The relationship between the physical features (arterial stiffness) and constitutive parameters is determined in different regions. Subsequently, we present the ranges of material parameters and propose an integrative method to characterize the region-dependent material parameters for the nonlinear anisotropic materials.

Kim and Baek (Kim and Baek, 2011) and Kim et al. (Kim et al., 2013) report the spatial variations in the stiffness of the aorta for both circumferential and longitudinal regions *via* the extension-inflation test. In this study, uniaxial tensile tests present consistent significant differences. The circumferential specimen is stiffer than the longitudinal specimen in both the low- and high-stiffness regimes, and the circumferential and longitudinal differences are found among several regions. In particular, the DP exhibits the stiffest slope for each of the circumferential and longitudinal loading directions in both low- and high-stiffness regimes. This is likely due to the non-uniform fiber orientations on the different test regions of the aorta. Various histological and mechanical analyses indicate diverse fiber orientations of the intimal, medial, and adventitial strips (Huang et al., 2016; Niestrawska et al., 2016; Yu et al., 2018; Babici et al., 2020; Concannon et al., 2020; Jadidi et al., 2020; Díaz et al., 2021). Because the DP is the thinnest region of the aorta, the transmural variation in the fiber orientation and the contribution of fibers to the stress–stretch relationship in the DP may differ from those of the other test regions.

Although the material behavior of the aorta is described by a constitutive model, it is not uniquely determined for the best representation. Complex anisotropic materials, such as biological tissues, typically have a single isotropic plane, so

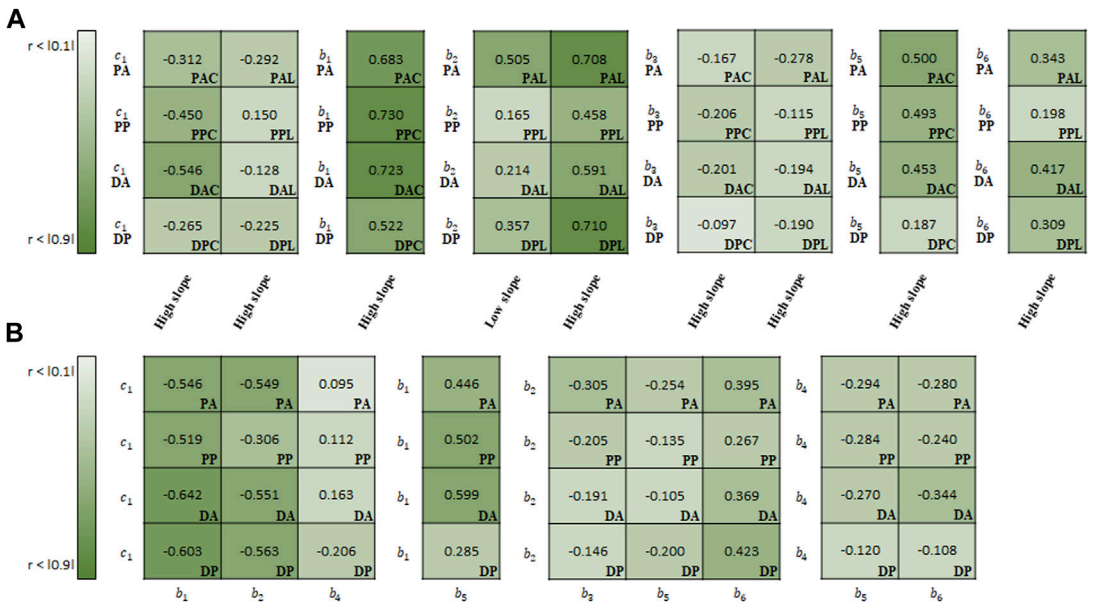

FIGURE 9
Spearman rank correlation coefficients **(A)** between material parameters of Fung model and experimental results and **(B)** among the material parameters.

that they can be idealized as transversely isotropic in hyperelastic models (O'Shea et al., 2019). In this study, the aorta is assumed to be a transversely isotropic material to simulate the uniaxial tensile test. Although this approach has limitations in ensuring the positive definiteness of the fourth-order stiffness tensor, it provides a stable solution to elasticity problems if a proposed model is calibrated based on experimental data (O'Shea et al., 2019). In addition, in the uniaxial test, the transversely isotropic model to consider only I_4 invariant shows responses similar to that of the method considering both I_4 and I_5 invariants (Feng et al., 2016). In shear deformation, however, both should be considered, as the results depend on whether I_5 invariant is considered.

In this study, three constitutive models, i.e., the Fung model, Holzapfel model, and CMM, are considered with this methodology to describe the material responses in the uniaxial test. All three models present good fits with the stress–stretch curves obtained from the uniaxial test. The Fung model has the advantage of fitting curves with a large variation, whereas the Holzapfel model and CMM have the significant advantage of considering vascular constituents such as elastin and collagen. In the CMM, the highest number of material parameters is used, including the pre-stretch value in the homeostatic state. Nevertheless, it presents a substantial advantage in that it can accurately describe nonlinear behavior of the aorta, particularly in the high-stiffness regime. To improve the computational efficiency of the CMM composed of many parameters, the estimation method is classified into two steps in a previous study (Seyedsalehi et al., 2015). However, unlike the previous study, the method used in this study involves integrating material parameters for the two loading directions into the virtual biaxial behavior. No significant difference in the computational efficiency is observed between the two methods regardless of integration.

This study shows that the material parameters of each constitutive model can express the mechanical behavior of the regional aortic tissue. There are significant differences in the material parameters with respect to the regions. For example, the material parameter γ in the Holzapfel model and the material parameter α in the CMM exhibit the fiber orientation of the artery depending on the test regions. It is, however, important to note that, although γ and α represent the fiber orientations, the single parameter alone cannot have much weight on interpreting the physical meaning due to its inter-correlation with other parameters. Evidently, γ in the Holzapfel model indicated the highest mean for the PA, whereas α in the CMM indicated the highest mean for the DP.

In addition to regional differences, strong correlations are presented between regional aortic behavior and material parameters or among material parameters for the same test region. As shown in Figures 9–11, a higher absolute value of the correlation coefficient indicates a stronger correlation. In the Fung model, the material parameters c_1, b_1, b_2, b_3, b_5, and b_6 correlate with the slope of the high-stiffness regime. Although the material parameters of the Fung model provide a description of the stress–stretch relationship phenomenologically, they are distinct with respect to the regions and regimes when describing the mechanical behavior with the physical characteristics and slopes.

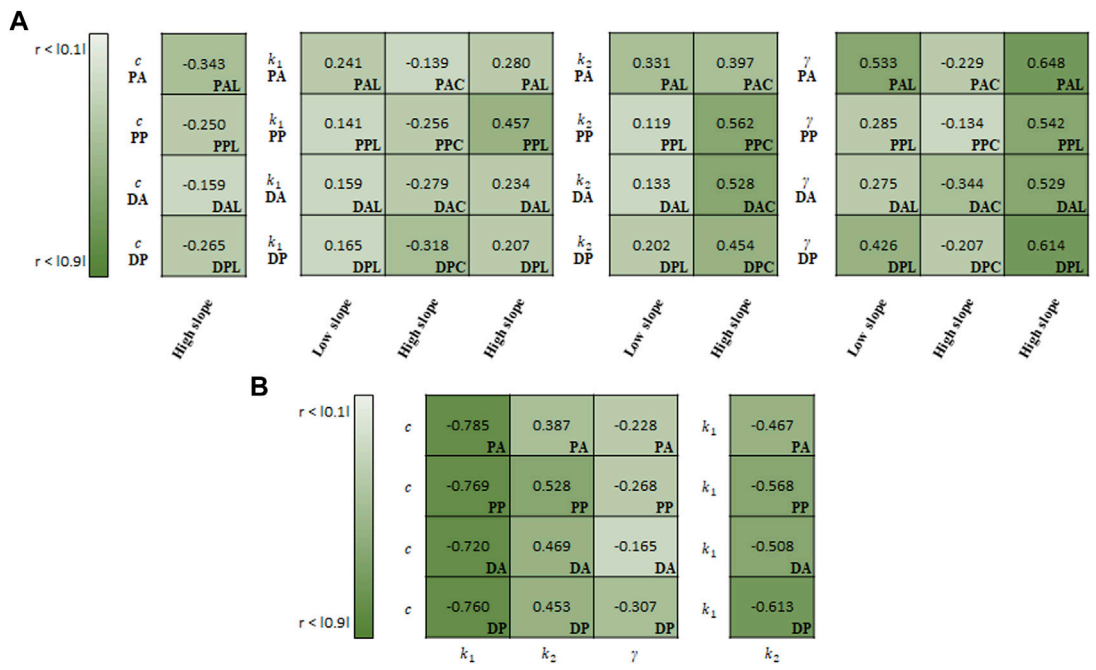

FIGURE 10
Spearman rank correlation coefficients **(A)** between material parameters of Holzapfel model and experimental results and **(B)** among the material parameters.

FIGURE 11
Spearman rank correlation coefficients **(A)** between material parameters of CMM and experimental results and **(B)** among the material parameters.

In particular, the material parameters b_1 and b_2 have a direct effect on the simulating the stiffness of the materials in each loading direction, because they are multiplied by the stretch in each loading direction. The ratio of b_1/b_2 can be used to characterize the anisotropic behavior of the materials. In this study, this ratio may give a better way to represent the behavior of materials in the correlation study between the ratio and stiffness regime. It ranges from −0.473 to −0.171 among the slopes in the low-stiffness regime for longitudinal specimens, and from 0.298 to 0.503/from −0.645 to −0.473 among the slopes in the high-stiffness regime for circumferential/longitudinal specimens, respectively. In the Holzapfel model, all parameters correlate with the slope in the high-stiffness regime, while the parameters k_1, k_2, and γ correlate with the slope in the low-stiffness regime for the longitudinal specimens. In addition, the parameter c is inter-correlated with all other parameters, and particularly has the strongest negative correlation with k_1. Finally, in the CMM, the parameters c_2^1, c_2^2, c_3^1, G_h, and α correlate with the slope in the high-stiffness regime, while G_h and α show the correlation with the slope in the low-stiffness regime for the longitudinal specimens. In particular, G_h has the greatest inter-correlation with others, c_1, c_2^1, c_2^2, c_3^1, and c_3^2 with c_2^1 showing the strongest correlation. In this correlation study, these findings support the assumption that the three constitutive models can simulate the region-dependent mechanical behavior of the aorta in both low- and high-stiffness regimes.

There are limitations of this study. For the experimental protocol, the deformation of aortic segments is assumed to be uniform, whereas the sample might not deform uniformly since the blood vessel is a composite material. However, the specimens are small, and their spatial variations are generally neglected in the uniaxial tensile test. Especially, the stretch is defined by the change in distance between two microspheres because it gives an accurate estimation of local deformation at the central region, instead of measuring the grip movement in the uniaxial test. Nonetheless, the specimens are not necessarily ruptured in the central region between the two microspheres so the uniformity assumption cannot apply to the rupture behavior. To further investigate the nonuniform deformation, adding more markers to the sample or utilizing the digital image correlation technique may be an alternative.

The statistical analysis performed in this study confirms that the statistical significance of key parameters is important in differentiating the regional mechanical behavior of the aorta. However, the constitutive models used in this study are nonlinear and, as shown in the correlation studies, the physical characteristics (e.g., stiffness in high-stiffness regime) are highly correlated with the material parameters of each model. Analyzing such multidimensional data (regions, loading directions, low- and high-stiffness regimes, constitutive models and material parameters, and enhanced experimental measurements) requires further studies using a machine learning approach to predict the regional mechanical behavior of the blood vessel for the virtual aorta.

Due to the complexity between the clinical features and model parameters, the number of model parameters is reduced to estimate the physical features within the model. A decrease in the number of independent parameters may be more advantageous, based on overall nonlinear sensitivity analysis and model uncertainty quantification. For example, a multidimensional virtual dataset can quantify model uncertainties through correlation studies. A linear regression model with Bayesian inference approaches can be used to describe significant material parameters using backward elimination (Akkoyun et al., 2020). Alternatively, the Gaussian mixture model is based on an unsupervised machine learning approach involving an uncertainty measure (probability) (Paalanen et al., 2006), which determines how much the material parameters are associated with a specific region by considering the mean and covariance of each cluster and mixing probability. Therefore, the combination of material parameters can improve the prediction capability of the model with respect to the different regions and the selection of a constitutive model, appropriately characterizing the regional mechanical behavior of the blood vessel based on a machine learning approach.

In summary, this study presents the region-dependent mechanical characterization of the porcine thoracic aorta by generating virtual 2D datasets from the uniaxial test using three constitutive models. Physics-based modeling is essential to associate with physical and clinical features. The development of computational models can further promote the era of “virtual human” or “virtual aorta.” However, the development of specific models is hampered by the scarcity of material test data for individual patients, which are relevant to clinical setups. In particular, tissue mechanical tests of young human aortic specimens are rarely available, even if they exist. The virtual biaxial data presented herein may serve as an alternative to material behavior in young human aortas.

Data availability statement

The original contributions presented in the study are included in the article/Supplementary Material, further inquiries can be directed to the corresponding author.

Ethics statement

Ethical review and approval were not required in this study because the porcine aortas used in this study were provided by a local slaughterhouse.

Author contributions

DR, SB, and JK contributed to conception and design of the study. JK performed the experiments and data analysis.

DR performed computation and statistical analysis. SB developed the theoretical and computational framework and verified the analytical methods. JK and DR wrote the first draft of the manuscript. All authors discussed and contributed to manuscript revision and approved the submitted version.

Funding

This study was supported partially by the National Institute of Health (R01HL115185), the National Research Foundation of Korea (NRF) grant funded by the Korea government (No. 2021R1C1C2004703), and the Basic Science Research Program through the NRF funded by the Ministry of Education (No. 2021R1I1A3059740).

Acknowledgments

The authors acknowledge that Dr. Emrah Akkoyun provided data-driven learning expertise and assisted in the editing of the manuscript.

Conflict of interest

The authors declare that the research was conducted in the absence of any commercial or financial relationships that could be construed as a potential conflict of interest.

Publisher's note

All claims expressed in this article are solely those of the authors and do not necessarily represent those of their affiliated organizations, or those of the publisher, the editors and the reviewers. Any product that may be evaluated in this article, or claim that may be made by its manufacturer, is not guaranteed or endorsed by the publisher.

Supplementary material

The Supplementary Material for this article can be found online at: https://www.frontiersin.org/articles/10.3389/fbioe.2022.937326/full#supplementary-material

References

Akkoyun, E., Kwon, S. T., Acar, A. C., Lee, W., and Baek, S. (2020). Predicting abdominal aortic aneurysm growth using patient-oriented growth models with two-step Bayesian inference. *Comput. Biol. Med.* 117, 103620. doi:10.1016/j.compbiomed.2020.103620

Annaidh, A. N., Bruyère, K., Destrade, M., Gilchrist, M. D., Maurini, C., Otténio, M., et al. (2012). Automated estimation of collagen fibre dispersion in the dermis and its contribution to the anisotropic behaviour of skin. *Ann. Biomed. Eng.* 40 (8), 1666–1678. doi:10.1007/s10439-012-0542-3

Babici, D., Kudej, R. K., McNulty, T., Zhang, J., Oydanich, M., Berkman, T., et al. (2020). Mechanisms of increased vascular stiffness down the aortic tree in aging, premenopausal female monkeys. *Am. J. Physiology-Heart Circulatory Physiology* 319 (1), H222–H234. doi:10.1152/ajpheart.00153.2020

Chakshu, N. K., Sazonov, I., and Nithiarasu, P. (2021). Towards enabling a cardiovascular digital twin for human systemic circulation using inverse analysis. *Biomech. Model. Mechanobiol.* 20 (2), 449–465. doi:10.1007/s10237-020-01393-6

Chuong, C. J., and Fung, Y. C. (1983). Three-dimensional stress distribution in arteries. *J. Biomech. Eng.* 105 (3), 268–274. doi:10.1115/1.3138417

Concannon, J., Dockery, P., Black, A., Sultan, S., Hynes, N., McHugh, P. E., et al. (2020). Quantification of the regional bioarchitecture in the human aorta. *J. Anat.* 236 (1), 142–155. doi:10.1111/joa.13076

de Rooij, R., and Kuhl, E. (2016). Constitutive modeling of brain tissue: Current perspectives. *Appl. Mech. Rev.* 68 (1), 010801. doi:10.1115/1.4032436

Díaz, C., Peña, J. A., Martínez, M. A., and Peña, E. (2021). Unraveling the multilayer mechanical response of aorta using layer-specific residual stresses and experimental properties. *J. Mech. Behav. Biomed. Mat.* 113, 104070. doi:10.1016/j.jmbbm.2020.104070

Feng, Y., Okamoto, R. J., Genin, G. M., and Bayly, P. V. (2016). On the accuracy and fitting of transversely isotropic material models. *J. Mech. Behav. Biomed. Mat.* 61, 554–566. doi:10.1016/j.jmbbm.2016.04.024

Harkness, M. L. R., Harkness, R. D., and McDonald, D. A. (1957). The collagen and elastin content of the arterial wall in the dog. *Proc. R. Soc. Lond. B Biol. Sci.* 146 (925), 541–551. doi:10.1098/rspb.1957.0029

Holzapfel, G. A., Gasser, T. C., and Ogden, R. W. (2000). A new constitutive framework for arterial wall mechanics and a comparative study of material models. *J. Elast.* 61, 1–48. doi:10.1023/A:1010835316564

Hose, D. R., Lawford, P. V., Huberts, W., Hellevik, L. R., Omholt, S. W., and van de Vosse, F. N. (2019). Cardiovascular models for personalised medicine: Where now and where next? *Med. Eng. Phys.* 72, 38–48. doi:10.1016/j.medengphy.2019.08.007

Huang, A. H., Balestrini, J. L., Udelsman, B. V., Zhou, K. C., Zhao, L., Ferruzzi, J., et al. (2016). Biaxial stretch improves elastic fiber maturation, collagen arrangement and mechanical properties in engineered arteries. *Tissue Eng. Part C. Methods* 22 (6), 524–533. doi:10.1089/ten.TEC.2015.0309

Humphrey, J. D., and Rajagopal, K. R. (2002). A constrained mixture model for growth and remodeling of soft tissues. *Math. Models Methods Appl. Sci.* 12 (3), 407–430. doi:10.1142/S0218202502001714

Jadidi, M., Habibnezhad, M., Anttila, E., Maleckis, K., Desyatova, A., Mactaggart, J., et al. (2020). Mechanical and structural changes in human thoracic aortas with age. *Acta Biomater.* 103, 172–188. doi:10.1016/j.actbio.2019.12.024

Kim, J., and Baek, S. (2011). Circumferential variations of mechanical behavior of the porcine thoracic aorta during the inflation test. *J. Biomech.* 44 (10), 1941–1947. doi:10.1016/j.jbiomech.2011.04.022

Kim, J., Hong, J.-W., and Baek, S. (2013). Longitudinal differences in the mechanical properties of the thoracic aorta depend on circumferential regions. *J. Biomed. Mater. Res. Part A* 101A, 1525–1529. doi:10.1002/jbm.a.34445

Martins, P. A. L. S., Natal Jorge, R. M. N., and Ferreira, A. J. M. (2006). A comparative study of several material models for prediction of hyperelastic properties: Application to silicone-rubber and soft tissues. *Strain* 42 (3), 135–147. doi:10.1111/j.1475-1305.2006.00257.x

Niederer, S. A., Aboelkassem, Y., Cantwell, C. D., Corrado, C., Coveney, S., Cherry, E. M., et al. (2020). Creation and application of virtual patient cohorts of heart models. *Phil. Trans. R. Soc. A* 378, 20190558. doi:10.1098/rsta.2019.0558

Niestrawska, J. A., Viertler, C., Regitnig, P., Cohnert, T. U., Sommer, G., and Holzapfel, G. A. (2016). Microstructure and mechanics of healthy and aneurysmatic abdominal aortas: Experimental analysis and modelling. *J. R. Soc. Interface* 13 (124), 20160620. doi:10.1098/rsif.2016.0620

Ogden, R. W. (1997). *Non-linear elastic deformations*. New York: Dover Publication, Inc.

O'Shea, D. J., Attard, M. M., and Kellermann, D. C. (2019). Hyperelastic constitutive modelling for transversely isotropic composites and orthotropic biological tissues. *Int. J. Solids Struct.* 169, 1–20. doi:10.1016/j.ijsolstr.2018.07.013

Paalanen, P., Kamarainen, J. K., Ilonen, J., and Kälviäinen, H. (2006). Feature representation and discrimination based on Gaussian mixture model probability densities—practices and algorithms. *Pattern Recognit. DAGM.* 39 (7), 1346–1358. doi:10.1016/j.patcog.2006.01.005

Schroeder, F., Polzer, S., Slažanský, M., Man, V., and Skácel, P. (2018). Predictive capabilities of various constitutive models for arterial tissue. *J. Mech. Behav. Biomed. Mat.* 78, 369–380. doi:10.1016/j.jmbbm.2017.11.035

Seyedsalehi, S., Zhang, L., Choi, J., and Baek, S. (2015). Prior distributions of material parameters for Bayesian calibration of growth and remodeling computational model of abdominal aortic wall. *J. Biomech. Eng.* 137 (10), 101001. doi:10.1115/1.4031116

Yu, X., Wang, Y., and Zhang, Y. (2018). Transmural variation in elastin fiber orientation distribution in the arterial wall. *J. Mech. Behav. Biomed. Mat.* 77, 745–753. doi:10.1016/j.jmbbm.2017.08.002

Zeinali-Davarani, S., Sheidaei, A., and Baek, S. (2011). A finite element model of stress-mediated vascular adaptation: Application to abdominal aortic aneurysms. *Comput. Methods Biomechanics Biomed. Eng.* 9, 803–817. doi:10.1080/10255842.2010.495344

Zulliger, M. A., Fridez, P., Hayashi, K., and Stergiopulos, N. (2004). A strain energy function for arteries accounting for wall composition and structure. *J. Biomech.* 37 (7), 989–1000. doi:10.1016/j.jbiomech.2003.11.026

frontiers | Frontiers in Bioengineering and Biotechnology

TYPE Original Research
PUBLISHED 16 November 2022
DOI 10.3389/fbioe.2022.1033713

OPEN ACCESS

EDITED BY
Shireen Y. Elhabian,
The University of Utah, United States

REVIEWED BY
Pablo Martinez-Legazpi,
Gregorio Marañón Hospital, Spain
Edem Binka,
The University of Utah, United States

*CORRESPONDENCE
Patricia Lopes,
patricia.Lopes@materialise.be

SPECIALTY SECTION
This article was submitted to Biomechanics,
a section of the journal
Frontiers in Bioengineering and Biotechnology

RECEIVED 31 August 2022
ACCEPTED 31 October 2022
PUBLISHED 16 November 2022

CITATION
Lopes P, Van Herck PL, Ooms JF, Van Mieghem NM, Wirix-Speetjens R, Sijbers J, Vander Sloten J and Bosmans J (2022), Automated mitral valve assessment for transcatheter mitral valve replacement planning.
Front. Bioeng. Biotechnol. 10:1033713.
doi: 10.3389/fbioe.2022.1033713

Automated mitral valve assessment for transcatheter mitral valve replacement planning

Patricia Lopes[1,2,3]*, Paul L. Van Herck[3], Joris F. Ooms[4], Nicolas M. Van Mieghem[4], Roel Wirix-Speetjens[1], Jan Sijbers[5], Jos Vander Sloten[2] and Johan Bosmans[3]

[1]Materialise N.V, Medical Department, Leuven, Belgium, [2]Division of Biomechanics—BMe, Department of Mechanical Engineering, KU Leuven, Leuven, Belgium, [3]Department of Cardiology, University Hospital Antwerp, Antwerp, Belgium, [4]Department of Cardiology, Erasmus M.C, Rotterdam, Netherlands, [5]imec-VisionLab, Physics Department, University of Antwerp, Antwerp, Belgium

Transcatheter mitral valve replacement (TMVR) has emerged as a minimally invasive alternative for treating patients suffering from mitral valve disease. The number of TMVR procedures is expected to rise as devices currently in clinical trials obtain approval for commercialization. Automating the planning of such interventions becomes, therefore, more relevant in an attempt to decrease inter-subject discrepancies and time spent in patient assessment. This study evaluates the performance of an automated method for detection of anatomical landmarks and generation of relevant measurements for device selection and positioning. Cardiac CT scans of 70 patients were collected retrospectively. Fifty scans were used to generate a statistical shape model (SSM) of the left heart chambers at ten different timepoints, whereas the remaining 20 scans were used for validation of the automated method. The clinical measurements resulting from the anatomical landmarks generated automatically were compared against the measurements obtained through the manual indication of the corresponding landmarks by three observers, during systole and diastole. The automatically generated measurements were in close agreement with the user-driven analysis, with intraclass correlation coefficients (ICC) consistently lower for the saddle-shaped (ICC_{Area} = 0.90, $ICC_{Perimeter\ 2D}$ = 0.95, $ICC_{Perimeter\ 3D}$ = 0.93, $ICC_{AP\text{-}Diameter}$ = 0.71, $ICC_{ML\text{-}Diameter}$ = 0.90) compared to the D-shaped annulus (ICC_{Area} = 0.94, $ICC_{Perimeter\ 2D}$ = 0.96, $ICC_{Perimeter\ 3D}$ = 0.96, $ICC_{AP\text{-}Diameter}$ = 0.95, $ICC_{ML\text{-}Diameter}$ = 0.92). The larger differences observed for the saddle shape suggest that the main discrepancies occur in the aorto-mitral curtain. This is supported by the fact that statistically significant differences are observed between the two annulus configurations for area ($p < 0.001$), 3D perimeter ($p = 0.009$) and AP diameter ($p < 0.001$), whereas errors for 2D perimeter and ML diameter

Abbreviations: AP, antero-posterior; ICC, intraclass correlation coefficient; LVOT, left ventricular outflow tract; ML, medio-lateral; MR, mitral regurgitation; SSM, statistical shape model; TMVR, transcatheter mitral valve replacement; TT, trigone-to-trigone.

remained almost constant. The mitral valve center deviated in average 2.5 mm from the user-driven position, a value comparable to the inter-observer variability. The present study suggests that accurate mitral valve assessment can be achieved with a fully automated method, what could result in more consistent and shorter pre-interventional planning of TMVR procedures.

KEYWORDS

pre-interventional planning, automated mitral valve assessment, saddle- and D-shaped mitral annulus, statistical shape model (SSM), transcatheter mitral valve replacement (TMVR), cardiac CT

1 Introduction

Transcatheter mitral valve replacement (TMVR) therapies have been adopted as a reliable option in the treatment of mitral regurgitation (MR), in an attempt to address the high risk posed by surgical treatment and the limitations of edge-to-edge transcatheter mitral valve repair (Alperi et al., 2021; Aoun et al., 2021). Due to the minimally invasive nature of these interventions, pre-procedural imaging plays a crucial role in guaranteeing successful outcomes (Natarajan et al., 2016). Upon assessment of the valve pathology and severity of valve dysfunction, including the morphologic and anatomic characterization of mitral leaflets (Mackensen et al., 2018), the assessment of the mitral annulus is a pivotal step in TMVR planning. When considering device sizing, excessive oversizing may result in annular rupture or left ventricular outflow tract (LVOT) obstruction. Reversely, insufficient oversizing may result in paravalvular regurgitation or prosthesis embolization (Thériault-Lauzier et al., 2016; Murphy et al., 2017). The non-planar saddle shape of the mitral annulus, in combination with the dynamic changes that it undergoes during the cardiac cycle, represent, however, undeniable challenges in device size estimation.

The mitral annulus' shape approximates a hyperbolic paraboloid, with peaks located anteriorly and posteriorly, and valleys located medially and laterally in close proximity to the fibrous trigones. The anterior horn is anatomically coupled with the aortic valve, in the so-called aorto-mitral continuity, and spans between the two trigones. The posterior annulus encompasses the remainder of the annular perimeter at the insertion of the posterior mitral valve leaflet (Silbiger, 2012; Blanke et al., 2014; Weir-McCall et al., 2018). For the pre-interventional assessment of the mitral valve, the annulus is typically represented as a cubic spline fitted to points placed at regular intervals around the mitral valve center. The annular plane is defined as the least-squares plane fitted to the 3D annular contour. Quantification of the mitral annulus dimensions is performed both in two and three dimensions, with the area commonly calculated based on the 2D spline resulting from the projection of the annular contour onto the annular plane. The maximum and minimum diameters, or alternatively antero-posterior (AP) and medio-lateral (ML) diameters, are evaluated either in 2D or 3D, depending on the study. The annulus perimeter, however, is often evaluated based on both the original 3D and the projected 2D contours (Blanke et al., 2014) (Figure 1).

(Blanke et al., 2014) have proposed the exclusion of the anterior horn of the saddle-shaped annulus for TMVR assessment, creating a D-shaped annulus suitable for planar measurements, with the anterior border a virtual line connecting the fibrous trigones. The main motivation for representing the saddle-shaped mitral annulus as a D-shaped ring is related to the potential mismatch between the device shape and the annular landing zone. Because some devices are cylindrical whereas others are D-shaped, the estimation of the device size needs to take into account the potential obstruction of the LVOT.

Throughout the cardiac cycle, the annulus moves in a passive manner determined by the contraction and relaxation of the

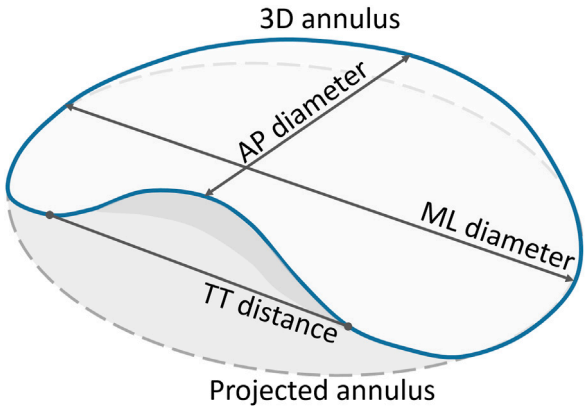

FIGURE 1
Quantification parameters of the mitral annulus. The full blue curve represents the 3D saddle-shaped annulus, whereas the grey dashed curve represents the projection of the mitral annulus onto its best-fit plane. Both the 3D and the projected 2D perimeters were measured. Only the grey area, corresponding to the projected curve, was calculated. The two main diameters, namely the AP and ML diameters, were measured based on the 3D annulus curve. The TT distance was measured in 3D, with the TT-line replacing the anterior portion of the saddle-shaped curve to represent the D-shaped annulus.

adjacent atrial and ventricular walls, and the motion of the aortic root (Silbiger, 2012). Such motion can have a considerable impact in the mitral annulus dimensions across the cardiac cycle, which can determine the success or failure of a device to be implanted through a transcatheter approach.

As the number of procedures is expected to rise, a consistent methodology to characterize the mitral valve and identify the most suitable TMVR device for each patient is of paramount importance. Automated methods can be particularly attractive, as they provide consistent results, while being faster than the standard manual approach. However, the accuracy of such methods needs to be ensured. Therefore, with this study, we aimed at evaluating the performance of a fully automated approach for the assessment of the mitral valve apparatus during pre-interventional planning of TMVR procedures. Specifically, we compare the accuracy of the measurements resulting from this automated method with those resulting from manual indications by three observers, in both diastole and systole.

2 Materials and methods

2.1 Study population

This retrospective study was approved by the institutional Ethical Committee (Antwerp University Hospital).

The study population consisted of 70 consecutive patients, who underwent a retrospective ECG-gated cardiac CT between November 2017 and January 2019. The CT scan was acquired as a routine diagnostic procedure for the evaluation of thoracic pain. All patients aged 18 or more, with no coronary artery disease and no mitral valve dysfunction were considered eligible for enrolment in the study. Exclusion criteria were insufficient computed tomographic image quality and prior valvular heart intervention.

2.2 Imaging protocol

Cardiac CT examinations were performed using a 64-slice GE Lightspeed scanner (GE Healthcare, Milwaukee, WI, United States). Images were obtained with a 64 mm × 0.625 mm slice collimation and a gantry rotation time of 0.35 ms. Tube voltage and current were adapted to patient's body mass index (100–120 kV; 450–350 mA). A retrospective ECG-triggered scanning protocol was used. For contrast-enhanced image acquisition, a non-ionic contrast agent (Iomeron 350, 110 ml) and saline flush (60 ml) was injected into an antecubital vein using a Nemoto injection system. This injection protocol is triphasic, with 80 ml contrast at a flow rate of 5 ml/s, followed by 30 ml contrast + 30 ml saline at 2.5 ml/s and finally 30 ml saline at 2.5 ml/s.

CT data were subsequently reconstructed at regular locations of the RR-interval, resulting in 10 time points of the cardiac cycle.

2.3 Statistical shape model generation

2.3.1 End-diastolic model

The first cardiac phase of each CT scan, corresponding to end-diastole, was segmented in Mimics 21.0 (Materialise N.V., Leuven, Belgium), using a semi-automated left heart segmentation tool. Manual adjustments were performed when deemed necessary, with special attention for the region at the level of the mitral valve. Surface models were then generated from the segmentation masks of the left atrium, left ventricle and aorta. These surface models were subsequently imported in 3-matic 13.0 (Materialise N.V., Leuven, Belgium) for editing, namely by 1) trimming of the pulmonary veins and the ascending aorta, 2) Boolean Union of the three surfaces into a single manifold surface, 3) smoothing, and 4) mesh optimization. Finally, the different surfaces included in the final manifold were labelled using prime numbers between 2 and 19 and the boundaries between surfaces were labelled using the product of the two adjoining surfaces, in a similar manner to that described by (Hoogendoorn, 2013). This resulted in a total of 15 unique labels with values ranging between 2 and 133, for identification of the left heart structures and their boundaries.

Once the surface models of the left heart for the fifty subjects containing analogous surface information were available, a point correspondence method was employed. A template-based method, built upon the works of (Amberg et al., 2007), (Danckaers et al., 2014), and (van Dijck, 2021), was modified to take into account the surface labeling, preventing corresponding points from belonging to different anatomical structures. Finally, a principal component analysis (PCA) was performed to construct the end-diastolic SSM.

2.3.2 Dynamic model

The segmentation of the left heart obtained for the end-diastolic phase was propagated to the subsequent cardiac phases using an automated method available in Mimics 21.0. The end-diastolic SSM was then fitted to the resulting surface models to obtain surface correspondence between the multiple time points of the cardiac cycle and the different subjects. A new SSM was generated including the 500 instances, containing information on both anatomical and dynamic variation between subjects.

The following landmarks were manually indicated on the mean instance of the dynamic SSM: the three aortic valve cusps, namely right coronary, left coronary and non-coronary cusps; the medial and lateral trigones, and the left ventricular apex.

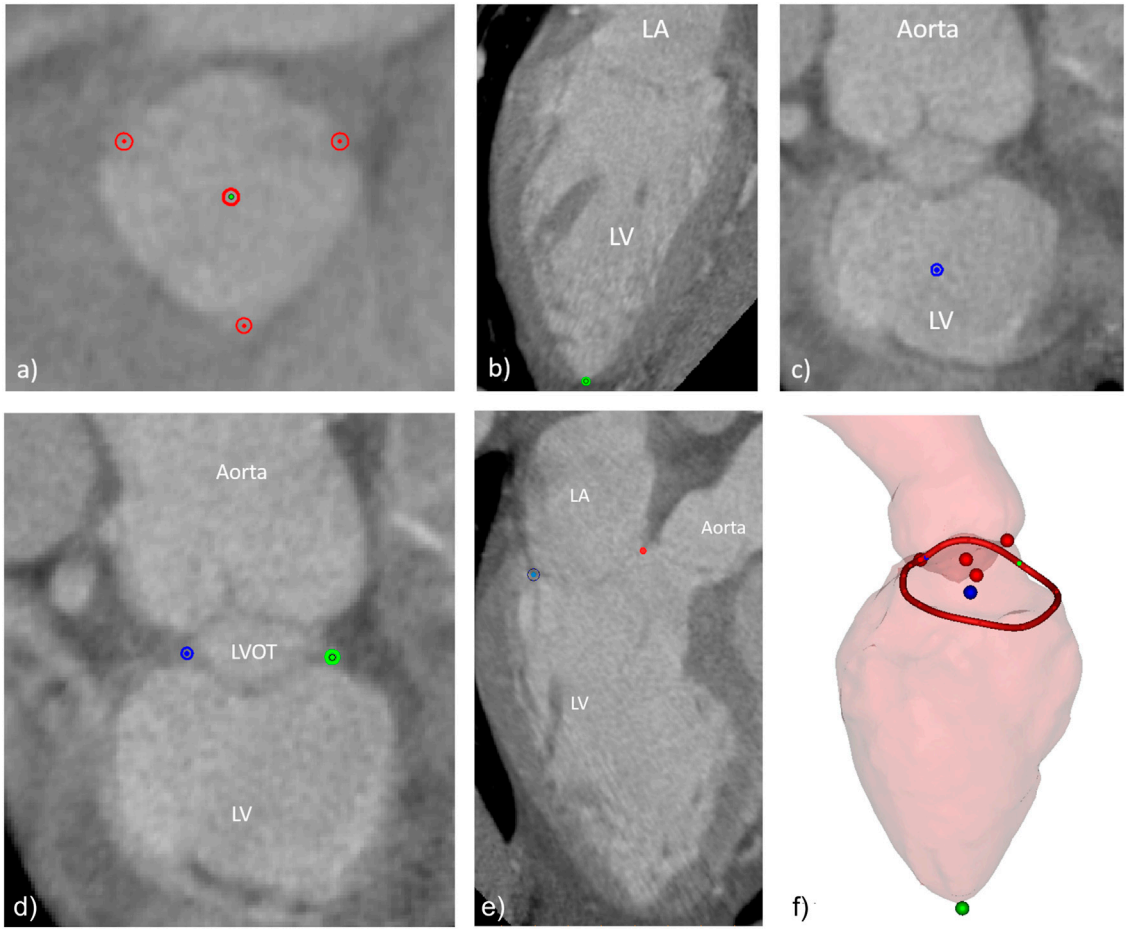

FIGURE 2
Manually indicated landmarks, including **(A)** aortic valve cusps and center, **(B)** left ventricular apex, **(C)** mitral valve center, **(D)** fibrous trigones, **(E)** mitral annulus points in one of the long axis planes around the mitral valve center, and **(F)** overview of final set of landmarks and the 3D surfaces of the LV and the aortic root (the LA surface was excluded for clarity).

2.4 Automated mitral valve assessment

The automated method for assessment of the mitral valve was run on the twenty validation cases, for both the end-diastolic and end-systolic phases, as these correspond to the most relevant phases for TMVR planning. The method was initiated by running a fully automated segmentation method available in Mimics for the separation of the aorta, left ventricle and left atrium, and subsequent generation of the corresponding surface models. Thereafter, the dynamic SSM was aligned with the target case using first a point-set registration based on the centers of mass of the three structures and the centers of the boundaries corresponding to the aortic and mitral valves, followed by an iterative closest point registration. The SSM was subsequently fitted onto the target surfaces using a correspondence-based fitting method as described by (van Dijck, 2021). Finally, the fitted SSM was warped to the target surface for improved matching. The node indices corresponding to landmarks indicated on the mean instance of the SSM are used to extract the coordinates of the landmarks on the target case. Additionally, the mitral and aortic valve annuli are defined by the boundaries of the respective structures (left atrium and left ventricle for the mitral valve, and left ventricle and aorta for the aortic valve).

2.5 Manual mitral valve assessment

Three observers, with various backgrounds and experience levels with the image analysis software, performed the manual indication of the mitral annulus landmarks in both the end-diastolic and end-systolic phase. The first observer (PVH) is a cardiologist with more than 10 years of imaging experience and no direct experience with the Mimics software; the second observer (PL) is a biomedical engineer with 7 years of

experience in cardiac image analysis, and more than 10 years of advanced use of the Mimics software; and the third observer (JO) is a clinical researcher with 3 years of experience, which included 1 year of regular use of the Mimics software and similar tools.

A dedicated workflow was developed, in such way that all users would follow approximately the same procedure, this way avoiding potential methodological discrepancies linked to their experience with the software. The workflow included the indication of the aortic cusps and aortic valve center (Figure 2A), the left ventricular apex (Figure 2B), the mitral valve center (Figure 2C), the medial and lateral trigones (Figure 2D), and the mitral annulus (Figure 2E). All landmarks were visually assessed on the 3D representations of the left heart and adjustments performed when deemed necessary. Figure 2F shows the manually indicated landmarks visualized on the 3D representations of the aorta and left ventricle (the left atrium was excluded for clarity).

2.6 Statistical analysis

The ground-truth for each anatomical landmark was defined as the average position of the three points indicated by the observers. For each landmark, the Euclidean distance between the landmark indicated by each of the observers was measured in relation to the average location of the three observers. The inter-observer error was defined as the mean of the three distances. In the case of the automated approach, the inter-method error was defined as the difference between the landmark predicted by the algorithm and the mean landmark location for the three observers. The average landmarks and the measurements were automatically generated using a dedicated software plugin in the Mimics software.

To understand the clinical impact of the errors in the automated approach, a set of relevant measurements to characterize the mitral annulus were estimated. These measurements include 2D and 3D mitral annulus perimeter, the projected mitral annulus area, the antero-posterior (AP) and medio-lateral (ML) diameters, the inter-trigone (TT) distance, the annulus height, and the aorto-mitral angle. For both the manual and automatic approaches, these measurements were generated in a fully automated manner based on the landmarks.

The mean and standard deviation (SD), as well as the median and inter-quartile range were calculated for the measurements performed by the three observers. Furthermore, the inter-observer variability was evaluated by comparing the measurement performed by each observer with the mean measurement of the three observers. Results are presented as mean ± SD. Moreover, the intraclass correlation coefficients (ICC) and 95% confidence intervals were estimated using a single measure, absolute-agreement, two-way random model. Reliability was measured according to the following values of ICC: < 0.5 poor, 0.5–0.75 moderate, 0.75–0.9 good, and >0.9 excellent reliability (Koo and Li, 2016). The inter-method variability, expressed as mean ± SD, was evaluated by comparing the average measurement by the three observers and the automatically generated measurement. The agreement between the manual and the automatic approaches was assessed using single measures, absolute-agreement, two-way mixed effects model. Finally, the agreement between each of the measurements for the manual and automated approaches was investigated through linear regression and Bland-Altman analyses. The statistical analysis was done with Python 3.7, using standard Python libraries (NumPy, SciPy, Pandas).

3 Results

3.1 Study population

The group of 50 patients used to generate the SSM included 18 males (36%) and had a mean age of 49 ± 10.1 years, whereas 10 of the 20 patients included in the validation group were male (50%) with a mean age of 48 ± 14.8 years.

3.2 Statistical shape model

The mean instance of the generated end-diastolic and dynamic models can be seen in Figure 3. The labels represent the structures and boundaries of the left heart, with labels 3, 5, and 7 for the aorta, left ventricle and left atrium, respectively. Correspondingly, the aortic and mitral annuli are represented by labels 15 and 35.

3.3 Manual mitral valve assessment

Table 1 displays the calculated means and standard deviations (SD), as well as medians and interquartile ranges of the mitral annulus measurements resulting from manual indications by the three observers. Statistically significant differences were registered between systolic and diastolic phases for the AP diameter ($p = 0.0037$), the annulus height ($p = 0.043$), and the aorto-mitral angle ($p < 0.001$). When comparing the measurements resulting from the saddle-shaped annulus with the D-shaped curve, all presented significant differences, except for the projected area.

The impact of the discrepancy in the position of the landmarks on the mitral annulus measurements is represented as box plots in Figure 4. All relative errors were well below 10%, with the exception of the mitral annulus height and the inter-trigone distance. This trend in the inter-observer agreement was also seen for the intraclass correlation coefficients (ICC), with values between 0.23 and 0.71 for the annulus height and of 0.23 for the inter-trigone distance. In addition, the aorto-mitral

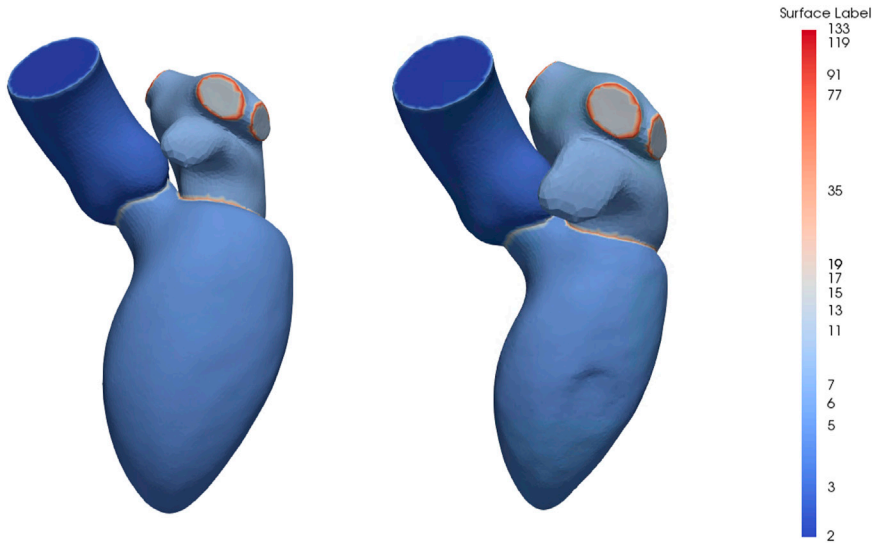

FIGURE 3
Mean instance of the generated statistical shape models of the left heart chambers for the diastolic phases (left) and full cardiac cycle (right). The labels are prime numbers representing the different structures and the boundaries are obtained by multiplying the labels of the adjoining structures. Specifically, the aorta, left ventricle and left atrium are represented by labels 3, 5 and 7, respectively, resulting in labels 15 for the aortic annulus and label 35 for the mitral annulus.

TABLE 1 Mitral annulus measurements.

Measurement	Units	Saddle-shaped annulus	
		Diastole	Systole
		Mean ± SD	Mean ± SD
Area 2D	[cm^2]	9.50 ± 1.8	9.78 ± 1.6
Perimeter 2D	[mm]	116.95 ± 10.4	116.21 ± 8.9
Perimeter 3D	[mm]	123.26 ± 10.9	123.95 ± 9.5
AP Diameter	[mm]	28.90 ± 3.5	30.69 ± 2.7
ML Diameter	[mm]	38.84 ± 3.7	38.13 ± 3.7
Annulus height	[mm]	5.79 ± 1.4	6.65 ± 1.9
Aorto-mitral angle	[°]	127.10 ± 6.7	119.45 ± 8.1
TT-distance	[mm]	23.64 ± 2.4	22.82 ± 2.5
		D-shaped annulus	
Area 2D	[cm^2]	9.59 ± 1.8	9.77 ± 1.6
Perimeter 2D	[mm]	114.03 ± 10.5	114.25 ± 9.3
Perimeter 3D	[mm]	118.71 ± 10.8	119.23 ± 9.7
AP Diameter	[mm]	28.67 ± 3.1	29.80 ± 2.8
ML Diameter	[mm]	39.29 ± 3.6	38.43 ± 3.6
Annulus height	[mm]	3.62 ± 1.2	4.09 ± 1.5
Aorto-mitral angle	[°]	128.81 ± 7.2	122.07 ± 8.7
TT-distance	[mm]	23.64 ± 2.4	22.82 ± 2.5

angle was also associated with a low ICC, especially in the diastolic phase (ICC = 0.55 for saddle-shaped and ICC = 0.54 for D-shaped annulus), despite the low absolute and relative errors. These results might suggest that for these three measurements the average of the three observers cannot be reliably used as ground-truth for comparison with the automated approach. Significant differences were detected for the inter-observer agreement between the two annulus curve types for the 2D annulus perimeter ($p = 0.005$, the AP diameter ($p = 0.04$) and the annulus height ($p < 0.001$). The first two measurements were associated with a significantly lower error in the D-shaped annulus compared to the saddle shape, whereas the annulus height error was significantly higher in the D-shape configuration. A more detailed overview of the inter-observer variability for the saddle- and D-shaped annulus configurations can be found in Table 2, containing the mean absolute and relative inter-observer variability for the selected measurements, including the intraclass correlation coefficients values and corresponding 95% confidence interval.

3.4 Automated mitral valve assessment

A representative example of the manually indicated and automatically predicted annulus curves is shown in Figure 5 for both cardiac phases and annulus configurations. In the top row, it is possible to appreciate how the manual and automated curves follow

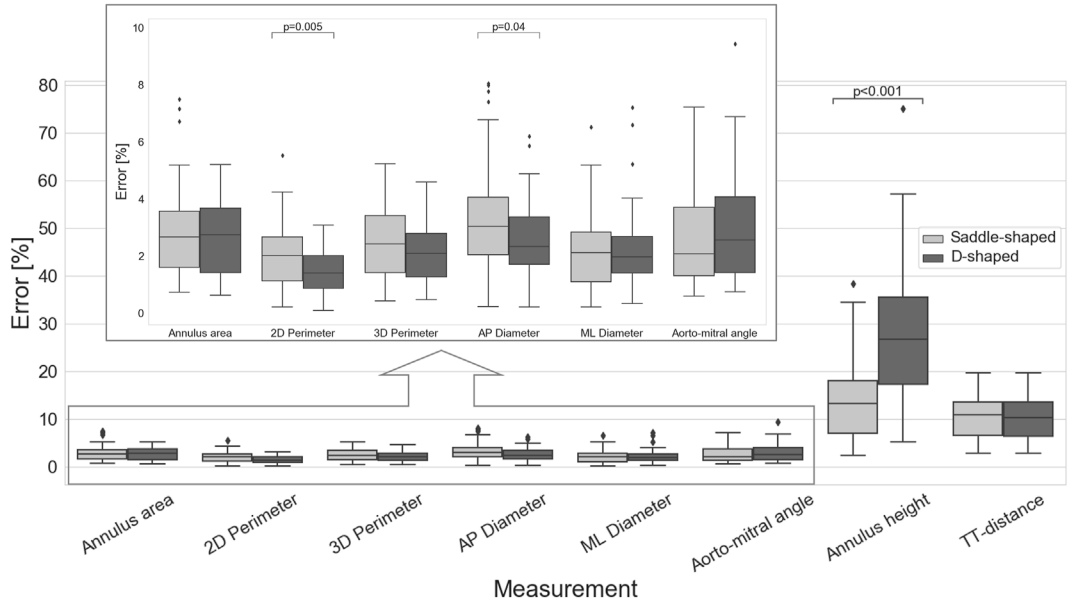

FIGURE 4
Inter-observer variability for the multiple measurements (*p*-values are shown for statistically significant differences between the saddle- and D-shaped annulus curves).

TABLE 2 Inter-observer variability for mitral valve measurements.

	Saddle-shaped annulus					
	Diastole			Systole		
	Absolute	Relative	ICC (95%CI)	Absolute	Relative	ICC (95%CI)
Area 2D	0.27 ± 0.2 cm^2	2.81 ± 1.8%	0.95 [0.89–0.98]	0.28 ± 0.2 cm^2	2.91 ± 1.7%	0.93 [0.80–0.98]
Perimeter 2D	2.15 ± 1.2 mm	1.85 ± 1.0%	0.90 [0.74–0.96]	2.60 ± 1.5 mm	2.21 ± 1.4%	0.82 [0.50–0.93]
Perimeter 3D	2.76 ± 1.7 mm	2.22 ± 1.3%	0.86 [0.61–0.95]	3.43 ± 1.6 mm	2.78 ± 1.4%	0.77 [0.52–0.90]
AP Diameter	1.05 ± 0.6 mm	3.62 ± 1.9%	0.81 [0.61–0.91]	0.97 ± 0.6 mm	3.21 ± 2.2%	0.73 [0.52–0.87]
ML Diameter	0.62 ± 0.4 mm	1.57 ± 1.0%	0.93 [0.83–0.97]	1.08 ± 0.6 mm	2.84 ± 1.4%	0.83 [0.46–0.94]
Annulus height	0.99 ± 0.5 mm	18.2 ± 10.0%	0.38 [0.11–0.65]	0.71 ± 0.4 mm	11.1 ± 6.1%	0.71 [0.50–0.86]
Aorto-mitral angle	3.19 ± 2.4°	2.53 ± 2.0%	0.54 [0.29–0.76]	3.31 ± 1.7°	2.79 ± 1.5%	0.70 [0.48–0.85]
TT-distance	2.34 ± 1.0 mm	10.1 ± 4.7%	0.23 [0.00–0.51]	2.29 ± 1.0 mm	10.1 ± 4.7%	0.23 [0.00–0.51]
	Saddle-shaped annulus					
Area 2D	0.26 ± 0.17 cm^2	2.67 ± 1.4%	0.95 [0.90–0.98]	0.26 ± 0.1 cm^2	2.69 ± 1.5%	0.94 [0.86–0.98]
Perimeter 2D	1.69 ± 1.01 mm	1.46 ± 0.8%	0.94 [0.87–0.97]	1.68 ± 0.9 mm	1.46 ± 0.8%	0.92 [0.80–0.97]
Perimeter 3D	2.63 ± 1.51 mm	2.19 ± 1.2%	0.87 [0.76–0.94]	2.50 ± 1.2 mm	2.11 ± 1.1%	0.87 [0.73–0.94]
AP Diameter	0.66 ± 0.32 mm	2.33 ± 1.1%	0.90 [0.80–0.95]	0.87 ± 0.5 mm	2.96 ± 1.6%	0.81 [0.61–0.91]
ML Diameter	0.74 ± 0.40 mm	1.86 ± 0.9%	0.91 [0.75–0.96]	1.03 ± 0.7 mm	2.70 ± 1.8%	0.81 [0.46–0.93]
Annulus height	0.96 ± 0.59 mm	27.39 ± 16.4%	0.23 [0.00–0.52]	1.22 ± 0.7 mm	30.21 ± 14.4%	0.26 [0.01–0.54]
Aorto-mitral angle	3.48 ± 2.67°	2.74 ± 2.2%	0.55 [0.27–0.77]	3.83 ± 1.9°	3.18 ± 1.7%	0.67 [0.44–0.84]
TT-distance	2.34 ± 1.00 mm	10.1 ± 4.7%	0.23 [0.00–0.51]	2.29 ± 1.0 mm	10.1 ± 4.7%	0.23 [0.00–0.51]

AP, antero-posterior; CI, confidence interval; ML, medio-lateral; TT, trigone-to-trigone; ICC, intraclass correlation.

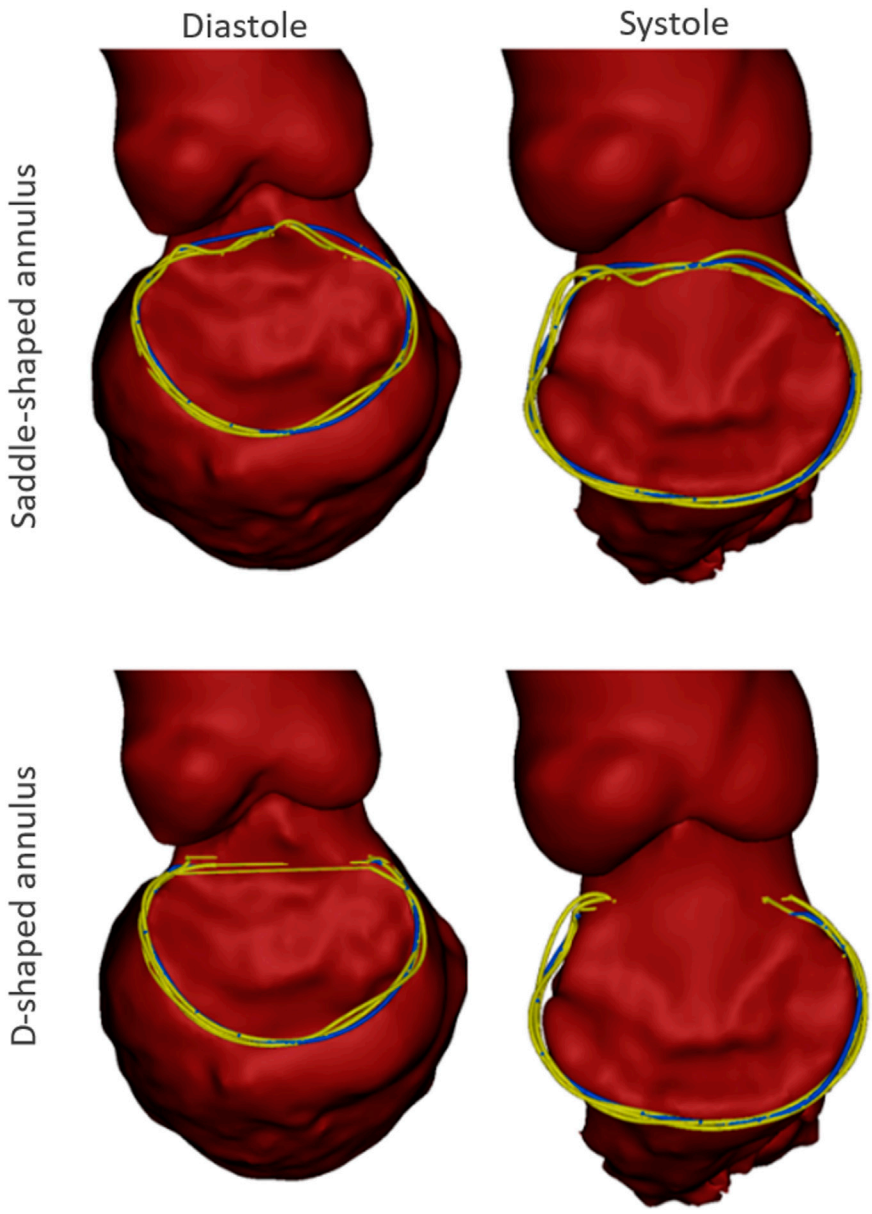

FIGURE 5
Example case with the manual annulus curves displayed in yellow and the automatically predicted annulus represented in blue, for both the saddle- (Top) and D-shaped (bottom) configurations, as well as for the diastolic (left) and systolic (right) phase. The LA was excluded for visualization purposes.

a similar path, with the main discrepancies occurring in the aorto-mitral curtain. In the bottom row, a smaller discrepancy is observed, although it is still possible to appreciate that the inter-trigone line is slightly different for the three manual indications.

A detailed inter-method variability analysis is included in Table 3. In the case of the saddle-shaped annulus, the relative errors for the annulus height and the inter-trigone distance were the highest, with values around 30%. Also, for the aorto-mitral angle, the inter-method analysis resulted in low ICC values, despite relatively low errors. These were the three measurements associated with the lowest interobserver agreement.

When considering the annulus area and antero-posterior diameter, both had a relative error of about 10%, a value considerably larger than those observed for the perimeters and medio-lateral diameter. The intraclass correlation coefficients show that these two measurements had limited reliability, with lower ICC values of 0.17 and 0.10 for diastole and systole, respectively, in the case of the projected area. For the

TABLE 3 Inter-method variability for mitral valve measurements.

	Saddle-shaped annulus					
	Diastole			Systole		
	Absolute	Relative	ICC (95%CI)	Absolute	Relative	ICC (95%CI)
2D Area	0.93 ± 0.7 cm^2	10.34 ± 8.6%	0.90 [0.17–0.97]	0.95 ± 0.4 cm^2	10.2 ± 5.9%	0.88 [0.10–0.97]
2D Perimeter	3.38 ± 2.8 mm	2.95 ± 2.5%	0.95 [0.88–0.98]	2.81 ± 2.0 mm	2.40 ± 1.7%	0.96 [0.90–0.98]
3D Perimeter	4.87 ± 2.8 mm	3.94 ± 2.2%	0.93 [0.82–0.97]	3.46 ± 2.5 mm	2.80 ± 2.0%	0.94 [0.86–0.98]
AP Diameter	5.65 ± 4.3 mm	12.01 ± 8.4%	0.71 [0.00–0.92]	3.59 ± 1.5 mm	11.9 ± 5.5%	0.61 [0.00–0.89]
ML Diameter	1.65 ± 1.5 mm	4.26 ± 3.8%	0.90 [0.76–0.96]	1.43 ± 0.9 mm	3.86 ± 2.4%	0.94 [0.85–0.98]
Annulus height	1.76 ± 1.1 mm	32.3 ± 21.7%	0.50 [0.00–0.79]	1.71 ± 1.2 mm	29.7 ± 26.6%	0.56 [0.00–0.83]
Aorto-mitral angle	3.58 ± 3.3°	2.78 ± 2.5%	0.82 [0.51–0.93]	5.27 ± 4.6°	4.42 ± 3.8%	0.69 [0.24–0.88]
TT-distance	6.71 ± 2.4 mm	29.1 ± 12.0%	0.21 [0.00–0.62]	6.16 ± 2.8 mm	28.1 ± 15.5%	0.17 [0.00–0.56]
	D-shaped annulus					
2D Area	0.66 ± 0.6 cm^2	7.48 ± 6.8%	0.94 [0.77–0.98]	0.57 ± 0.4 cm^2	5.94 ± 4.6%	0.95 [0.87–0.98]
2D Perimeter	3.14 ± 2.6 mm	2.82 ± 2.4%	0.96 [0.89–0.99]	2.38 ± 2.0 mm	2.11 ± 1.9%	0.97 [0.92–0.99]
3D Perimeter	3.30 ± 2.3 mm	2.78 ± 2.0%	0.96 [0.91–0.99]	2.85 ± 2.2 mm	2.40 ± 1.9%	0.96 [0.89–0.99]
AP Diameter	0.99 ± 0.8 mm	3.66 ± 3.4%	0.95 [0.88–0.98]	1.52 ± 1.10 mm	5.15 ± 4.7%	0.86 [0.64–0.94]
ML Diameter	1.63 ± 1.2 mm	4.13 ± 2.9%	0.92 [0.88–0.98]	1.28 ± 1.0 mm	3.42 ± 2.9%	0.94 [0.84–0.98]
Annulus height	1.96 ± 1.2 mm	52.8 ± 26.5%	0.26 [0.00–0.68]	1.58 ± 1.1 mm	36.7 ± 20.6%	0.51 [0.00–0.83]
Aorto-mitral angle	4.10 ± 3.5°	3.26 ± 2.9%	0.62 [0.42–0.80]	6.06 ± 4.6°	4.84 ± 2.1%	0.69 [0.15–0.88]
TT-distance	6.71 ± 2.4 mm	29.1 ± 12.0%	0.21 [0.00–0.62]	6.16 ± 2.8 mm	28.1 ± 15.5%	0.17 [0.00–0.56]

AP, antero-posterior; CI, confidence interval; ML, medio-lateral; TT, trigone-to-trigone; ICC, intraclass correlation.

AP diameter, the lower ICC values were of 0.00 in both phases. When analyzing the errors for the D-shaped annulus, it is possible to appreciate that these were considerably lower, and the ICC values higher when compared to the saddle-shaped representation. Figure 6 shows that the annulus area, 3D perimeter and AP-diameter are associated with statistically significant error differences between the two configurations, whereas the errors for the 2D perimeter and the ML-diameter remained nearly unchanged. For a more in-depth analysis of the effects of the annulus configuration in the different measurements, the linear regression and Bland-Altman plots can be consulted in Figure 7 and Figure 8, respectively.

The mean error for the mitral annulus area decreased from 94.3 ± 64.1 mm^2 in the saddle-shaped annulus to 61.6 ± 38.6 mm^2 in the D-shaped configuration. Furthermore, the coefficient of determination (r^2) increased for the diastolic and systolic phases. Also, the bias in the Bland-Altman analysis was reduced from almost −100 mm^2 to about −50 mm^2. The AP-diameter error decreased from 3.5 ± 1.77 mm for the saddle-shaped annulus to 1.25 ± 0.99 mm in the D-shaped configuration. Through the analysis of the Bland-Altman plot, it is possible to assess that the bias was eliminated, as its value decreased from about 4 mm to 0 mm. Regarding the coefficient of determination, while it largely increased from 0.67 to 0.84 for the diastolic phase, it decreased from 0.61 to 0.56 for the systolic phase.

There was a statistically significant difference in the relative and absolute errors of the 3D perimeter for the saddle- and D-shaped annulus. The mean absolute error decreased from about 4.2 ± 2.7 mm for the saddle-shaped annulus to 3.1 ± 2.2 mm for the D-shaped annulus. The linear regression also shows an improvement for the 3D perimeter in the D-shaped compared to the saddle-shaped configuration based on the slight increase in the coefficient of determination. In the Bland-Altman analysis, it is possible to appreciate that the bias shifted from 1.44 mm for the saddle-shaped annulus to -1.43 mm for the D-shaped curve. For the 2D perimeter, the bias increased from −0.17 for the saddle-shape to −1.29 for the D-shape. Lastly, the error for the medio-lateral diameter is almost the same for the two annulus configurations, around 1.5 ± 1.1 mm, and no obvious differences are observed between the two configurations in the regression and Bland-Altman analyses.

4 Discussion

Accurate pre-interventional assessment of the mitral valve is essential for successful outcome of TMVR procedures. This study

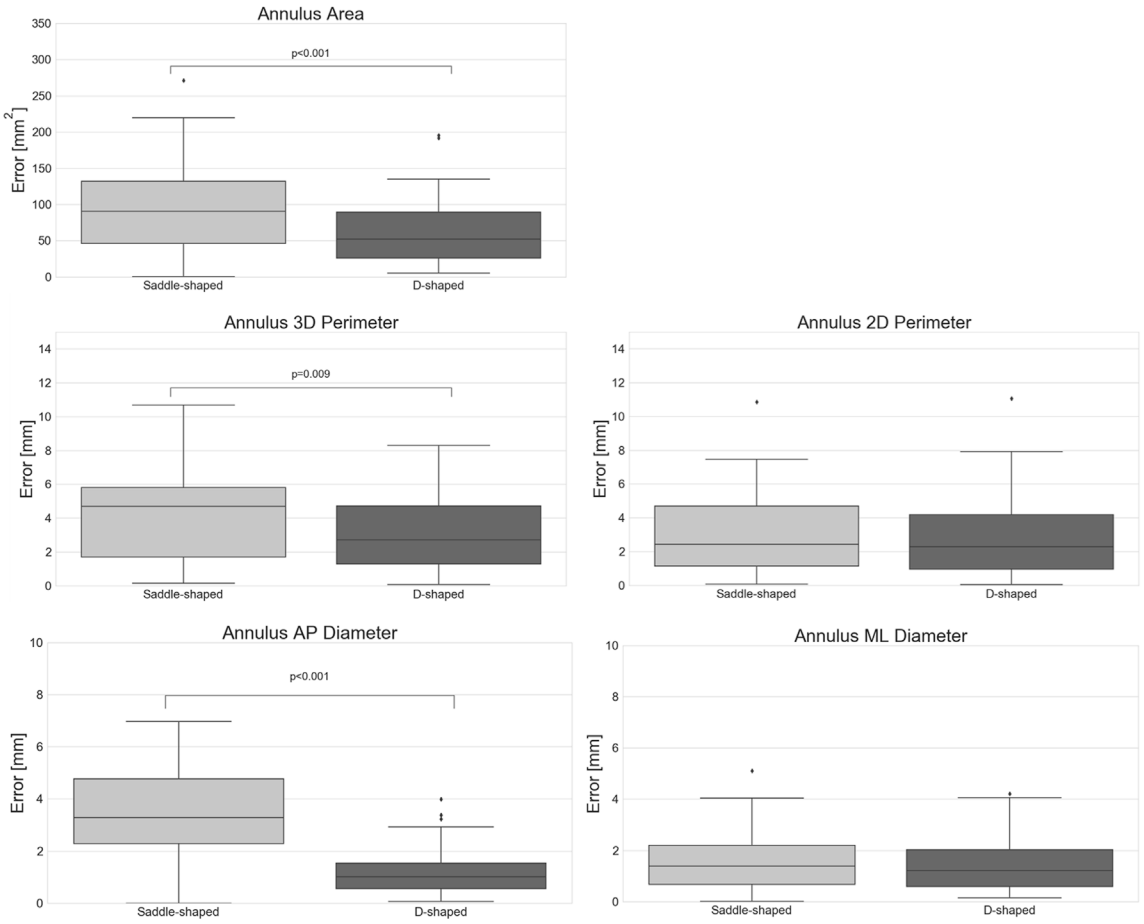

FIGURE 6
Absolute error of the automatically predicted annulus measurements for the saddle- and D-shaped annulus (p-values are shown for statistically significant differences between the saddle- and D-shaped annulus curves).

evaluated the accuracy of a fully automated method for the detection of the main anatomical landmarks, which might contribute to a shorter and more consistent analysis process.

The inspection of the inter-method results indicates that the measurements generated using the proposed method showed good agreement with the measurements resulting from the user-driven approach, particularly for the diameters, perimeters, and area. Due to the low inter-observer agreement for the annulus height, aorto-mitral angle, and trigone-to-trigone distance, these measurements were considered ill-suited for the validation of the automatic method. The lower inter-observer agreement observed for these measurements is possibly related to the challenge of unambiguously defining the mitral annulus at the level of the aorto-mitral curtain. Because the fibrous skeleton is not associated with changes in image intensity compared to surrounding structures, discrepancies in the identification of the trigones position can occur, unavoidably leading to differences in the inter-trigone distance. Furthermore, the identification of the annulus horn is also prone to variations, contributing to large differences in the annulus height values. Because the aorto-mitral angle is directly related to the annulus plane orientation, variations in the annulus horn will also lead to significant differences in the angle with the aortic plane. The inter-method agreement was consistently higher for the D-shaped than for the saddle-shaped annulus. The fact that the relative error was significantly higher for the annulus area ($p < 0.001$), AP diameter ($p < 0.001$), and 3D perimeter ($p = 0.009$) in the saddle-shaped annulus compared to the D-shaped curve, and that no statistically significant differences were observed for the ML diameter and 2D perimeter, suggests that the discrepancies in the annulus curve might be local. The most logical explanation is that these errors occur in the anterior portion of the mitral annulus, as the delineation of the annulus in this region is known to be particularly challenging.

The understanding of the impact of these errors on the selected device as well as on the estimated device position is determinant to establish if the proposed automated method can be used in the pre-interventional planning of TMVR procedures. The device size is

10.3389/fbioe.2022.1033713

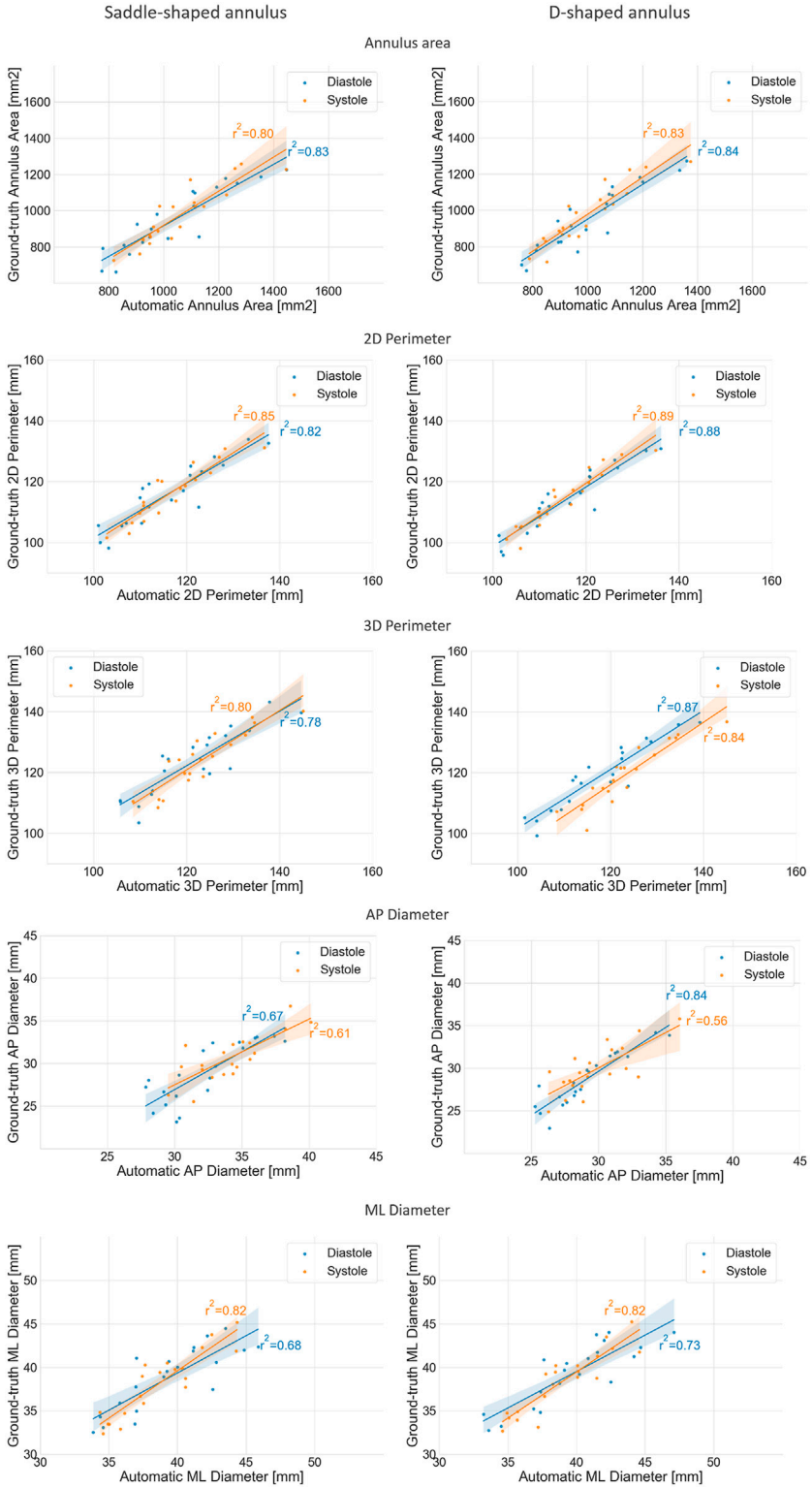

FIGURE 7
Regression plots comparing the mean annulus measurements obtained for the three observers and those calculated from the automatically detected landmarks, for both the saddle- (left) and D-shaped (right) configurations.

10.3389/fbioe.2022.1033713

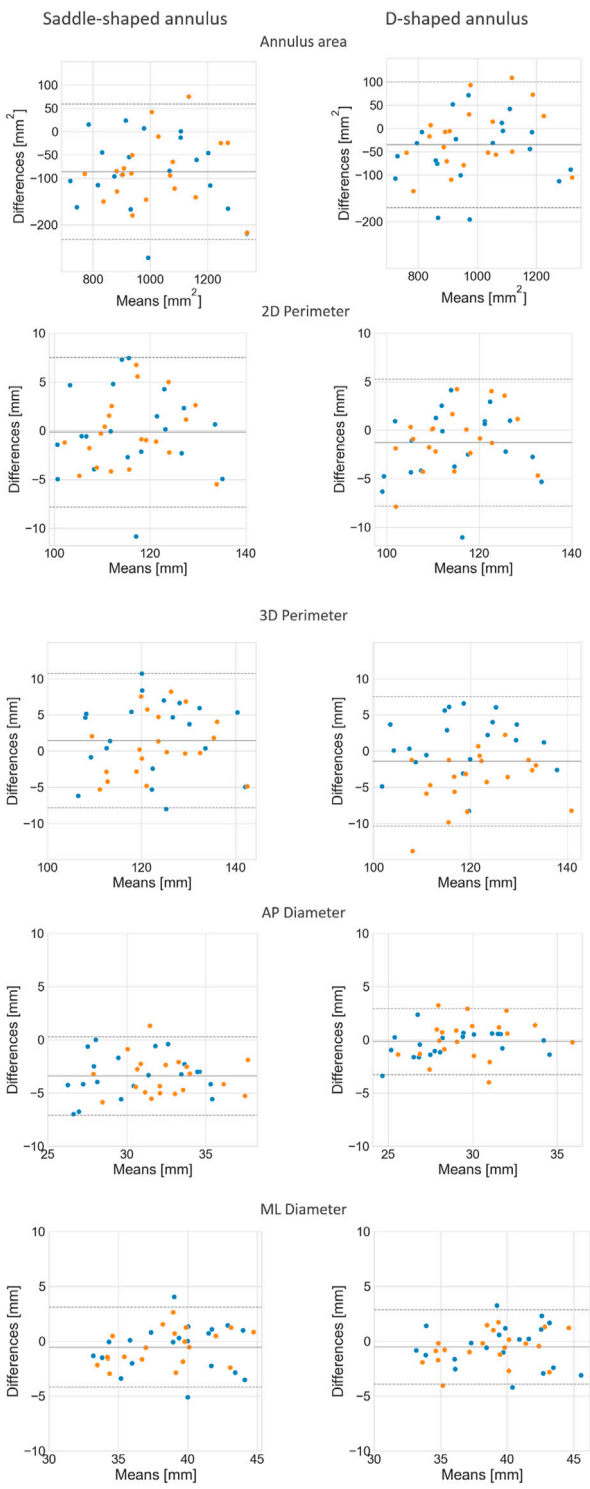

FIGURE 8
Bland-Altman plots comparing the mean annulus measurements obtained for the three observers and those calculated from the automatically detected landmarks, for both the saddle- (left) and D-shaped (right) configurations.

usually determined by a combination of measurements, namely area, perimeters, and diameters. This study suggested that by using the D-shaped configuration, the sizing of the device can be accurately performed. In case the saddle-shaped annulus description is used for the device selection, due to protocol specifications, a visual assessment and potential correction of the automatically generated annulus curve by an expert might be required. Regarding the position of the device in the cardiac anatomy, mainly determined by the annulus plane, the automated method estimated the mitral annulus and its center with a mean absolute difference of about 2.5 mm compared to the ground-truth. This is equivalent to the inter-observer variability, suggesting that an accurate planning can still be achieved with the proposed method. Nevertheless, further research is required to confirm this hypothesis.

This study presents inevitably some limitations. The number of validation cases is restricted, and a larger cohort might be required for a full understanding of the potential shortcomings associated to the method evaluated in this study. Another simplification related to the validation dataset is the fact that the subjects present no mitral valve pathology. It is expected that patients referred to TMVR procedures present multiple characteristics that might constitute a challenge in the automatic detection of the selected landmarks. Some examples are the presence of calcium, previous devices, challenging anatomy, such as extremely dilated heart chambers, among others. The evaluation of the proposed method on patients referred to TMVR procedures has been initiated and preliminary results for native cases indicate that the accurate identification of the mitral annulus is possible in patients presenting dilated left atrium or ascending aorta, as well as hypertrophic left ventricles. However, further validation is necessary to confirm these initial observations. An additional limitation is the fact that the present study evaluates the performance of the algorithm on two cardiac phases, whereas a thorough pre-interventional planning might require the analysis of the anatomy throughout the complete cardiac cycle. Finally, the automated algorithm is intended to be run on native cases, and therefore not suitable to plan valve-in-valve, valve-in-ring, and valve-in-MAC cases. These types of procedures represent a large part of the interventions currently being performed. However, due to the difficulty in establishing unambiguous guidelines for the device position on the existing structures, automating such procedures is currently implausible.

Despite these limitations, this study suggests that automated methods could contribute to increased consistency through the reduction of inter-observer variability, while shortening the time spent in the pre-interventional assessment.

Data availability statement

The data analyzed in this study is subject to the following licenses/restrictions: No authorization to share externally. Requests to access these datasets should be directed to PL, Patricia.Lopes@materialise.be.

Ethics statement

The studies involving human participants were reviewed and approved by the Institutional Ethical Committee at Antwerp University Hospital, reference number 20/16/203.

Author contributions

PL performed the segmentations, generated the statistical shape model, designed the algorithm, and performed manual landmark indications for validations. PVH performed data collection and manual landmark indications. JO performed manual landmark indications. All authors assisted in the study conceptualization and article drafting.

Funding

This work was supported by Flanders Innovation and Entrepreneurship (grant number IWT 140247).

Conflict of interest

PL and RW-S are full time employees of Materialise. JVS is a member of the Board of Directors with stock options at Materialise. NVM has research grant support from Abbott, Boston Scientific, Medtronic, Edwards Lifesciences, PulseCath BV, Abiomed, Pie Medical.

The remaining authors declare that the research was conducted in the absence of any commercial or financial relationships that could be construed as a potential conflict of interest.

Publisher's note

All claims expressed in this article are solely those of the authors and do not necessarily represent those of their affiliated organizations, or those of the publisher, the editors and the reviewers. Any product that may be evaluated in this article, or claim that may be made by its manufacturer, is not guaranteed or endorsed by the publisher.

References

Alperi, A., Granada, J. F., Bernier, M., Dagenais, F., and Rodés-Cabau, J. (2021). Current status and future prospects of transcatheter mitral valve replacement: JACC state-of-the-art review. *J. Am. Coll. Cardiol.* 77, 3058–3078. doi:10.1016/j.jacc.2021.04.051

Amberg, B., Romdhani, S., and Vetter, T. (2007). "Optimal step nonrigid ICP algorithms for surface registration brian," in Proceedings of the IEEE Computer Society Conference on Computer Vision and Pattern Recognition, 1–8. Available at: https://gravis.dmi.unibas.ch/publications/2007/CVPR07_Amberg.pdf.

Aoun, J., Reardon, M. J., and Goel, S. S. (2021). Transcatheter mitral valve replacement: An update. *Curr. Opin. Cardiol.* 36, 384–389. doi:10.1097/HCO.0000000000000884

Blanke, P., Dvir, D., Cheung, A., Ye, J., Levine, R. A., Precious, B., et al. (2014). A simplified D-shaped model of the mitral annulus to facilitate CT-based sizing before transcatheter mitral valve implantation. *J. Cardiovasc. Comput. Tomogr.* 8, 459–467. doi:10.1016/j.jcct.2014.09.009

Danckaers, F., Huysmans, T., Lacko, D., Ledda, A., Verwulgent, S., van Dongen, S., et al. (2014). Correspondence preserving elastic surface registration with shape model prior. Proceedings – International Conference on Pattern Recognition, 2143–2148. doi:10.1109/ICPR.2014.373

Hoogendoorn, C. (2013). *A statistical dynamic cardiac atlas for the virtual physiological human: Construction and application*.

Koo, T. K., and Li, M. Y. (2016). A guideline of selecting and reporting intraclass correlation coefficients for reliability research. *J. Chiropr. Med.* 15, 155–163. doi:10.1016/j.jcm.2016.02.012

Mackensen, G. B., Lee, J. C., Wang, D. D., Pearson, P. J., Blanke, P., Dvir, D., et al. (2018). Role of echocardiography in transcatheter mitral valve replacement in native mitral valves and mitral rings. *J. Am. Soc. Echocardiogr.* 31, 475–490. doi:10.1016/j.echo.2018.01.011

Murphy, D. J., Ge, Y., Don, C. W., Keraliya, A., Aghayev, A., Morgan, R., et al. (2017). Use of cardiac computerized tomography to predict neo-left ventricular outflow tract obstruction before transcatheter mitral valve replacement. *J. Am. Heart Assoc.* 6, 1–13. doi:10.1161/JAHA.117.007353

Natarajan, N., Patel, P., Bartel, T., Kapadia, S., Navia, J., Stewart, W., et al. (2016). Peri-procedural imaging for transcatheter mitral valve replacement. *Cardiovasc. Diagn. Ther.* 6, 144–159. doi:10.21037/cdt.2016.02.04

Silbiger, J. J. (2012). Anatomy, mechanics, and pathophysiology of the mitral annulus. *Am. Heart J.* 164, 163–176. doi:10.1016/j.ahj.2012.05.014

Thériault-Lauzier, P., Mylotte, D., Dorfmeister, M., Spaziano, M., Andalib, A., Mamane, S., et al. (2016). Quantitative multi-slice computed tomography assessment of the mitral valvular complex for transcatheter mitral valve interventions part 1: Systematic measurement methodology and inter-observer variability. *EuroIntervention* 12, e1011–e1020. doi:10.4244/EIJY15M11_09

Van Dijck, C. (2021). *Mass personalisation of preoperative planning for total knee arthroplasty*.

Weir-McCall, J. R., Blanke, P., Naoum, C., Delgado, V., Bax, J. J., and Leipsic, J. (2018). Mitral valve imaging with CT: Relationship with transcatheter mitral valve interventions. *Radiology* 288, 638–655. doi:10.1148/radiol.2018172758

frontiers | Frontiers in Bioengineering and Biotechnology

TYPE Original Research
PUBLISHED 17 November 2022
DOI 10.3389/fbioe.2022.930724

OPEN ACCESS

EDITED BY
Emmanuel A. Audenaert,
Ghent University, Belgium

REVIEWED BY
Alessio Gizzi,
Campus Bio-Medico University, Italy
Andrew E. Anderson,
The University of Utah, United States

*CORRESPONDENCE
Laura Bartsoen,
laura.bartsoen@kuleuven.be

SPECIALTY SECTION
This article was submitted to Biomechanics, a section of the journal Frontiers in Bioengineering and Biotechnology

RECEIVED 28 April 2022
ACCEPTED 30 August 2022
PUBLISHED 17 November 2022

CITATION
Bartsoen L, Faes MGR, Wirix-Speetjens R, Moens D, Jonkers I and Sloten JV (2022), Probabilistic planning for ligament-balanced TKA—Identification of critical ligament properties.
Front. Bioeng. Biotechnol. 10:930724.
doi: 10.3389/fbioe.2022.930724

Probabilistic planning for ligament-balanced TKA—Identification of critical ligament properties

Laura Bartsoen[1]*, Matthias G. R. Faes[2], Roel Wirix-Speetjens[3], David Moens[1], Ilse Jonkers[4] and Jos Vander Sloten[1]

[1]Department of Mechanical Engineering, KU Leuven, Leuven, Belgium, [2]Chair for Reliability Engineering, TU Dortmund, Dortmund, Germany, [3]Materialise NV, Leuven, Belgium, [4]Movement Science Department, KU Leuven, Leuven, Belgium

Total knee arthroplasty (TKA) failures are often attributed to unbalanced knee ligament loading. The current study aims to develop a probabilistic planning process to optimize implant component positioning that achieves a ligament-balanced TKA. This planning process accounts for both subject-specific uncertainty, in terms of ligament material properties and attachment sites, and surgical precision related to the TKA process typically used in clinical practice. The consequent uncertainty in the implant position parameters is quantified by means of a surrogate model in combination with a Monte Carlo simulation. The samples for the Monte Carlo simulation are generated through Bayesian parameter estimation on the native knee model in such a way that each sample is physiologically relevant. In this way, a subject-specific uncertainty is accounted for. A sensitivity analysis, using the delta-moment-independent sensitivity measure, is performed to identify the most critical ligament parameters. The designed process is capable of estimating the precision with which the targeted ligament-balanced TKA can be realized and converting this into a success probability. This study shows that without additional subject-specific information (e.g., knee kinematic measurements), a global success probability of only 12% is estimated. Furthermore, accurate measurement of reference strains and attachment sites critically improves the success probability of the pre-operative planning process. To allow more precise planning, more accurate identification of these ligament properties is required. This study underlines the relevance of investigating *in vivo* or intraoperative measurement techniques to minimize uncertainty in ligament-balanced pre-operative planning results, particularly prioritizing the measurement of ligament reference strains and attachment sites.

KEYWORDS

total knee arthroplasty, probabilistic planning, ligament balancing, musculoskeletal knee model, ligament properties, surgical precision

1 Introduction

Even though total knee arthroplasty (TKA) is widely accepted to treat end-stage osteoarthritis (OA), a revision rate of 5–10% within 10 years (Lidgren et al., 2004) is reported. Survival analysis, however, underestimates the problem, as 20–30% of patients (Delport et al., 2013) present with persistent pain, joint stiffness, and/or are limited in performing activities of daily living (e.g., going upstairs) (Bourne et al., 2010). Noble et al. (2005) even reported that 52% of TKA subjects have functional limitations. Nam et al. (2014) showed that only 66% of the patients indicated that their knees felt "normal" and 54% had residual symptoms. In 47.4% of the cases, revision surgery was related to joint stiffness, instability, or implant loosening (Sharkey et al., 2014). These failures are most often related to sub-optimal patient-specific implant alignment, resulting in unbalanced loading of the surrounding ligaments.

Pre-operative planning can aid the surgeon in identifying the ideal, patient-specific implant position. When performing this pre-operative plan, surgical precision is a large source of uncertainty as has been shown in Bartsoen et al. (2021). Table 1 shows the precision of three different surgical techniques, namely, conventional surgery (De Vloo et al., 2017), patient-specific guides (De Vloo et al., 2017), and robot-assisted surgery (RAS). The precision of RAS from two different systems is reported, namely, MAKO (Hampp et al., 2019) and TSolution One (Cosendey et al., 2021), where Hampp et al. (2019) did not report on all degrees of freedom, long-plural form = degrees of freedom (DOFs). The precision required to achieve a surgical precision for 90% success probability ($Pr_{90\%}$) (Bartsoen et al., 2021) is given as well, meaning that this surgical precision leads to a 90% probability of TKA surgery resulting in ligament balancing within the post-TKA safe zone, on the condition that patient-specific ligament properties can accurately be measured. Bartsoen et al. (2021) and the current study consider TKA as balanced when forces are generated in the medial and lateral ligaments throughout the squat motion and ligament strains do not exceed 6%. This zone will be further referred to as the "post-TKA safe zone."

Currently, pre-operative planning does not consider soft tissue loading, which may contribute to a non-optimal implant position despite pre-operative planning. The importance of ligament balancing was already highlighted in 1977 by Freeman et al. (1977). However, even today, no clear consensus exists on the best method/surgical technique. Typically, knee ligaments are considered to "mainly" be mechanical joint stabilizers. They, however, have a sensory function that also contributes to joint stabilization (Delport et al., 2013). Qualitatively, TKA is considered ligament balanced when the ligaments are appropriately tensioned to provide passive stability without inducing stiffness or pain or limiting motion. The difficulty is, however, to quantify "appropriately tensioned." Although a few studies (Kuster et al., 2004; Delport et al., 2015; Twiggs et al., 2018) identified a set of quantifiable requirements resulting in a positive outcome, no study has so far identified a conclusive safe zone.

The incorporation of a computational knee model that generates a precise estimation of tibio-femoral (TF) kinematics and consequent ligament strains for each individual patient could be a dedicated approach to account for ligament balancing in pre-operative planning. Most published knee models are rigid-body musculoskeletal models (Smith et al., 2016; Vanheule et al., 2017) and finite

TABLE 1 Surgical precision—according to the literature—is reachable with conventional surgery (De Vloo et al., 2017), patient-specific guides (De Vloo et al., 2017), RAS (MAKO (Hampp et al., 2019) and TSolution One (Cosendey et al., 2021)), and $Pr_{90\%}$ (Bartsoen et al., 2021). It is to be noted that Hampp et al. (2019) did not report on all DOFs; the non-reported DOFs are indicated with "NA."

Technique		Conventional	Psg	RAS	$Pr_{90\%}$
Femur	Medial/lateral (mm)	NA	NA	NA and 0.26	1.18
	Anterior/posterior (mm)	NA	NA	NA and 0.33	0.23
	Proximal/distal (mm)	NA	NA	NA and 0.36	0.23
	Flexion/extension (°)	3.32	2.37	0.45 and 0.5	1.19
	Varus/valgus (°)	1.99	1.47	0.18 and 0.3	0.33
	Internal/external (°)	1.97	2.27	0.30 and 0.5	0.28
Tibia	Medial/lateral (mm)	NA	NA	NA and 0.28	0.88
	Anterior/posterior (mm)	NA	NA	NA and 0.43	0.64
	Proximal/distal (mm)	NA	NA	NA and 0.29	0.18
	Slope (°)	2.28	2.42	0.38 and 1.6	0.85
	Varus/valgus (°)	1.81	1.66	0.32 and 0.4	0.23
	Internal/external (°)	9.0	6.28	NA and 0.73	1.87

element models (Beidokhti et al., 2017). When introducing such a model-based simulation step, the planning process based on a computational knee model introduces uncertainty on several subject-specific parameters (e.g., ligament material properties) that are currently not identifiable in clinical practice in addition to the previously discussed uncertainty introduced by the surgical precision. Not only in rigid-body models but also in finite element models, the ligaments are typically simplified as line elements. The force–strain behavior of such an element can then be described as tension-only with a linear relation between force and strain presenting a quadratic toe region (see Supplementary Material for detailed implementation). This material model requires two subject-specific parameters, namely, the linear stiffness k and the reference strain ϵ_r. Measurements of these material properties are generally scarce. Some studies (Trent et al., 1976; Woo et al., 1991; Sugita and Amis, 2001; LaPrade et al., 2005; Robinson et al., 2005; Chandrashekar et al., 2006) attempted measuring linear stiffness. From the studies that are available, it can be seen that inter-subject variability is large. In addition, almost no or very limited information on the reference strain is available. Bartsoen et al. (2023) estimated a collection of sets of ligament properties while accounting for physiologically relevant ligament strains, based on *in vitro* experimental squatting data of a knee rig experiment, which typically suffers from measurement errors. The study failed to identify a narrow range of ligament properties applicable to multiple tested specimens. The authors concluded that accounting for uncertainty in each individual ligament property, independent of the other properties, would overestimate surgical outcome uncertainty as a reference strain, and attachment points are highly correlated. They suggested representing uncertainty as a subject-specific collection of sets of ligament properties.

In vivo measurement techniques to measure ligament properties not only are emerging (Slane et al., 2017; Pedersen et al., 2019) but also impose specific challenges. For most modeling approaches, it is, however, unknown how the uncertainty of these input parameters affects the simulation results. Such an analysis is, however, highly relevant to evaluate if it is even worthwhile investing in developing *in vivo* measurement methods to identify ligament parameters for application in musculoskeletal knee models (MSKMs) for pre-operative TKA planning. A few studies have investigated the effect of ligament properties on simulated TF kinematics and contact forces (Smith et al., 2016; Beidokhti et al., 2017; Pianigiani et al., 2017). They reported an important influence of the ligament material properties on the TF contact forces. None of these studies, however, investigated the effect of ligament properties on the planned implant position. Such an analysis would be needed to assess if introducing extra measurements obtained based on newly developed measurement techniques needs to be included in the computational knee model for pre-operative planning of TKA.

The current study aims to design and evaluate a planning process for ligament-balanced TKA that accounts for uncertainty in ligament material properties, attachment sites, and surgical precision. The uncertainty in the planned implant position is quantified and reported with a success probability of the ligament-balanced TKA. The uncertainty in the ligament material properties and attachment sites is quantified through a subject-specific collection of sets of ligament properties. In addition, a sensitivity analysis (SA) identifies the most critical ligament properties of the success probability.

2 Materials and methods

An overview of the planning process is illustrated in Figure 1. The figure consists of two parts. The top part illustrates how subject-specific uncertainty (Section 2.2) in the ligament properties is quantified, whereas the bottom part optimizes the implant position such that the success probability is maximized. The reader should note that the described success probability indicates the probability of success when the proposed plan is rigorously executed without further adjustments to the implant position and/or ligament releases based on the surgeon's expertise. In short, the top part illustrates that the subject-specific uncertainty is quantified by identifying a collection of sets (further referred to as "set family") of ligament properties satisfying a native safe zone.

To generate a set family of matching input parameters, Bayesian parameter estimation (BPE) can be applied given a statistical distribution of the output parameters satisfying the native safe zone. To this end, given the physiologically relevant ligament strains, a set family of subject-specific ligament properties can then be established. To ensure a feasible computational cost, BPE is applied to a surrogate model of the MSKM, simulating a squat motion of the native knee joint. This set family is used to quantify the uncertainty in the planned ligament-balanced implant position parameters. To achieve this, the mean implant position is optimized in order to maximize the global success probability (GSP) (Section 2.4) on a ligament-balanced outcome.

The bottom part of Figure 1 illustrates the optimization of the implant position. Two surgical scenarios are evaluated, namely, RAS (Cosendey et al., 2021) and $Pr_{90\%}$ (Bartsoen et al., 2021), as well as three different set families are used for describing ligament uncertainty. To ensure a feasible computational cost, this method is executed by training a surrogate model of the MSKM (Section 2.1) simulating a squat motion of the post-TKA knee joint. As a surrogate model, an artificial neural network (ANN) (Section 2.3) is used in order to design an optimization process with a feasible computational time. A sensitivity analysis (SA) (Section 2.5) is performed to identify the most critical ligament properties. More methodological details are provided in the subsequent sections.

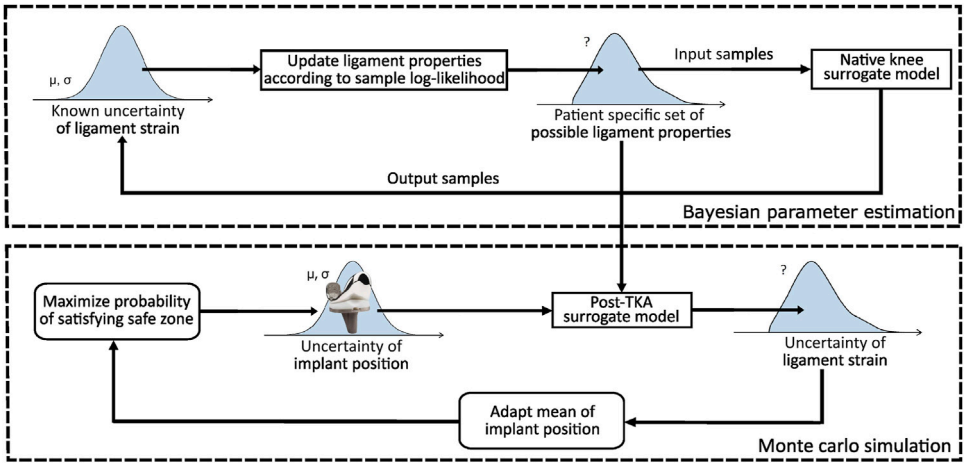

FIGURE 1
Overview of the probabilistic planning process for TKA.

2.1 Knee model

The knee model is a rigid body MSKM, implemented into the AnyBody Modeling System 7.3.0 (AnyBody Technology A/S, Aalborg, Denmark). The model is based on the knee model described by Vanheule et al. (2017). The implant system is a posterior-stabilized (PS) system (Performance, Biomet Inc., Warsaw, IN, United States). A squat motion from 20° to 120° of flexion is simulated. The model is validated using seven cadaveric specimens, to which a squat motion is applied using a dynamic knee simulator system. The boundary conditions of the dynamic knee simulator are based on the study of Victor et al. (2009a). The authors validated the simulated native and replaced kinematics. The hip joint is allowed to slide vertically and flex/extend. The ankle joint is allowed to rotate along all DOFs and to translate mediolaterally. To each of the hamstring attachments, a force of 50 N is exerted. A variable force is exerted on the quadriceps such that a vertical ankle force of 111 N is achieved. During the simulation, similar DOFs and forces as in the experiment are applied to the knee model. A full description of the MSKM simulation pipeline is presented in the previously published work by our group (Vanheule et al., 2017).

In short, the secondary knee kinematics are computed using force-dependent kinematics (FDK) (Skipper Andersen et al., 2017). This means that eleven DOFs are computed with FDK, five of the TF joints (medial/lateral (M/L), anterior/posterior (A/P), proximal/distal (P/D), varus/valgus (V/V), and internal/external (I/E)) and six of the patellofemoral (PF) joint. This is in contrast with the original model of Vanheule et al. (2017), where the patella tendon length was kept constant, reducing the number of DOFs calculated by FDK to five. FDK is implemented in the AnyBody Modeling System (AnyBody Technology A/S, Aalborg, Denmark).

The model is made as subject-specific as would currently be feasible in a clinical setting. More specifically, the bone geometry and cartilage geometry are segmented from MR images using Mimics 17.0 (Materialise N.V., Leuven, Belgium). As the ligament attachment sites are not clearly visible on MRI, these are initially estimated based on the literature and then perturbed in the parameter estimation. The medial collateral ligament (MCL), lateral collateral ligament (LCL), anterolateral ligament (ALL), popliteofibular ligament (PFL), posterior capsule (PC), anterior cruciate ligament (ACL) with an anteromedial and posterolateral bundle, and posterior cruciate ligament (PCL) with an anterolateral and posteromedial bundle are modeled. Details on the implementation of the ligament material model can be found in the Supplementary Material. The PF ligaments are modeled as spring elements with linear elastic properties between the patella and femur to reduce the computation time.

2.2 Subject-specific uncertainty

The subject-specific set family of ligament properties is defined using BPE. BPE allows generating a set family of input parameters based on a given statistical distribution of the output parameters. The native safe zone describes a set of requirements for the model outputs (ligament strains and TF kinematics) that match the behavior of a native knee joint. Through BPE, a set family of knee model input parameters is collected that result in outputs within the requirements. As no consensus exists on the quantification of physiologically relevant knee ligament strains, the current study compares three different

TABLE 2 Training bounds of the ANN for the ligament material properties.

Ligaments	ϵ_r		k [N]		Femur [mm]		Tibia [mm]	
	Min	Max	Min	Max	x_F	y_F	x_T	y_T
deepMCL	−0.2	0.3	2000	9,000	[−10, 10]	[−8, 8]	[−10, 10]	
supMCL	−0.2	0.2	2000	9,000	[−10, 10]	[−8, 8]	[−10, 10]	
LCL	−0.2	0.2	2000	9,000	[−8, 8]	[−8, 8]	[−5, 5]	
ALL	−0.3	0.2	2000	9,000	[−8, 8]	[−8, 8]	[−10, 10]	
PFL	−0.3	0.2	2000	9,000	[−10, 10]	[−6, 6]		
ACL0	−0.2	0.4	4,000	10,000	[−6, 6]	[−6, 6]	[−8, 8]	[−8, 8]
ACL1	−0.2	0.4	4,000	10,000	[−6, 6]	[−6, 6]	[−8, 8]	[−8, 8]
PCL0	−0.5	0.4	4,000	12,000	[−6, 6]	[−6, 6]	[−8, 8]	[−8, 8]
PCL1	−0.5	0.4	4,000	12,000	[−6, 6]	[−6, 6]	[−8, 8]	[−8, 8]
PC	0.05	0.2	5,000	10,000				

set families of ligament properties: 1) the first native safe zone solely accounts for a damage criterion. As ligament damage is unlikely during a squat movement of a healthy knee, ligament property sets that lead to a maximal strain exceeding 6% are excluded from the set family, as Provenzano et al. (2002) and Guo et al. (2015) indeed indicated that ligament damage occurs from this strain level onwards. As no preference for a specific strain is required, a uniform posterior distribution is associated with the maximal ligament strain between the physiological ranges of −2% and 6%. 2) A second native safe zone accounts for damage and stability. Stability is ensured when forces are generated in the medial (deepMCL and supMCL), lateral (LCL, ALL, and PFL), and central ligaments (ACL and PCL) throughout the squat motion. This is based on the study of Victor et al. (2009b) and Delport et al. (2015) that showed that in the native knee, the MCL remains isometric throughout flexion and the LCL stays isometric throughout early and mid-flexion, while tension decreases toward deep flexion. Likewise, Harner et al. (1995) showed the engagement of the ACL in early to mid-flexion, while the PCL ensures anterior/posterior stability from mid to deep flexion. This constraint is quantified as the maximal strain of the medial, lateral, and central ligaments being greater than 0% throughout the squat motion. Similar to the damage constraint, there is no preference for a specific strain. Consequently, a uniform posterior distribution is enforced. 3) A third safe zone assumes that measured kinematics of a squat motion is available, while also accounting for damage. The posterior distribution of the TF kinematics is modeled as normally distributed with a mean equal to the measured kinematics and standard deviation of 0.5 mm or 0.5° for M/L and A/P translation and I/E rotation and 1.0 mm or 1.0° for P/D translation and V/V rotation. These safe zones will be referred to as SZ_D, $SZ_{D\&S}$, and $SZ_{D\&K}$, respectively. Further details on the definition of the posterior distributions can be found in Bartsoen et al. (2023).

For each of the native safe zones, a set family of 10,000 sets of ligament parameters is collected using BPE. We collect 10,000 sets to ensure enough data to train the post-TKA surrogate model (Section 2.3). These sets are defined within the sampling bounds given in Table 2. The analysis is performed with a feasible computational cost by using an ANN as a surrogate model of the native MSKM. The transitional Markov chain Monte Carlo (TMCMC) (Ching and Chen, 2007; Betz et al., 2016) algorithm is used to perform the BPE. For further details on the implementation, we refer to Bartsoen et al. (2023). This study determines the possible ligament properties based on experimental measurement data of the kinematics of a squat motion. The gathered sets of ligament properties are consistent with $SZ_{D\&K}$. Comparison of the set families of ligament properties between specimens allows to study the variation in properties throughout the population.

2.3 TKA surrogate model

The developed TKA knee surrogate model is an ANN. This network is implemented using TensorFlow 2.4.0 (Abadi et al., 2016). This results in a network with respectively 51 and 45 input parameters for the native and post-TKA MSKM. Further information on the ANN for the native MSKM can be found in Bartsoen et al. (2023). Although, where the native ANN is trained on the entire input parameter range has been given in Table 2, this is not required for the post-TKA ANN. The post-TKA ANN can be trained on the set family satisfying SZ_D. As $SZ_{D\&S}$ and $SZ_{D\&K}$ are subfamilies of SZ_D, the network will also be valid for those native safe zones. The implant position parameters and flexion angle are assigned using Sobol sampling. The sampling bounds are taken at [−8,8] mm or ° with respect to the implant position consistent with

mechanical alignment (Knee Planner of Materialise N.V., Leuven, Belgium).

The ANN has a fully connected architecture [45:128:256:512:256:128:64:11] with an activation function called Softplus given in Eq. 1. Further details on the training can be found in the Supplementary Material. The post-TKA network is only trained for subject 1.

$$a(x) = log(exp(x) + 1). \tag{1}$$

2.4 Implant position optimization

To quantify the GSP of the ligament-balanced pre-operative planning, the mean (planned) implant position is optimized toward the position that results in the largest success probability given surgical precision and uncertainty in the ligament properties. The optimization is performed for the three set families of physiologically relevant ligament properties according to SZ_D, $SZ_{D\&S}$, and $SZ_{D\&K}$. Two different types of surgical methods are evaluated, namely, RAS (Cosendey et al., 2021) and $Pr_{90\%}$ (Bartsoen et al., 2021). Evaluation of the objective function requires an evaluation of uncertainty caused by surgical precision and ligament properties. This is performed by applying a Monte Carlo simulation (MCS) with 4,096 samples for seven flexion angles equally divided between 20° and 120°. The number of samples is chosen based on a convergence analysis. Further details can be found in the Supplementary Material.

The samples for the MCS are taken by random sampling of normally distributed implant position parameters with a mean of 0.0 mm or ° and standard deviations given in Table 1. This set family of samples is indicated with $S_{MCS}^{\boldsymbol{x}=\boldsymbol{0}}$. To avoid differences between iterations due to statistical noise on the output of the MCS, $S_{MCS}^{\boldsymbol{x}=\boldsymbol{0}}$ is constant throughout the optimization and transformed based on the mean of the implant position parameters of the current iteration. In Eq. 2, $\boldsymbol{x}$ represents the 12 DOFs of the implant position, and $S_{MCS}^{\boldsymbol{x}}$ represents the transformed samples.

$$S_{MCS}^{\boldsymbol{x}} = S_{MCS}^{\boldsymbol{x}=\boldsymbol{0}} + \boldsymbol{x}. \tag{2}$$

The transformed set family of samples $S_{MCS}^{\boldsymbol{x}}$ is combined with samples from the subject-specific set family of ligament properties, resulting in the set family of samples S_{MCS} used for estimating global uncertainty.

The optimization toward the implant position is defined as in Eq. 3, where $\boldsymbol{x}$ represents the 12 DOFs of the implant position, S_{MCS} represents the samples from the MCS, n_{MCS} is the number of samples in the MCS, θ_{FE} is the knee flexion angle (20°–120°), ϵ is the strain in a ligament, L is the set of all ligaments (deepMCL, supMCL, LCL, ALL, PFL, and PC), L_{lat} is the set of all lateral ligaments (LCL, ALL, and PFL), and L_{med} is the set of all medial ligaments (deepMCL and supMCL). $\epsilon_{max}^{L_{lat}}$ and $\epsilon_{max}^{L_{med}}$ are the maximal strains in L_{lat} and L_{med}, respectively. $\epsilon_{max}^{t} = 6\ \%$ is the upper bound on the maximal strain in the ligaments.

$$\min_{\boldsymbol{x}} \quad \frac{10}{n_{MCS}} \sum_{S_{MCS}} (u_1 + u_2) + 0.005 \sum_{1}^{12} x_i^2,$$
$$with \quad \begin{cases} u_1 &= \sum_{L} \sum_{\theta_{FE}:\, \epsilon > \epsilon_{max}^{t}} \left(\epsilon - \epsilon_{max}^{t}\right)^2 \\ u_2 &= \sum_{\theta_{FE}:\, \epsilon_{max}^{L_{lat}} < 0} \left(\epsilon_{max}^{L_{lat}}\right)^2 + \sum_{\theta_{FE}:\, \epsilon_{max}^{L_{med}} < 0} \left(\epsilon_{max}^{L_{med}}\right)^2 \end{cases}. \tag{3}$$

The package pymoo (Blank and Deb, 2020) is used to perform the optimization. A genetic algorithm is applied as this is a global optimization algorithm, which has the large advantage that it is unlikely to converge to a local minimum of the objective function as long as the population size is chosen large enough. Further details on the implementation can be found in the Supplementary Material.

2.5 Sensitivity analysis

To collect samples for the SA, the same optimization as described in Section 2.4 is performed but with constant ligament properties. This optimization is executed for 750 sets of ligament properties that were gathered with BPE using $SZ_{D\&S}$. To quantify the uncertainty caused by the implant position parameters, a quasi-Monte Carlo simulation (QMCS) is used. A QMCS uses a low-discrepancy sequence to generate the samples for the MCS. The application of a low-discrepancy sequence allows the convergence of the set of samples toward the aimed statistical distribution with a smaller number of samples compared to a random generation of samples as used with standard MCS. In this study, the Sobol sequence is applied as a low-discrepancy sequence. A convergence analysis shows that 256 samples are required. Details on the convergence analysis can be found in the Supplementary Material.

To identify the most critical parameters for the critical implant position parameters (as identified by Bartsoen et al. (2021)) and the success probability, the delta moment-independent sensitivity measure (Borgonovo, 2007) is computed. This measure is based on the difference in probability density of the model output parameter including all parameters and keeping one parameter constant. In contrast to variance-based global sensitivity measures, like Sobol indices (Sobol, 2001), the delta moment-independent measure does not rely on a single moment, for example, variance, to assess parameter sensitivity. The measure takes into account the entire input/output distribution. The SALib Python library (Herman and Usher, 2017) is applied.

A convergence analysis is performed to identify the required number of samples. A convergence measure is defined that quantifies the changes in the 10 most critical ligament parameters with respect to the ground truth 10 most critical. The ground truth set is defined based on the total number of samples

TABLE 3 Pre-operative planning results with different native safe zones and surgical precisions. OO = optimization objective; GSP = global success probability.

	SZ_D		$SZ_{D\&S}$		$SZ_{D\&K}$	
	OO	**GSP**	**OO**	**GSP**	**OO**	**GSP**
RAS	328.2	3.44%	131.7	12.0%	48.1	15.6%
$Pr_{90\%}$	329.0	3.03%	132.1	12.9%	53.6	12.9%

gathered. For every ground truth, the critical ligament property that is not in the evaluated set of 10 critical properties, a penalty is added to the convergence measure. The size of this penalty depends on the rank (r) in the ground truth most critical, where the most critical parameter receives $r = 1$ and the least critical receives $r = 10$. The penalties are determined according to Eq. 4.

$$p = \frac{10.0}{r}. \tag{4}$$

3 Results

The subject-specific uncertainty in the ligament properties represented by a set family shows a similar variation for SZ_D and $SZ_{D\&S}$ and a slightly smaller variation for $SZ_{D\&K}$. As in Bartsoen et al. (2023), a high correlation between the reference strain and attachment sites has been identified. This correlation is nevertheless more pronounced for $SZ_{D\&K}$. Further details on the subject-specific uncertainty can be found in the Supplementary Material.

The validation accuracy of the post-TKA neural network was aimed at a 90th percentile of the absolute error (AE) below 3% for each of the ligament strains. This accuracy is minimally required compared to an optimization objective specifying the maximal strain at 6%. A total of 18,929 samples is required to achieve this accuracy objective. Details on the post-TKA neural network validation error can be found in the Supplementary Material.

The results of the implant position optimization are discussed in more detail in Section 3.1 for each of the three evaluated native safe zones and the two surgical precisions. Part 3.2 gives the results on the identification of the critical ligament properties. This section closes with an evaluation of the computational efficiency of the developed method (Section 3.3).

3.1 Implant position optimization

Table 3 gives the optimization objective (OO)—as computed with Eq. 3—and the GSP for the different native safe zones (SZ_D, $SZ_{D\&S}$, and $SZ_{D\&K}$) and for two different surgical precisions (RAS (Cosendey et al., 2021) and $Pr_{90\%}$ (Bartsoen et al., 2021)). It can be seen that the 90% success probability of $Pr_{90\%}$, which solely included surgical precision, is reduced to 3.0%, 13.0%, and 13.0% for SZ_D, $SZ_{D\&S}$, and $SZ_{D\&K}$, respectively, due to the uncertainty introduced by the ligament properties. It can be seen that the results are similar to the RAS surgical precision. $SZ_{D\&S}$ and $SZ_{D\&K}$ show similar success probabilities, but OO is, however, halved. As OO is based on the square of the difference between the ligament strain and the post-TKA safe zone, this shows a reduction in variation due to ligament properties when pre-operative squat kinematics is known.

3.2 Sensitivity analysis

Figure 2 shows the results of the convergence analysis, implying that SA has converged after 510 samples.

Figure 3 shows the box plots of the means of the different implant position parameters for $Pr_{90\%}$ with variation in the ligament properties according to $SZ_{D\&S}$. This figure illustrates that the uncertainty of the critical implant position parameters (indicated with *) due to the uncertainty in the ligament properties (blue) is large compared to the required surgical error that was established in Bartsoen et al. (2021) (red). The success probability does not vary largely.

Table 4 presents the results of SA. The table gives the 10 most critical parameters, out of the 50 ligament properties, for each of the critical implant position parameters, as identified by Bartsoen et al. (2021), as well as the success probability. Each of the critical ligament properties is further divided according to their corresponding delta moment-independent sensitivity measure. The three largest measures are indicated as most critical, the next three are indicated as mid-critical, and the remaining four are indicated as least critical. Mainly, the reference strain and, to a slightly lesser extent, the attachment sites are most critical. The linear stiffness is of lesser importance. It can also be seen that for every ligament, at least one of the properties is critical.

3.3 Computational efficiency

The optimization process to quantify GSP requires 4,096 knee model evaluations for seven flexion angles per chain, with a total of 64 offspring per generation. As each optimization requires on average 400 iterations, this results in a total of 734 million evaluations per optimization. With an evaluation time of ±4 min for the knee model directly, this analysis would be infeasible. Using the ANN as a surrogate results in an evaluation time of ±1 ms, allowing optimization in 10 days on the "AMD EPYC 7601 32-core processor." The neural network nevertheless requires training with 17,036 training samples and 1,893 validation samples. With 12 parallel workers, this takes about 47 h to sample on "Intel Xeon CPU E5-2630."

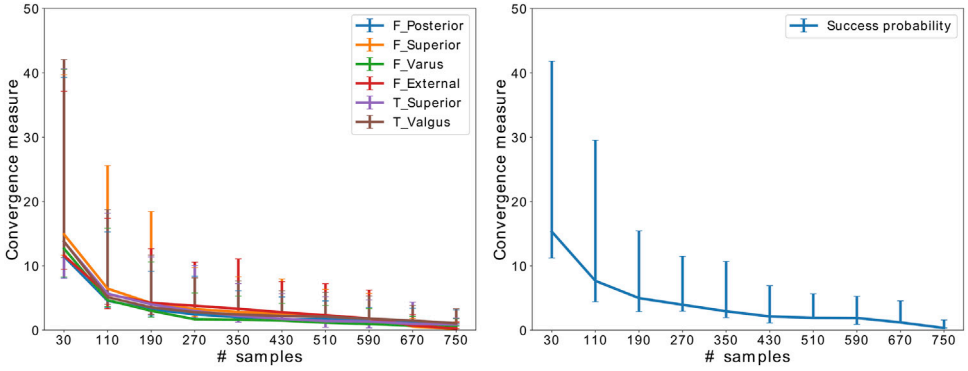

FIGURE 2
Convergence of SA for the critical implant position parameters and success probability. The error bars indicate the variation throughout 50 random samplings.

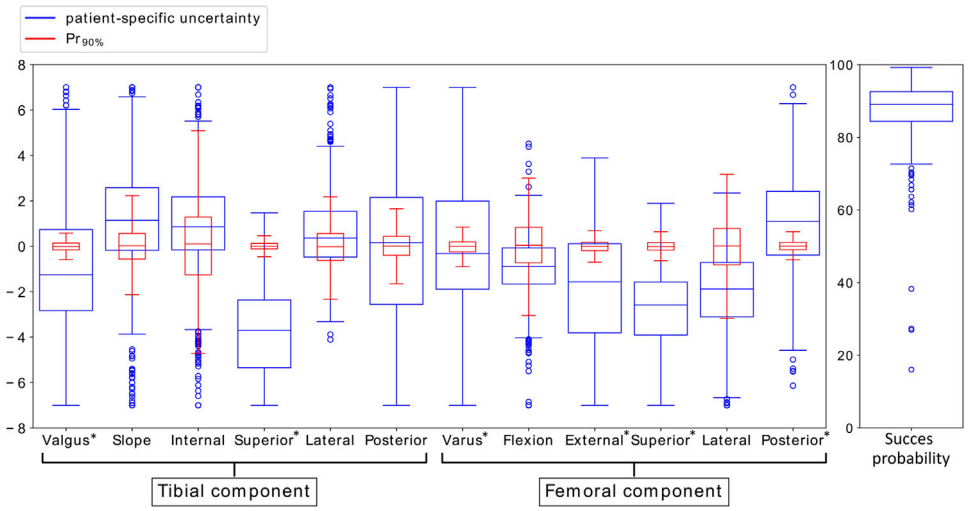

FIGURE 3
Variation in mean implant position parameters and success probability due to variation in ligament properties accounting for $SZ_{D\&S}$ (blue) and due to the surgical precision $Pr_{90\%}$ (red). The critical implant position parameters, identified by Bartsoen et al. (2021), are indicated with *.

4 Discussion

We developed a ligament-balanced probabilistic planning tool that accounts for subject-specific and surgical uncertainty with a feasible computational cost. Three different native safe zones (SZ_D, $SZ_{D\&S}$, and $SZ_{D\&K}$), representing physiological ligament strains, were evaluated along using two different surgical transfer techniques (RAS and $Pr_{90\%}$). Our results show that the OO values and the GSP are similar between RAS and $Pr_{90\%}$. It is important to note that the RAS precision quantified by Cosendey et al. (2021) is based on experimental measurements on sawbones but not in a clinical setting and documents the precision of the cuts and not the final implant position. Actual errors are thus most likely larger but are not available in the literature for all DOFs of the implant position.

With solely accounting for ligament damage, only 3% GSP can be achieved, meaning that without exact measurements of the ligament properties, the success probability is reduced by 87%. Even if an extra constraint on stability is applied, the GSP only increases to 13%. When squat kinematics are measured, the GSP does not increase further. The OO is, however, more than halved, showing that the total variation in the ligament strain is considerably reduced. Interestingly, the results show that measuring native kinematics can reduce ligament properties' uncertainty, but that solely measuring kinematics during a squat movement is insufficient. Combining different movements, for example, laxity trials in several DOFs, could potentially offer a large enough reduction in ligament properties' uncertainty. A device allowing this type of measurement is being studied by Pedersen et al. (2019).

TABLE 4 Ten most critical ligament properties (out of 50) for the critical implant position parameters and success probability. The 10 most critical ligament properties are further classified into the three most critical, three mid-critical, and four least critical.

	Output	Critical	Reference strain	Stiffness	Attachment	
					Femur	*Tibia*
Femur	A/P	Most	deepMCL and PFL		deepMCL	
		Mid	ALL and PC			ACL1
		Least			ACL0 and supMCL	ACL0 and PCL1
	P/D	Most	ALL and PFL			PCL1
		Mid	LCL		ACL0	ACL1
		Least	deepMCL	supMCL	PFL	PCL0
	V/V	Most	ALL and PFL		ACL0	
		Mid	LCL			ACL0 and PCL0
		Least			deepMCL and PFL	ACL1 and PCL1
	I/E	Most	ALL, deepMCL, and PFL			
		Mid	LCL		deepMCL	PCL1
		Least	ACL0, PC, and supMCL		ACL0	
Tibia	P/D	Most	ALL, deepMCL, and LCL			
		Mid			deepMCL and PFL	PCL1
		Least	PC and PFL		ACL0	ACL1
	V/V	Most	ALL and PFL			ACL0
		Mid	LCL		ACL0 and deepMCL	
		Least	deepMCL and PC		PFL	PCL1
	Success probability	Most	ALL, LCL, and PFL			
		Mid	deepMCL		deepMCL	PCL1
		Least		ALL	ACL0	ACL0 and ACL1

They developed an arthrometer that is applied in combination with a biplanar x-ray system to measure knee joint laxity in four DOFs.

It has to be highlighted that the success probabilities, as estimated in the current study, do not account for the experience of the surgeon. The success probabilities indicate the probability of success when the proposed plan would be blindly executed without further adjustments of the implant position and/or ligament releases based on the surgeon's expertise. Consequently, in the literature, reported patient satisfaction is higher.

The results of the SA show that the variance in reference strain and attachment sites causes the small GSP, where the linear stiffness is of lesser importance. A single most critical ligament could not be identified, where even the attachment sites of the ACL and PCL are of high importance even when a PS implant is implanted. The high importance of ACL and PCL also partially explains the low success probabilities as their effect cannot be accounted for using a PS implant, where the cruciate ligaments are sacrificed. The small GSP, while imposing native squat kinematics, could also partially be explained by the use of a PS implant, where other studies have shown that it cannot entirely replicate native kinematics. Zhao et al. (2015), for example, concluded that the PS implant had an abnormal forward displacement, insufficient rollback of the lateral femoral condyle, and the tibia presented insufficient internal rotation during early flexion. Dejtiar et al. (2020), however, showed that a cruciate retaining (CR) implant is capable of approximating native kinematics. Therefore, it would be interesting to perform the same analysis with a CR implant to investigate how implant type affects the success probability.

This study needs to be considered in light of the following limitations. The conclusions are based on a single subject. The computational knee model is based on an *in vitro* squat simulation, where only the quadriceps and hamstring muscles are modeled and considered passive structures through which an external, known force is applied. A model with active muscles would require the introduction of extra patient-specific input parameters to the knee model, which would introduce extra uncertain parameters that have to be accounted for in the probabilistic knee model.

To allow clinical application of the designed pre-operative planning process in the future, the native and post-TKA safe zones need to be verified. The different safe zones are based on strain measurements and experimental damage testing in ligaments but have not been linked to patient satisfaction yet.

Another requirement to facilitate clinical application is to increase computational knee model robustness. Indeed, the current knee model formulation assumes each ligament with one strand with

the exception of ACL and PCL where two strands are used. To reduce the effect of the attachment sites, each ligament could be modeled with multiple strands. As the attachment sites and reference strain are highly correlated, this approach will also decrease the influence of the reference strain. If this approach still proves insufficient to further reduce ligament-balanced implant position uncertainty, the focus of future research should be on identifying reference strain and attachment sites prior to surgery to achieve an accurate prediction. Research has been investigating *in vivo* measurement techniques to measure ligament strains. Slane et al. (2017), for example, discussed ultrasound elastography for measuring knee ligament properties *in vivo*. However, issues related to the measurement of 3D ligament movement using 2D imaging techniques are limiting accurate strain measurements. Alternatively, the pre-operative planning could be tuned intra-operatively. RAS or augmented reality (AR) systems could allow extra measurements of ligament properties through tracking of passive movements and force measurements. The motion and/or force data can be converted into an estimation of the ligament properties as shown in the current study in the estimation of the set family corresponding to $SZ_{D\hat{e}K}$. This set family identifies the ligament properties corresponding to the kinematics of a squat movement. The same procedure could be followed to quantify a set family of ligament properties corresponding to other movements and/or forces as well. As performed in the current study, the computed set family can be translated into remaining uncertainty in the ligament strains or other knee model output parameters that might be of interest.

A final step toward clinical applicability is to further decrease computational costs. Even though the use of an ANN as a surrogate for the knee model reduces the computational time of the pre-operative planning process significantly, its application in clinical practice is still infeasible as a global optimization with subject-specific and surgical uncertainty still requires several days. A possibility to further reduce this is by the application of a single loop scheme—as, for example, presented by Hong et al. (2022) through their Bayesian augmented space learning (BASL) method—where a direct prediction of the optimized mean implant position along with its remaining uncertainty would be performed. This would allow prediction of the pre-operatively planned implant position in a few milliseconds. In addition, the ANN should be trained on a patient-specific basis. Future versions of the network should therefore include patient geometry, allowing the definition of one single ANN for the pre-operative planning of individual (unseen) patients.

5 Conclusion

We developed a ligament-balancing probabilistic planning tool for TKA that accounts for uncertainty in ligament properties and surgical precision. Through inverse uncertainty quantification, a set family of ligament properties was identified that satisfies different physiologically relevant native safe zones. We concluded that only a GSP of 12% can be reached, meaning that without extra measurements of kinematics and/or direct measurements of ligament properties, uncertainty is too large to reduce the risk of ligament damage. A SA showed that the reference strain and to a lesser extent also the attachment sites were the most critical parameters. However, no single ligament could be identified as being the most critical parameter.

Data availability statement

The raw data supporting the conclusion of this article will be made available by the authors, without undue reservation.

Author contributions

LB conceptualized the study, drafted and edited the manuscript, and performed the analysis of the data. MF, RW-S, DM, IJ, and JS conceptualized the study and edited the manuscript.

Funding

This research was funded by the Materialise Chair for Image-Based, Patient-Specific Biomechanics.

Conflict of interest

RW-S is a paid employee of Materialise NV

The remaining authors declare that the research was conducted in the absence of any commercial or financial relationships that could be construed as a potential conflict of interest.

The authors declare that this study received funding from Materialise. The funder had the following involvement with the study: Payment of scholarship to LB, Involvement in analysis, interpretation of data and writing of this article.

Publisher's note

Supplementary material

The Supplementary Material for this article can be found online at: https://www.frontiersin.org/articles/10.3389/fbioe.2022.930724/full#supplementary-material

References

Abadi, M., Agarwal, A., Barham, P., Brevdo, E., Chen, Z., Citro, C., et al. (2016). Tensorflow: Large-scale machine learning on heterogeneous distributed systems. arXiv preprint arXiv:1603.04467.

Bartsoen, L., Faes, M. G., Wesseling, M., Wirix-Speetjens, R., Moens, D., Jonkers, I., et al. (2021). Computationally efficient optimization method to quantify the required surgical accuracy for a ligament balanced tka. *IEEE Trans. Biomed. Eng.* 68, 3273–3280. doi:10.1109/tbme.2021.3069330

Bartsoen, L., Faes, M. G., Andersen, M. S., Wirix-Speetjens, R., Moens, D., Jonkers, I., et al. (2023). Bayesian parameter estimation of ligament properties based on tibio-femoral kinematics during squatting. *Mech. Syst. Signal Process.* 182, 109525. doi:10.1016/j.ymssp.2022.109525

Beidokhti, H. N., Janssen, D., van de Groes, S., Hazrati, J., Van den Boogaard, T., and Verdonschot, N. (2017). The influence of ligament modelling strategies on the predictive capability of finite element models of the human knee joint. *J. Biomech.* 65, 1–11. doi:10.1016/j.jbiomech.2017.08.030

Betz, W., Papaioannou, I., and Straub, D. (2016). Transitional markov chain monte carlo: observations and improvements. *J. Eng. Mech.* 142, 04016016. doi:10.1061/(asce)em.1943-7889.0001066

Blank, J., and Deb, K. (2020). pymoo: Multi-objective optimization in python. *IEEE Access* 8, 89497–89509. doi:10.1109/access.2020.2990567

Borgonovo, E. (2007). A new uncertainty importance measure. *Reliab. Eng. Syst. Saf.* 92, 771–784. doi:10.1016/j.ress.2006.04.015

Bourne, R. B., Chesworth, B. M., Davis, A. M., Mahomed, N. N., and Charron, K. D. (2010). Patient satisfaction after total knee arthroplasty: who is satisfied and who is not? *Clin. Orthop. Relat. Res.* 468, 57–63. doi:10.1007/s11999-009-1119-9

Chandrashekar, N., Mansouri, H., Slauterbeck, J., and Hashemi, J. (2006). Sex-based differences in the tensile properties of the human anterior cruciate ligament. *J. Biomech.* 39, 2943–2950. doi:10.1016/j.jbiomech.2005.10.031

Ching, J., and Chen, Y.-C. (2007). Transitional markov chain monte carlo method for bayesian model updating, model class selection, and model averaging. *J. Eng. Mech.* 133, 816–832. doi:10.1061/(asce)0733-9399(2007)133:7(816)

Cosendey, K., Stanovici, J., Mahlouly, J., Omoumi, P., Jolles, B. M., and Favre, J. (2021). Bone cuts accuracy of a system for total knee arthroplasty including an active robotic arm. *J. Clin. Med.* 10, 3714. doi:10.3390/jcm10163714

De Vloo, R., Pellikaan, P., Dhollander, A., and Vander Sloten, J. (2017). Three-dimensional analysis of accuracy of component positioning in total knee arthroplasty with patient specific and conventional instruments: a randomized controlled trial. *Knee* 24, 1469–1477. doi:10.1016/j.knee.2017.08.059

Dejtiar, D. L., Bartsoen, L., Perez, M. A., Vander Sloten, J., Wirix-Speetjens, R., and Wesseling, M. (2020). Standard cruciate-retaining total knee arthroplasty implants can reproduce NativeKinematics. Tech. rep.

Delport, H. P., Vander Sloten, J., and Bellemans, J. (2013). New possible pathways in improving outcome and patient satisfaction after tka. *Acta Orthop. Belg.* 79, 250–254.

Delport, H., Labey, L., Innocenti, B., De Corte, R., Vander Sloten, J., and Bellemans, J. (2015). Restoration of constitutional alignment in tka leads to more physiological strains in the collateral ligaments. *Knee Surg. Sports Traumatol. Arthrosc.* 23, 2159–2169. doi:10.1007/s00167-014-2971-z

Freeman, M., Insall, J. N., Besser, W., Walker, P. S., and Hallel, T. (1977). Excision of the cruciate ligaments in total knee replacement. *Clin. Orthop. Relat. Res.* 126, 209–212. doi:10.1097/00003086-197707000-00039

Guo, Z., Freeman, J. W., Barrett, J. G., and De Vita, R. (2015). Quantification of strain induced damage in medial collateral ligaments. *J. Biomech. Eng.* 137. doi:10.1115/1.4030532

Hampp, E. L., Chughtai, M., Scholl, L. Y., Sodhi, N., Bhowmik-Stoker, M., Jacofsky, D. J., et al. (2019). Robotic-arm assisted total knee arthroplasty demonstrated greater accuracy and precision to plan compared with manual techniques. *J. Knee Surg.* 32, 239–250. doi:10.1055/s-0038-1641729

Harner, C. D., Xerogeanes, J. W., Livesay, G. A., Carlin, G. J., Smith, B. A., Kusayama, T., et al. (1995). The human posterior cruciate ligament complex: an interdisciplinary study: Ligament morphology and biomechanical evaluation. *Am. J. Sports Med.* 23, 736–745. doi:10.1177/036354659502300617

Herman, J., and Usher, W. (2017). SALib: An open-source python library for sensitivity analysis. *J. Open Source Softw.* 2, 97. doi:10.21105/joss.00097

Hong, F., Wei, P., Song, J., Faes, M., Valdebenito, M., and Beer, M. (2022). Combining data and physical model for probabilistic analysis: A bayesian augmented space learning perspective. *J. Comput. Phys.* (Preprint under review).

Kuster, M., Bitschnau, B., and Votruba, T. (2004). Influence of collateral ligament laxity on patient satisfaction after total knee arthroplasty: a comparative bilateral study. *Arch. Orthop. Trauma Surg.* 124, 415–417. doi:10.1007/s00402-004-0700-7

LaPrade, R. F., Bollom, T. S., Wentorf, F. A., Wills, N. J., and Meister, K. (2005). Mechanical properties of the posterolateral structures of the knee. *Am. J. Sports Med.* 33, 1386–1391. doi:10.1177/0363546504274143

Lidgren, L., Robertsson, O., and W-Dahl, A. (2004). *The Swedish knee arthroplasty register: Annual report 2004*. Lund: Lund University Hospital.

Nam, D., Nunley, R., and Barrack, R. (2014). Patient dissatisfaction following total knee replacement: a growing concern? *Bone Jt. J.* 96, 96–100. doi:10.1302/0301-620x.96b11.34152

Noble, P. C., Gordon, M. J., Weiss, J. M., Reddix, R. N., Conditt, M. A., and Mathis, K. B. (2005). Does total knee replacement restore normal knee function? *Clin. Orthop. Relat. Res.* 431, 157–165. doi:10.1097/01.blo.0000150130.03519.fb

Pedersen, D., Vanheule, V., Wirix-Speetjens, R., Taylan, O., Delport, H. P., Scheys, L., et al. (2019). A novel non-invasive method for measuring knee joint laxity in four dof: *In vitro* proof-of-concept and validation. *J. Biomech.* 82, 62–69. doi:10.1016/j.jbiomech.2018.10.016

Pianigiani, S., Croce, D., D'Aiuto, M., Pascale, W., and Innocenti, B. (2017). Sensitivity analysis of the material properties of different soft-tissues: implications for a subject-specific knee arthroplasty. *Muscle Ligaments Tendons J.* 7, 546. doi:10.32098/mltj.04.2017.09

Provenzano, P. P., Heisey, D., Hayashi, K., Lakes, R., and Vanderby, R., Jr (2002). Subfailure damage in ligament: a structural and cellular evaluation. *J. Appl. Physiol.* 92, 362–371. doi:10.1152/jappl.2002.92.1.362

Robinson, J. R., Bull, A. M., and Amis, A. A. (2005). Structural properties of the medial collateral ligament complex of the human knee. *J. Biomech.* 38, 1067–1074. doi:10.1016/j.jbiomech.2004.05.034

Sharkey, P. F., Lichstein, P. M., Shen, C., Tokarski, A. T., and Parvizi, J. (2014). Why are total knee arthroplasties failing today—has anything changed after 10 years? *J. Arthroplasty* 29, 1774–1778. doi:10.1016/j.arth.2013.07.024

Skipper Andersen, M., De Zee, M., Damsgaard, M., Nolte, D., and Rasmussen, J. (2017). Introduction to force-dependent kinematics: theory and application to mandible modeling. *J. Biomech. Eng.* 139. doi:10.1115/1.4037100

Slane, L. C., Slane, J. A., D'hooge, J., and Scheys, L. (2017). The challenges of measuring *in vivo* knee collateral ligament strains using ultrasound. *J. Biomech.* 61, 258–262. doi:10.1016/j.jbiomech.2017.07.020

Smith, C. R., Vignos, M. F., Lenhart, R. L., Kaiser, J., and Thelen, D. G. (2016). The influence of component alignment and ligament properties on tibiofemoral contact forces in total knee replacement. *J. Biomech. Eng.* 138, 021017. doi:10.1115/1.4032464

Sobol, I. M. (2001). Global sensitivity indices for nonlinear mathematical models and their monte carlo estimates. *Math. Comput. Simul.* 55, 271–280. doi:10.1016/s0378-4754(00)00270-6

Sugita, T., and Amis, A. A. (2001). Anatomic and biomechanical study of the lateral collateral and popliteofibular ligaments. *Am. J. Sports Med.* 29, 466–472. doi:10.1177/03635465010290041501

Trent, P. S., Walker, P. S., and Wolf, B. (1976). Ligament length patterns, strength, and rotational axes of the knee joint. *Clin. Orthop. Relat. Res.* 117, 263–270. doi:10.1097/00003086-197606000-00034

Twiggs, J. G., Wakelin, E. A., Roe, J. P., Dickison, D. M., Fritsch, B. A., Miles, B. P., et al. (2018). Patient-specific simulated dynamics after total knee arthroplasty correlate with patient-reported outcomes. *J. Arthroplasty* 33, 2843–2850. doi:10.1016/j.arth.2018.04.035

Vanheule, V., Delport, H. P., Andersen, M. S., Scheys, L., Wirix-Speetjens, R., Jonkers, I., et al. (2017). Evaluation of predicted knee function for component malrotation in total knee arthroplasty. *Med. Eng. Phys.* 40, 56–64. doi:10.1016/j.medengphy.2016.12.001

Victor, J., Van Glabbeek, F., Vander Sloten, J., Parizel, P. M., Somville, J., and Bellemans, J. (2009a). An experimental model for kinematic analysis of the knee. *J. Bone Jt. Surg.* 91, 150–163. doi:10.2106/jbjs.i.00498

Victor, J., Wong, P., Witvrouw, E., Vander Sloten, J., and Bellemans, J. (2009b). How isometric are the medial patellofemoral, superficial medial collateral, and lateral collateral ligaments of the knee? *Am. J. Sports Med.* 37, 2028–2036. doi:10.1177/0363546509337407

Woo, S. L.-Y., Hollis, J. M., Adams, D. J., Lyon, R. M., and Takai, S. (1991). Tensile properties of the human femur-anterior cruciate ligament-tibia complex: the effects of specimen age and orientation. *Am. J. Sports Med.* 19, 217–225. doi:10.1177/036354659101900303

Zhao, Z.-X., Wen, L., Qu, T.-B., Hou, L.-L., Xiang, D., and Bin, J. (2015). Kinematic analysis of a posterior-stabilized knee prosthesis. *Chin. Med. J.* 128, 216–221. doi:10.4103/0366-6999.149205

frontiers | Frontiers in Bioengineering and Biotechnology

TYPE Original Research
PUBLISHED 18 November 2022
DOI 10.3389/fbioe.2022.1042441

OPEN ACCESS

EDITED BY
Bernardo Innocenti,
Université libre de Bruxelles, Belgium

REVIEWED BY
Fengyuan Zhao,
Peking University Third Hospital, China
Elizabeth Yanik,
Washington University in St. Louis, United States

*CORRESPONDENCE
E. Audenaert,
emmanuel.audenaert@ugent.be

SPECIALTY SECTION
This article was submitted to Biomechanics, a section of the journal Frontiers in Bioengineering and Biotechnology

RECEIVED 12 September 2022
ACCEPTED 07 November 2022
PUBLISHED 18 November 2022

CITATION
Van Oevelen A, Van den Borre I, Duquesne K, Pizurica A, Victor J, Nauwelaers N, Claes P and Audenaert E (2022), Wear patterns in knee OA correlate with native limb geometry. *Front. Bioeng. Biotechnol.* 10:1042441. doi: 10.3389/fbioe.2022.1042441

Wear patterns in knee OA correlate with native limb geometry

A. Van Oevelen[1,2,3], I. Van den Borre[4], K. Duquesne[1,2], A. Pizurica[4], J. Victor[1,2], N. Nauwelaers[5,6], P. Claes[5,6,7,8] and E. Audenaert[1,2,3,9]*

[1]Department of Orthopedic Surgery and Traumatology, Ghent University Hospital, Ghent, Belgium, [2]Department of Human Structure and Repair, Ghent University, Ghent, Belgium, [3]Department of Electromechanics, InViLab Research Group, University of Antwerp, Antwerp, Belgium, [4]TELIN-GAIM, Faculty of Engineering and Architecture, Ghent University, Ghent, Belgium, [5]Medical Imaging Research Center, MIRC, University Hospitals Leuven, Leuven, Belgium, [6]Department of Electrical Engineering, ESAT/PSI KU Leuven, Leuven, Belgium, [7]Department of Human Genetics, KU Leuven, Leuven, Belgium, [8]Murdoch Childrens Research Institute, Royal Children's Hospital, Melbourne, VIC, Australia, [9]Department of Trauma and Orthopedics, Addenbrooke's Hospital, Cambridge University Hospitals NHS Foundation Trust, Cambridge, United Kingdom

Background: To date, the amount of cartilage loss is graded by means of discrete scoring systems on artificially divided regions of interest (ROI). However, optimal statistical comparison between and within populations requires anatomically standardized cartilage thickness assessment. Providing anatomical standardization relying on non-rigid registration, we aim to compare morphotypes of a healthy control cohort and virtual reconstructed twins of end-stage knee OA subjects to assess the shape-related knee OA risk and to evaluate possible correlations between phenotype and location of cartilage loss.

Methods: Out of an anonymized dataset provided by the Medacta company (Medacta International SA, Castel S. Pietro, CH), 798 end-stage knee OA cases were extracted. Cartilage wear patterns were observed by computing joint space width. The three-dimensional joint space width data was translated into a two-dimensional pixel image, which served as the input for a principal polynomial autoencoder developed for non-linear encoding of wear patterns. Virtual healthy twin reconstruction enabled the investigation of the morphology-related risk for OA requiring joint arthroplasty.

Results: The polynomial autoencoder revealed 4 dominant, orthogonal components, accounting for 94% of variance in the latent feature space. This could be interpreted as medial (54.8%), bicompartmental (25.2%) and lateral (9.1%) wear. Medial wear was subdivided into anteromedial (11.3%) and posteromedial (10.4%) wear. Pre-diseased limb geometry had a positive predictive value of 0.80 in the prediction of OA incidence (r 0.58, $p < 0.001$).

Conclusion: An innovative methodological workflow is presented to correlate cartilage wear patterns with knee joint phenotype and to assess the distinct knee OA risk based on pre-diseased lower limb morphology. Confirming previous research, both alignment and joint geometry are of importance in knee OA disease onset and progression.

KEYWORDS

statistical shape analysis, knee diagnostic imaging, osteoarthritis, alignment, knee wear

1 Introduction

Osteoarthritis (OA) globally ranks among the most prevalent disabling diseases, affecting over 500 million people worldwide, which accounts for 7% of the world's population (Vos et al., 2012; Hunter et al., 2020; Boer et al., 2021). Specifically for an adult USA population, it is estimated that 1 out of 4 inhabitants have some form of arthritis. The OA prevalence is rapidly increasing and is estimated to raise by 50% by the year 2040 [Centers for Disease Control and Prevention (CDC), 2006]. Of the global disease burden for OA, knee OA constitutes 83% (Vos et al., 2012).

However, the precise pathophysiology of OA and drivers for disease progression remain poorly understood (Grässel et al., 2021). Recent literature demonstrates OA being a multi-faceted total joint disease (Boer et al., 2021; Grässel et al., 2021). In the early stage of OA, the cartilage thickness increases as the water fraction raises due to a damaged collagen network. Once the microscopically damaged cartilage fails to counterbalance extrinsic loading, a catabolic reaction initiates superficial articular cartilage loss. Degradation products initiate an inflammatory chain reaction worsening total joint degradation (Grässel et al., 2021). Yet, improved insight in disease onset and progression not exclusively depends on the understanding of these inflammatory pathways. To date, most theoretical approaches of knee OA development and progression assume a synergetic effect of mechanical factors and the systemic milieu. In essences, higher vulnerability in a susceptible environment is assumed to promote disease onset and progression. Inversely, this implies a possible presence of at risk joint mechanics with minimal intra-articular cartilage decay (Sharma et al., 2010).

Recent research strongly emphasizes the link of lower limb alignment and knee joint morphotype on the one hand with the development and progression of knee osteoarthritis on the other hand. Whereas the link between the joint mechanics and OA disease progression is becoming generally accepted, the impact of joint morphology and alignment on the risk of incident knee OA is ambiguously defined. Based on multiple longitudinal observational investigations, varus alignment contributes to incident knee OA with a growing risk for worse varus malalignment. Fewer consensus is observed for valgus alignment (Sharma et al., 2010; Felson et al., 2013; Sharma et al., 2013). From a biomechanical point of view, mild to moderate valgus malalignment is often considered not damaging, as the ground reaction force extending from the center of the foot towards the center of mass passes medially of the center of the knee (Sharma et al., 2010; Sharma et al., 2013; Dell'Isola and Steultjens, 2018). Nevertheless, findings of Felson and colleagues suggest mild to moderate valgus malalignment already promotes incident lateral compartment knee joint OA (Felson et al., 2013).

Few studies have investigated susceptible phenotypes for generalized multicompartment OA, as opposed to unicompartmental disease. In this respect, the most trustworthy method to observe and analyze risk factors for disease onset and progression in a cohort and evaluate mediating factors on the process involves controlled longitudinal follow-up studies. However, in the case of slow progressive and chronic diseases such as OA, the time-dependent character of these experiments limits their discovery power (Murphy, 2021). Furthermore, this multifaceted interaction of joint morphotypes, altered loading conditions and systemic factors results in an extremely heterogenous disease presentation, complicating conceptualization and radiographic classification of knee OA (van der Esch et al., 2014).

Taking into account the co-existence of systemic and local factors, the hypothesis of knee OA being exclusively a unicompartmental disease is more frequently being abandoned. Recent findings of van der Esch and colleagues confirm the combination of a multicompartmental disease process with radiographic features present in the entire joint, on one hand, and a more localized compartmental disease process on the other hand. Based on a bifactor model, joint space narrowing and osteophyte formation are features of both the multicompartmental and the compartmental disease process. As such, osteophyte formation is not useful as a joint overload localizer. Considering both systemic and mechanical factors are involved in the etiology of knee OA, this disease model aligns with the typically observed complex pattern of associations between radiographic features between and within compartments (van der Esch et al., 2014). Typically, the radiographic features describing severity and disease progression are obtained from ordinary X-ray imaging and are subsequently translated into discrete grading systems (e.g., the Kellgren-Lawrence classification) (Kohn et al., 2016). Doing so, a complex three-dimensional problem is simplified to a 2D projection and quantized into a discrete scoring system impeding profound disease phenotyping and classification (Schiphof et al., 2008). Furthermore, the inability to visualize the cartilage layer, negatively impacts the accuracy of the collected data (Favre et al., 2013).

This can be mitigated using volumetric imaging such as Computed Tomography (CT) or Magnetic Resonance Imaging (MRI). Both methods allow for a regional analysis of the joint space width and the detection and description of local erosion (Favre et al., 2013). Usually and for the purpose of comparison between multiple subjects, average cartilage thickness of specific Regions of Interest (ROI) are then obtained. Although being an

improvement to standard X-ray measures, this method still fails to a certain extent to comprehensively describe the location and severity of erosion (Favre et al., 2017). Recent studies indeed indicate that the ROI-based methods both under clinical and experimental conditions poorly reflect mild (or early) phases of disease, still demonstrate wide interobserver variation and are very non-linear over the range from mild to advanced disease status (Altman and Gold, 2007; Favre et al., 2013; Kohn et al., 2016; Favre et al., 2017).

To tackle the shortcomings of the above described methods and thus allowing the statistical comparison of groups of knees, Favre and colleagues described a novel method to establish anatomical correspondence among the entire articular surface of the knee joint (i.e., providing an anatomical standardization) (Favre et al., 2013; Favre et al., 2017). As such, cartilage thickness can be measured for any given point on the subchondral layer within a single subject (Favre et al., 2013). Their pattern-based approach considered overall "thickness maps (images)" therefore allows for improved characterization of features that are lost when cartilage thickness is reduced to a few independent mean thickness measures (Favre et al., 2013; Favre et al., 2017).

Progress in computer vision and image analysis now offers efficient methods to establish anatomical correspondence between knee shapes and to describe the joint space to perform statistical comparison and pattern analysis of sets of joint space narrowing maps (i.e., convolutional neural networks following conformal mesh parameterization) (Audenaert et al., 2019a; Nauwelaers et al., 2021). Whereas Favre and colleagues aimed for anatomical correspondence relying on standardized two-dimensional pixel-maps, anatomical correspondence in 3D can be obtained by non-rigid surface registration of a reference template thereby providing a dense set of homologous landmarks amenable to statistical analysis (Williams et al., 2010; Favre et al., 2013; Audenaert et al., 2019a; van Houcke et al., 2020; Peiffer et al., 2022). This permits statistical comparison between and within populations of skeletal shape and related joint space geometry (Williams et al., 2010; Audenaert et al., 2019a; Nauwelaers et al., 2021). Furthermore and by comparison with healthy data, disease severity and progression can be quantified and even a virtual healthy twin can be generated (Fuessinger et al., 2019; Ahmadian et al., 2022).

In the present study, virtual healthy twins are generated from a large cohort of cases presenting with end-grade knee OA, using a validated lower limb shape model (SSM). The latter was constructed, from a healthy cohort of over 600 cases (Audenaert et al., 2019b). Hence, the aim is to return backwards by reconstructing the original alignment and joint morphology prior to OA onset. Doing so, we intend to confirm existing associations and establish new phenotypes at risk for OA onset and progression. In addition to improving the description of cartilage morphology, identifying characteristic wear patterns could provide new insights into the function and degradation process of knee cartilage in relation to the limb alignment and joint morphotype.

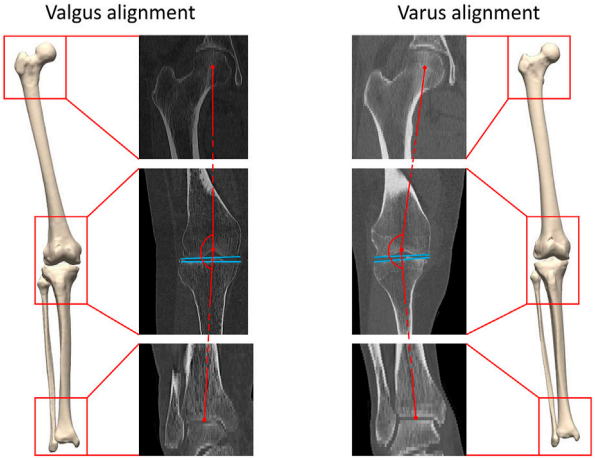

FIGURE 1
A three-dimensional lower limb model is developed starting from the available CT data. Both valgus alignment (left) and varus alignment (right) are visualized. Typically, valgus alignment (left) is defined as a hip-knee-ankle (HKA) angle smaller than or equaling 177° whereas varus alignment (right) involves a HKA angle equaling or exceeding 183° (Hirschmann et al., 2019). The HKA angle is formed interconnecting the center of the hip, of the knee and of the ankle in the coronal plane, visualized in red. The tangent to the distal femoral bone and to the proximal tibia plateau are visualized in blue.

2 Materials and methods

2.1 Sample/data

2.1.1 Osteoarthritis group

Digital bony shapes of the proximal and distal femur and the proximal and distal tibia were extracted from a retrospective database of 933 patients (460 females and 473 males), provided in anonymized form by the Medacta company (Medacta International SA, Castel S. Pietro, CH). The patients reported localized knee pain associated with mechanical knee instability at staging time. Diagnostic imaging confirmed different degrees of cartilage defects, femoral osteophytes, and shape abnormalities, mainly at the condylar regions of the distal femur and at the tibial plateau. All patients underwent knee resurfacing or knee replacement surgery by means of a Patient Specific Instrumentation (PSI) between July 2012 and April 2020. For surgical planning purposes, 3D imaging by CT scanning of the lower limb joints was acquired. The image acquisition protocol included CT scans of the knee, hip, and ankle regions. A minimum of 512 × 512 pixels was acquired for each scan. The thickness of a single slice was 2 mm for the hip and ankle joint and 6 mm for the

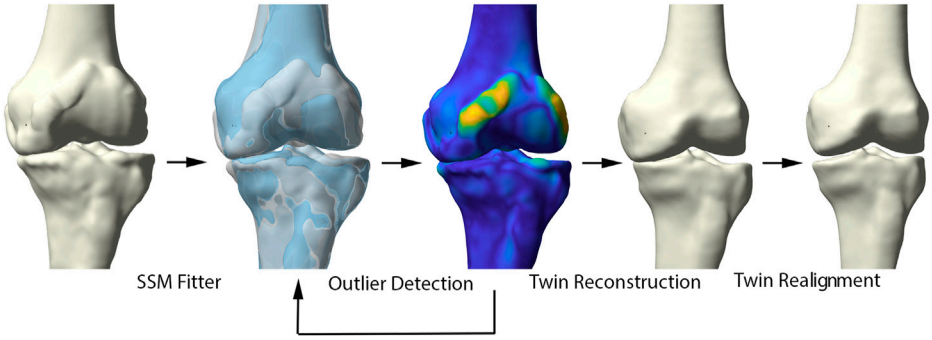

FIGURE 2
Representation of the healthy virtual twin reconstruction. Left to right: starting from a diseased sample, healthy femur and tibia were fitted to the arthritic knee. Outlier detection aided in osteophyte localization. Following, the healthy statistical shape model was fitted to the diseased sample, excluding disease related morphological changes. The virtual healthy twin was then reassembled based on the healthy, articulated lower limb model.

knee joint (Figure 1). All subjects gave written informed consent for data collection and processing before enrollment in the study database. Exclusion criteria were defined as the presence of hip, knee or ankle arthroplasty, the presence of osteosynthesis material, or osteological evidence of former osteosynthesis for trauma or osteotomy reasons as defined by cortical interruptions and the presence of former drilling holes. This study was executed conform the Helsinki guidelines and was approved by the ethics committee of the Ghent University Hospital.

2.1.2 Articulated statistical shape model of the nonarthritic lower limb

For the purpose of reconstruction of a healthy virtual twin, an articulated statistical shape model (SSM) of nonarthritic lower limb cases was used. The Ghent lower limb model is the largest articulated SSM of the lower limb previously reported in the literature, including 622 samples obtained from 311 lower limb CT scans of non-arthritic cases. Additional details about model development and validation are published by Audenaert et al. (Audenaert et al., 2019a). As the SSM was developed based on healthy subjects, osteoarthritis-related deformities are unknown to the model (Sharma et al., 2010; Dell'Isola and Steultjens, 2018).

2.2 Healthy virtual twin reconstruction

The virtual healthy twin can be considered the patient-specific original lower limb constitution before the onset of osteoarthritic joint deformation. To generate the healthy twins, the healthy SSM was fitted to a combined femoral head, knee joint and distal tibia. In detail, the following pipeline was used for the reconstruction of the unaffected, pre-disease configuration for each knee OA case.

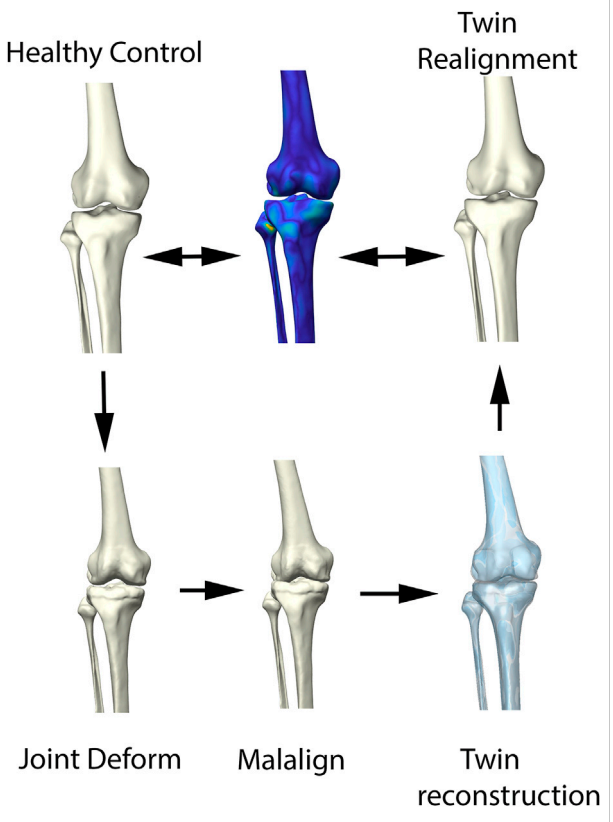

FIGURE 3
Visual representation of the synthetic validation experiment. Starting from the healthy control subjects, osteophytes are artificially imposed based on available outlier distance maps. Following, misalignment of the femur and tibia was enforced. The virtual twin reconstruction pipeline was then conducted and the virtual, realigned healthy twin was compared with the original healthy control input.

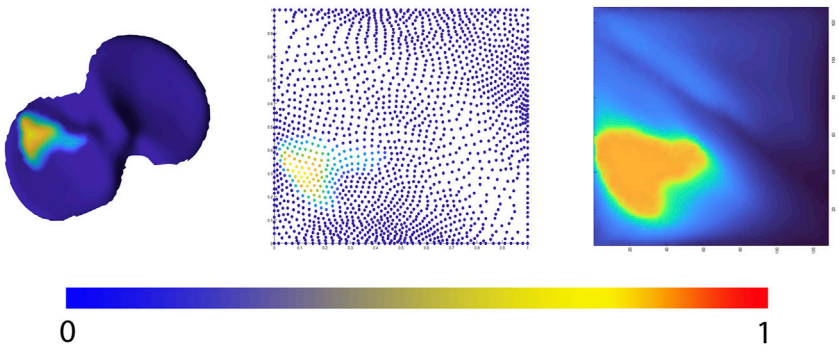

FIGURE 4
Representation of the 2D joint space mapping workflow. Starting from an anatomically standardized distance map (left) a 2D parameterization (center) is developed. Spline-based interpolation provides a pixel image (right). The continuum from intact cartilage towards complete cartilage erosion is color-coded, ranging respectively from blue = 0 (completely intact cartilage) to red = 1, (complete cartilage erosion).

Healthy virtual twin geometries of respectively femur and tibia were constructed by iteratively fitting the healthy shape model to the patient geometries. The fitting iteratively defined correspondences and excluded outlier candidate pairs, which were assumed to represent local deformations induced by the disease. Outlier vertices were identified by evaluating the distance between each pair of points and defined to deviate more than 2 standard deviations from the mean. Dense correspondences and the deformation are computed in an interleaved fashion until convergence. Following, the healthy reconstructions of femur and tibia were aligned according to the healthy articulated model of the lower limb. The process of reassembly of multiple components according to a control statistical shape model was previously validated by Audenaert et al. (Murphy, 2021). The workflow is illustrated in detail in Figure 2.

The ability of the above described process to reconstruct a patient's pre-diseased state was evaluated in a synthetic validation experiment. Healthy cases, not included in the non-arthritic lower limb SSM were randomly provided with outlier deformities around the knee joint, based on distance maps generated from the OA population. Consecutively, misalignment in combination with joint space narrowing was enforced. Following, the reconstruction pipeline was used to reconstruct the native input geometry. The reconstruction error was evaluated by means of the overall root mean square (RMS) reconstruction error and mean absolute angular reconstruction error in the coronal plane (varus -valgus). This process is visualized in Figure 3.

2.3 2D Joint space mapping

Allowing statistical comparison of joint space loss between samples, femorotibial joint distance maps were defined, benefitting from the anatomical correspondence established by the shape modelling pipeline. Following, the corresponding distance maps were unwrapped towards a square boundary 2D mesh using a conformal mapping technique. The distance information, visualized in the 2D mesh as colored dots, was subsequently spline-based interpolated to provide a 128 by 128 isotropic pixel image to be used in neural-based learning. Joints space measures were normalized and inverted in such way that a value 1 corresponds with complete cartilage erosion or a joint space width of 0 mm. The workflow is illustrated in Figure 4.

2.4 Non-linear encoding of wear patterns: Principal polynomial autoencoder

Principal Component Analysis (PCA) is a widespread statistical technique for dimensionality reduction. Linearly transforming the data in a new coordinate system, variation in the data is captured in multiple principal components. The previously obtained joint space images, however, are inherently non-linear and are as such not amenable for analysis by classical linear techniques including PCA (Nauwelaers et al., 2021). Nevertheless, this type of data is ideal for use in neural-based learning. In this domain, autoencoder networks represent the standard for unsupervised feature learning of nonlinear input data. Here we present a new extension of the technique: the principal polynomial autoencoder (PPAE). The PPAE has the structure of a common AE, except for the bottleneck; i.e. the last layer of the encoder and the first layer of the decoder, which are replaced by a low-rank singular value decomposition and consequent polynomial regression to ensure decorrelated scores (Figure 5).

AE networks have been introduced as a non-linear generalizations of PCA. AE are classified as unsupervised learning methods for pattern identification in complex

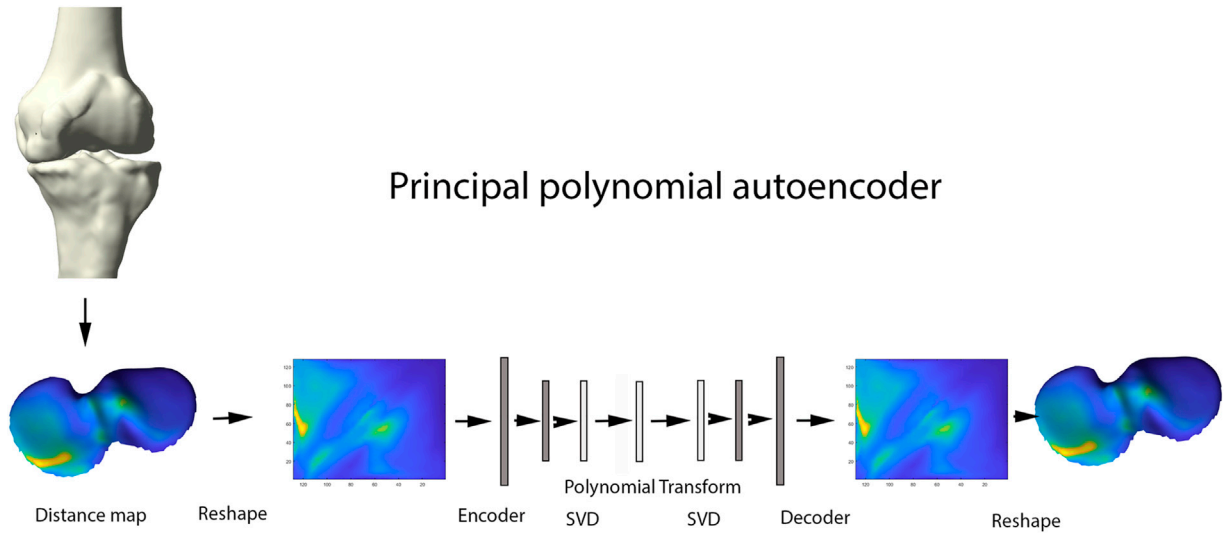

FIGURE 5
Representation of the principal polynomial autoencoder (PPAE). Anatomically standardized distance maps are encoded to pixel images, serving as input for the autoencoder. Singular value decomposition and consequent polynomial regression replace the last layer of the encoder and the first layer of the decoder.

biological data. The commonly used AE networks consisted of two main parts: an encoder and a decoder. The encoder compresses the data into a small number of variables where the decoder aims to reconstruct the original data from that compact representation. One advantage of using an AE over using popular data compression methods such as PCA, is that linearity is not assumed. As such, non-linear cartilage wear patterns can be captured at different stages of OA progression. An important disadvantage of using AE however, is the resulting variables not necessarily being uncorrelated, opposed to the strictly uncorrelated outcome variables following PCA (Hinton and Salakhutdinov, 1979). Nauwelaers and colleagues effectively combined the power of PCA with the flexibility of deep learning for 3D palatal shape modelling (Nauwelaers et al., 2021). Nonetheless, PCA decomposition is hampered by enforcing complex data in linear independent components, while biological features often present non-linear relations. To overcome the latter, Duquesne et al. introduced principal polynomial regression (PPSA) on a linear feature space such as shape analysis. This technique builds further on Principal Polynomial Analysis (PPA), which itself is an adaptation on PCA enabling to capture non-linear behavior of data. Being very computational expensive, Duquesne and colleagues introduced PCA prior to PPA to reduce the dimensionality in the PPSA technique. Based on this PPSA technique, we extend the concept of singular autoencoder analysis to its non-linear upgrade of principal polynomial analysis on the linear latent feature space to increase specificity and enhanced interpretability of the observations (Duquesne et al., 2022).

Considering an unbalanced incidence between medio-lateral and antero-posterior compartment wear, data augmentation based on left-right and antero-posterior mirroring was conducted prior to the encoding of the original distance plots towards the pixel images, which serve as input for the autoencoder (step 3). This way, 4 times as much training data was offered for neural network training. A simple model architecture was adopted, consisting of two fully connecting layers to encode the input distance images into a compact latent space of 15 dimensions. Model and hyperparameter performance was evaluated by means of the mean squared error metric with L2 and sparsity regularization.

2.5 Correlation between wear and morphotype

Following unsupervised feature learning and consequent polynomial parameterization of wear patterns, Uniform Manifold Approximation and Projection (UMAP), was applied to generate a 2-dimensional visual interpretation of the resulting 15-dimensional feature space (Becht et al., 2019; Dorrity et al., 2020). Contrary to PCA, a dimensionality reduction technique based on linear projection of data, UMAP is a non-linear dimension reduction technique. Proven to largely preserve the global structure of the data and maintain high visualization quality, it is often used for data visualization purposes (Becht et al., 2019; Dorrity et al., 2020). Similarly, the combined shape space of healthy twin reconstructions and

healthy controls was visualized by this dimensionality reduction method. Canonical correlation analysis is a statistical tool to assess correlation between two sets of variables. Extended from the multiple regression concept, canonical correlation analysis is applied in the presence of multiple intercorrelated outcome variables. Therefore, it was applied to investigate the correlation with alignment and respectively femoral and tibial bony phenotypes, avoiding manual measurements of alignment. Focusing on the presence of correlation, canonical correlation analysis is unable to perform risk assessment. Therefore, the morphology related risk for knee OA requiring joint arthroplasty was evaluated by Linear Discriminant Analysis, benchmarking the geometry of the healthy twins of the arthritic samples against the control population. Linear discriminant analysis (LDA) is a statistical technique that compares to logistic regression. In the case of normally distributed predictor variables, however, it has proven to be a more efficient classifier (Efron, 1975). More specifically, a LDA classifier was trained using the principal component loadings of the shape entries as predictors, outputting a binary scoring for OA requiring joint arthroplasty. The performance of the LDA classifier was than evaluated in a k-fold leave-one-out cross-validation. Shape features were normalized in the Mahalanobis space to decrease the impact of confounding variance of dominant, unrelated features such as size (Audenaert et al., 2019a; Audenaert et al., 2020). The LDA classifier was evaluated in terms of positive predictive value (PPV), sensitivity and specificity.

A negative control experiment was performed using a cohort of healthy controls with artificially introduced deformities and misalignment. The aim of this second validation was to evaluate to what account the twin reconstruction pipeline impacted on the prediction accuracy of the so called native geometry on the associated risk for AO development. As the deformities were induced randomly, there is no expected correlation with the underlying morphotypes. and any correlation observed in this negative control experiment would then be attributable to the reconstruction pipeline and not the native geometry itself.

3 Results

3.1 Demographics

Out of the 933 subjects from the provided retrospective database, a total of 798 cases (399 females and 399 males) were found to fit the inclusion criteria and were therefore eligible for retrospective assessment. In the female population, a total of 61 cases were excluded for the presence of hip prosthesis (n = 40), knee prosthesis (n = 5), osteosynthesis material (n = 2) or for the existence of segmentation and/or registration errors (n = 14). Similarly, combining the number of cases presenting with hip prosthesis (n = 42), knee prosthesis (n = 5), osteosynthesis material (n = 15) or segmentation and/or registration errors (n = 12), a total of 74 cases were excluded in the male population. The mean age of the included subjects was 70.5 (±8.2) years. The control population, underpinning the healthy articulated SSM, consisted of 622 non-arthritic limbs obtained from 311 patients (181 males and 130 females). The average age was 68.3 (±11.8) years (Audenaert et al., 2019a).

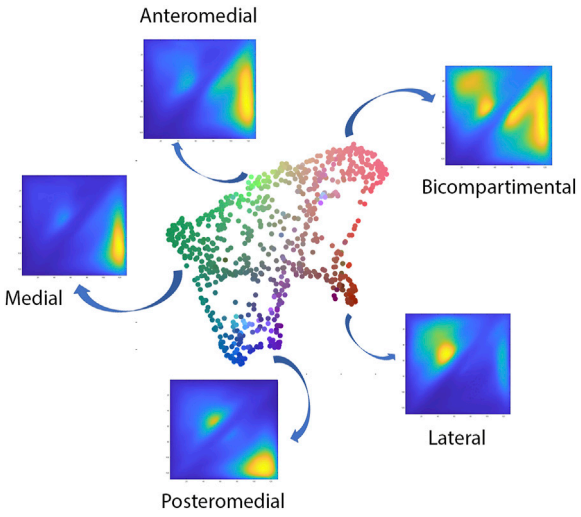

FIGURE 6
Visual representation of the projected shape space of OA cases with RGB coloring according to the observed value of the first three principal polynomial components.

3.2 Synthetic validation experiment

Out of the first validation experiment, the reconstruction error was estimated at an RMS of 0.56 mm (±0.53 mm). The respective bone reconstruction error was 0.64 mm (±0.63 mm) for the femur and 0.53 (±0.47 mm) for the tibia. Errors introduced by the joint realignment were evaluated by comparing the predicted versus original geometries and measured 1.29° (±1.05°) in the coronal plane.

3.3 Cartilage wear pattern analysis

The polynomial autoencoder revealed 4 dominant, orthogonal components, cumulatively accounting for 94% of variance in the latent feature space. Clinically, the obtained modes or cartilage wear patterns could be interpreted as medial (54.8%), bicompartmental (25.2%) and lateral (9.1%) wear. Two particular wear patterns were present within the polynomial components describing respectively a distinct subtype of medial wear, namely anteromedial (11.3%) versus

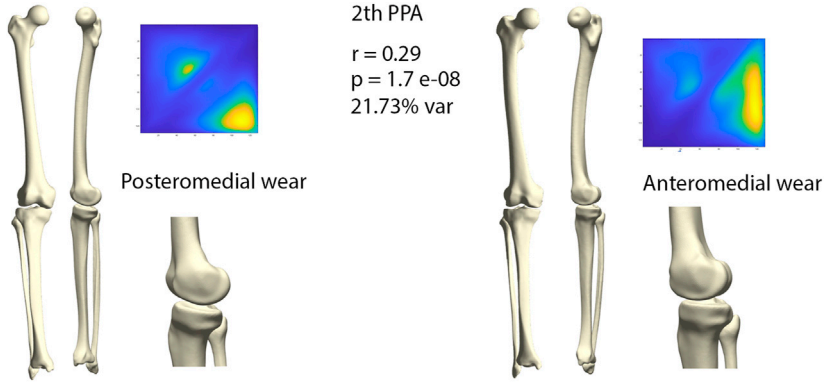

FIGURE 7
Comparison of limb geometry corresponding with posteromedial (left) and anteromedial (right) cartilage wear. Posteromedial wear is correlated with neutral to varus alignment, increased tibial slope and external tibial torsion. Anteromedial wear is correlated with a constitutional varus, increased femur bowing, decreased femoral torsion and a neutral tibial slope. For visualization purposes, differences obtained following the canonical correlation analysis were amplified with a factor 4.

posteromedial (10.4%) wear, as well as tibial spine impingement (4.5%) as observed in coronal tibiofemoral subluxation. A 2D projection of the polynomial encoder feature space using UMAPS is presented in Figure 6.

When evaluating the correlation of the wear pattern with native limb geometry, significant relations were observed, most prominent with varus valgus-alignment. When visualizing the shape configurations correlating with the observed wear patterns the following observations were made. The primary mode of variation, indicating medial towards bicompartmental wear accounted for nearly half of the variance within the latent space (49.5%). This component correlated significantly with the healthy twin geometry, in particular varus alignment (r = 0.4, p = 1.43E-19). Varus alignment correlating with this wear type presented with associated lateral bowing, proximal femoral varus, a decreased femoral version and increased tibial internal torsion.

The second orthogonal component was found to further differentiate medial wear into anteromedial and posteromedial wear (r = 0.29, p = 1.71E-08) (Figure 7). Limb geometry corresponding with posteromedial wear demonstrated a neutral to varus alignment, increased tibial slope as well as increased external tibial torsion, whereas the limb geometry corresponding with anteromedial wear corresponded mostly with what is clinically considered as a constitutional varus, increased femur bowing, decreased femoral torsion and a neutral tibial slope.

A distinct pattern of lateral wear was captured within the 3rd mode of variance, correlating with valgus alignment. Within this component, 9.12% of wear was described as lateral (r = 0.25, p = 2.01 Ee-05). Valgus alignment correlating with this wear pattern presented with associated medial bowing, proximal femoral valgus, increased femoral anteversion and increased tibial external torsion.

Finally, the 4th mode of variation described respectively lateral and medial spinal wear or impingement, accounting for 4.53% of feature space variance. This pattern of wear correlated the least with native joint geometry and with the lowest significance value (r = 0.19, p = 0.013).

3.4 Morphology based osteoarthritis risk assessment

When benchmarking the geometry of the healthy twins of the arthritic samples against the control population there was a relevant and significant correlation between native geometry and the risk of OA development requiring joint arthroplasty (r = 0.58, p = 6.31 E-119). When projecting the shape space in 2D (UMPAS) the healthy control group and OA healthy twins, representing the native limb geometry of the currently diseased cases, delineated as distinct phenotypes (Figure 8). Shape features were normalized to minimize the impact of confounding variance of dominant features such as patient size. Limb alignment and shape demonstrated an overall positive predicted value of 0.80 for OA requiring joint arthroplasty development and a negative predictive value of 0.74. The observed sensitivity and specificity equaled respectively 0.81 and 0.73. The sex specific positive predictive values was 0.83 and 0.76 for respectively the male and female sex, whereas the sex specific negative predictive value was 0.81 and 0.72 for again respectively male and female cases.

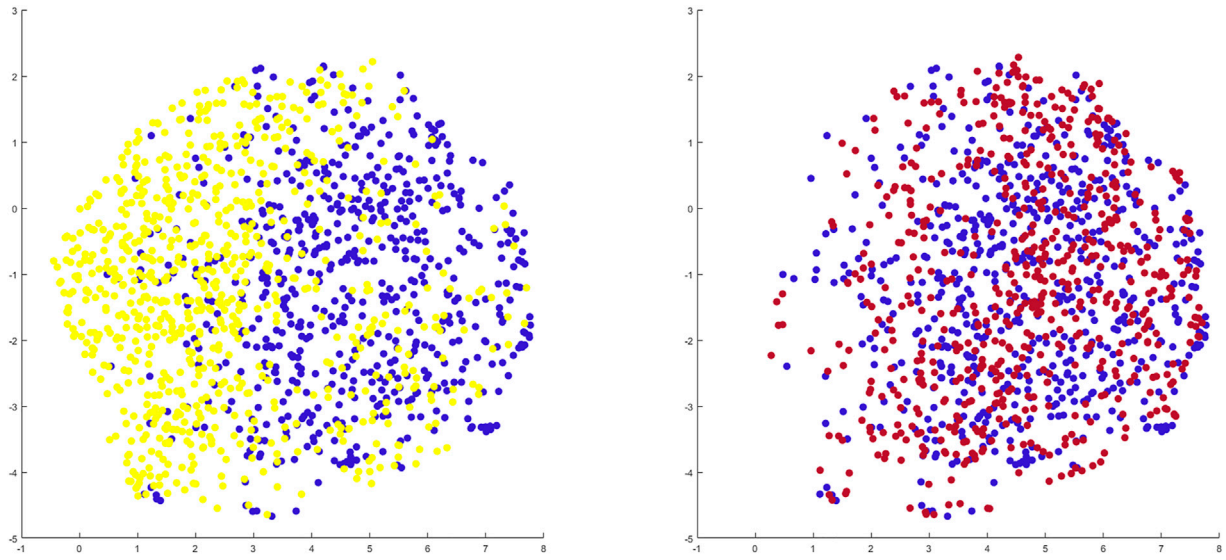

FIGURE 8
2D representation of multiple shape spaces using UMAPS The depicted shape spaces represent the healthy control population (blue), the virtually reconstructed healthy twins from the diseased subjects (yellow) left panel and the virtually reconstructed healthy twins from the artificially deformed and misaligned healthy control samples (red) right panel. Largely overlapping shape spaces are observed for the heathy control subjects and their virtual reconstruction following artificial deformation whereas distinct phenotypes are delineated between the healthy control samples and the virtual healthy twins, reconstructed out of the arthritic samples.

3.5 Negative control experiment

Benchmarking the geometry of the virtual healthy twins, reconstructed out of healthy samples that were artificially deformed and misaligned, against the original healthy control samples, a negligible and non-significant correlation between both was detected (r = 0.06, p = 0.72). As shape space was projected in 2D (UMAPS), largely overlapping phenotypes were observed (Figure 8).

4 Discussion

The understanding of cartilage wear patterns is important to improve insight in knee OA disease onset and progression. In this study, cartilage thickness was assessed in an anatomically standardized manner. As a consequence, the results aid in the understanding of spatial variation in cartilage degeneration in knee OA. Furthermore, assessing the correlation between limb morphology and the risk for knee OA requiring joint arthroplasty assists in the identification of morphometric risk factors potentially affecting the course of the disease.

In the present study, unsupervised learning was applied on a large cohort of degenerative knee joints to asses distinct patterns in cartilage wear and establish the relation with limb alignment and local joint geometry. The polynomial autoencoder revealed medial and lateral wear to be related to respectively varus and valgus malalignment, confirming previously published findings (Sharma et al., 2010; Sharma et al., 2013; Dell'Isola and Steultjens, 2018; Siddiqi et al., 2022). However, Siddiqi and colleagues assumed coronal plane malalignment being rather a response than a cause of knee OA. In contrast, we found it to be present already in a pre-diseased state (Siddiqi et al., 2022). As such, we consider it to be part of an arthritic phenotype rather than being uniquely a result of knee OA.

Within the group of medial cartilage wear, the polynomial autoencoder revealed a further differentiation into anteromedial and posteromedial wear. Whereas anteromedial wear appeared to correspond with the classic description of constitutional varus, posteromedial wear demonstrated a rather neutral to slight varus alignment in combination with a more pronounced posterior tibial slope. Multiple authors linked greater posterior tibial slope to an increased ACL rupture risk (Lansdown and Ma, 2018; Kim et al., 2019; Mortazavi and Vosoughi, 2022). As the femoral condyle translation increases, the ACL is forced to elongate and the tension placed on the ligament intensifies (Lansdown and Ma, 2018). For ACL deficient knees, the wear pattern was suggested to be distinct and posteromedial as opposed to anteromedial wear in ACL intact varus deformity. Rout and colleagues confirmed these findings by describing a shift from anteromedial wear in ACL intact knees towards progressively

more posteromedial wear for increasing ACL damage. These findings suggested ACL deficiency to be a causative factor for posteromedial cartilage wear as it allows greater anteroposterior movements in the tibiofemoral joint (Rout et al., 2013). Having identified a specific phenotype related to posteromedial cartilage wear, our findings were supportive to previous clinical observations. However lacking information about the soft tissue status, we cannot differentiate whether posteromedial wear is solely based on a specific phenotype that additionally increases the ACL rupture risk or whether it develops following ACL rupture, as the specific knee joint morphology makes the subject susceptible for ACL rupture.

Observing the correlation between limb morphology and the risk for knee OA requiring joint arthroplasty, a negative control experiment revealed largely overlapping shape spaces of both the virtually reconstructed healthy twins of the artificially deformed healthy subjects and the healthy control group. As such, the perceived correlation between the predicted native joint geometry and the risk for knee OA requiring arthroplasty is not affected by the reconstruction pipeline. To our knowledge, we are the first to enable distinct knee OA risk assessment based on knee joint morphology in the absence of disease-induced abnormalities. These findings enable accurate and early identification of subjects at risk and so enlarges the number of joint preserving treatment possibilities.

One of the nowadays routinely used preventive treatment options, is joint preserving knee osteotomy surgery (He et al., 2021). As coronal plane malalignment impacts knee joint OA progression, restoring the mechanical axis by joint realignment positively impacts disease advancement (Sharma et al., 2010; Sharma et al., 2013; He et al., 2021). Following osteotomy surgery, knee joint loading is redistributed and knee joint contact pressures are altered (He et al., 2021). We believe that the observed correlation between native joint geometry and the risk for incident knee OA requiring joint arthroplasty enables identification of young, healthy subjects at risk. As a result, those with a high risk can then be treated with joint realignment surgery in a pre-diseased state. Aiming to detect the drivers in joint development and morphology, the genetic background becomes of importance. Although rapidly evolving, genetic research for orthopedic purposes is a relatively recent research domain. Regarding the hip joint for example, Evangelou et al. performed a Genome Wide Association Study (GWAS) meta-analysis on cartilage thickness of the hip joint to detect genetic polymorphisms (Evangelou et al., 2014; Boer et al., 2021). Similar research for detection of knee OA drivers is currently lacking. However, the identification of genetic polymorphisms that lead to knee OA promoting phenotypes can aid in early detection of at risk subjects.

Currently, the identification of subjects at risk is hampered by the inability to detect early changes in cartilage thickness based on the available OA scoring and classification systems. The amount of cartilage degeneration is typically graded using discrete scoring systems in multiple artificially separated regions of interest (Sharma et al., 2010; Sharma et al., 2013; Favre et al., 2017). Aiming to avoid both artificial separating the cartilage layer and grading the amount of degeneration by means of discrete scoring systems, our data collection relies on anatomically standardized cartilage thickness measurements. Similarly, Favre and colleagues described the use of anatomical cartilage thickness maps (Favre et al., 2017; Favre et al., 2021). Williams et al., on the other hand, established anatomical correspondence relying on SSM (Williams et al., 2010). In general, establishing anatomical correspondence among knees for the entire articular surface (i.e., providing an anatomical standardization) allows statistical comparison of groups of knees. Pattern-based approaches considering overall "thickness maps (images)" can then allow for the characterization of features that are lost when cartilage thickness is reduced to a few independent mean thickness measures (Favre et al., 2013). Population-wide analysis allows documenting disease progression and response to therapy assessments (Williams et al., 2010). In the present work we leverage this approach towards unsupervised learning applications and variance models.

4.1 Strengths

Some of the major strengths of this research lies in the innovative methodology. First, reconstructing the original alignment and the joint morphology offers the unique advantage to return to a pre-diseased state.

Second, we present the concept of converting anatomically corresponding color-coded distance maps into pixel images for use in neural-based learning. As biomechanical information is often represented using colormaps, the presented workflow on color-based images for use in neural learning can be extrapolated towards numerous biomechanical research applications. For example, estimation of articular joint contact stresses by means of FEA or DEA typically provides a similar color-coded output (van Houcke et al., 2020).

Finally, conclusions regarding both the phenotype-based distinct knee OA risk and the correlation between cartilage wear patterns and limb morphology were based on a substantial research population of 1420 cases.

4.2 Limitations

Besides the strengths, we have to admit some limitations. As we present here a proof of concept for cartilage wear pattern

recognition built on neural-based unsupervised learning, we developed a rather straightforward autoencoder consisting of two fully connecting layers. Extending this approach for other, possibly more complex, biomechanical problems as described above, convolutional neural networks might are more appropriate to handle pixel images.

Furthermore, the main focus of the present work lies on the assessment of cartilage wear patterns and on finding correlations between the development of knee OA requiring joint arthroplasty and knee phenotypes. Although the extraction of information about osteophyte formation is possible from the available dataset, this was not evaluated. We opted to focus on joint space narrowing, especially as osteophyte formation is triggered by both local and systemic factors according to the hypothesis of total joint involvement. Thus, osteophyte formation is not necessarily localized close to cartilage erosion but can be seen in the complete joint. Osteophyte formation at the intercondylar notch has been related to increased stress and local wear in case of malalignment and is considered an early sign of OA (Sasho et al., 2017). More detailed research regarding variations in intercondylar notch osteophyte formation is needed, especially since the polynomial autoencoder revealed the 4th orthogonal component to describe medial and lateral notch impingement.

Lastly, although our findings are based on a substantial dataset consisting of both a large number of diseased subjects and a healthy control group, an important limitation of our findings relates to the amount of available clinical information of the patients investigated. For example, information regarding soft tissue status, and in particular the ACL, is absent. Similar and although known to contribute to knee OA disease progression data about Body Mass Index (BMI) and lifestyle-related knee joint loading is lacking (Blazek et al., 2014). Furthermore, a possible selection bias is introduced by excluding the cases present with hip and/or ankle arthroplasty, excluding cases probably suffering OA driven by systemic factors rather than by knee-specific risk factors. However, aiming to establish phenotypes at risk for development of end-stage knee OA, identification of knee-specific risk factors is prioritized in this study rather than identification of systemic risk factors. Lastly, as the results are based on a single homogenous population of Western European Descent, the extent of which findings can be extrapolated to other populations is unknown. The complex interaction between genes, culture and the environment results in a population-based variation, with several studies showing that the appropriate evaluation of this variation requires specific standards for each population (Rissech et al., 2013; San-Millán et al., 2017). Nevertheless, in general we expect our results to be representative by extension for a Western European population.

5 Conclusion

In the present study, we developed an innovative methodological workflow to correlate cartilage wear patterns with knee joint phenotype and to assess the distinct knee OA risk based on pre-diseased samples. Our findings confirm previous studies suggesting that both alignment and joint geometry are highly and significantly correlated with the risk of OA onset and progression. Further, particular morphological phenotypes correlate with distinct cartilage wear patterns.

Data availability statement

The data analyzed in this study is subject to the following licenses/restrictions: Digital bony shapes of the proximal and distal femur and the proximal and distal tibia were extracted from a retrospective database of 933 patients (460 females and 473 males), provided in anonymized form by the Medacta company (Medacta International SA, Castel S. Pietro, CH). Requests to access these datasets should be directed to Info@Medacta.ch.

Author contributions

EA, AP, and PC conceived of the presented idea. AVO, KD, and IVdB developed the theory and performed the computations. EA, and PC. verified the analytical methods. JV supervised the clinical findings of this work. All authors discussed the results and contributed to the final manuscript.

Funding

AVO is funded by a junior PhD Fellowship by the Research Foundation—Flanders (#1122821N, FWO). EA is funded by a Senior Clinical Research Fellowship by the Research Foundation—Flanders (#1842619N, FWO).

Conflict of interest

The authors declare that the research was conducted in the absence of any commercial or financial relationships that could be construed as a potential conflict of interest.

Publisher's note

All claims expressed in this article are solely those of the authors and do not necessarily represent those of their affiliated organizations, or those of the publisher, the editors and the reviewers. Any product that may be evaluated in this article, or claim that may be made by its manufacturer, is not guaranteed or endorsed by the publisher.

References

Ahmadian, H., Mageswaran, P., Walter, B. A., Blakaj, D. M., Bourekas, E. C., Mendel, E., et al. (2022). A digital twin for simulating the vertebroplasty procedure and its impact on mechanical stability of vertebra in cancer patients. *Int. J. Numer. Method. Biomed. Eng.* 38 (6), e3600. doi:10.1002/cnm.3600

Altman, R. D., and Gold, G. E. (2007). Atlas of individual radiographic features in osteoarthritis, revised. *Osteoarthr. Cartil.* 15, A1–A56. doi:10.1016/j.joca.2006.11.009

Audenaert, E. A., Pattyn, C., Steenackers, G., de Roeck, J., Vandermeulen, D., and Claes, P. (2019). Statistical shape modeling of skeletal anatomy for sex discrimination: Their training size, sexual dimorphism, and asymmetry. *Front. Bioeng. Biotechnol.* 7, 302. doi:10.3389/fbioe.2019.00302

Audenaert, E. A., van den Eynde, J., de Almeida, D. F., Steenackers, G., Vandermeulen, D., and Claes, P. (2020). Separating positional noise from neutral alignment in multicomponent statistical shape models. *Bone Rep.* 12, 100243. doi:10.1016/j.bonr.2020.100243

Audenaert, E. A., van Houcke, J., Almeida, D. F., Paelinck, L., Peiffer, M., Steenackers, G., et al. (2019). Cascaded statistical shape model based segmentation of the full lower limb in CT. *Comput. Methods Biomech. Biomed. Engin.* 22 (6), 644–657. doi:10.1080/10255842.2019.1577828

Becht, E., McInnes, L., Healy, J., Dutertre, C. A., Kwok, I. W. H., Ng, L. G., et al. (2019). Dimensionality reduction for visualizing single-cell data using UMAP. *Nat. Biotechnol.* 37 (1), 38–44. doi:10.1038/nbt.4314

Blazek, K., Favre, J., Asay, J., Erhart-Hledik, J., and Andriacchi, T. (2014). Age and obesity alter the relationship between femoral articular cartilage thickness and ambulatory loads in individuals without osteoarthritis. *J. Orthop. Res.* 32 (3), 394–402. doi:10.1002/jor.22530

Boer, C. G., Hatzikotoulas, K., Southam, L., Stefánsdóttir, L., Zhang, Y., Coutinho de Almeida, R., et al. (2021). Deciphering osteoarthritis genetics across 826,690 individuals from 9 populations. *Cell.* 184 (18), 6003–6005. e17. doi:10.1016/j.cell.2021.11.003

Centers for Disease Control and Prevention (CDC) (2006). Prevalence of doctor-diagnosed arthritis and arthritis-attributable Activity limitation-United States, 2003-2005. *MMWR. Morb. Mortal. Wkly. Rep.* 55, 1089–1092.

Dell'Isola, A., and Steultjens, M. (2018). Classification of patients with knee osteoarthritis in clinical phenotypes: Data from the osteoarthritis initiative. *PLoS One* 13 (1), e0191045. doi:10.1371/journal.pone.0191045

Dorrity, M. W., Saunders, L. M., Queitsch, C., Fields, S., and Trapnell, C. (2020). Dimensionality reduction by UMAP to visualize physical and genetic interactions. *Nat. Commun.* 11 (1), 1537. doi:10.1038/s41467-020-15351-4

Duquesne, K., Nauwelaers, N., Claes, P., and Audenaert, E. A. (2022). Principal polynomial shape analysis: A non-linear tool for statistical shape modeling. *Comput. Methods Programs Biomed.* 220, 106812. doi:10.1016/j.cmpb.2022.106812

Efron, B. (1975). The efficiency of logistic regression compared to normal discriminant analysis. *J. Am. Stat. Assoc.* 70 (352), 892–898. doi:10.1080/01621459.1975.10480319

Evangelou, E., Kerkhof, H. J., Styrkarsdottir, U., Ntzani, E. E., Bos, S. D., Esko, T., et al. (2014). A meta-analysis of genome-wide association studies identifies novel variants associated with osteoarthritis of the hip. *Ann. Rheum. Dis.* 73 (12), 2130–2136. doi:10.1136/annrheumdis-2012-203114

Favre, J., Babel, H., Cavinato, A., Blazek, K., Jolles, B. M., and Andriacchi, T. P. (2021). Analyzing femorotibial cartilage thickness using anatomically standardized maps: Reproducibility and reference data. *J. Clin. Med.* 10 (3), 461. doi:10.3390/jcm10030461

Favre, J., Erhart-Hledik, J. C., Blazek, K., Fasel, B., Gold, G. E., and Andriacchi, T. P. (2017). Anatomically standardized maps reveal distinct patterns of cartilage thickness with increasing severity of medial compartment knee osteoarthritis. *J. Orthop. Res.* 35 (11), 2442–2451. doi:10.1002/jor.23548

Favre, J., Scanlan, S. F., Erhart-Hledik, J. C., Blazek, K., and Andriacchi, T. P. (2013). Patterns of femoral cartilage thickness are different in asymptomatic and osteoarthritic knees and can be used to detect disease-related differences between samples. *J. Biomech. Eng.* 135 (10), 101002–101010. doi:10.1115/1.4024629

Felson, D. T., Niu, J., Gross, K. D., Englund, M., Sharma, L., Cooke, T. D. v., et al. (2013). Valgus malalignment is a risk factor for lateral knee osteoarthritis incidence and progression: Findings from the multicenter osteoarthritis study and the osteoarthritis initiative. *Arthritis Rheum.* 65 (2), 355–362. doi:10.1002/art.37726

Fuessinger, M. A., Schwarz, S., Neubauer, J., Cornelius, C. P., Gass, M., Poxleitner, P., et al. (2019). Virtual reconstruction of bilateral midfacial defects by using statistical shape modeling. *J. Cranio-Maxillofacial Surg.* 47 (7), 1054–1059. doi:10.1016/j.jcms.2019.03.027

Grässel, S., Zaucke, F., and Madry, H. (2021). Osteoarthritis: Novel molecular mechanisms increase our understanding of the disease pathology. *J. Clin. Med.* 10 (9), 1938. doi:10.3390/jcm10091938

He, M., Zhong, X., Li, Z., Shen, K., and Zeng, W. (2021). Progress in the treatment of knee osteoarthritis with high tibial osteotomy: A systematic review. *Syst. Rev.* 10 (1), 56. doi:10.1186/s13643-021-01601-z

Hinton, G. E., and Salakhutdinov, R. R. (1979). Reducing the dimensionality of data with neural networks. *Science* 313 (5786), 504–507. doi:10.1126/science.1127647

Hirschmann, M., Moser, L., Amsler, F., Behrend, H., Leclerq, V., and Hess, S. (2019). Functional knee phenotypes: A novel classification for phenotyping the coronal lower limb alignment based on the native alignment in young non-osteoarthritic patients. *Knee Surg. Sports Traumatol. Arthrosc.* 27 (5), 1394–1402. doi:10.1007/s00167-019-05509-z

Hunter, D. J., March, L., and Chew, M. (2020). Osteoarthritis in 2020 and beyond: A lancet commission. *Lancet* 396, 1711–1712. doi:10.1016/s0140-6736(20)32230-3

Kim, G. B., Kim, K. I., Song, S. J., and Lee, S. H. (2019). Increased posterior tibial slope after medial open-wedge high tibial osteotomy may result in degenerative changes in anterior cruciate ligament. *J. Arthroplasty* 34 (9), 1922–1928. doi:10.1016/j.arth.2019.04.032

Kohn, M. D., Sassoon, A. A., and Fernando, N. D. (2016). Classifications in brief: Kellgren-lawrence classification of osteoarthritis. *Clin. Orthop. Relat. Res.* 474 (8), 1886–1893. doi:10.1007/s11999-016-4732-4

Lansdown, D., and Ma, C. B. (2018). The influence of tibial and femoral bone morphology on knee kinematics in the anterior cruciate ligament injured knee. *Clin. Sports Med.* 37 (1), 127–136. doi:10.1016/j.csm.2017.07.012

Mortazavi, S. M. J., and Vosoughi, F. (2022). Association of alignment variables, posteromedial tibial cartilage wear and anterior cruciate ligament insufficiency in participants with varus knee osteoarthritis: A cross-sectional study. *Int. Orthop.* 46 (5), 1029–1036. doi:10.1007/s00264-022-05358-5

Murphy, S. W. (2021). Longitudinal studies 1: Determinants of risk. *Methods Mol. Biol.* 2249, 83–101. doi:10.1007/978-1-0716-1138-8_6

Nauwelaers, N., Matthews, H., Fan, Y., Croquet, B., Hoskens, H., Mahdi, S., et al. (2021). Exploring palatal and dental shape variation with 3D shape analysis and geometric deep learning. *Orthod. Craniofac. Res.* 24 (S2), 134–143. doi:10.1111/ocr.12521

Peiffer, M., Burssens, A., Duquesne, K., Last, M., de Mits, S., Victor, J., et al. (2022). Personalised statistical modelling of soft tissue structures in the ankle. *Comput. Methods Programs Biomed.* 218, 106701. doi:10.1016/j.cmpb.2022.106701

Rissech, C., Márquez-Grant, N., and Turbón, D. (2013). A collation of recently published western European formulae for age estimation of subadult skeletal remains: Recommendations for forensic anthropology and osteoarchaeology. *J. Forensic Sci.* 58, S163–S168. doi:10.1111/1556-4029.12011

Rout, R., McDonnell, S., Hulley, P., Jayadev, C., Khan, T., Carr, A., et al. (2013). The pattern of cartilage damage in antero-medial osteoarthritis of the knee and its relationship to the anterior cruciate ligament. *J. Orthop. Res.* 31 (6), 908–913. doi:10.1002/jor.22253

San-Millán, M., Rissech, C., and Turbón, D. (2017). Shape variability of the adult human acetabulum and acetabular fossa related to sex and age by geometric morphometrics. Implications for adult age estimation. *Forensic Sci. Int.* 272, 50–63. doi:10.1016/j.forsciint.2017.01.005

Sasho, T., Akagi, R., Tahara, M., Katsuragi, J., Nakagawa, R., Enomoto, T., et al. (2017). Osteophyte formation on medial wall of the intercondylar notch of femur is an early sign of osteoarthritic knee development using osteoarthritis initiative data. *Osteoarthr. Cartil.* 25, S33. doi:10.1016/j.joca.2017.02.066

Schiphof, D., Boers, M., and Bierma-Zeinstra, S. M. A. (2008). Differences in descriptions of Kellgren and Lawrence grades of knee osteoarthritis. *Ann. Rheum. Dis.* 67 (7), 1034–1036. doi:10.1136/ard.2007.079020

Sharma, L., Chmiel, J. S., Almagor, O., Felson, D., Guermazi, A., Roemer, F., et al. (2013). The role of varus and valgus alignment in the initial development of knee cartilage damage by MRI: The MOST study. *Ann. Rheum. Dis.* 72 (2), 235–240. doi:10.1136/annrheumdis-2011-201070

Sharma, L., Song, J., Dunlop, D., Felson, D., Lewis, C. E., Segal, N., et al. (2010). Varus and valgus alignment and incident and progressive knee osteoarthritis. *Ann. Rheum. Dis.* 69 (11), 1940–1945. doi:10.1136/ard.2010.129742

Siddiqi, A., Anis, H., Borukhov, I., and Piuzzi, N. S. (2022). Osseous morphological differences in knee osteoarthritis. *J. Bone Jt. Surg.* 104 (9), 805–812. doi:10.2106/jbjs.21.00892

van der Esch, M., Knol, D. L., Schaffers, I. C., Reiding, D. J., van Schaardenburg, D., Knoop, J., et al. (2014). Osteoarthritis of the knee: Multicompartmental or compartmental disease? *Rheumatology* 53 (3), 540–546. doi:10.1093/rheumatology/ket393

van Houcke, J., Audenaert, E. A., Atkins, P. R., and Anderson, A. E. (2020). A combined geometric morphometric and discrete element modeling approach for hip cartilage contact mechanics. *Front. Bioeng. Biotechnol.* 8, 318. doi:10.3389/fbioe.2020.00318

Vos, T., Flaxman, A. D., Naghavi, M., Lozano, R., Michaud, C., Ezzati, M., et al. (2012). Years lived with disability (YLDs) for 1160 sequelae of 289 diseases and injuries 1990–2010: A systematic analysis for the global burden of disease study 2010. *Lancet* 380 (9859), 2163–2196. doi:10.1016/S0140-6736(12)61729-2

Williams, T. G., Holmes, A. P., Waterton, J. C., Maciewicz, R. A., Hutchinson, C. E., Moots, R. J., et al. (2010). Anatomically corresponded regional analysis of cartilage in asymptomatic and osteoarthritic knees by statistical shape modelling of the bone. *IEEE Trans. Med. Imaging* 29 (8), 1541–1559. doi:10.1109/tmi.2010.2047653

frontiers | Frontiers in Bioengineering and Biotechnology

TYPE Original Research
PUBLISHED 25 November 2022
DOI 10.3389/fbioe.2022.1059129

OPEN ACCESS

EDITED BY
Claire Brockett,
University of Leeds, United Kingdom

REVIEWED BY
Harriet Talbott,
University of Hull, United Kingdom
Mike Backhouse,
University of Warwick, United Kingdom

*CORRESPONDENCE
François Rousseau,
francois.rousseau@imt-atlantique
Sylvain Brochard,
sylvain.brochard@chu-brest.fr

†These authors share first authorship

SPECIALTY SECTION
This article was submitted to Biomechanics, a section of the journal Frontiers in Bioengineering and Biotechnology

RECEIVED 30 September 2022
ACCEPTED 07 November 2022
PUBLISHED 25 November 2022

CITATION
Cheng Y, Bailly R, Scavinner-Dorval C, Fouquet B, Borotikar B, Ben Salem D, Brochard S and Rousseau F (2022), Comprehensive personalized ankle joint shape analysis of children with cerebral palsy from pediatric MRI.
Front. Bioeng. Biotechnol. 10:1059129.
doi: 10.3389/fbioe.2022.1059129

Comprehensive personalized ankle joint shape analysis of children with cerebral palsy from pediatric MRI

Yue Cheng[1†], Rodolphe Bailly[2†], Claire Scavinner-Dorval[1], Benjamin Fouquet[1], Bhushan Borotikar[3], Douraied Ben Salem[4], Sylvain Brochard[4*] and François Rousseau[1*]

[1]IMT Atlantique, LaTIM U1101 INSERM, Brest, France, [2]Fondation Ildys, LaTIM U1101 INSERM, Brest, France, [3]Symbiosis Centre for Medical Image Analysis, Pune, India, [4]CHU, UBO, LaTIM U1101 INSERM, Brest, France

Cerebral palsy, a common physical disability in childhood, often causes abnormal patterns of movement and posture. To better understand the pathology and improve rehabilitation of patients, a comprehensive bone shape analysis approach is proposed in this article. First, a group analysis is performed on a clinical MRI dataset using two state-of-the-art shape analysis methods: ShapeWorks and a voxel-based method relying on Advanced Normalization Tools (ANTs) registration. Second, an analysis of three bones of the ankle is done to provide a complete view of the ankle joint. Third, a bone shape analysis is carried out at subject level to highlight variability patterns for personnalized understanding of deformities.

KEYWORDS

shape analysis, ankle joint, MRI, cerebral palsy, morphometry

1 Introduction

Cerebral palsy (CP) is the most common physical disability in childhood, affecting 2.1 out of every 1,000 individuals born. As a result of this non-progressive condition, abnormal movements and postures may occur, as well as impairments in cognitive function and sensory function, such as equinus, the most common musculo-skeletal deformity in children with CP (Davis et al. (1991); Metaxiotis et al. (2002)). In children with bilateral cerebral palsy, equinus prevalence is 83.3% and tends to increase with age. It manifests poor muscle control and weakness around the ankle and foot, leading to abnormal gait patterns and bone deformations during growth (Perry et al. (1974)). It has been reported that muscle morphology has been assessed (Schlegl et al. (2019)), but very little information is available on changes of bone structure. Pediatric MRI studies remain difficult to conduct due to complex acquisition settings (Mitchell et al. (2018); Makki et al. (2019)), however, according to our preliminary analysis, volume differences can be observed between controls and children with CP (see Figure 1 for volume measurements of calcaneus and talus). It suggests that a more detailed

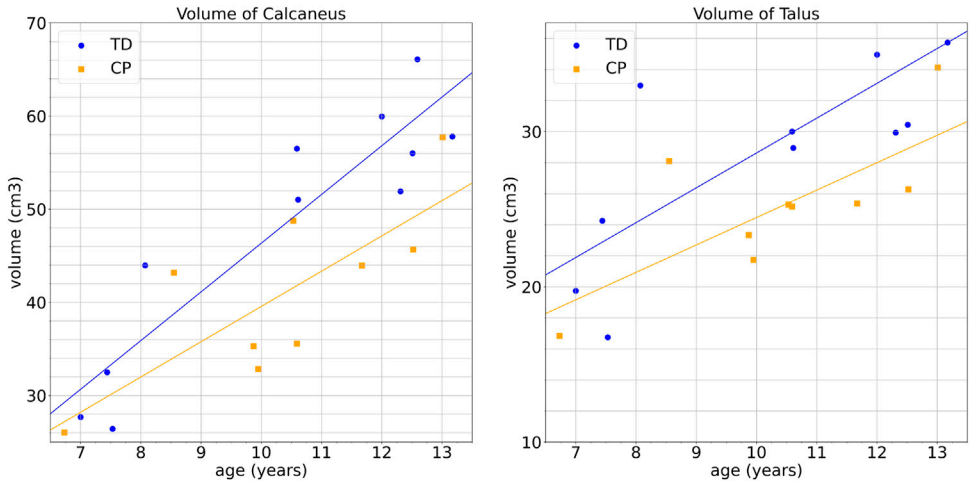

FIGURE 1
Bone and growth cartilage volumes of children with CP and typical developping (TD) children according to age: left: calcaneus, right: talus.

approach to studying the morphology of the ankle joint could lead to a better understanding of CP and personalized management of patients.

To determine whether an intervention is effective, studies report mean differences between groups in clinical trials setting. However, even in the case of statistically significant mean group effects, the intervention may not be effective for every participant in the study. A personalized approach to medical care is currently required (Damiano (2014)). It may also be the case that even for interventions deemed highly effective in CP, a range of individual responses may be observed, from a negative response to a strong positive effect. In order to better respond to the various needs of patients, it appears necessary to develop tools allowing a personalized approach based on a fine morphological analysis to propose a dedicated effective follow-up.

For this purpose, it is required to rely on dedicated analysis of the morphology of the ankle joint for each subject. Shape analysis aims at providing an automatic approach to compare shapes, to classify shapes by similarity or to detect morphological deformations. An analysis of the shape of the ankle bones could be used to identify and visualize the deformities, which could provide a better understanding of CP at the individual level as well as a more suitable rehabilitation program for those individuals (Kedem and Scher (2015)). Litterature reports the application of statistical shape model (SSM) on bone structures reconstruction, population-wise comparison and pathology detection, included but not limited to femur (Ebert et al. (2022); Asvadi et al. (2021); Boutillon et al. (2022); Shi et al. (2022)), pelvis (Vanden Berghe et al. (2017); Shi et al. (2022)), tibia (Shi et al. (2022); Schmutz et al. (2019)), fibula (Shi et al. (2022)) and scapula (Plessers et al. (2018); Boutillon et al. (2022); Salhi et al. (2020)).

However, a recent study (Goparaju et al. (2022)) has shown the importance of evaluation and validation of these tools in clinical applications. Specifically, this study compared three widely used state-of-the-art SSM tools, namely ShapeWorks (Cates et al. (2017)), Deformetrica (Durrleman et al. (2014); Bône et al. (2018)) and SPHARM-PDM (Styner et al. (2006)). The quantitative and qualitative results show that the SSM tools have different levels of consistency and different abilities to capture variability at the population level. What becomes apparent through this study is the need to compare results obtained using multiple shape analysis methods.

The objective of this work is therefore to provide comprehensive shape analysis of the ankle joint based on imaging studies. In order to propose a customized approach, we focus on tools to provide informative deformation maps at population level and also for each CP child based on shape analysis approaches. Morphometry, which is the study of the geometry of shapes, can be performed using voxel-based methods or surface-based approaches. In this work, we propose to investigate both types of approaches to provide the most comprehensive analysis possible at the patient level. Shape analysis relies on mapping (also called registration or matching) between subjects (or templates). Using a reference template, information about the individual shapes can be encoded in the deformation fields (Ashburner et al. (1998)). In such a context, personalized shape analysis is the study of the deformation fields for each subject.

In this article, we study the shape of the ankle joint of children with CP from high-resolution MRI data using two shape analysis approaches. More specifically, our contributions are three-folds: 1) a group analysis using two SSM methods, 2) an analysis of three ankle bones for a complete visualization of the

TABLE 1 Demographic characteristics of the children included per group.

	Age (*years*)	Weight (*kg*)	Height (*cm*)	BMI (kg/m^2)
TD (mean ± std)	10.38 ± 1.95	38.89 ± 13.21	146.55 ± 14.75	17.93 ± 3.09
CP (mean ± std)	10.35 ± 2.39	32.7 ± 6.65	140.39 ± 11.01	16.54 ± 2.69
p-value	0.97	0.22	0.48	0.30

joint, and 3) a subject analysis for a fine study of the deformation patterns for each child.

2 Materials and methods

2.1 Acquisition and preprocessing of clinical data

In this work, we focus on three bone shapes of the ankle joint: calcaneus, talus and tibia. Eleven TD children and nine children with CP with age ranged from 6 to 14 years old participated in this study which was approved by the regional ethics committee. The CP group includes seven males and two females and the TD group consists of seven males and four females with no history of pathology of the lower limbs. The demographic characteristics including age, weight, height and BMI of two groups are demonstrated in Table 1. The *T*-test is performed on these characteristics and no significant inter-group difference is noticed ($p > 0.05$). The details of demographic characteristics of each child included in the experiment are available in Supplementary Materials. All children were selected with no contraindications to MRI and with no history of lower limb musculo-skeletal injury or surgery in the past 6 months. MRI data were acquired in a single visit after parents signed informed consent forms.

3D MRI data have been acquired using a 3T MR scanner (Achieva dStream, Philips Medical Systems, Best, Netherlands) with a resolution of $0.26 \times 0.26 \times 0.8\ mm^3$ and resampled to $0.5 \times 0.5 \times 0.5\ mm^3$ for the purpose of adaptation to clinic (T1-weighted gradient-echo, flip angle 10, matrix 576 × 576, FOV 150 mm × 150 mm, TR/TE 7.81/2.75 ms, mean acquisition duration: 424.32 s). Images of the ankle were taken on the CP group's paretic lower limb, and on the non-dominant lower limb for the TD group. The acquisition protocol was detailed in Makki et al. (2019) and Garetier et al. (2020).

In order to extract the shape of the 3 bones of interest, we make use of a semi-automatic segmentation approach. Age variability induces developmental variability of bones and cartilages. To overcome such shape variability, the considered regions of interest include bones and growth cartilages. First, 3 subjects at different ages (7, 10 and 12) are manually segmented by an expert. A registration-based label propagation method is then used to segment the subjects of the data sets, with manual correction if necessary. Newly segmented subjects are included at each propagation stage. Finally, smooth segmentation maps are computed by training a standard patch-based unet network Ronneberger et al. (2015) trained on the expert-based segmentation maps and manually corrected if required (see Figure 2).

The bone volume is an anatomical indice that related to muscle quality and thus the function, especially with cerebral palsy. The bone volume can be influenced by age, spasticity, muscle strength, and dorsiflexion range. In this study, we compare the volume of calcaneus and talus, including their growth cartilage, according to age. Figure 1 shows volume measurements of calcaneus and talus. These results, discussed in Section 3.1, tend to highlight morphological differences between the two groups, which we study next more precisely using two SSM approaches.

2.2 Surface-based shape analysis

Statistical Shape Modeling is a mathematical approach to quantify 3D shape variation. One approach for SSM is to analyze meshes computed for image segmentation. In this work, we rely on the surface-based SSM software called Shapeworks (Cates et al. (2017)) 1 that has been recently used for ankle joint analysis using weightbearing computed tomography (Krähenbühl et al. (2020); Lenz et al. (2021)). Recent benchmarking study has shown the potential of Shapeworks with respect to other surface-based SSM (Goparaju et al. (2022)). ShapeWorks is a groupwise particle-based shape modeling method that does not rely on surface parameterizations. Shapeworks handles each surface mesh as a set of particles that describe the surface geometry. Such a particle-based representation avoids many of the problems inherent in parametric representations (i.e. limitation to specific topologies for instance). Shapeworks takes as input binary segmentation of each bone of every subjects. Correspondences between surfaces (relying on particles) are estimated using signed distance images. Procrustes analysis is used to remove scaling (i.e. size) from the shape modeling analysis. Mean shapes are generated for CP

1 https://sciinstitute.github.io/ShapeWorks.

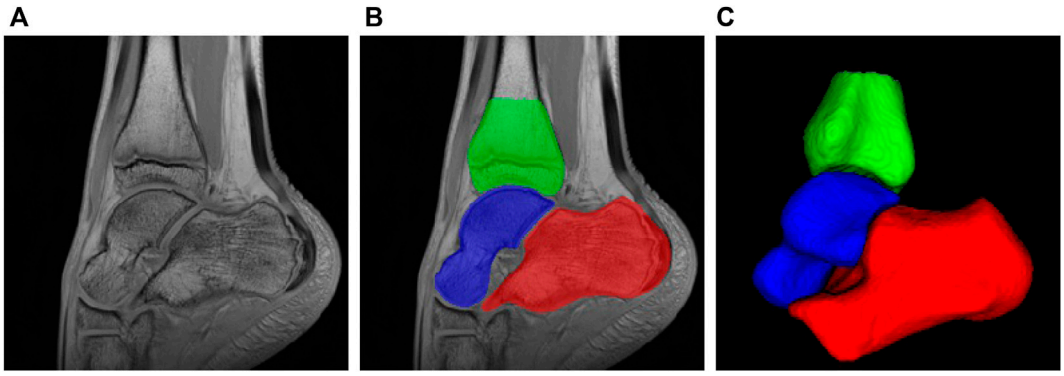

FIGURE 2
MRI of ankle joint and bone of interest: **(A)** Sagittal view of ankle static 3D MRI; **(B)** Segmentation of bone of interest: red: calcaneus, blue: talus, green: tibia; **(C)** 3D rendering of the three bones of interest.

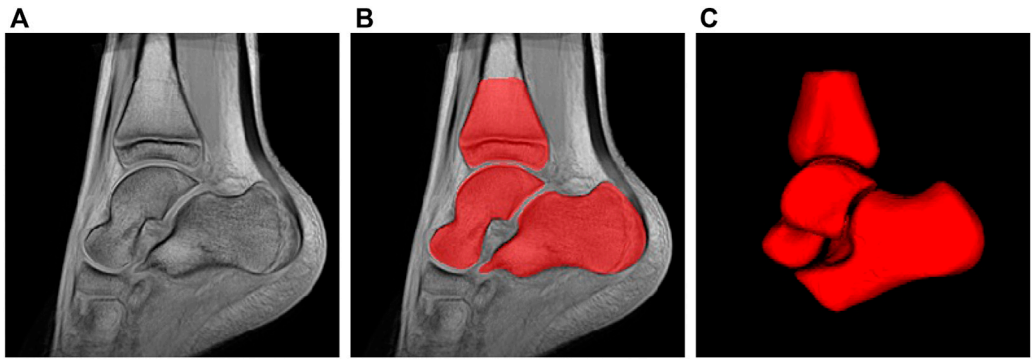

FIGURE 3
Estimated ankle atlas of TD population using the voxel-based approach: **(A)** sagittal view, **(B)** segmentation, **(C)** 3D rendering.

and TD groups and deformation fields between the two groups are used to study the shape differences.

2.3 Voxel-based shape analysis

For the voxel-based approach, we make use of an image registration-based framework to compute a mean image model of the TD population. To deal with the high variability in shape and appearance of the bones, we compute the TD template using a group-wise diffeomorphic algorithm (Avants and Gee (2004)) by not only considering image intensity but also bone segmentation maps using signed distance maps. Such a multivariate approach ensures realistic template estimation (see Figure 3) with sharp details of cortical bones and cartilage. Then, for each subject of the dataset, deformation fields are estimated by non-linear multivariate registration onto the mean TD template previously computed. The template estimation and the patient-to-template registration stages are performed with Advanced Normalization Tools (ANTs)2.

3 Results

3.1 Global scale analysis–volumetric quantification

In a first step, we perform a bone volumetric quantification of calcaneus and talus, from a global perspective, to provide a global view of bone morphological difference caused by equinus. The mean calcaneus volume of TD and CP group are 48,172.9 mm^3 and 41,001.6 mm^3, and for talus are 29,404.1 mm^3 and

2 http://stnava.github.io/ANTs/.

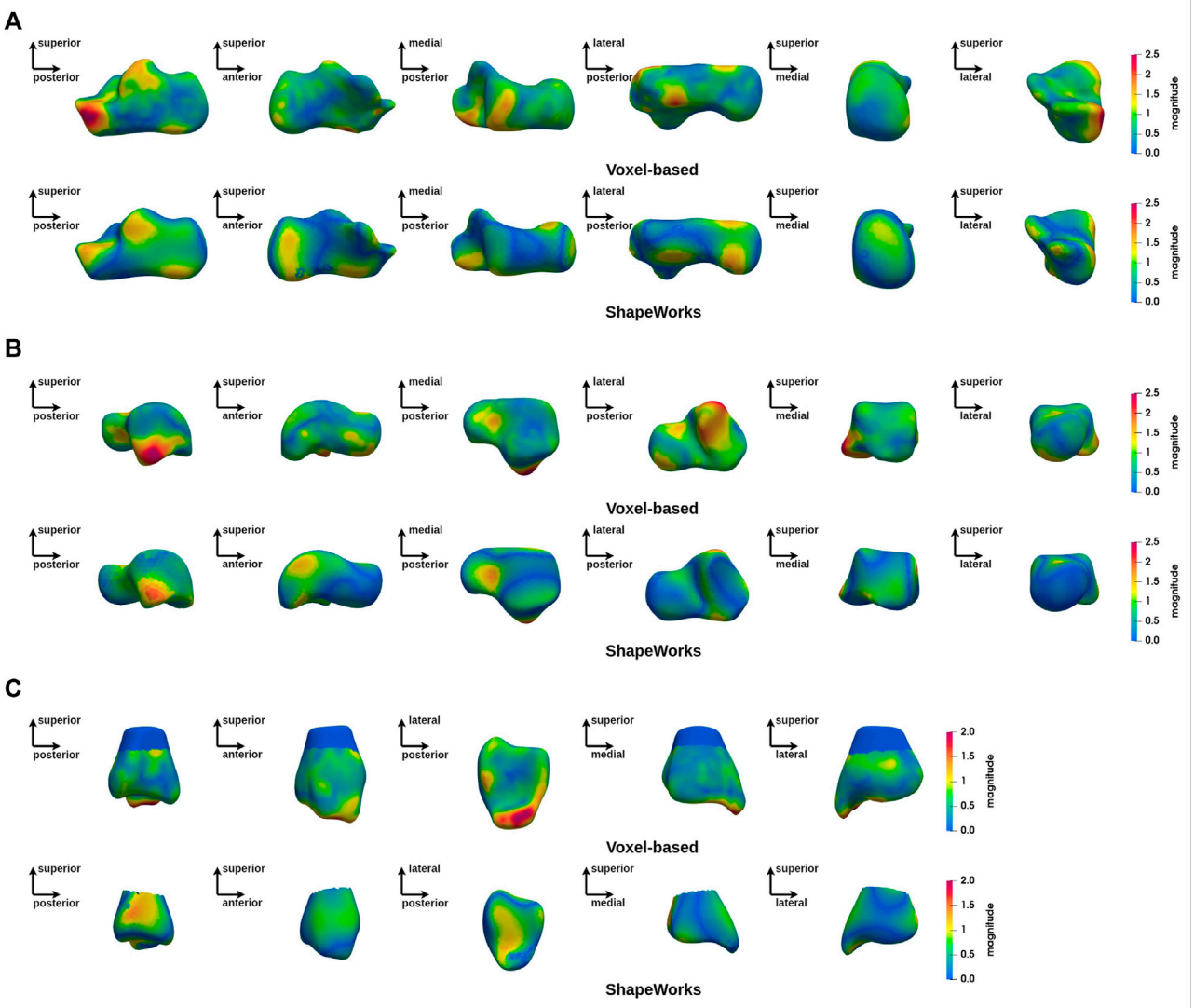

FIGURE 4
Magnitude of deformation fields at group level (CP vs. TD) using ShapeWorks and voxel-based methods: **(A)** calcaneus, **(B)** talus, **(C)** tibia.

25,138.3 mm^3. Both calcaneus and talus are decreased by 15% in CP group compared to TD group. The gap between 2 groups is increased with age, as presented in Figure 1.

3.2 Analysis at group level

Our first objective is to provide a comparison between the two groups of interest (CP and TD), with the voxel-based and particle-based methods. Figure 4 shows the magnitude of the deformation fields for the 3 bones of interest from the CP group toward the TD group. These deformations correspond to the average shape variations between the two populations. This figure indicates that the two SSM methods studied in this work provide similar results regarding the main deformation regions of talus and calcaneus. These results tend to show that both SSM methods capture the same patterns of shape variation at the group level for these two bones.

Figure 5 shows a group-wide deformation zone in the lateral process of the talus and a deformation zone on the anterolateral aspect of the calcaneus. These two areas are anatomically opposite each other. A zone of deformity is also seen on the inferolateral aspect of the tibial malleolus.

3.3 Analysis at subject level

The group-level analysis shows shape differences on some regions of the bones of interest. However, the group-level analysis only provides average deformation patterns, without allowing a

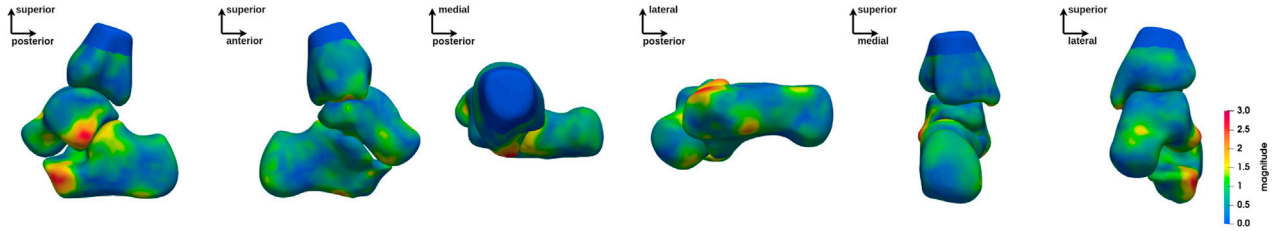

FIGURE 5
Magnitude of deformation fields at group level (CP vs. TD) using the voxel-based analysis.

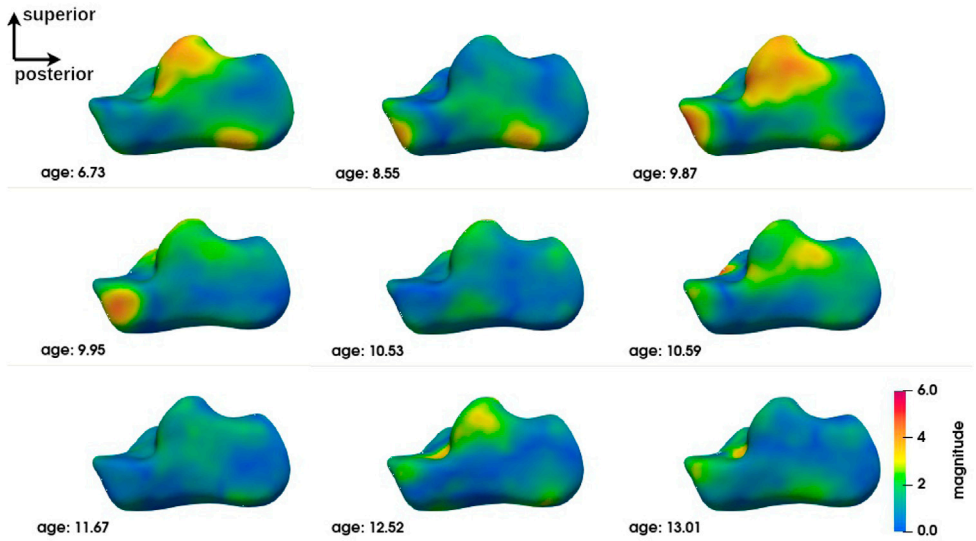

FIGURE 6
Subject-level shape analysis of calcaneus in lateral view of CP population.

personalized analysis for each child. An analysis at the individual level is necessary to propose a more personalized approach. Figures 6–8 show the magnitude of the deformation fields between each CP subject (ordered by age) and the TD atlas using the voxel-based method for respectively, the calcaneus, the talus and the tibia in one view. The other views can be found in Supplementary Materials. The main deformation patterns revealed by the group analysis may be observed in some subjects, but not necessarily in all subjects. Age does not seem to be related to the observed deformation patterns.

4 Discussion

Motivated by the observed volume difference of calcaneus and talus between TDs and CPs, this study is aimed to investigate the ankle joint bone morphology relevant to fixed equinus caused by cerebral palsy. To understand population-wise pathological change and to adjust patient-adapted rehabilitation program, the morphological analysis was performed on both on population level and individual level. To this end, we make use of two SSM methods. Such an analysis provides the possibility to analyse the morphological properties and detect large deformations than can be caused by pathology (Frondelius et al. (2022); Brown et al. (2017)).

4.1 Cross-approach comparison

In Gao et al. (2014) and Goparaju et al. (2022), authors described different levels of consistency between SSM tools and stressed the importance of validating these tools in medical applications. Different SSM methods can lead to results with

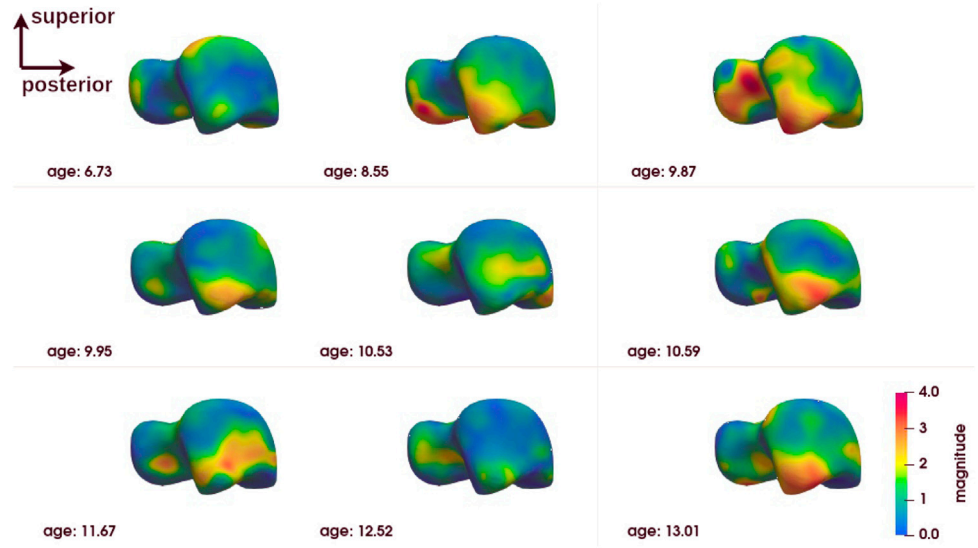

FIGURE 7
Subject-level shape analysis of talus in lateral view of CP population.

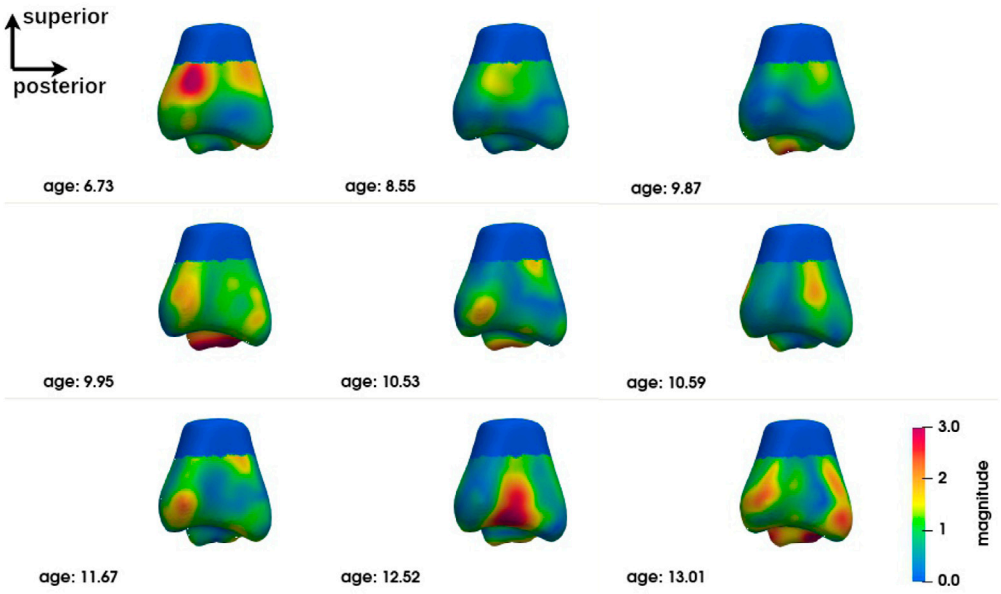

FIGURE 8
Subject-level shape analysis of tibia in lateral view of CP population.

large variations. Under these conditions, a comparison between several shape analysis methods is necessary.

In this study, we adopt a surface-based approach and a voxel-based approach. Both methods capture similar group-level deformation regions for talus and calcaneus. Indeed, both methods reveal deformations of the anterior lateral edge of the calcaneus, which is located near the cuboid facet and the anterior facet of the subtalar joint, as well as the posterior-lateral edge of the posterior facet of the subtalar joint and the lateral process of the calcaneal tuberosity. In the talus, the area showing obvious deformity in both methods is the lateral process, as well as the neck of the talus. Compared to the calcaneus and the talus,

the results for the tibia show less similarity between the methods. However, deformities of the infero-lateral part of the tibial malleolus are evident, which in relation to the deformities found in the calcaneus and talus can be explained by the valgus deformity of the hindfoot frequently found in children with CP and equinus gait. This deformity, exacerbated by weight-bearing, causes dislocation of the hindfoot with malalignement of the ankle bones, increasing local mechanical stress (Otjen et al. (2020)). The increase in stress is consistent with the deformities seen in the lateral-anterior border of the calcaneus, the lateral process of the talus and the tibial malleolus.

However, differences still exist between two methods. In calcaneus, the calcaneus tuberosity and its medial process have large deformation magnitude in surface-based approach, while this change is not reported by voxel-based approach. In talus, the lateral side of posterior facet is reported by voxel-based approach but not by mesh-based approach. In tibia, the fibula notch region obtained with mesh-based method has a magnitude of 1 mm while approximately 0.5 mm in voxel-based analysis.

4.2 Subject-level analysis

The subject-level analysis reveals the deformation pattern of each CP subject. As presented in Section 3.3, the subject-level analysis may correspond to the group analysis, but not necessarily.

Interestingly, the talus appears to be the bone with the least variation in inter-subject deformation. At the same time, it appears to be the bone of the ankle complex with the most deformation. This may be related to its anatomical-physiological characteristics (absence of muscle insertion, poor vascularisation) and its anatomical position at the crossroads of the mechanical constraints of the talus and tibia (Dufour (2015)). Just as it is more sensitive to osteochondral lesions in sportsmen and women (Barbier et al. (2021)), it seems to be more sensitive to deformation in CP individuals with equinus gait. This suggests that the evolution of the shape of the talus should be monitored more closely.

Despite this trend, no precise deformation pattern is observed for any of the three bones of the ankle complex. Although individual #3 (age 9.87) appears to be closest to the deformation pattern described above at the group level and some individuals are close to it in some deformations, alternative patterns are found for each individual. This does not mean that these individuals do not have deformities that could be explained by their loaded foot position or their gait. Further exploration is required to establish these relationships. The presence of major deformities at the individual level means that individualised diagnostic imaging assessment, in conjunction with gait analysis, should be encouraged in order to provide specific and personalized treatment.

4.3 Limitations and perspectives

This study offers exciting new information concerning the bone morphology of children with cerebral palsy and equinus. However, it is necessary to continue such a study in order to confirm these results. Firstly, this study is performed on a limited-size dataset due to the scarcity of pediatric datasets. Although the similar deformation pattern is revealed from our dataset with different tools, it would be better to confirm our results by increasing the number of subjects included. The inter-group difference (in terms of age and sex) of the subjects who participated in the study requires caution in interpreting the results. The results must therefore be analysed in relation to the study population and must be confirmed on the basis of a larger data set. Secondly, as already highlighted in Gao et al. (2014) and Goparaju et al. (2022), this work confirms the need to analyze the results obtained with SSM methods with care and a future line of research must be the understanding of the potential variability of the results obtained by SSM tools. It is essential to provide simple and efficient tools for shape analysis in a personalized context.

Data availability statement

The raw data supporting the conclusion of this article will be made available by the authors, without undue reservation.

Ethics statement

The studies involving human participants were reviewed and approved by Comité d'Ethique du CHU de Brest. Written informed consent to participate in this study was provided by the participants' legal guardian/next of kin.

Author contributions

RB, BB, DB, and SB conceived and directed the data collection. YC, RB, CS-D, and FR analysed the data and performed the segmentation steps. YC, BF, and FR carried out the computational and visualization tools. YC and FR performed the experiments. RB and SB aided in interpreting the results. YC, RB, SB and FR drafted the manuscript and designed the figures. All authors discussed the results and commented on the manuscript.

Funding

The research leading to these results has received funding from ANR (AI4CHILD ANR-19-CHIA-0015-01), Philips, Fondation de l'Avenir, Paris, France, and Fondation Motrice, Paris, France.

Conflict of interest

The authors declare that the research was conducted in the absence of any commercial or financial relationships that could be construed as a potential conflict of interest.

Publisher's note

All claims expressed in this article are solely those of the authors and do not necessarily represent those of their affiliated organizations, or those of the publisher, the editors and the reviewers. Any product that may be evaluated in this article, or claim that may be made by its manufacturer, is not guaranteed or endorsed by the publisher.

Supplementary material

The Supplementary Material for this article can be found online at: https://www.frontiersin.org/articles/10.3389/fbioe.2022.1059129/full#supplementary-material

References

Ashburner, J., Hutton, C., Frackowiak, R., Johnsrude, I., Price, C., and Friston, K. (1998). Identifying global anatomical differences: Deformation-based morphometry. *Hum. Brain Mapp.* 6, 348–357. doi:10.1002/(sici)1097-0193(1998)6:5/6<348::aid-hbm4>3.0.co;2-p

Asvadi, A., Dardenne, G., Troccaz, J., and Burdin, V. (2021). Bone surface reconstruction and clinical features estimation from sparse landmarks and statistical shape models: A feasibility study on the femur. *Med. Eng. Phys.* 95, 30–38. doi:10.1016/j.medengphy.2021.07.005

Avants, B., and Gee, J. C. (2004). Geodesic estimation for large deformation anatomical shape averaging and interpolation. *Neuroimage* 23, S139–S150. doi:10.1016/j.neuroimage.2004.07.010

Barbier, O., Amouyel, T., de l'Escalopier, N., Cordier, G., Baudrier, N., Benoist, J., et al. (2021). Osteochondral lesion of the talus: What are we talking about? *Orthop. Traumatology Surg. Res.* 107, 103068. doi:10.1016/j.otsr.2021.103068

Bône, A., Louis, M., Martin, B., and Durrleman, S. (2018). "Deformetrica 4: An open-source software for statistical shape analysis," in *International workshop on shape in medical imaging* (Springer), 3–13.

Boutillon, A., Salhi, A., Burdin, V., and Borotikar, B. (2022). Anatomically parameterized statistical shape model: Explaining morphometry through statistical learning. *IEEE Trans. Biomed. Eng.* 69, 2733–2744. doi:10.1109/tbme.2022.3152833

Brown, J. M., Ross, E., Desanti, G., Saghir, A., Clark, A., Buckley, C., et al. (2017). Detection and characterisation of bone destruction in murine rheumatoid arthritis using statistical shape models. *Med. image Anal.* 40, 30–43. doi:10.1016/j.media.2017.05.006

Cates, J., Elhabian, S., and Whitaker, R. (2017). "Shapeworks: Particle-based shape correspondence and visualization software," in *Statistical shape and deformation analysis* (Elsevier), 257–298.

Damiano, D. L. (2014). Meaningfulness of mean group results for determining the optimal motor rehabilitation program for an individual child with cerebral palsy. *Dev. Med. Child. Neurol.* 56, 1141–1146. doi:10.1111/dmcn.12505

Davis, R. B., III, Ounpuu, S., Tyburski, D., and Gage, J. R. (1991). A gait analysis data collection and reduction technique. *Hum. Mov. Sci.* 10, 575–587. doi:10.1016/0167-9457(91)90046-z

Dufour, M. (2015). "2 - ostéologie," in *Anatomie de l'appareil locomoteur - tome 1 (3ème édition)*. Editor M. Dufour (Paris: Elsevier Masson), 37–115. 3ème édition edn. doi:10.1016/B978-2-294-74502-7.00002-5

Durrleman, S., Prastawa, M., Charon, N., Korenberg, J. R., Joshi, S., Gerig, G., et al. (2014). Morphometry of anatomical shape complexes with dense deformations and sparse parameters. *NeuroImage* 101, 35–49. doi:10.1016/j.neuroimage.2014.06.043

Ebert, L. C., Rahbani, D., Lüthi, M., Thali, M. J., Christensen, A. M., and Fliss, B. (2022). Reconstruction of full femora from partial bone fragments for anthropological analyses using statistical shape modeling. *Forensic Sci. Int.* 332, 111196. doi:10.1016/j.forsciint.2022.111196

Frondelius, T., Kauppinen, S., Fercher, D., Barreto, G., Zenobi-Wong, M., Finnilä, M., et al. (2022). Automatic detection of osteophytes from contrast enhanced μct-imaged rat tibias using statistical shape models. *Osteoarthr. Cartil.* 30, S280–S281. doi:10.1016/j.joca.2022.02.378

Gao, Y., Riklin-Raviv, T., and Bouix, S. (2014). Shape analysis, a field in need of careful validation. *Hum. Brain Mapp.* 35, 4965–4978. doi:10.1002/hbm.22525

Garetier, M., Borotikar, B., Makki, K., Brochard, S., Rousseau, F., and Ben Salem, D. (2020). Dynamic mri for articulating joint evaluation on 1.5 t and 3.0 t scanners: Setup, protocols, and real-time sequences. *Insights Imaging* 11, 66–10. doi:10.1186/s13244-020-00868-5

Goparaju, A., Iyer, K., Bone, A., Hu, N., Henninger, H. B., Anderson, A. E., et al. (2022). Benchmarking off-the-shelf statistical shape modeling tools in clinical applications. *Med. Image Anal.* 76, 102271. doi:10.1016/j.media.2021.102271

Kedem, P., and Scher, D. M. (2015). Foot deformities in children with cerebral palsy. *Curr. Opin. Pediatr.* 27, 67–74. doi:10.1097/mop.0000000000000180

Krähenbühl, N., Lenz, A. L., Lisonbee, R. J., Peterson, A. C., Atkins, P. R., Hintermann, B., et al. (2020). Morphologic analysis of the subtalar joint using statistical shape modeling. *J. Orthop. Res.* 38, 2625–2633. doi:10.1002/jor.24831

Lenz, A. L., Krähenbühl, N., Peterson, A. C., Lisonbee, R. J., Hintermann, B., Saltzman, C. L., et al. (2021). Statistical shape modeling of the talocrural joint using a hybrid multi-articulation joint approach. *Sci. Rep.* 11, 7314–14. doi:10.1038/s41598-021-86567-7

Makki, K., Borotikar, B., Garetier, M., Brochard, S., Salem, D. B., and Rousseau, F. (2019). *In vivo* ankle joint kinematics from dynamic magnetic resonance imaging using a registration-based framework. *J. biomechanics* 86, 193–203. doi:10.1016/j.jbiomech.2019.02.007

Metaxiotis, D., Siebel, A., and Doederlein, L. (2002). Repeated botulinum toxin a injections in the treatment of spastic equinus foot. *Clin. Orthop. Relat. Research®* 394, 177–185. doi:10.1097/00003086-200201000-00021

Mitchell, J., Bishop, A., Feng, Y., Farley, D., Hetzel, S., Ploeg, H.-L., et al. (2018). Residual equinus after the ponseti method: An mri-based 3-dimensional analysis. *J. Pediatr. Orthop.* 38, e271–e277. doi:10.1097/bpo.0000000000001147

Otjen, J., Menashe, S. J., Maloney, E., Iyer, R. S., Ngo, A.-V., Sousa, T. C., et al. (2020). Foot and ankle musculoskeletal imaging of pediatric patients with cerebral palsy. *Am. J. Roentgenol.* 214, 1389–1397. doi:10.2214/ajr.19.22354

Perry, J., Hoffer, M. M., Giovan, P., Antonelli, D., and reenberg, R. (1974). Gait analysis of the triceps surae in cerebral palsy: A preoperative and postoperative clinical and electromyographic study. *J. Bone Jt. Surg.* 56, 511–520. doi:10.2106/00004623-197456030-00008

Plessers, K., Berghe, P. V., Van Dijck, C., Wirix-Speetjens, R., Debeer, P., Jonkers, I., et al. (2018). Virtual reconstruction of glenoid bone defects using a statistical shape model. *J. shoulder Elb. Surg.* 27, 160–166. doi:10.1016/j.jse.2017.07.026

Ronneberger, O., Fischer, P., and Brox, T. (2015). "U-net: Convolutional networks for biomedical image segmentation," in *International Conference on Medical image computing and computer-assisted intervention* (Springer), 234–241.

Salhi, A., Burdin, V., Boutillon, A., Brochard, S., Mutsvangwa, T., and Borotikar, B. (2020). Statistical shape modeling approach to predict missing scapular bone. *Ann. Biomed. Eng.* 48, 367–379. doi:10.1007/s10439-019-02354-6

Schlegl, T., Seeböck, P., Waldstein, S. M., Langs, G., and Schmidt-Erfurth, U. (2019). f-anogan: Fast unsupervised anomaly detection with generative adversarial networks. *Med. image Anal.* 54, 30–44. doi:10.1016/j.media.2019.01.010

Schmutz, B., Rathnayaka, K., and Albrecht, T. (2019). Anatomical fitting of a plate shape directly derived from a 3d statistical bone model of the tibia. *J. Clin. Orthop. trauma* 10, S236–S241. doi:10.1016/j.jcot.2019.04.019

Shi, B., Barzan, M., Nasseri, A., Carty, C. P., Lloyd, D. G., Davico, G., et al. (2022). Development of predictive statistical shape models for paediatric lower limb bones. *Comput. Methods Programs Biomed.* 225, 107002. doi:10.1016/j.cmpb.2022.107002

Styner, M., Oguz, I., Xu, S., Brechbühler, C., Pantazis, D., Levitt, J. J., et al. (2006). Framework for the statistical shape analysis of brain structures using spharm-pdm. *Insight J.* 242, 242–250. doi:10.54294/owxzil

Vanden Berghe, P., Demol, J., Gelaude, F., and Vander Sloten, J. (2017). Virtual anatomical reconstruction of large acetabular bone defects using a statistical shape model. *Comput. methods biomechanics Biomed. Eng.* 20, 577–586. doi:10.1080/10255842.2016.1265110

frontiers | Frontiers in Bioengineering and Biotechnology

TYPE Original Research
PUBLISHED 05 December 2022
DOI 10.3389/fbioe.2022.1056536

OPEN ACCESS

EDITED BY
Yang Liu,
Hong Kong Polytechnic University,
Hong Kong SAR, China

REVIEWED BY
Jan Kubicek,
VSB-Technical University of Ostrava,
Czechia
Rui B. Ruben,
Polytechnic Institute of Leiria, Portugal

*CORRESPONDENCE
Amy L. Lenz,
amy.lenz@utah.edu

†These authors share senior authorship

SPECIALTY SECTION
This article was submitted to Biomechanics,
a section of the journal
Frontiers in Bioengineering and Biotechnology

RECEIVED 28 September 2022
ACCEPTED 03 November 2022
PUBLISHED 05 December 2022

CITATION
Peterson AC, Lisonbee RJ, Krähenbühl N, Saltzman CL, Barg A, Khan N, Elhabian SY and Lenz AL (2022), Multi-level multi-domain statistical shape model of the subtalar, talonavicular, and calcaneocuboid joints.
Front. Bioeng. Biotechnol. 10:1056536.
doi: 10.3389/fbioe.2022.1056536

Multi-level multi-domain statistical shape model of the subtalar, talonavicular, and calcaneocuboid joints

Andrew C. Peterson[1], Rich J. Lisonbee[1], Nicola Krähenbühl[2], Charles L. Saltzman[1], Alexej Barg[1,3], Nawazish Khan[4,5], Shireen Y. Elhabian[4,5†] and Amy L. Lenz[1,6,7*†]

[1]Department of Orthopaedics, University of Utah, Salt Lake City, UT, United States, [2]University Hospital Basel, Basel, Switzerland, [3]University Medical Center Hamburg-Eppendorf, Hamburg, Germany, [4]School of Computing, College of Engineering, University of Utah, Salt Lake City, UT, United States, [5]Scientific Computing and Imaging Institute, College of Engineering, University of Utah, Salt Lake City, UT, United States, [6]Department of Biomedical Engineering, College of Engineering, University of Utah, Salt Lake City, UT, United States, [7]Department of Mechanical Engineering, College of Engineering, University of Utah, Salt Lake City, UT, United States

Traditionally, two-dimensional conventional radiographs have been the primary tool to measure the complex morphology of the foot and ankle. However, the subtalar, talonavicular, and calcaneocuboid joints are challenging to assess due to their bone morphology and locations within the ankle. Weightbearing computed tomography is a novel high-resolution volumetric imaging mechanism that allows detailed generation of 3D bone reconstructions. This study aimed to develop a multi-domain statistical shape model to assess morphologic and alignment variation of the subtalar, talonavicular, and calcaneocuboid joints across an asymptomatic population and calculate 3D joint measurements in a consistent weightbearing position. Specific joint measurements included joint space distance, congruence, and coverage. Noteworthy anatomical variation predominantly included the talus and calcaneus, specifically an inverse relationship regarding talar dome heightening and calcaneal shortening. While there was minimal navicular and cuboid shape variation, there were alignment variations within these joints; the most notable is the rotational aspect about the anterior-posterior axis. This study also found that multi-domain modeling may be able to predict joint space distance measurements within a population. Additionally, variation across a population of these four bones may be driven far more by morphology than by alignment variation based on all three joint measurements. These data are beneficial in furthering our understanding of joint-level morphology and alignment variants to guide advancements in ankle joint pathological care and operative treatments.

KEYWORDS

foot and ankle, statistical shape modeling, computational morphometrics, midtarsal joint locking, weightbearing computed tomography

1 Introduction

Historically, the complex nature of foot and ankle joint morphology has primarily been analyzed individually from two-dimensional (2D) measurements on conventional radiographs (Lopez-Ben, 2015; Krähenbühl et al., 2017). These methods fail to illustrate the complexity of the foot and ankle joints and their spatial relationships. The subtalar, talonavicular, and calcaneocuboid joints are specifically challenging to assess radiographically due to their intricate morphologies and locations within the ankle (Ebraheim et al., 1999; Willauer et al., 2014; Krähenbühl et al., 2017; Bernasconi et al., 2021). Yet, accurately visualizing these three joints is crucial to comprehending the compensatory joint mechanics as well as treatment for multiple pathologies, such as osteoarthritis and progressive collapsing flatfoot deformity (PCFD) (Sammarco, 2004; Bruening et al., 2018; Welte et al., 2021). However, advancements in volumetric imaging, including computed tomography (CT), have made it possible and practical to generate high-resolution three-dimensional (3D) reconstructions of bones throughout the foot and ankle (Hayes et al., 2006; Barg et al., 2018). While these imaging modalities are typically performed in a non-weightbearing position, weightbearing cone-beam CT (WBCT) technology allows for the analysis of joint relationships in a natural and consistent position with the presence of load (Colin et al., 2014; Burssens et al., 2016; Krähenbühl et al., 2016). A better understanding of hind- and midfoot morphometrics could assist in diagnosing and treating multiple joint diseases. However, it can be challenging to quantitatively extract morphological metrics from 3D surface reconstructions while maintaining anatomical relevance.

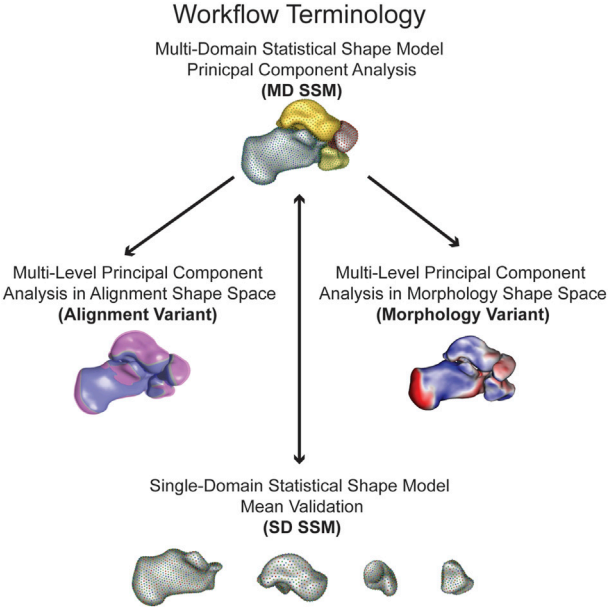

FIGURE 1
Workflow terminology for the model analysis performed with the simplified terminology bolded. The multi-domain statistical shape model principal component analysis (MD SSM) is a four bone model maintaining anatomical joint relationships analyzing morphology and alignment. The multi-level principal component analysis in alignment shape space (alignment variant) is a four bone model maintaining anatomical joint relationships solely analyzing alignment. The multi-level principal component analysis in morphology shape space (morphology variant) is a four bone model maintaining anatomical joint relationships solely analyzing morphology. The single-domain statistical shape model mean validation (SD SSM) is four single bone models to validate morphology variation to the MD SSM.

Statistical shape modeling (SSM) is a population-based mathematical approach to objectively quantify these morphological metrics (Davies et al., 2002; Styner et al., 2003; Cates et al., 2007; Datar et al., 2009; Datar et al., 2011; Goparaju et al., 2022). Using SSM, a statistical model can be created to compare mean bone shape morphology and identify anatomical modes of variation. Previous ankle SSM studies have been limited to a single bone and could not, therefore, evaluate multi-domain joint relationships (Melinska et al., 2015; Melinska et al., 2017; Tümer et al., 2019a; Tümer et al., 2019b; Gabrielli et al., 2020; Krähenbühl et al., 2020; Liu et al., 2020; Schmutz et al., 2021; Arbabi et al., 2022; Peiffer et al., 2022; Vafaeian et al., 2022). A multi-domain technique can be implemented to capture morphological and alignment changes for multiple bones throughout a population. Additionally, multi-level analyses allow for separating morphology and alignment to identify their individual contributions to joint relationships.

Using a multi-domain SSM approach, individual joint-level 3D morphometrics can be calculated to predict variations within the joints based on the original alignment from WBCT scans. These joint metrics include coverage area, joint space distance, and joint congruence. The coverage area is a mathematically derived calculation of the joint's articulating region. Coverage area is also used to quantify morphology variation, such as osteoarthritis development (Schaefer et al., 2012), and alignment variation, such as joint subluxation (Louie et al., 2014). Calculated from within the joint's coverage area, the joint space distance is calculated from the Euclidean distance across the joint, and the congruence index rates how well the two articular surfaces match one another (Ateshian et al., 1992; Lenz et al., 2021). Similar to coverage area variations, joint space distance can help clinically indicate degenerative diseases like osteoarthritis (Day et al., 2020) and pathologies with varying alignments, such as PCFD (Bernasconi et al., 2021). These analyses allow for a holistic understanding of bone relationships in the foot and ankle that can guide implant design and development while providing insight into the involvement of multiple joints within various pathological diseases.

This study aims to characterize asymptomatic joint-level morphology and alignment differences throughout statistically

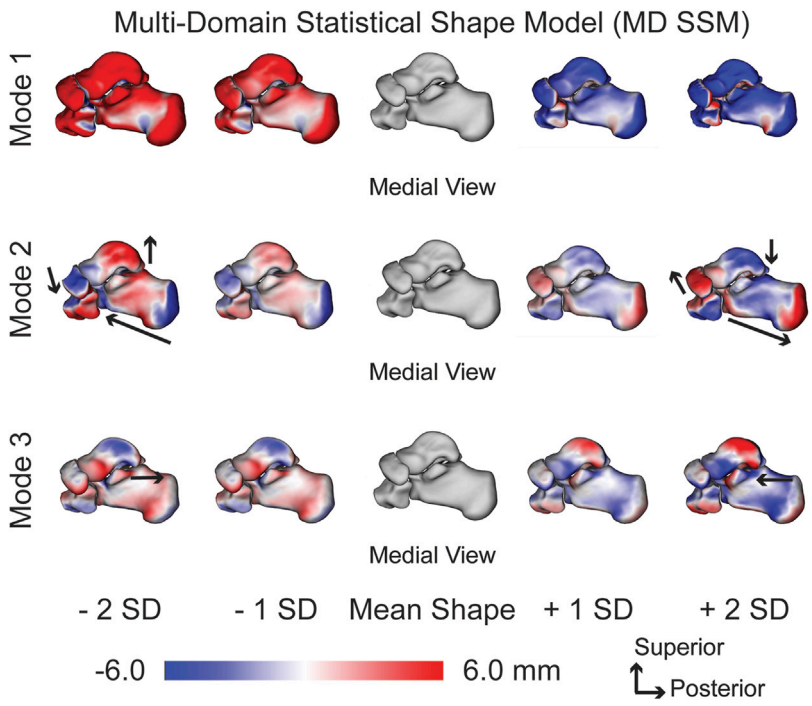

FIGURE 2
MD SSM modes of variation one to three showing both morphological and alignment significant variations at ± 1 and 2 standard deviations from the mean shape. Black arrows highlight key anatomical feature variations. Red regions are larger than the mean shape and blue regions are smaller than the mean shape with a scale in millimeters (mm).

significant modes of variation and the joint-level measurements within the subtalar, talonavicular, and calcaneocuboid joints. Additionally, this study aims to determine which, if any, multi-level multi-domain SSM modes of variation that seek to separate morphology from joint alignment can be used to predict joint-level measurements across a population. The validity of the multi-domain SSM approach was assessed by comparing the multi-domain statistical models to models run *via* a single-domain SSM approach. We hypothesized that the first mode of variation could predict joint coverage, distance, and congruence for the population. We also hypothesized that multi-domain SSM does not affect the mean shape compared to single-domain SSM. To accomplish these aims and test these hypotheses, we have presented a new computation approach to evaluate multi-domain influences of morphology and alignment in the case of four bones within the ankle and statistically evaluated the downstream joint measurements.

2 Materials and methods

Twenty-seven asymptomatic participants (age: 50.0 ± 7.3 years; height: 169.4 ± 6.4 cm; BMI: 25.3 ± 3.8 kg/m^2; seven males) were enrolled with IRB approval from an ethics committee (Kantonsspital Baselland, Switzerland; University of Utah). Individuals between 40 and 70 years of age without a history of ankle injury or surgery were considered. Before the study, a clinical and radiographic assessment was performed to exclude participants with a planovalgus or cavovarus deformity.

Each participant underwent a unilateral weightbearing CT (WBCT) scan (Planmed Verity, Planmed Oy, Helsinki, Finland; 0.4 mm isotropic pixel resolution). The WBCT scans were segmented, decimated, and smoothed to generate 3D surface models of the talus, calcaneus, navicular, and cuboid (Amira, v6.0.1, Visage Imaging, San Diego, CA, United States).

2.1 Statistical shape modeling

For each of the twenty-seven individuals, the talus, calcaneus, navicular, and cuboid were used to create two types of statistical models utilizing an opensource SSM software (ShapeWorks v6.2.1, University of Utah; www.shapeworks.sci.utah.edu). This constructed Particle-based Shape Models (PSM) that automatically placed a dense set of corresponding landmarks on the given set of shapes using an entropy-based optimization scheme (Cates et al., 2017). The SSM approaches included a single-domain SSM (SD SSM) of only the individual bones and a

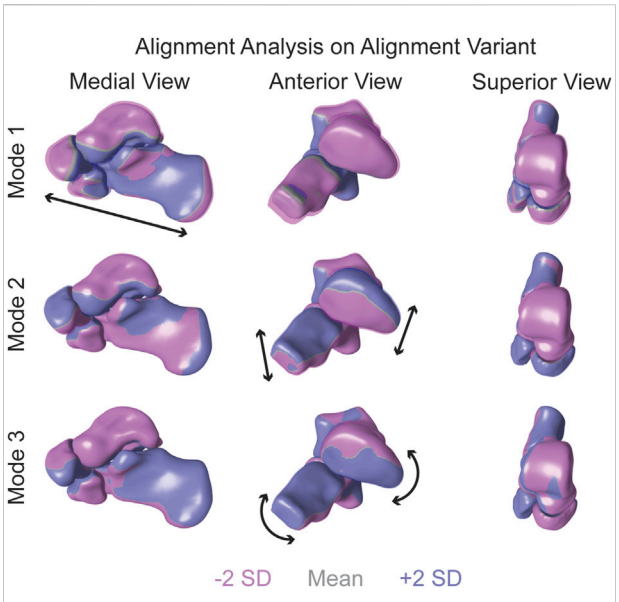

FIGURE 3
Alignment variant modes of variation one to three showing significant alignment variations at ± 2 standard deviations from the mean shape. Black arrows highlight key anatomical feature variations. Dark purple regions are +2 standard deviations and pink regions are -2 standard deviations from the mean shape in gray.

multi-domain SSM (MD SSM) comprised of all four bones in their anatomical alignment (Figure 1). Before optimizing the shape model, any bone models from a left limb were reflected to the right. Using a global iterative closest point algorithm, the input bones for each of the statistical models were aligned. The individual bones were aligned separately for the single-domain model, and each of the four bones were aligned together for the multi-domain model. Aligning the bone models together maintained the individual anatomical alignments from the WBCTs (Wilm, 2022).

The shape model for the four bones is built together by a multi-domain shape modeling approach (Cates et al., 2008), where point correspondences for all the surfaces are optimized in the full joint space of the object complex. A total particle count of 1,024 for the talus, 2,048 for the calcaneus, 512 for the navicular, and 512 for the cuboid was used for both the single and multi-domain statistical models. These correspondence particles were used to define mean shapes and statistically quantify shape differences between bones within the different statistical models. A Procrustes analysis was not applied for these statistical models to remove scale as a factor. Patient specific joint measurements include size variations across the population. In order to compare our population joint level measurements with SSM models, we chose not to use Procrustes for equivalent statistical comparisons. A principal component analysis (PCA) was used to simplify the data to a smaller set of linearly uncorrelated components, or modes of variation. Using a parallel analysis algorithm, statistically significant modes of variation were calculated ($p < 0.05$) (Horn, 1965; Ledesma and Valero-Mora, 2007). For each significant mode of variation, the surface distances between the mean and first and second standard deviation (SD) shapes were calculated and visualized *via* CloudCompare (v2.11. alpha, www.cloudcompare.org). The shape model was analyzed using two different approaches. The first is the multi-domain approach (MD SSM), where PCA analysis is done on the entire multi-bone joint structure treated as a single bone complex reflecting the modes of variation of the entire multi-object complex. The other analysis approach is the multi-level technique, where PCA analysis is done separately on the shape of each individual bone and on the alignment of the entire multi-bone joint structure. This multi-level approach allowed for separately analyzing the alignment shape space model (alignment variant) and the morphology shape space model (morphology variant) (Figure 1). The same significant modes of variation were used for subsequent calculations. For the morphology variant, surface distances between the mean shape and ±1 SD shapes were calculated and visualized *via* CloudCompare, similar to the MD SSM approach. And for the alignment variant, the mean shape and ±1 SD shapes for each mode were overlaid on each other to visualize those variations.

2.2 Joint coverage, distance, and congruence index calculations

The correspondence particles from each statistical model were used to automatically calculate and compare the joint-level measurements with an available toolbox (Peterson, 2022). Joint coverage was calculated automatically using normal vectors from the faces of the individual bone models. For a given bone of a joint, if the normal vectors from that bone intersected with a face of the opposing bone, they were considered within the coverage region for that side of the joint. The surface area of the coverage region was then calculated by summing the surface area of the faces that comprised the coverage region. Subject-specific correspondence particles within the coverage region would then be used for that bone's side of the joint analysis. These identified correspondence particles were paired with their nearest neighboring surface mesh node. It was from this paired node that the joint space distance and congruence index calculations were made. This was necessary as calculating the congruence index requires the mean and Gaussian curvatures of the two opposing surfaces. The joint space distance at a correspondence particle was calculated as the Euclidean distance between its paired node and the nearest opposing surface node. The congruence index for that correspondence particle was then calculated between these two nodes. Congruence index, first described by Ateshian *et al.*, is a rating of how well two surfaces match one another, with a

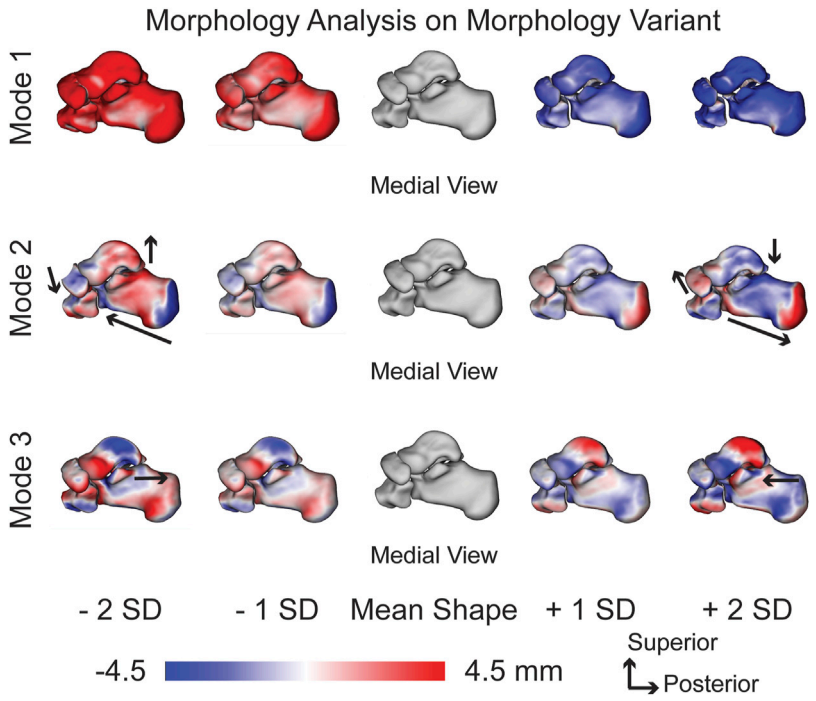

FIGURE 4
Morphology variant modes of variation one to three showing significant morphology variations at ± 1 and 2 standard deviations from the mean shape. Black arrows highlight key anatomical feature variations. Red regions are larger than the mean shape and blue regions are smaller than the mean shape with a scale in millimeters (mm).

congruence index of 0 mm^{-1} being rated as perfectly congruent (Ateshian et al., 1992; Lenz et al., 2021). Both results were mapped to that specific correspondence particle. For visualization, correspondence particles with a distance value greater than 6 mm were colored white for both joint space distance and congruence index. Subsequent statistics were performed on all correspondence particles within the coverage regions

2.3 Population vs. PCA modal comparison

The mean and ± 1 SD for coverage across the twenty-seven participants for all four joints were automatically calculated. These average values will be referred to as population calculations throughout this study. Due to the nature of correspondence particles, each distance value and congruence index were paired with identical correspondence particles across the entire population. Thus, the mean and ± 1 SD for distance and congruence can be calculated at each correspondence particle

These calculations for each measurement across the population were statistically compared to the mean and ±1 SD for each significant mode of variation using an unpaired *t*-test based on the means, SDs, and population size. This statistical comparison was also used to compare the alignment and morphology of multi-level multi-domains to the population. A *p*-value less than 0.05 indicates that the two groups are significantly different from one another.

3 Results

3.1 Statistical shape model

Statistical analysis is performed using Principal Component Analysis (PCA) for the MD SSM, morphology variant and alignment variant, where the mean shape and modes of variation are computed based on the optimized MD SSM (Figure 1). This study observed three statistically significant PCA modes of variation, accounting for 74.8% of the overall shape variation. The three modes represented 63.8%, 6.3%, and 4.7% of the variation. Additionally, when comparing the SD SSM of each bone to the MD SSM, there were negligible differences (<0.1 mm) in mean shape using the previously mentioned surface distance calculations in CloudCompare. Computationally, this statistical shape model took about 40 min to run optimization and the joint measurement

TABLE 1 Average coverage surface area ± standard deviation (SD) for the subtalar joint (split between the posterior and anteromedial facet), talonavicular joint, and calcaneocuboid joint on both involved surfaces. *p*-values are reported from each mode and variant to the population, and *p*-values reported between each bone within each joint. Bolded *p*-values are statistically significant to the population and between each bone, respectively.

	Joint Coverage (mm^2)													
	Subtalar			**Subtalar Posterior Facet**			**Subtalar Anteromedial Facet**			**Talonavicular**			**Calcaneocuboid**		
	Talus	**Calcaneus**	***p*-Value**	**Talus**	**Calcaneus**	***p*-Value**	**Talus**	**Calcaneus**	***p*-Value**	**Talus**	**Navicular**	***p*-Value**	**Calcaneus**	**Cuboid**	***p*-Value**
Population	1519.34	1435.99	0.0995	805.39	862.60	0.0867	365.28	384.33	0.3636	471.22	541.36	**0.0007**	393.92c	406.46	0.4015
	± 193.22	± 171.36		± 112.42	± 127.85		± 74.76	± 77.94		± 67.08	± 75.05		55.07	± 53.86	
MD SSM Mode 1	1474.63	1377.59	0.0235	765.62	869.49	**0.0001**	340.84	329.94	0.3392	439.42	527.94	**0.0001**	368.92	383.57	0.1211
	± 168.08	± 135.69		± 54.76	± 39.55		± 33.25	± 48.39		± 52.03	± 55.15		± 33.06	± 35.21	
p-Value	0.3685	0.1710		0.1044	0.7901		0.1267	**0.0033**		0.0570	0.4574		**0.04**83	0.0702	
MD SSM Mode 2	1471.97	1374.17	**0.0001**	767.25	860.47	**0.0001**	340.92	338.70	0.7088	437.12	526.96	**0.0001**	368.09	380.56	**0.0001**
	± 15.15	± 19.35		± 5.58	± 28.98		± 0.99	± 30.70		± 4.33	± 2.82		± 0.83	± 7.05	
p-Value	0.2097	0.0682		0.0842	0.9330		0.0964	**0.0066**		0.0110	0.3237		**0.0089**	**0.0165**	
MD SSM Mode 3	1472.02	1370.44	**0.0001**	765.82	866.81	**0.0001**	336.23	324.99	**0.0001**	438.29	526.68	**0.0001**	365.49	380.44	**0.0001**
	± 53.63	± 38.34		± 64.85	± 63.68		± 5.97	± 12.30		± 3.37	± 7.13		± 16.75	± 7.96	
p-Value	0.2256	0.0578		0.1192	0.8789		0.0769	**0.0003**		0.0138	0.3163		**0.0132**	**0.0163**	
Alignment Variant	1468.19	1371.21	**0.0001**	767.49	869.14	**0.0001**	342.85	321.93	0.1095	440.07	526.87	**0.0001**	368.03	382.79	**0.0126**
Mode 1	± 33.88	± 22 44		± 48.18	± 35.90		± 56.53	± 35.50		± 45.32	± 4.50		± 20.50	± 21.44	
p-Value	0.1813	0.0569		0.1134	0.7990		0.2193	**0.0004**		0.0508	0.3213		**0.0261**	**0.0387**	
Alignment Variant	1471.55	1369.96	**0.0001**	765.48	864.13	**0.0001**	341.21	328.89	**0.0006**	436.97	526.51	**0.0001**	165.15	380.30	**0.0001**
Mode 2	± 5.24	± 1.97		± 16.84	± 25.28		± 11.56	± 13.17		± 8.27	± 0.30		± 2.86	± 2.67	
p-Value	0.2046	0.0505		0.0739	0.9516		0.1043	**0.0006**		0.0111	0.3086		**0.0091**	**0.0147**	
Alignment Variant	1471.21	1370.27	**0.0001**	765.42	872.61	**0.0001**	341.10	321.44	**0.0001**	436.38	526.55	**0.0001**	364.54	380.27	**0.0001**
Mode 3	± 1.04	± 1.05		± 2.44	± 9.88		± 3.07	± 7.11		± 1.24	± 1.28		± 3.03	± 2.50	
p-Value	0.2013	0.0515		0.0704	0.6867		0.0991	**0.0001**		0.0094	0.3100		**0.0078**	**0.0147**	
Morphology	1470.33	1381.86	0.0755	770.51	863.70	**0.0086**	342.50	341.38	0.9595	443.62	528.10	**0.0004**	371.68	386.73	0.3726
Variant Mode 1	± 196.84	± 159.62		± 148.24	± 97.37		± 89.03	± 71.42		± 99.22	± 60.69		± 55.72	± 56.18	
p-Value	0.3601	0.2352		0.3345	0.9712		0.3133	0.0 I%		0.2366	0.4785		**0.1462**	0.1935	
Morphology	1470.23	1373.01	**0.0001**	766.01	847.47	**0.0001**	340.39	349.92	0.3863	436.58	527.26	**0.0001**	364.65	380.65	**0.0001**
Variant Mode 2	± 31.80	± 28.77		± 48.30	± 75.36		± 1.76	± 56.65		± 12.19	± 7.04		± 0.60	± 2.13	
p-Value	0.1983	0.0652		0.5985	0.5985		0.0897	0.0692		**0.0109**	0.3356		**0.0079**	**0.0161**	
Morphology	1470.95	1373.02	**0.0001**	766.22	866.99	**0.0001**	338.35	326.76	**0.0042**	438.57	527.12	**0.0001**	365.55	380.65	**0.0001**
Variant Mode 3	± 35.16	± 20.83		± 63.87	± 43.78		± 9.09	± 17.97		± 4.82	± 3.51		± 17.26	± 7.55	
p-Value	0.2061	0.0636		0.1215	0.8666		0.0688	**0.0005**		**0.0147**	0.3293		**0.0136**	**0.0170**	

10.3389/fbioe.2022.1056536

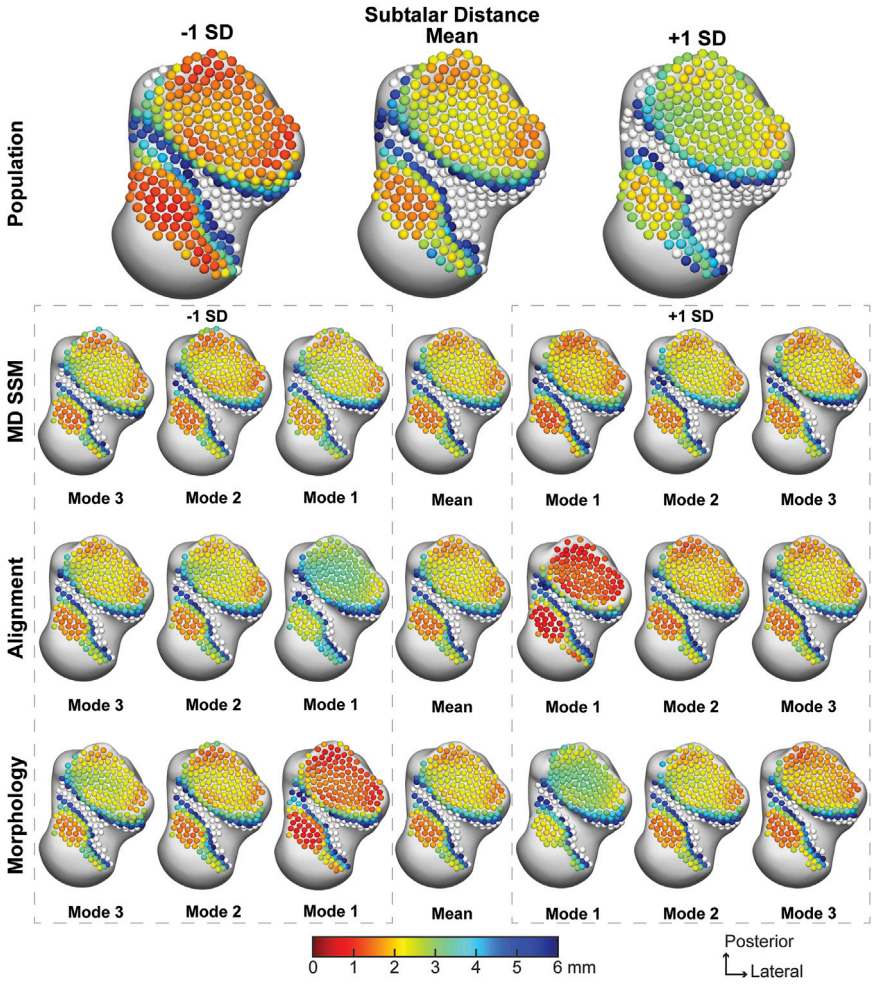

FIGURE 5
Average joint space distance with ±1 standard deviation for the subtalar articular region. Results are visualized for the population, MD SSM modes one to three, alignment variant modes one to three and morphology variant modes one to three *via* correspondence particles. Results are reported in millimeters (mm). Values larger than 6 mm in joint space distance are colored white.

analysis took an average of about 3 min to run per patient for the largest joint.

3.1.1 Multi-domain statistical shape model analysis (MD SSM)

Substantial morphological and configurational variations were observed while maintaining joint articular relationships within the MD SSM approach. The first PCA mode of variation highlighted size variation primarily, with overall growth and shrinkage of all four bones simultaneously (Figure 2). The second PCA mode is multifaceted in the presented variation. The primary regions of change occur in the inverse relationship between the talus and calcaneus. Concerning the talus, as the talar dome heightens, the posterior process diminishes. Concerning the calcaneus, as the calcaneus lengthens, the posterior facet's slope decreases. Analyzing the two bones simultaneously, as the talar dome heightens and the posterior process diminishes, the calcaneus shortens, and the posterior facet's slope increases (Figure 2). Additionally, as the talar dome heightens, the navicular and cuboid move inferiorly with minimal rotation about the anterior-posterior axis. The third PCA mode primarily varies with the anteromedial facet moving anterior to posterior throughout the SDs. There is minor talar dome variation but little else of note within this general multi-domain approach (Figure 2).

3.1.2 Multi-level analysis in alignment shape space (alignment variant)

When focusing on the alignment variant, notable anatomical alignment variations were observed. The first PCA mode of variation shows an overall outward and

TABLE 2 Average joint space distance ±standard deviation (SD) for the subtalar joint, talonavicular joint, and calcaneocuboid join. *p*-values are reported from each mode and variant to the population. Bolded *p*-values are statistically significant to the population.

Joint distance (mm)	Subtalar	Talonavicular	Calcaneocuboid
Population	3.33 ± 2.06	1.32 ± 0.43	1.67 ± 0.62
MD SSM Mode 1	3.51 ± 2.07	1.33 ± 0.21	1.65 ± 0.38
p-value	0.7500	0.9140	0.8869
MD SSM Mode 2	3.52 ± 2.07	1.32 ± 0.24	1.64 ± 0.38
p-value	0.7367	1.0000	0.8311
MD SSM Mode 3	3.48 ± 2.05	1.31 ± 0.19	1.64 ± 0.37
p-value	0.7896	0.9124	0.8299
Alignment Variant Mode 1	3.54 ± 2.12	1.35 ± 0.88	1.73 ± 1.13
p-value	0.7135	0.8742	0.8098
Alignment Variant Mode 2	3.54 ± 2.08	1.32 ± 0.30	1.64 ± 0.38
p-value	0.7109	1.0000	0.8311
Alignment Variant Mode 3	3.50 ± 2.10	1.32 ± 0.19	1.64 ± 0.39
p-value	0.7652	1.0000	0.8323
Morphology Variant Mode 1	3.40 ± 2.10	1.27 ± 0.83	1.70 ± 1.10
p-value	0.9021	0.7822	0.9022
Morphology Variant Mode 2	3.50 ± 2.10	1.31 ± 0.32	1.64 ± 0.39
p-value	0.7652	0.9231	0.8323
Morphology Variant Mode 3	3.50 ± 2.00	1.32 ± 0.21	1.65 ± 0.38
p-value	0.7596	1.0000	0.8869

inward movement between the bones, effectively increasing and decreasing joint space distance (Figure 3). The second PCA mode primarily highlights the superior and inferior motion of the four bones. Specifically, as the talus moves superiorly, the calcaneus, cuboid, and navicular move inferiorly (Figure 3). And the third PCA mode identifies the medial and lateral movement of the talus and calcaneus; as the talus moves medially, the calcaneus moves laterally. Additionally, as the talus moves medially, the navicular rotates superior and lateral, and the cuboid rotates inferior and medial (Figure 3).

3.1.3 Multi-level analysis in morphology shape space (morphology variant)

With just observing the morphological variant, the first PCA mode of variation shows each bone growing and shrinking individually (Figure 4). The second PCA mode of variation primarily has the lengthening of the calcaneus with a decreasing posterior facet slope. There are still slight talar dome changes and slight navicular and cuboid changes, but they are not as prominent as the general multi-domain approach (Figure 4). The third PCA mode shows a similar anterior/posterior anteromedial facet variation; however, it illustrates more of a rotational component. The anteromedial facet's slope changes throughout the SDs from a steep slope to a more flattened slope (Figure 4).

3.2 Joint measurements

3.2.1 Coverage

3.2.1.1 Subtalar joint

The coverage area for the subtalar joint was calculated for the entire subtalar joint and the posterior and anteromedial facets. The coverage area across the population for the entire joint averaged 1,519.34 ± 193.22 mm^2 for the talus and 1,435.99 ± 171.36 mm^2 for the calcaneus. None of the modes of variation within the MD SSM, morphology variant, or alignment variant were significantly different from the population. Moreover, the talus had a consistently larger coverage area than the calcaneus (Table 1).

The coverage area across the population for the posterior facet averaged 805.39 ± 112.42 mm^2 for the talus and 862.60 ± 127.85 mm^2 for the calcaneus. Similarly to the entire subtalar joint, none of the modes of variation within the MD SSM, morphology variant, or alignment variant differed significantly from the population. However, unlike the entire subtalar joint, the calcaneus had a consistently larger coverage area than the talus (Table 1).

The coverage area across the population for the anteromedial facet averaged 365.28 ± 74.76 mm^2 for the talus and 384.33 ± 77.94 mm^2 for the calcaneus. While none of the modes of variation within the MD SSM, morphology variant, or alignment variant for the talus were significantly different from the population, most of them were different when comparing the calcaneus to the population. Additionally, the

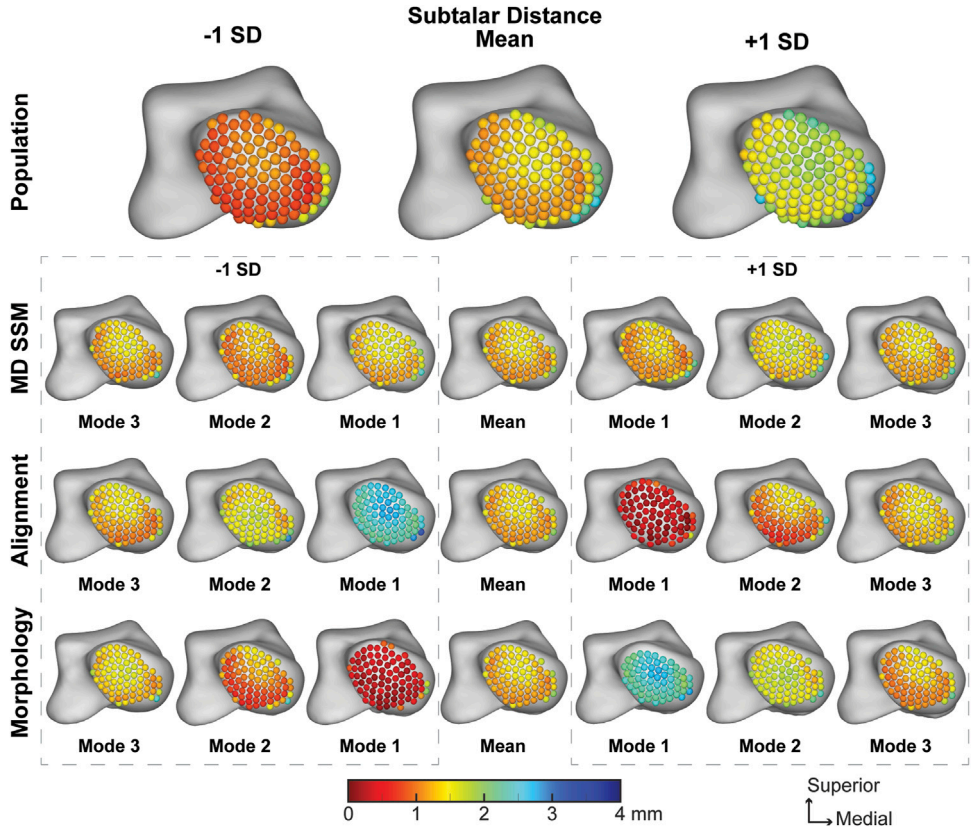

FIGURE 6
Average joint space distance with ±1 standard deviation for the talonavicular articular region. Results are visualized for the population, MD SSM modes one to three, alignment variant modes one to three and morphology variant modes one to three *via* correspondence particles. Results are reported in millimeters (mm). Values larger than 6 mm in joint space distance are colored white.

talus coverage area is generally larger compared to the calcaneus coverage area, even though that is not true for the population (Table 1).

3.2.1.2 Talonavicular joint

The coverage area across the population for the talonavicular joint averaged 471.22 ± 67.08 mm^2 for the talus and 541.36 ± 55.15 mm^2 for the navicular. Mode one for the MD SSM, morphology variant and alignment variant was the only mode that was significantly similar to the population for the talar coverage area, each with p-values greater than 0.05. None of the p-values showed significant differences for the MD SSM, morphology variant or alignment variant compared to the population (Table 1). Additionally, the navicular had a significantly larger coverage area when compared to the talus in every analysis, including the population.

3.2.1.3 Calcaneocuboid joint

The coverage area across the population for the calcaneocuboid joint average 393.92 ± 55.07 mm^2 for the calcaneus and 406.46 ± 53.86 mm^2 for the cuboid. For the calcaneus, only the first mode of the morphology variant was significantly similar compared to the population. For the cuboid, only the first modes of the MD SSM and morphology variant were significantly similar compared to the population. When comparing the coverage area of the calcaneus to the cuboid, most were significantly different (Table 1). Still, the population, MD SSM mode one, and all modes in the morphology variant were not significantly different between the bones. However, the cuboid had a larger coverage area when compared to the calcaneus for every analysis, including the population.

3.2.2 Joint space distance

3.2.2.1 Subtalar joint

The population across the entire subtalar joint averaged a joint space distance of 3.33 ± 2.06 mm, with a narrower joint space in the posterior and lateral regions of the posterior facet and the medial region of the anteromedial facet (Figure 5). The average joint space distance throughout the first three modes of the MD SSM, alignment variant and morphology variant ranged

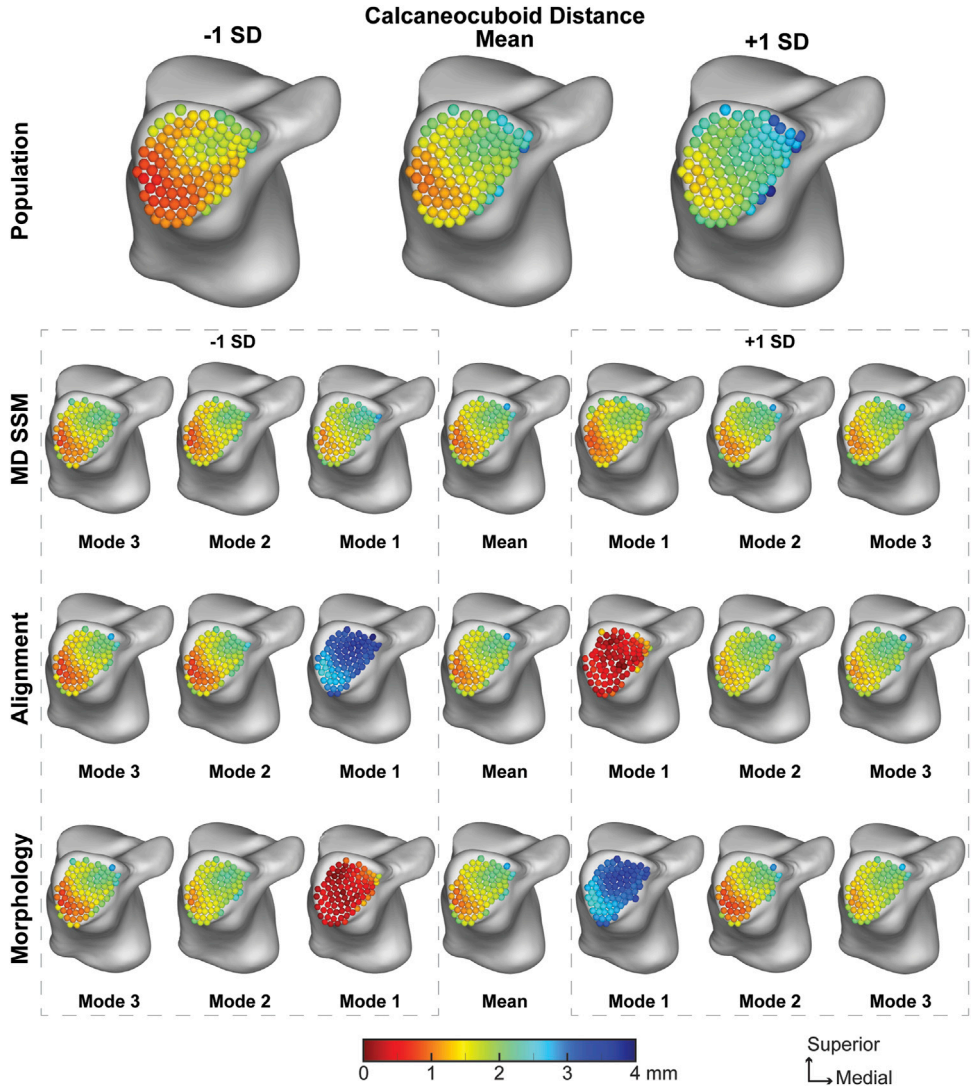

FIGURE 7
Average joint space distance with ±1 standard deviation for the calcaneocuboid articular region. Results are visualized for the population, MD SSM modes one to three, alignment variant modes one to three and morphology variant modes one to three *via* correspondence particles. Results are reported in millimeters (mm). Values larger than 6 mm in joint space distance are colored white.

from 3.40 ± 2.10 mm to 3.54 ± 2.12 mm (Table 2). There were minor variations across the joints throughout the second and third modes of variation. And while the first mode of variation had large changes across the first SDs, none of the subtalar distance values had a *p*-value lower than 0.7109 compared to the population (Table 2).

3.2.2.2 Talonavicular joint

The average talonavicular joint space distance for the population was 1.32 ± 0.43 mm, with a slight widening of the medial and central aspects of the joint (Figure 6). The average joint space distance throughout the first three modes of the MD SSM, alignment variant and morphology variant ranged from 1.27 ± 0.83 mm to 1.35 ± 0.88 mm (Table 2). While the first mode expectedly had larger changes across the first SD, the second mode also had substantial variation in both morphology and alignment variants. However, they all had a similar pattern of widening distance towards the central aspect of the joint, and none had a *p*-value lower than 0.7822 compared to the population (Table 2).

3.2.2.3 Calcaneocuboid joint

The population across the calcaneocuboid joint averaged a joint space distance of 1.67 ± 0.62 mm with a narrowing in the inferolateral region of the joint (Figure 7). The average joint space

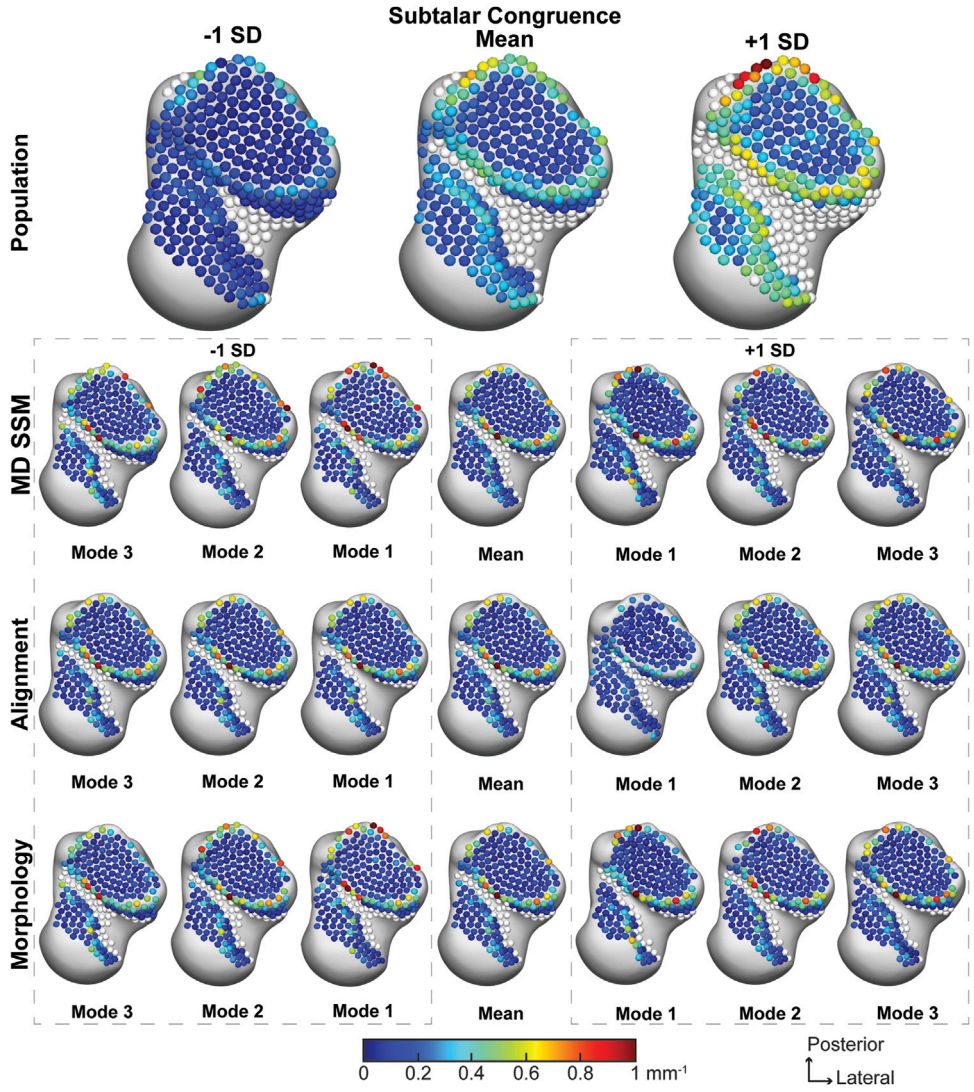

FIGURE 8
Average joint congruence indices with ±1 standard deviation for the subtalar articular region. Results are visualized for the population, MD SSM modes one to three, alignment variant modes one to three and morphology variant modes one to three *via* correspondence particles. Results are reported in inverse millimeters (mm^{-1}). Values larger than 6 mm in joint space distance are colored white.

distance throughout the first three modes of the MD SSM, alignment variant and morphology variant ranged from 1.64 ± 0.37 mm to 1.73 ± 1.13 mm (Table 2). Similar to the previous joints, the first mode has the widest variation across the SD, with modes two and three showing a similar pattern as the mean. Additionally, none of the calcaneocuboid distance values had a *p*-value lower than 0.8098 compared to the population (Table 2).

3.2.3 Joint congruence index

3.2.3.1 Subtalar joint

The population across the entire subtalar joint had an average congruence index of 0.24 ± 0.16 mm^{-1}. With a worsening congruence index on the outer edge of the joint (Figure 8). The average joint congruence index throughout the first three modes of the MD SSM, alignment variant and morphology variant ranged from 0.16 ± 0.14 mm^{-1} to 0.20 ± 0.18 mm^{-1} (Table 2). All modes and variants had similar congruence patterns and none had a *p*-value lower than 0.0559 compared to the population (Table 3). Overall, the population congruence was consistently higher than the MD SSM, morphology variant and alignment variant.

3.2.3.2 Talonavicular joint

The average talonavicular joint congruence index across the population was 0.23 ± 0.12 $mm^{-1,}$ with subjectively

TABLE 3 Average congruence index ±standard deviation (SD) for the subtalar joint, talonavicular joint, and calcaneocuboid join. *p*-values are reported from each mode and variant to the population. Bolded *p*-values are statistically significant to the population.

Congruence index (mm^{-1})	Subtalar	Talonavicular	Calcaneocuboid
Population	0.24 ± 0.16	0.23 ± 0.12	0.30 ± 0.18
MD SSM Mode 1	0.20 ± 0.18	0.16 ± 0.06	0.22 ± 0.15
p-value	0.3921	**0.0091**	0.0819
MD SSM Mode 2	0.18 ± 0.16	0.17 ± 0.06	0.21 ± 0.15
p-value	0.1742	**0.0241**	0.0512
MD SSM Mode 3	0.20 ± 0.16	0.16 ± 0.06	0.21 ± 0.14
p-value	0.3626	**0.0091**	**0.0453**
Alignment Variant Mode 1	0.16 ± 0.14	0.17 ± 0.06	0.21 ± 0.12
p-value	0.0559	**0.0241**	**0.0353**
Alignment Variant Mode 2	0.20 ± 0.16	0.16 ± 0.06	0.21 ± 0.14
p-value	0.3626	**0.0091**	**0.0453**
Alignment Variant Mode 3	0.20 ± 0.16	0.16 ± 0.06	0.21 ± 0.14
p-value	0.3626	**0.0091**	**0.0453**
Morphology Variant Mode 1	0.20 ± 0.18	0.22 ± 0.07	0.22 ± 0.15
p-value	0.3921	0.7099	0.0819
Morphology Variant Mode 2	0.20 ± 0.16	0.17 ± 0.06	0.21 ± 0.14
p-value	0.3626	**0.0241**	**0.0453**
Morphology Variant Mode 3	0.20 ± 0.16	0.16 ± 0.06	0.21 ± 0.14
p-value	0.3626	**0.0091**	**0.0453**

consistent congruence across the joint (Figure 9). The average joint congruence index throughout the first three modes of the MD SSM, alignment variant and morphology variant ranged from 0.16 ± 0.06 mm^{-1} to 0.22 ± 0.07 mm^{-1} (Table 3). While all the modes and variants had similar congruence patterns, the only variant with a *p*-value larger than 0.05 was the first mode in the morphology variant (0.7099). All other congruence values were significantly different in a more congruent fashion compared to the population. Overall, the population congruence was consistently higher than the MD SSM, morphology variant and alignment variant.

3.2.3.3 Calcaneocuboid joint

The average calcaneocuboid joint congruence index across the population was 0.30 ± 0.18 mm^{-1} with worsening congruence towards the edge of the joint (Figure 10). The average joint congruence index throughout the first three modes of the MD SSM, alignment variant and morphology variant ranged from 0.21 ± 0.12 mm^{-1} to 0.22 ± 0.15 mm^{-1} (Table 3). Only the first and second MD SSM modes and the first alignment variant mode had a *p*-value larger than 0.05. All other congruence values were significantly different in a more congruent fashion compared to the population. Overall, the population congruence was consistently higher than the MD SSM, morphology variant and alignment variant.

4 Discussion

The study's primary aim was to use multi-domain SSM to characterize asymptomatic joint-level morphology and alignment variations throughout a population and determine joint-level measurements within the subtalar, talonavicular, and calcaneocuboid joints. Using those population-based joint-level measurements, we also aimed to determine if SSM can predict joint-level measurements. Moreover, we aimed to determine the validity of the multi-domain mean shapes compared to the single-domain mean shapes. The most relevant findings include: I) joint space distance is the only joint-level measurement statistically similar across all modes of variation for the MD SSM, morphology variant and alignment variant; II) the first mode in the morphology variant is statistically similar to the population across all joint-level measurements except the coverage area on the calcaneal anteromedial facet; III) MD SSM does preserve the mean shape when compared to the SD SSM mean shape.

Our MD SSM shape variations finding agree with the limited studies performed on the talus, calcaneus, navicular and cuboid. We found that the primary anatomical morphological variations included the talar trochlea height, calcaneal lengthening, and minimal variation throughout the navicular and cuboid (Melinska et al., 2015; Melinska et al., 2017; Tümer et al., 2019a; Krähenbühl et al., 2020; Lenz et al., 2021). However, we also found the relationship between the talar trochlea and

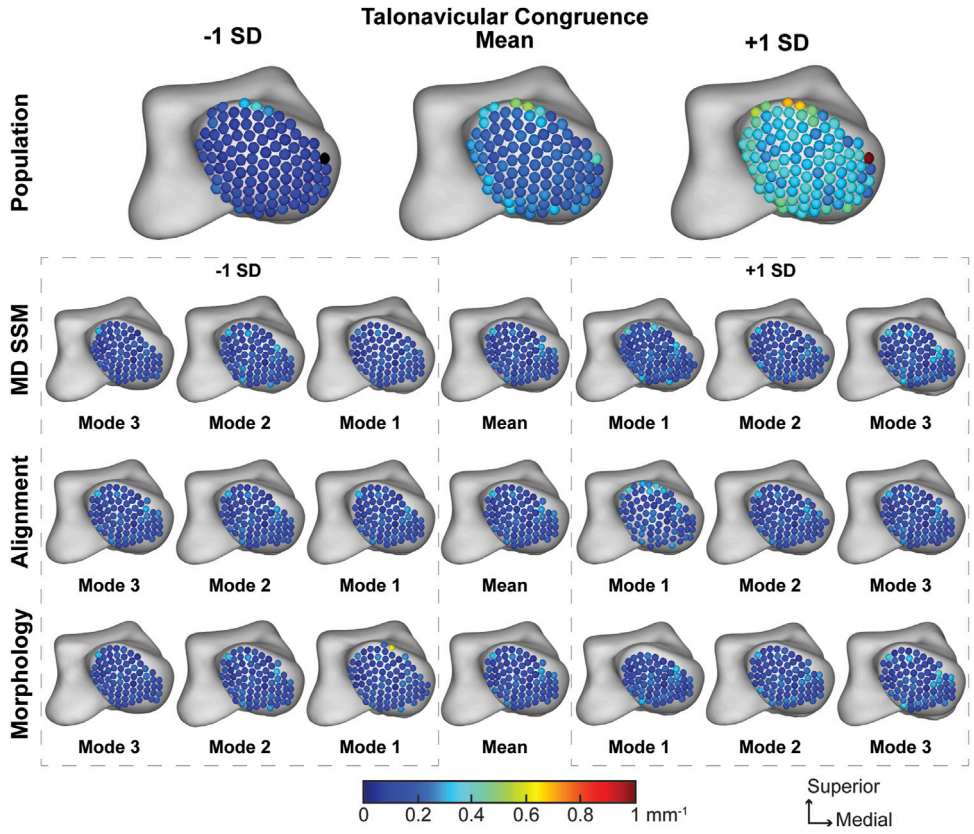

FIGURE 9
Average joint congruence indices with ±1 standard deviation for the talonavicular articular region. Results are visualized for the population, MD SSM modes one to three, alignment variant modes one to three and morphology variant modes one to three *via* correspondence particles. Results are reported in inverse millimeters (mm^{-1}). Values larger than 6 mm in joint space distance are colored white.

calcaneal length to be interrelated. Additionally, the novel multi-level approach allowed for the separation of alignment from morphology. This approach provides insight of the talonavicular and calcaneocuboid alignment variations. Primary alignment variation occurred between the talus, navicular and cuboid. Specifically, when the talus moves inferiorly, the navicular and cuboid move superiorly and *vice versa*. But when the talus moves medially or laterally, the navicular and cuboid rotate about the anterior-posterior axis. Multiple studies have attempted to analyze and understand the role these midfoot joints have on human locomotion but have reached a wide range of conclusions. Some studies have found the talonavicular and calcaneocuboid joints to rotate throughout gait creating what is known as a locking and unlocking mechanism based on the axes of the transverse tarsal joint in one plane (Elftman, 1960; Suckel et al., 2008; Sarrafian, 2011); yet others have determined the motion within these joints did not significantly increase during gait (Blackwood et al., 2005). Moreover, other studies have determined that the plantar fascia has more of a role *via* the windlass mechanism in producing movement during gait (Hicks, 1954; Welte et al., 2021) and that there was not any observed midtarsal movement during gait (Bruening et al., 2018). There is still much to be understood about these different mechanisms and the role that the hind- and mid-foot joints have during gait, but multi-domain models may be a step towards understanding how morphology and alignment during static positioning influence these well-debated topics clinically.

Few studies have performed weightbearing joint space distance calculations of these three joints. One study that has calculated the asymptomatic subtalar joint distance for the joint as a whole reported 3.29 ± 0.87 mm compared to our measurement of 3.33 ± 2.06 mm, and when compared determined to not be statistically different from one another (p = 0.95) (Dibbern et al., 2021). While a small number of studies have calculated talonavicular and calcaneocuboid joint space distance, the most comparable to this study also used WBCT scans (Bernasconi et al., 2021). Bernasconi et al. reported average talonavicular and calcaneocuboid distance

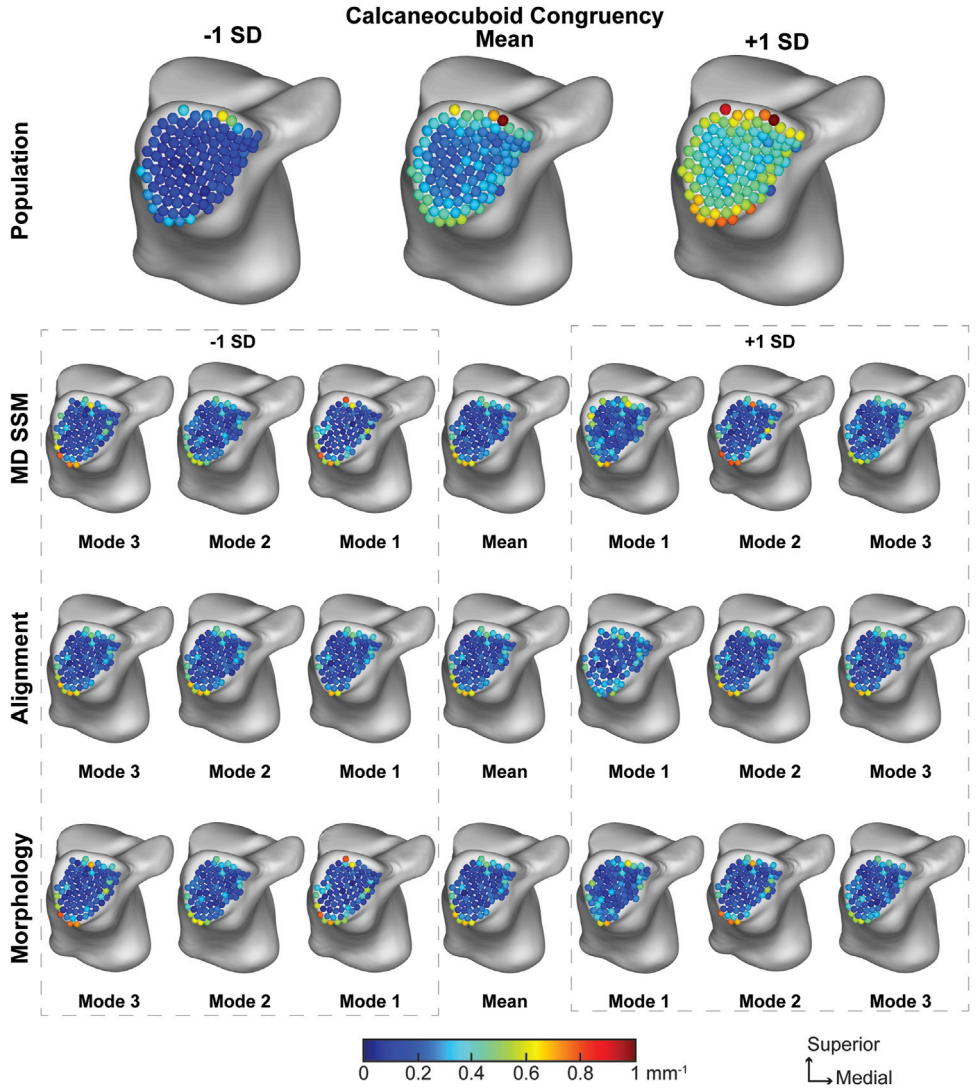

FIGURE 10
Average joint congruence indices with ±1 standard deviation for the calcaneocuboid articular region. Results are visualized for the population, MD SSM modes one to three, alignment variant modes one to three and morphology variant modes one to three *via* correspondence particles. Results are reported in inverse millimeters (mm^{-1}). Values larger than 6 mm in joint space distance are colored white.

measurements of 1.14 ± 0.49 mm and 1.67 ± 1.26 mm, respectively. Compared to our measurements of 1.32 ± 0.43 mm for the talonavicular and 1.67 ± 0.62 mm for the calcaneocuboid, these measurements were statistically similar to one another (talonavicular: $p = 0.28$ and calcaneocuboid: $p = 1.0$). As previously mentioned, the first relevant finding of this study was that joint space distance was the only joint-level measurement statistically similar between the population and all modes of variation for the MD SSM, morphology variant and alignment variant. This finding may indicate that MD SSM, morphology variant and alignment variant models have the potential to predict joint distance measurements within a population.

When separating alignment (alignment variant) from morphology (morphology variant) in the first mode of variation, the relationship between size and joint space can be determined. As seen in the SSM figures, as the models get larger towards -2 SDs (Figure 4), they also become further apart (Figure 3). This relationship can be further seen in the joint space distance figures (Figures 5–7) with the morphology indicating that joint space is narrowing as the bone models get larger, but the alignment indicating that they are simultaneously moving further apart. This pattern indicates that individuals with larger bones subsequently have greater joint space. While joint space has been previously correlated to sex, height and weight measurements (Goker et al., 2009),

further correlation to bone size and shape in the foot and ankle may be concluded from this approach. Additionally, the second relevant finding referring to the first mode of variation in the morphology variant being generally statistically similar to the population gives potential relevance to another predictive conclusion. With the first mode of the morphology variant producing the most statistically similar joint measurement results to the population, it may indicate that this specific mode can be used to predict all three measurements within a population. It also may indicate that variation across a population of these four bones is driven far more by morphology than by alignment variation. To further support this postulate, identifying patient populations with morphological variations, such as those with asymmetric ankle osteoarthritis, those suffering from PCFD, or after fracture reduction, could help better understand the role morphology plays in disease and deformity progression.

This study is not without its limitations. Soft tissues, specifically ligaments, tendons, and articular cartilage, were not included in this study. All joint-level measurements were calculated on subchondral bone surfaces, which do not consider the effects of these soft tissues when concerning alignment and joint distance. Second, WBCT scans are dependent on the native CT resolution and therefore maximum precision is 0.4 mm when considering CT segmentations for joint measurements. However, with the error spectrum being ±1 pixel, it is still less than 1 mm, therefore we feel confident in our ability to report clinically meaningful joint measurements. Third, static imaging does not capture the articulation behavior of these joints that imaging during human locomotion could capture. Further analyses on joint-level measurements during dynamic activities should be evaluated to further understand the true relationship these joints have with one another. Fourth, this study only includes bone models from healthy asymptomatic individuals. While this was intentionally done to determine healthy variations, incorporating pathological bone models in future studies could give better context of the morphological variations found in this healthy model. Further studies relating these findings to individuals with hindfoot ankle diseases will provide more relevance to clinical actions that should be taken.

In conclusion, joint-level morphology and alignment variations can be further understood using a multi-level multi-domain SSM. This study found joint space distance measurements across all modes of variation and the first mode of the morphology variation across all primary measurements to be statistically similar to the population. This may indicate using SSM to predict joint-level measurements in specific variants is a valid approach. Additionally, multi-domain SSM does preserve mean shape compared to a single-domain SSM mean shape and can confidently be used to further multi-domain SSM studies. Further studies include expanding multi-domain modeling to subsequent joints in the foot and ankle for asymptomatic and symptomatic populations. Additionally, performing multi-domain joint-level measurements during dynamic activities is necessary to fully understand the complex relationship between these joints in the foot and ankle. Future optimization schemes could be developed where the morphology and alignment variants are coherently reflected in the particle position updates of the optimized correspondence model.

Data availability statement

The raw data supporting the conclusions of this article will be made available by the authors, without undue reservation.

Ethics statement

The studies involving human participants were reviewed and approved by University of Utah Institutional Review Board. The patients/participants provided their written informed consent to participate in this study.

Author contributions

AP, NiK, CS, AB, and AL conceived and designed the experiment, NiK provided image data, AP, RL and AL generated surface models for all bones, NaK and SE developed statistical shape model software and multi-level analysis and provided technical oversight and troubleshoot on the use of the different modelling and analysis methods for the proposed study, AP conducted the statistical shape model development and analysis, AP, RL and AL conducted the joint analysis for coverage, distance, and congruence, and AP analyzed the results. All authors reviewed the manuscript.

Funding

The National Institutes of Health supported this work under grant numbers NIAMS-K01AR080221, NIBIB-U24EB029011, NIAMS-R01AR076120, and NIBIB-R01EB016701.

Conflict of interest

The authors declare that the research was conducted in the absence of any commercial or financial relationships that could be construed as a potential conflict of interest.

Publisher's note

All claims expressed in this article are solely those of the authors and do not necessarily represent those of their

affiliated organizations, or those of the publisher, the editors and the reviewers. Any product that may be evaluated in this article, or claim that may be made by its manufacturer, is not guaranteed or endorsed by the publisher.

Author disclaimer

The content is solely the responsibility of the authors and does not necessarily represent the official views of the National Institutes of Health.

References

Arbabi, S., Seevinck, P., Weinans, H., Jong, P. A., Sturkenboom, J., Hamersvelt, R. W., et al. (2022). Statistical shape model of the talus bone morphology: A comparison between impinged and nonimpinged ankles. *J. Orthop. Res.* doi:10.1002/jor.25328

Ateshian, G. A., Rosenwasser, M. P., and Mow, V. C. (1992). Curvature characteristics and congruence of the thumb carpometacarpal joint: Differences between female and male joints. *J. Biomech.* 25, 591–607. doi:10.1016/0021-9290(92)90102-7

Barg, A., Bailey, T., Richter, M., De Cesar Netto, C., Lintz, F., Burssens, A., et al. (2018). Weightbearing computed tomography of the foot and ankle: Emerging technology topical Review. *Foot Ankle Int.* 39, 376–386. doi:10.1177/1071100717740330

Bernasconi, A., De Cesar Netto, C., Siegler, S., Jepsen, M., and Lintz, F. (2021). Weightbearing CT assessment of foot and ankle joints in Pes Planovalgus using distance mapping. *Foot Ankle Surg.* 28, 775–784. doi:10.1016/j.fas.2021.10.004

Blackwood, C. B., Yuen, T. J., Sangeorzan, B. J., and Ledoux, W. R. (2005). The midtarsal joint locking mechanism. *Foot Ankle Int.* 26, 1074–1080. doi:10.1177/107110070502601213

Bruening, D. A., Pohl, M. B., Takahashi, K. Z., and Barrios, J. A. (2018). Midtarsal locking, the windlass mechanism, and running strike pattern: A kinematic and kinetic assessment. *J. Biomech.* 73, 185–191. doi:10.1016/j.jbiomech.2018.04.010

Burssens, A., Peeters, J., Buedts, K., Victor, J., and Vandeputte, G. (2016). Measuring hindfoot alignment in weight bearing CT: A novel clinical relevant measurement method. *Foot Ankle Surg. (N. Y).* 22, 233–238. doi:10.1016/j.fas.2015.10.002

Cates, J. E., Elhabian, S. Y., and Whitaker, R. T. (2017). ShapeWorks: Particle-Based shape correspondence and visualization software. *Stat. Shape Deformation Analysis* 2017, 257–298. doi:10.1016/B978-0-12-810493-4.00012-2

Cates, J., Fletcher, P. T., Styner, M., Hazlett, H. C., and Whitaker, R. (2008). Particle-based shape analysis of multi-object complexes. *Med. Image Comput. Comput. Assist. Interv.International Conf. Med. Image Comput. Computer-Assisted Intervention* 11, 477–485. doi:10.1007/978-3-540-85988-8_57

Cates, J., Fletcher, P. T., Styner, M., Shenton, M., and Whitaker, R. (2007). Shape modeling and analysis with entropy-based particle systems. *Inf. Process. Med. Imaging* 20, 333–345. doi:10.1007/978-3-540-73273-0_28

Colin, F., Horn Lang, T., Zwicky, L., Hintermann, B., and Knupp, M. (2014). Subtalar joint configuration on weightbearing CT scan. *Foot Ankle Int.* 35, 1057–1062. doi:10.1177/1071100714540890

Datar, M., Cates, J., Fletcher, P. T., Gouttard, S., Gerig, G., and Whitaker, R. (2009). Particle based shape regression of open surfaces with applications to developmental neuroimaging. *Med. Image Comput. Comput. Assist. Interv.* 12, 167–174. doi:10.1007/978-3-642-04271-3_21

Datar, M., Gur, Y., Paniagua, B., Styner, M., and Whitaker, R. (2011). Geometric correspondence for ensembles of nonregular shapes. *Med. Image Comput. Comput. Assist. Interv.* 14, 368–375. doi:10.1007/978-3-642-23629-7_45

Davies, R. H., Twining, C. J., Cootes, T. F., Waterton, J. C., and Taylor, C. J. (2002). A minimum description length approach to statistical shape modeling. *IEEE Trans. Med. Imaging* 21, 525–537. doi:10.1109/tmi.2002.1009388

Day, M. A., Ho, M., Dibbern, K., Rao, K., An, Q., Anderson, D. D., et al. (2020). Correlation of 3D joint space width from weightbearing CT with outcomes after intra-articular calcaneal fracture. *Foot Ankle Int.* 41, 1106–1116. doi:10.1177/1071100720933891

Dibbern, K. N., Li, S., Vivtcharenko, V., Auch, E., Lintz, F., Ellis, S. J., et al. (2021). Three-dimensional distance and coverage maps in the assessment of peritalar subluxation in progressive collapsing foot deformity. *Foot Ankle Int.* 42, 757–767. doi:10.1177/1071100720983227

Ebraheim, N. A., Haman, S. P., Lu, J., and Padanilam, T. G. (1999). Radiographic evaluation of the calcaneocuboid joint: A cadaver study. *Foot Ankle Int.* 20, 178–181. doi:10.1177/107110079902000307

Elftman, H. (1960). The transverse tarsal joint and its control. *Clin. Orthop.* 16, 41–46.

Gabrielli, A. S., Gale, T., Hogan, M., and Anderst, W. (2020). Bilateral symmetry, sex differences, and primary shape factors in ankle and hindfoot bone morphology. *Foot Ankle Orthop.* 5, 247301142090879. doi:10.1177/2473011420908796

Goker, B., Gonen, E., Demirag, M. D., and Block, J. A. (2009). Quantification of the radiographic joint space width of the ankle. *Clin. Orthop. Relat. Res.* 467, 2083–2089. doi:10.1007/s11999-009-0832-8

Goparaju, A., Iyer, K., Bône, A., Hu, N., Henninger, H. B., Anderson, A. E., et al. (2022). Benchmarking off-the-shelf statistical shape modeling tools in clinical applications. *Med. Image Anal.* 76, 102271. doi:10.1016/j.media.2021.102271

Hayes, A., Tochigi, Y., and Saltzman, C. L. (2006). Ankle morphometry on 3D-CT images. *Iowa Orthop. J.* 26, 1–4.

Hicks, J. H. (1954). The mechanics of the foot. II. The plantar aponeurosis and the arch. *J. Anat.* 88, 25–30.

Horn, J. L. (1965). A rationale and test for the number of factors in factor Analysis. *Psychometrika* 30, 179–185. doi:10.1007/bf02289447

Krähenbühl, N., Horn-Lang, T., Hintermann, B., and Knupp, M. (2017). The subtalar joint: A complex mechanism. *EFORT Open Rev.* 2, 309–316. doi:10.1302/2058-5241.2.160050

Krähenbühl, N., Lenz, A. L., Lisonbee, R. J., Peterson, A. C., Atkins, P. R., Hintermann, B., et al. (2020). Morphologic analysis of the subtalar joint using statistical shape modeling. *J. Orthop. Res.* 38, 2625–2633. doi:10.1002/jor.24831

Krähenbühl, N., Tschuck, M., Bolliger, L., Hintermann, B., and Knupp, M. (2016). Orientation of the subtalar joint: Measurement and reliability using weightbearing CT scans. *Foot Ankle Int.* 37, 109–114. doi:10.1177/1071100715600823

Ledesma, R. D., and Valero-Mora, P. (2007). Determining the number of factors to retain in EFA: An easy-to-use computer program for carrying out parallel analysis. *Pract. Assess. Res. Eval.* 12, 234. doi:10.7275/wjnc-nm63

Lenz, A. L., Krähenbühl, N., Peterson, A. C., Lisonbee, R. J., Hintermann, B., Saltzman, C. L., et al. (2021). Statistical shape modeling of the talocrural joint using a hybrid multi-articulation joint approach. *Sci. Rep.* 11, 7314. doi:10.1038/s41598-021-86567-7

Liu, T., Jomha, N. M., Adeeb, S., El-Rich, M., and Westover, L. (2020). Investigation of the average shape and principal variations of the human talus bone using statistic shape model. *Front. Bioeng. Biotechnol.* 8, 656. doi:10.3389/fbioe.2020.00656

Lopez-Ben, R. (2015). Imaging of the subtalar joint. *Foot Ankle Clin.* 20, 223–241. doi:10.1016/j.fcl.2015.02.009

Louie, P. K., Sangeorzan, B. J., Fassbind, M. J., and Ledoux, W. R. (2014). Talonavicular joint coverage and bone morphology between different foot types. *J. Orthop. Res.* 32, 958–966. doi:10.1002/jor.22612

Melinska, A. U., Romaszkiewicz, P., Wagel, J., Antosik, B., Sasiadek, M., and Iskander, D. R. (2017). Statistical shape models of cuboid, navicular and talus bones. *J. Foot Ankle Res.* 10, 6. doi:10.1186/s13047-016-0178-x

Melinska, A. U., Romaszkiewicz, P., Wagel, J., Sasiadek, M., and Iskander, D. R. (2015). Statistical, morphometric, anatomical shape model (atlas) of calcaneus. *PLoS One* 10, e0134603. doi:10.1371/journal.pone.0134603

Peiffer, M., Burssens, A., De Mits, S., Heintz, T., Van Waeyenberge, M., Buedts, K., et al. (2022). Statistical shape model-based tibiofibular assessment of syndesmotic ankle lesions using weight-bearing CT. *J. Orthop. Res.* doi:10.1002/jor.25318

Peterson, A. C. (2022). Static joint measurement analysis. [Online] Available: https://github.com/Lenz-Lab/StaticJointMeasureAnalysis.

Sammarco, V. J. (2004). The talonavicular and calcaneocuboid joints: Anatomy, biomechanics, and clinical management of the transverse tarsal joint. *Foot Ankle Clin.* 9, 127–145. doi:10.1016/s1083-7515(03)00152-9

Sarrafian, S. (2011). *Sarrafian's anatomy of the foot and ankle*. Philadelphia, Pennsylvania, United States: Lippincott Williams & Wilkins.

Schaefer, K. L., Sangeorzan, B. J., Fassbind, M. J., and Ledoux, W. R. (2012). The comparative morphology of idiopathic ankle osteoarthritis. *J. Bone Jt. Surgery-American Volume* 94, e181. doi:10.2106/jbjs.l.00063

Schmutz, B., Lüthi, M., Schmutz-Leong, Y. K., Shulman, R., and Platt, S. (2021). Morphological analysis of Gissane's angle utilising a statistical shape model of the calcaneus. *Arch. Orthop. Trauma Surg.* 141, 937–945. doi:10.1007/s00402-020-03566-5

Styner, M., Gerig, G., Lieberman, J., Jones, D., and Weinberger, D. (2003). Statistical shape analysis of neuroanatomical structures based on medial models. *Med. Image Anal.* 7, 207–220. doi:10.1016/s1361-8415(02)00110-x

Suckel, A., Muller, O., Langenstein, P., Herberts, T., Reize, P., and Wulker, N. (2008). Chopart's joint load during gait. *Gait Posture* 27, 216–222. doi:10.1016/j.gaitpost.2007.03.010

Tümer, N., Arbabi, V., Gielis, W. P., De Jong, P. A., Weinans, H., Tuijthof, G. J. M., et al. (2019a). Three-dimensional analysis of shape variations and symmetry of the fibula, tibia, calcaneus and talus. *J. Anat.* 234, 132–144. doi:10.1111/joa.12900

Tümer, N., Vuurberg, G., Blankevoort, L., Kerkhoffs, G. M. M. J., Tuijthof, G. J. M., and Zadpoor, A. A. (2019b). Typical shape differences in the subtalar joint bones between subjects with chronic ankle instability and controls. *J. Orthop. Res.* 37, 1892–1902. doi:10.1002/jor.24336

Vafaeian, B., Riahi, H. T., Amoushahi, H., Jomha, N. M., and Adeeb, S. (2022). A feature-based statistical shape model for geometric analysis of the human talus and development of universal talar prostheses. *J. Anat.* 240, 305–322. doi:10.1111/joa.13552

Welte, L., Kelly, L. A., Kessler, S. E., Lieberman, D. E., D'andrea, S. E., Lichtwark, G. A., et al. (2021). The extensibility of the plantar fascia influences the windlass mechanism during human running. *Proc. R. Soc. B* 288, 20202095. doi:10.1098/rspb.2020.2095

Willauer, P., Sangeorzan, B. J., Whittaker, E. C., Shofer, J. B., and Ledoux, W. R. (2014). The sensitivity of standard radiographic foot measures to misalignment. *Foot Ankle Int.* 35, 1334–1340. doi:10.1177/1071100714549188

Wilm, J. (2022). *Iterative closest point*. New York: MATLAB Central File Exchange.

frontiers | Frontiers in Bioengineering and Biotechnology

TYPE Original Research
PUBLISHED 09 December 2022
DOI 10.3389/fbioe.2022.1059003

OPEN ACCESS

EDITED BY
Shireen Y. Elhabian,
The University of Utah, United States

REVIEWED BY
Amy L. Lenz,
The University of Utah, United States
David M. Pierce,
University of Connecticut, United States

*CORRESPONDENCE
Clare K. Fitzpatrick,
clarefitzpatrick@boisestate.edu

SPECIALTY SECTION
This article was submitted to Biomechanics, a section of the journal Frontiers in Bioengineering and Biotechnology

RECEIVED 30 September 2022
ACCEPTED 25 November 2022
PUBLISHED 09 December 2022

CITATION
Gibbons KD, Malbouby V, Alvarez O and Fitzpatrick CK (2022), Robust automatic hexahedral cartilage meshing framework enables population-based computational studies of the knee. *Front. Bioeng. Biotechnol.* 10:1059003. doi: 10.3389/fbioe.2022.1059003

Robust automatic hexahedral cartilage meshing framework enables population-based computational studies of the knee

Kalin D. Gibbons, Vahid Malbouby, Oliver Alvarez and Clare K. Fitzpatrick*

Computational Biosciences Laboratory, Mechanical and Biomedical Engineering, Boise State University, Boise, ID, United States

Osteoarthritis of the knee is increasingly prevalent as our population ages, representing an increasing financial burden, and severely impacting quality of life. The invasiveness of *in vivo* procedures and the high cost of cadaveric studies has left computational tools uniquely suited to study knee biomechanics. Developments in deep learning have great potential for efficiently generating large-scale datasets to enable researchers to perform *population-sized* investigations, but the time and effort associated with producing robust hexahedral meshes has been a limiting factor in expanding finite element studies to encompass a population. Here we developed a fully automated pipeline capable of taking magnetic resonance knee images and producing a working finite element simulation. We trained an encoder-decoder convolutional neural network to perform semantic image segmentation on the Imorphics dataset provided through the Osteoarthritis Initiative. The Imorphics dataset contained 176 image sequences with varying levels of cartilage degradation. Starting from an open-source swept-extrusion meshing algorithm, we further developed this algorithm until it could produce high quality meshes for every sequence and we applied a template-mapping procedure to automatically place soft-tissue attachment points. The meshing algorithm produced simulation-ready meshes for all 176 sequences, regardless of the use of provided (manually reconstructed) or predicted (automatically generated) segmentation labels. The average time to mesh all bones and cartilage tissues was less than 2 min per knee on an AMD Ryzen 5600X processor, using a parallel pool of three workers for bone meshing, followed by a pool of four workers meshing the four cartilage tissues. Of the 176 sequences with provided segmentation labels, 86% of the resulting meshes completed a simulated flexion-extension activity. We used a reserved testing dataset of 28 sequences unseen during network training to produce simulations derived from predicted labels. We compared tibiofemoral contact mechanics between manual and automated reconstructions for the 24 pairs of successful finite element simulations from this set, resulting in mean root-mean-squared differences under 20% of their respective min-max norms. In combination with further advancements in deep learning, this framework

represents a feasible pipeline to produce *population* sized finite element studies of the natural knee from subject-specific models.

KEYWORDS

osteoarthritis, modeling, mesh generation, biomechanics, knee, finite element

1 Introduction

Osteoarthritis (OA) of the knee is increasingly prevalent as our population ages, affecting an estimated 654.1 million individuals aged 40 and over in 2020 worldwide, including 15.8% of the North American population (Cui et al., 2020). Patients suffering from OA report joint pain and stiffness, cracking or grinding noises with joint movement, and decreased function and mobility. These symptoms and prevalence has made OA a leading cause of pain and disability worldwide, representing a significant economic burden of approximately 2% of a given country's global domestic product (O'Neill et al., 2018). The disease is characterized by a deterioration of the cartilage, tendons and ligaments, and the development of osteophytic bone spurs within the joint (Lane et al., 2011). The study of knee OA presents several challenges to researchers, it is a multifactorial joint disease—confounding subject-specific factors include geometry, biomechanics, biology, and mechanobiological adaptations (Dell'Isola et al., 2016; Paz et al., 2021) — making it difficult to isolate features driving disease progression.

Researchers are limited in their ability to collect *in vivo* biomechanical data relating to the knee, with some researchers relying on externally attached pressure transducers, motion capture, electromyography (Paz et al., 2021), or using implants with telemetric sensors following joint replacement to estimate joint forces (Wang et al., 2015; Almouahed et al., 2017). *In vitro* studies relying on cadaveric tissue and joint specimens using mechanical joint simulators have been conducted in the past (DesJardins et al., 2000; Maletsky and Hillberry, 2005; Varadarajan et al., 2009; Colwell et al., 2011). Financial barriers associated with sourcing cadaveric specimens and employing surgeons to perform surgeries or joint assessments can be prohibitively high, limiting the scope of most cadaveric studies to a small number of subjects or activities. With their relative cost-effectiveness and inherent non-invasiveness, computational studies aim to complement *in vivo* and *in vitro* studies, using material properties and joint mechanics data from these studies to validate computational analyses.

Researchers can use validated models to simulate activities of daily living (Torry et al., 2011; Ivester et al., 2015) and, with large-volume simulations, they can use these data to link geometric and kinematic features to force and contact mechanics outputs using classic methods of inferential statistics (Bryan et al., 2010; Fitzpatrick and Rullkoetter, 2012; Gibbons et al., 2019). These statistical models are simple to use and require orders of magnitude less computing time when compared to the simulations they are derived from, making them more suitable for clinical applications. However, given the variability inherently present across the population, studies require hundreds or even thousands of subjects to adequately capture the spectrum of variability present across the population and develop reliable statistical models based on these data. Unfortunately, several bottlenecks have limited researchers to using simple parameterized or synthetically generated joint geometries in the past.

Developing a working FE simulation of a single knee typically begins with medical images, which then undergo segmentation, reconstruction, meshing, and mesh registration. Traditionally, the primary bottlenecks preventing clinical adoption are segmentation and meshing, which may take several days work per knee (Bolcos et al., 2018; Cooper et al., 2019). Recent advances in deep learning are reducing the segmentation process from hours or days of person-hours to only minutes of computing time, but are limited by the availability of training data (Ambellan et al., 2019; Burton et al., 2020; Ebrahimkhani et al., 2020). In FE simulations, hexahedral meshes are optimal for contact regions (e.g., articular contact of cartilage surfaces), as tetrahedral meshes overestimate stiffness while requiring a larger number of elements (Ramos and Simões, 2006; Tadepalli et al., 2011). While automatic triangular surface and tetrahedral volume meshing algorithms have existed for decades, robust hexahedral meshing algorithms are still being actively researched (Ito et al., 2009; Gregson et al., 2011; Livesu et al., 2020, 2013; Guan et al., 2020). Past researchers have used templated hexahedral meshes with control nodes to create fitted approximations of subject geometries (Baldwin et al., 2010; Rao et al., 2013), or custom swept-extrusion meshing algorithms validated on a small number of subject geometries (Rodriguez-Vila et al., 2017). However, to the authors' knowledge, no researchers have successfully generated subject-specific hexahedral knee cartilage meshes for hundreds of subjects in a fully automated fashion. The present study aims to answer the questions: 1) can automatic segmentation and meshing algorithms allow us to generate hundreds of *patient-specific* simulations in a fully automated fashion; 2) how closely do finite element meshes derived from deep learning segmentation labels match their manually segmented counterparts; and 3) how sensitive are the final simulation results to the predicted tissue labels?

2 Methods

To answer these questions, we have implemented a completely automated imaging-to-simulation pipeline (Figure 1). We used a

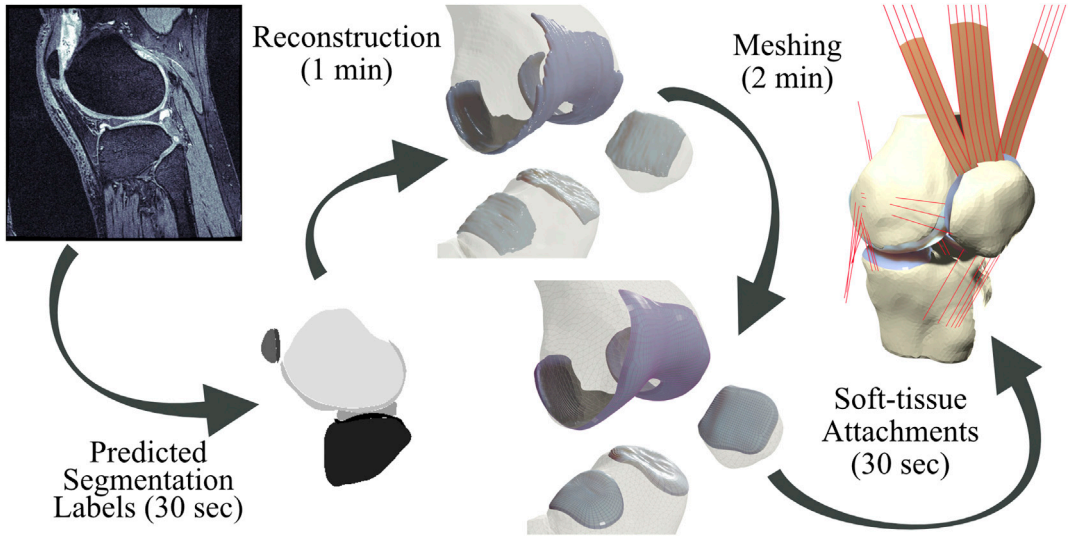

FIGURE 1
Pipeline from magnetic resonance images to simulation-ready finite element meshes. Segmentation labels produced by a neural network are used to produce reconstruction geometries. Bone geometries are then meshed using first-order triangular surface elements, and cartilage tissues are meshed using a customized swept-extrusion hexahedral meshing software. Soft-tissue attachment sites are placed using a nearest-neighbor search with a registered template mesh, resulting in a turn-key mesh ready to drop into existing finite element simulations.

simple convolutional neural network (CNN) to automate segmentation and we applied established visualization toolkits for geometric reconstruction and registration (Schroeder et al., 2006; Zhou et al., 2018; Sullivan and Kaszynski, 2019). We used standard triangular mesh generation tools to perform rigid body bone meshing (Hoppe et al., 1993; Valette et al., 2008). For the hexahedral cartilage meshes, we ported a publicly available Matlab-based hexahedral swept-extrusion algorithm (Rodriguez-Vila et al., 2017) to Python, and then customized and expanded upon this algorithm until it was sufficiently robust to produce hundreds of meshes. We subsequently enhanced the algorithm with a custom cartilage-to-bone interface blending algorithm and soft-tissue attachment site locator using a templated mesh with nearest neighbor search. This resulted in an efficient pipeline from image sequence to FE-ready mesh. We ran the output meshes in a simulated 90° knee flexion activity in three batches: our entire *manual* data set (train, validation, and test) excluding the added blending algorithm, again with blending, and the reserved test dataset utilizing *predicted* segmentation labels.

To quantify the effect of predicted segmentation labels on resulting meshes, we compared articular surface deviations between manual and predicted segmentations. We traced rays from the nodes of the predicted mesh to the nearest surface of the manual mesh and used these data to compute distributions of distances. To account for mismatches in overlapping edges, we only included rays within 20° of the surface normal which we reported as *percent nodal coverage* (Figure 2). Further down the pipeline, we ran FE simulations to predict contact pressure and area joint mechanics for the medial and lateral sides of the tibial cartilage tissues, and then compared these metrics between manually and automatically generated datasets using root-mean-square (RMS) differences.

2.1 Data source

We sourced image sequences and their respective segmentation labels for the knees of 88 subjects from the Imorphics dataset (Paproki et al., 2014), which is part of the publicly available Osteoarthritis Initiative database (National Institute of Arthritis and Musculoskeletal and Skin Diseases (NIAMS, 2004). Each subject attended baseline and 12-month follow up appointments, resulting in 176 image sequences, containing 3D double echo steady-state images consisting of $(384 \times 384 \times 160)$ voxels with a spatial resolution of $(0.37 \times 0.37 \times 0.70)$ mm in the sagittal plane. Segmented tissues included the menisci, femoral, patellar, and tibia cartilage with independent medio-lateral labels for the menisci and tibial cartilage. As stated in Paproki et al. (2014), one person, who trained under both an expert in segmentation and a musculoskeletal radiologist, performed the manual segmentations. Additionally, this user achieved an intra-observer coefficient of variation less than 3% on paired test images within the Imorphics cartilage segmentation training protocol, with the expert reviewing their final segmentation maps.

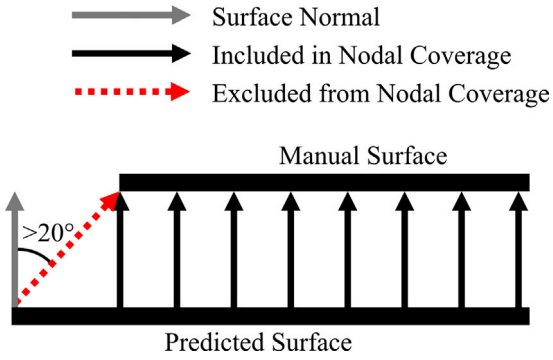

FIGURE 2
Exclusion criteria for nodal coverage. If the rays directed from the predicted surface to the nearest point on the manual surface deviated from the predicted surface normal by more than 20°, that ray was excluded from nodal normal calculations.

2.2 Image segmentation

We used a textbook 2D encoder-decoder CNN based on the popular U-Net architecture (Ronneberger et al., 2015) to perform automatic image segmentation. Each contractive block made use of batch normalization and rectified linear unit activations, while using strided convolution layers to downsample the image feature maps. We implemented residual connections around each contractive block. The network was four contractive-expansive blocks deep, with a final softmax activation. We augmented input images with up to a 30° rotation 50% of the time, as well as randomized brightness and contrast, elastic transformations, and grid distortions a maximum of 30% of the time. We trained this network on the image-label observations while reserving 14 *subjects* (each subject at baseline and 12-month timepoints, totaling 28 sequences) for a validation dataset used to detect overfitting, and reserved an additional 14 *subjects* (again, at both timepoints) for a final test set, unseen during training. We trained the model until the mean Dice similarity coefficient (DSC) of the validation set reached 89% (Taha and Hanbury, 2015). Resulting labels were based on probability scores for the four articular cartilage tissues present in the Imorphics segmentations, with our three additional bone tissues.

2.3 Reconstruction of tissue geometry

Segmentation labels for each tissue, whether processed manually or predicted, then underwent morphological closing with a five-voxel (cartilage) or three-voxel (bone) uniform kernel to remove segmentation artifacts before we reconstructed the surface using marching cubes (Lorensen and Cline, 1987). After viewing a subset of these raw surface reconstructions, we assumed all cartilage tissues consisted of singular connected volumes. We treated all but the largest enclosed volumes as segmentation artifacts, which we discarded. We then applied a decimation filter resulting in an 80% reduction in surface triangle density. The final step included nine iterations of Laplacian smoothing for all tissues. For every *bone* geometry, we applied the MeshFix algorithm to correct triangle intersections, singularities, or degenerate elements (Attene, 2010). To preserve physiological holes within *cartilage* tissues, we limited MeshFix to reversing inward-facing normals.

2.4 Meshing

For the tibia, femur, and patella bones, we created uniform triangular rigid body surface meshes using Voronoi clustering (Valette et al., 2008), with a target element size of 3 mm. For the remaining tissues, we ported an existing open-source cartilage meshing algorithm (Rodriguez-Vila et al., 2017) to the python programming language. The algorithm used a swept set of point origins and raytracing to place two matching rectangular grids along the bone-side and joint-side surfaces of cartilage reconstructions. We then connected these matching grids to form an initial set of ill-conditioned hexahedral elements, with a portion of the elements on the cartilage edges containing six nodes. We repaired these degenerate elements through the creation, deletion, or merging of nodes and edges. Once fully connected, the mesh underwent optimization to ensure every element had a non-negative scaled Jacobian (SJ). Individual elements then underwent an in-plane—not depth wise—subdivision to become four elements before undergoing an iterative optimization and smoothing process until every element's SJ was above 0.5. Finally, we subdivided the cartilage depth into multiple elements. Our parameter choices resulted in average element edge-length of approximately 1 mm, with cartilage depths divided into four linearly spaced elements.

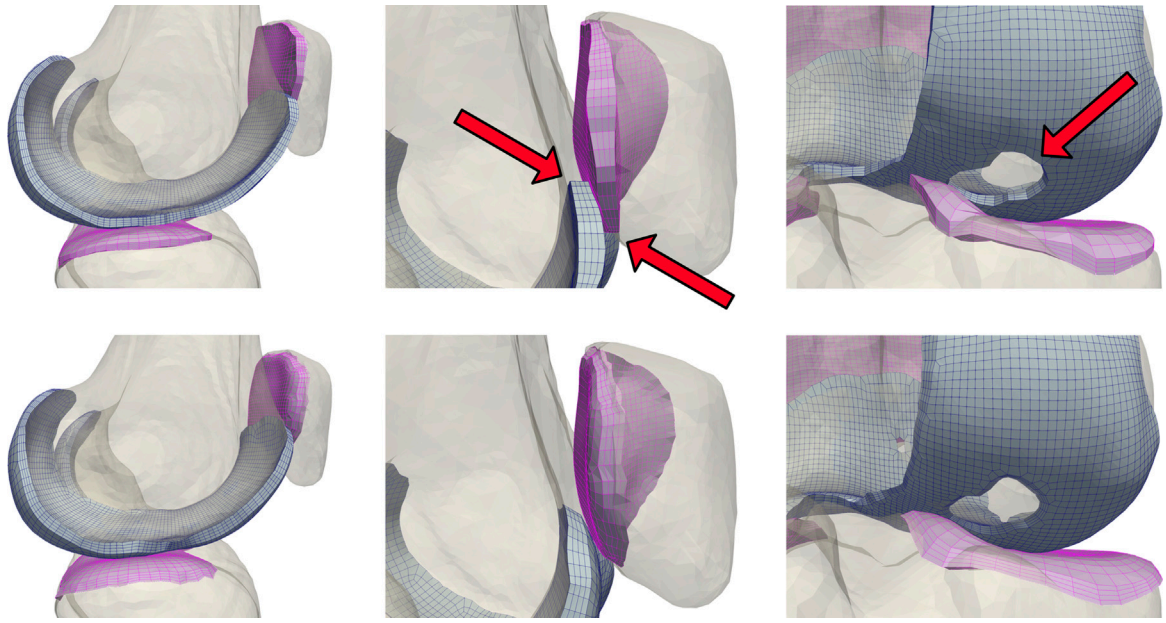

FIGURE 3
A comparison of unblended (top) and blended (bottom) cartilage profiles. Dynamic activities involving tangential motion of cartilage interfaces can result in the edges of articulating meshes catching on each other, causing simulation failures. This occurs most frequently near the trochlear groove of the patellofemoral joint, and in knees with significant cartilage loss in the tibiofemoral joint.

2.4.1 Hexahedral meshing algorithm modifications

Excluding a cartilage mesh blending step (detailed in Section 2.4.2 below), the bulk of our changes consisted of replacing low-level mathematical calculations with functionality built into 3D *Python* libraries, encapsulating novel logic into functions, and developing an object-oriented application point interface with unified helper methods allowing for simplified plotting and cell quality calculations during any step following creation of the ill-conditioned mesh. Making these changes allowed us to improve vectorization, locate and fix typographical errors resulting from repeated logic, and will facilitate future algorithm adaptation for other joints. We added patellar cartilage meshing by adapting the femoral cartilage algorithm. The initial tibial cartilage meshing algorithm based on raytracing an interior grid with radial sectors was prone to failure. Discarding back faces during a planar projection and basing placement of the interior grid on a *scaled* bounding box improved robustness. Meshing can still fail if a cartilage hole lies on the edge of the interior grid, so we added a fallback method using a rectilinear grid of rays bounded by the *unscaled* bounding box.

A primary failure mode of the original package was looping infinitely during the final mesh optimization, which we traced back to the misclassification of degenerate elements. We included additional controls to more accurately classify the configuration of six-node elements (*peaks*, *mirrors*, three element *stairs*, *steps* consisting of two elements, and single element internal *corners*), with each configuration treated separately to eliminate negative volumes or extreme skewed elements that resulted in an oscillating optimization solution. For example, we implemented logic confirming degenerate nodes were at the same topological indices when detecting step degenerates, which previously only checked if neighboring elements shared a single edge.

2.4.2 Cartilage mesh blending

Modeling cartilage as linearly subdivided brick elements results in a step interface with bones (Figure 3). These sharp corners can cause unresolvable impingement issues and unrealistic edge loading when modeling joint contact. As articulating surfaces transition from cartilage-bone to cartilage-cartilage contact, there is risk of simulation failure due to protruding nodes on the cartilage edge unable to resolve the excessive nodal forces and geometric constraints generated through contact between the corners of articulating meshes. Issues intensify when modeling subjects with significant cartilage degradation, as they frequently exhibit total cartilage loss near the trochlear groove of the patellofemoral joint, or holes within the tibiofemoral joint. To rectify this, we developed and incorporated a mesh blending step before the final depth-subdivision.

The blending algorithm operated on quadrilateral elements extracted from the *single-layer* hexahedral mesh surface. Smoothing the cartilage-bone transition required stretching

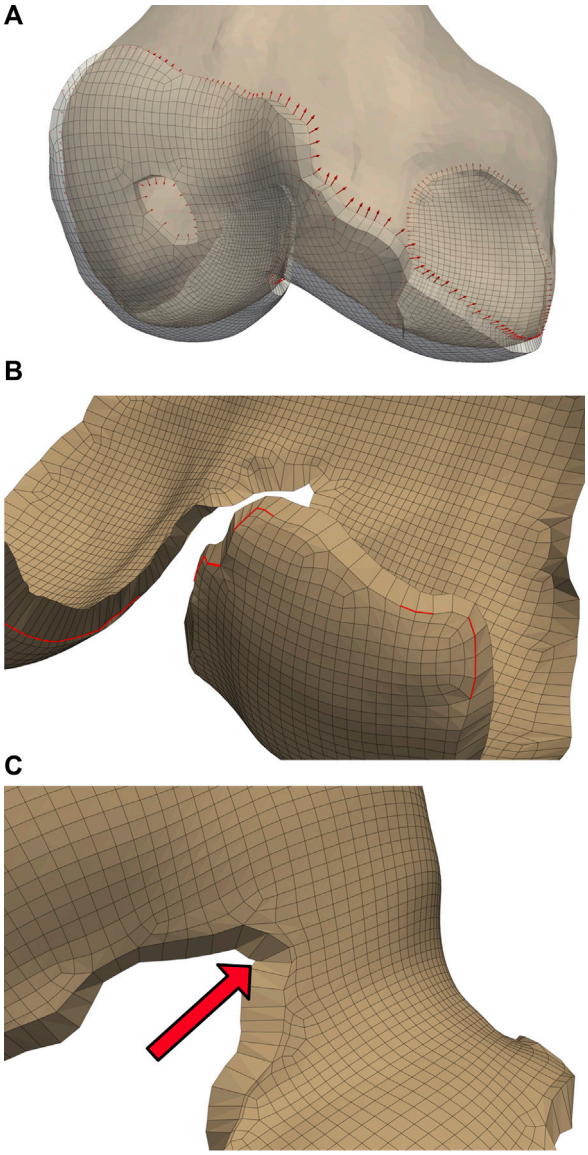

FIGURE 4
Initialized displacements for cartilage mesh blending. Vector lengths are based on cartilage depth at the edge, with 80% of the depth assigned to the bone-side nodes and the remaining 20% assigned to joint-side nodes **(A)**. Feature angles of the blended edge are required to be greater than 35°. The nodes attached to the red lines will have their displacement relaxed in 10% increments **(B)**. Element intersections caused by blending displacement, which occur frequently within cartilage holes and internal corners of the femoral cartilage. Savitsky-Golay filtering of the edge nodal location components can solve a case such as this **(C)**.

the edge nodes of the *bone-side* cartilage surface towards the exterior while compressing the corresponding nodes of the *joint-side* surface. We calculated the direction of these displacements using point normals of the mesh faces of the cartilage edges, then displaced the nodes until they created a 45° slope (Figure 4A). We weighted the bone-side nodes to perform 80% of the displacement. If possible, we attempted to translate the bone-side nodes to a paired bone mesh using a nearest element surface search between the bone elements and bone-side nodes of the cartilage mesh.

Some elements became skewed after displacement, which we corrected by iteratively reducing the bone-side nodal displacements until all joint-side edges attained a minimum feature angle of 35° (Figure 4B). We selected this feature angle through assessing a range of angles, and determining that this value resulted in a reasonable trade-off between sufficiently smooth interfaces, correcting for element skewness, and minimizing changes in cartilage surface area and computing time. Element intersections may appear along the edges of interior curves and small holes within the cartilage interior (Figure 4C), which we attempted to correct by smoothing the nodal locations of the edges with a 3rd degree Savitzky-Golay filter (Savitzky and Golay, 1964). If element intersections remained, we iteratively reduced the magnitude of our nodal displacements by 10%.

We applied independent Laplacian smoothing operations to the bone- and joint-side surfaces. We performed each smoothing operation iteratively, using an advancing front of quadrilateral faces beginning at the bone-side edge (Figure 5A). For each advance in the selection front, we decreased the number of smoothing iterations, resulting in a decrease of nodal displacements within the interior of the cartilage mesh. For the joint-side surface we stopped before elements skew, or when the blended feature angles reached a minimum of 30° (Figure 5C). For the bone-side surface, the front progressed from an element depth of two until five (Figure 5B), with the number of smoothing iterations halved for each advance. We empirically selected the initial number of smoothing iterations to be $\frac{550}{n_{surface}}(n_{surface} - n_{front})$, where $n_{surface}$ represented the number of quadrilateral faces present in the cartilage, and n_{front} was the selection subset. We required that interior elements had SJs exceeding 0.5 and blended element SJs remained positive.

2.4.3 Soft-tissue attachment locator

We mapped soft-tissue attachment sites from a manually segmented knee geometry based on MRI imaging with 160 manually segmented soft tissue attachment sites. We used this *template* mesh for the automatic selection of attachment sites for the Imorphics meshes. We registered input femoral meshes to the template using an iterative closest points algorithm (Chen and Medioni, 1992), with the resulting transformation applied to the remaining tissues. We applied a nearest neighbor search for each soft-tissue attachment site and nodal coordinates defining joint axes, before applying an inverse-transformation back to the original scaling and position (Ta, 2019; Malbouby et al., 2022).

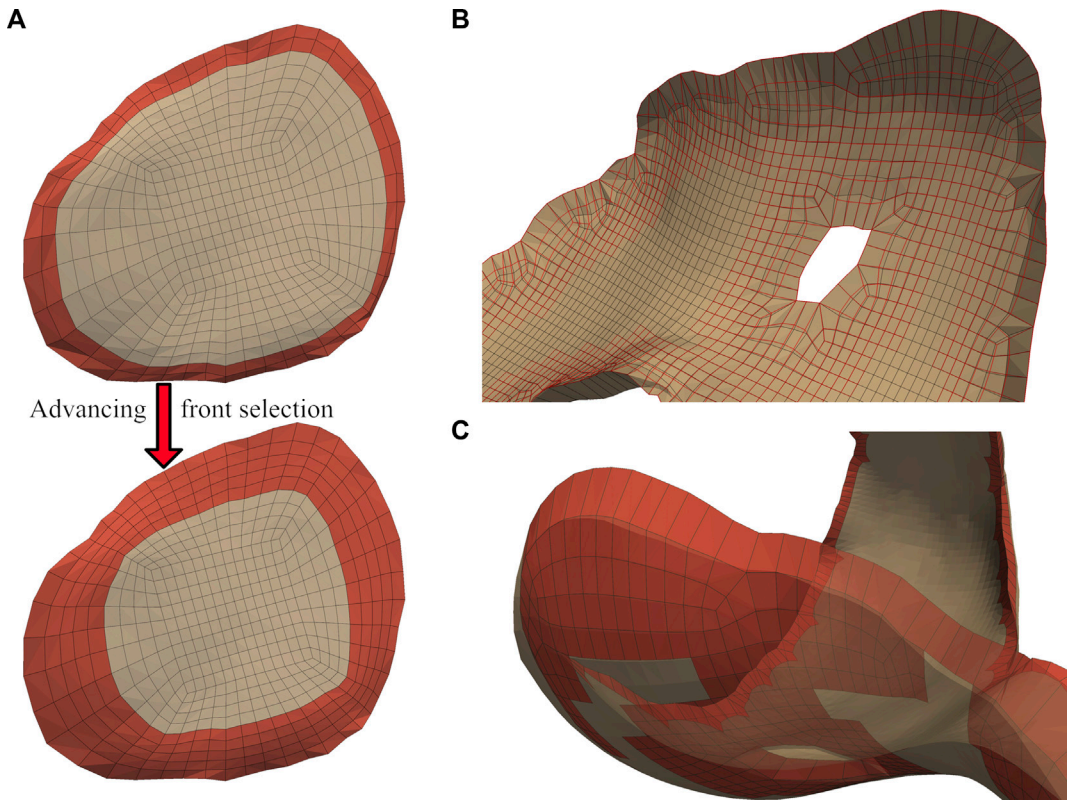

FIGURE 5
A graduated smoothing is performed using an advancing front of surface face selections **(A)**, independently for the joint- and bone- -side surface faces. The nodes on the cartilage edges are constrained while Laplacian smoothing iterations are reduced each time the front advances. The bone-side surface feature angles are now reduced to 30° **(B)**, while the joint side smoothing front advances once, but with a higher number of initial smoothing iterations **(C)**.

2.5 Knee flexion simulation

We adapted the knee flexion simulation from a previously published model of the implanted knee (Fitzpatrick and Rullkoetter, 2014, 2012; Gibbons et al., 2019), using the commercial FE solver, Abaqus/Explicit (Dassault Systèmes). Briefly, we applied knee loads and muscle forces through mechanical actuators, which we implemented using force- or moment-driven connector elements. We adopted ligament soft-tissue properties from a previously published study where passive laxity tests performed on a series of four cadaveric knees were used to calibrate reference strain and linear stiffness values of the major tibiofemoral ligaments (Harris et al., 2016). To create a 6-degree-of-freedom joint, we applied anterior-posterior force and internal-external torque to the femur, with medial-lateral translation free. We simulated knee flexion by balancing a vertical load applied at the hip with quadriceps and hamstring loads controlled by a proportional-integral controller implemented through a user subroutine. We derived flexion and joint loading profiles from data reported from five patients with telemetric knee implants (Heinlein et al., 2007; Kutzner et al., 2010). Due to the large number of simulations required, we excluded material deformation from cartilage representations–instead using linear pressure-overclosure contact definitions to compensate for rigid cartilage elements within the patellofemoral and tibiofemoral joint complexes (Halloran et al., 2005; Fitzpatrick et al., 2010; Hume et al., 2020).

3 Results

We used the original algorithm to analyze a subset of 23 knee reconstructions from the Imorphics dataset, with only six successfully meshing. After porting, implementing bugfixes, and adding additional degenerate element detection cases, our meshing algorithms successfully produced “watertight” bone and cartilage meshes with high-quality elements for all 176 image sequences, for both the manual and predicted segmentation maps (Figure 6). The average time to mesh eight tissues with cartilage blending was one min and 22 sec, with a maximum time

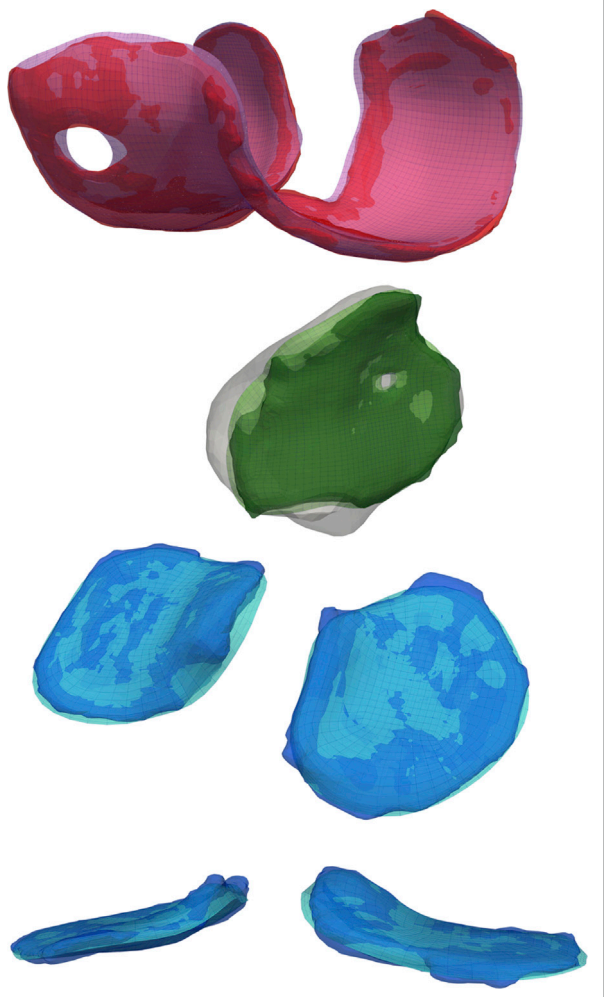

FIGURE 6
A comparison of the reconstructed geometry with triangular surface bone and hexahedral volume cartilage meshes. Blending the edges of the cartilage mesh will constrict holes and increase the planar surface, but the authors believe these negatives are offset by the reduction in joint dislocations during simulated activities.

of four min and nine sec. We performed these computations on an AMD Ryzen 5600X processor, using a parallel pool of three workers for bone meshing, followed by a pool of four workers meshing the four cartilage tissues.

Of the 704 total cartilage tissues that we meshed using manual segmentations, 87.4% resulted in blended meshes with every bone-side node fused to the bone surface. Of the 86 tissue meshes that failed to fuse the entire bone-side surface, 10 more were able to fuse using only the perimeter edge. The remaining 10.8% of all attempted geometries were blended without reference to the underlying bones. For the blended tissues, the five edge layers of elements altered by the algorithm saw average reductions in SJ qualities between 5.23% and 46.1%. The edge most layer saw the biggest decrease, from a mean SJ of 0.86 to 0.46. The remaining layers saw less than 25% reduction. Of the 352 tibial cartilage geometries, we needed to mesh 17 using a simplified grid (Table 1). Running each manually segmented simulation without cartilage blending resulted in 76.9% completing the flexion activity. Adding blending increased our success rate to 89%.

Test dataset DSC scores for the bones were each above 97%. Cartilage DSC scores for the patellar and lateral tibial cartilage were 79% and 77%, while the femoral and medial tibial cartilage resulted in scores of 84% each. Articular surface overlap and conformity between the predicted and manually derived cartilage meshes are shown in Figure 7; Figure 8. Nodal coverage of the predicted meshes was between 90% and 92% except for the lateral tibial cartilage, which had coverage of 85%. Kernel density estimates resulted in right-skewed distributions, with the patellar cartilage resulting in the highest median deviation of 0.39 mm and 75% of patellar deviations below 0.46 mm. The remaining cartilage meshes had median surface deviations of 0.23 mm or less, and 75% of their deviations were less than 0.27 mm. Maximum outlier deviations fell between 1.39 mm and 2.54 mm.

Simulations for the manual and predicted test datasets both succeeded 92% of the time, with independent failures leaving 24 matched comparisons between manual and predicted FE simulations. Simulated contact mechanics for those remaining resulted in mean normalized RMS differences were below 20% for both medial and lateral sides, and remained under 22% for the 75th percentile (Table 2). The worst case resulted in a medial contact pressure error of nearly half the min-max range, more than doubling the 75th percentile value. For the initial and final 15% of the flexion activity, predicted meshes tended to underestimate compressive pressure while overestimating contact area (Figure 9). Agreement throughout the middle 60% of the flexion cycle was excellent except for an overestimated medial contact pressure.

4 Discussion

Our first study objective was to develop automatic segmentation and meshing algorithms that would allow us to generate hundreds of working simulations in a fully automated fashion. We were able to create “watertight” triangular surface bone and high-quality hexahedral volume cartilage meshes for all 176 image sequences, both manual and predicted, in the Imorphics dataset. While 11% of our image sequences did not result in successful FE simulations, each of the failures exhibited excessive cartilage degradation resulting in bone contact which was not sufficiently captured in our current model definitions. This is a unique challenge when modeling osteoarthritic patients, as osteophytic bone spurs may increase the probability of deleterious bone-cartilage contact. However, a common mode

TABLE 1 Distribution of cartilage meshing fallback algorithms. If issues occur during the meshing process, features are turned off beginning with fusing bone-side cartilage nodes to the nearest bone surface, followed by a reduction in the nodal displacements during cartilage-to-bone blending. For the tibial cartilage, a simplified rectilinear grid can be used during raytracing, instead of a more complicated distribution based on sectors. Finally, a planar subdivision step may be performed earlier in the algorithm to better capture complicated cartilage edges, at the expense of speed.

	Count	Total	Percent (%)
Cartilage meshed successfully without fallbacks	615	704	87.4
Tibia cartilage meshed with simplified grid	17	352	5.40
Grid-based meshing required in-plane subdivision before raytracing	15	371	4.04
Interior bone-side surface nodes failed to fuse to bone surface	86	704	12.2
All bone-side nodes failed to fuse to bone surface	76	704	10.8

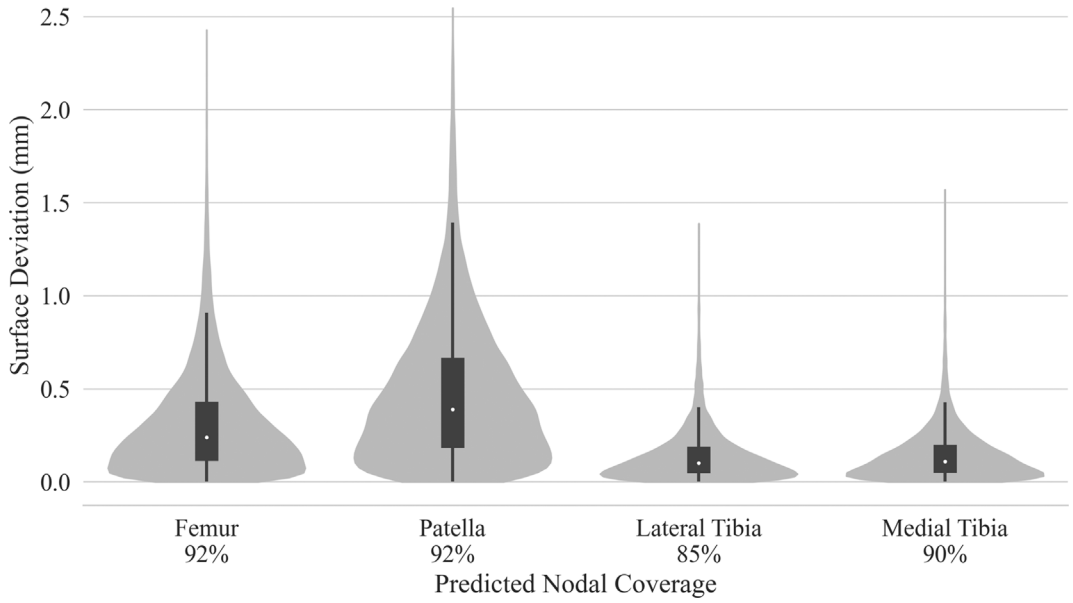

FIGURE 7
Kernel density estimated distributions of distance between predicted and manually segmented mesh surfaces, with box plots superimposed. Distances were traced from the nodes of the predicted mesh until intersection with element faces of the manual mesh. Nodal coverage denotes sample size determined by traced rays deviating no more than 20° from node normals at the base of each ray.

of failure is a sharp cartilage edge contacting the bone, causing excessive deformation and stress concentrations at the cartilage edge elements—exactly what our blending algorithm aims to correct. Adding the blending algorithm allowed an additional 21 simulations to run successfully, while only affecting five edgewise layers of elements. For our simulation parameters, we saw a 46% reduction in SJs for the first 0.5 mm of cartilage edge, which decayed to between 5% and 25% for the next 4 mm from the edge. However, in order to achieve a success rate closer to 100%, we must perform additional analysis and iteration of bone-cartilage contact definitions to determine a set of contact and meshing parameters that are optimally compatible with prominent osteophytes commonly present in the OA population.

Our next objective was to quantify the effect of segmentation labels generated by a CNN on downstream FE meshes. Articular surface conformities with sub-millimeter median deviations and a minimum of 85% and 92% surface overlap for the tibiofemoral and patellofemoral joints, respectively, are likely improvements over statistical shape modeling or mesh templating for aggregate population studies, which lack the subject-specificity of models developed from patient-specific imaging. However, we may require further improvement in algorithm accuracy before these

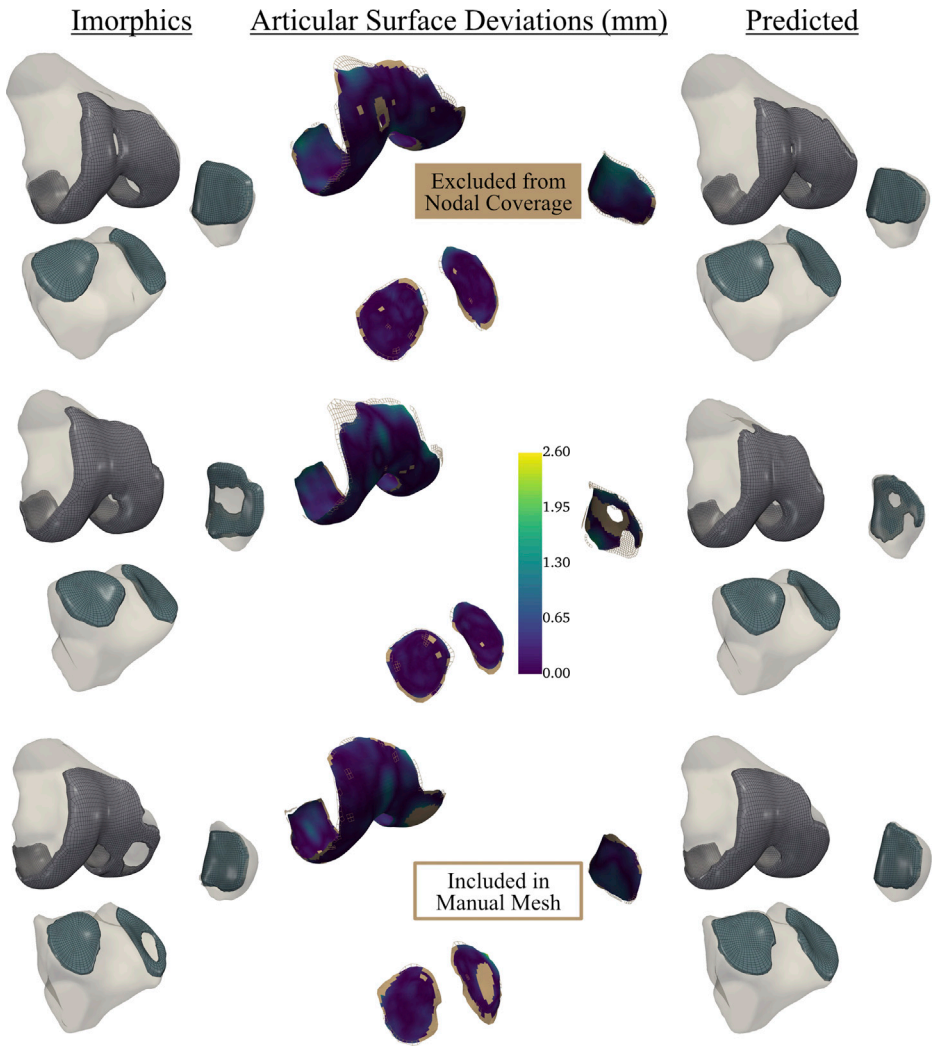

FIGURE 8
Articular surface deviations comparing representative meshes derived from the neural-network predicted segmentation labels, and the provided Imorphics labels from a reserved test dataset. Nodal coverage is represented by the scalar bar, while nodes within the solid tan region were excluded from distance calculations. This network tended to constrict cartilage holes, and would need fine-tuning before being used to study osteoarthritis. However, this also showcases the robustness of our automatic hexahedral meshing program, as each knee contained holes, of varying sizes, in one or more tissues.

data become clinically useful. While there are more sophisticated algorithms available, we implemented a relatively simple CNN, but that same simplicity makes it an accessible choice for applied researchers outside of computer science, using consumer hardware. Our test dataset cartilage DSC scores ranging from 77% to 84% leaves room for improvement, but our meshing and soft-tissue attachment algorithms handled resulting geometric differences without issue. However, surface deviations were found to be driven by nodal overlap; our CNN tended to shrink or fill cartilage holes when compared to the manual reconstructions, which resulted in surfaces around mismatched holes pulling away from each other following the optimization and blending steps. Mitigating this effect using more sophisticated models, such as those proposed by Ambellan et al. (2019), Gatti and Maly (2021), and Tack et al. (2018), will be critical for studying damaged tissue. Some researchers have shown that CNNs trained on osteoarthritic datasets improve when tested on healthy tissue (Gatti and Maly, 2021), so the effect may be less pronounced if our model was applied to healthy knees.

Our final objective was to quantify how predicted segmentation labels affect FE simulation joint mechanics results. Our data shows that 75% of simulation contact

TABLE 2 Contact area and pressure root-mean-squared error for tibial cartilage of the test dataset. Min-max normalized error terms are reported as percentages. Two of the predicted and an independent two from the manual sequences failed to finish the flexion activity, leaving 24 sequences for comparison.

	Contact area mean RMS error (mm^2)		Contact pressure RMS error (MPa)	
	Medial	**Lateral**	**Medial**	**Lateral**
Mean	43.9 (15.7%)	25.1 (9.94%)	4.71 (19.50%)	3.21 (13.7%)
Std. Dev	23.3 (7.75%)	13.6 (4.33%)	2.15 (9.52%)	1.35 (4.38%)
Minimum	15.0 (5.04%)	8.16 (5.59%)	1.79 (8.55%)	1.67 (8.55%)
25%	25.4 (9.74%)	13.5 (6.92%)	3.40 (12.7%)	2.27 (11.3%)
50%	36.0 (13.6%)	25.6 (8.12%)	4.29 (18.2%)	2.70 (12.4%)
75%	63.1 (20.7%)	29.2 (11.9%)	5.65 (21.6%)	3.98 (15.0%)
Max	88.3 (29.5%)	62.9 (21.1%)	11.1 (48.3%)	7.07 (23.5%)

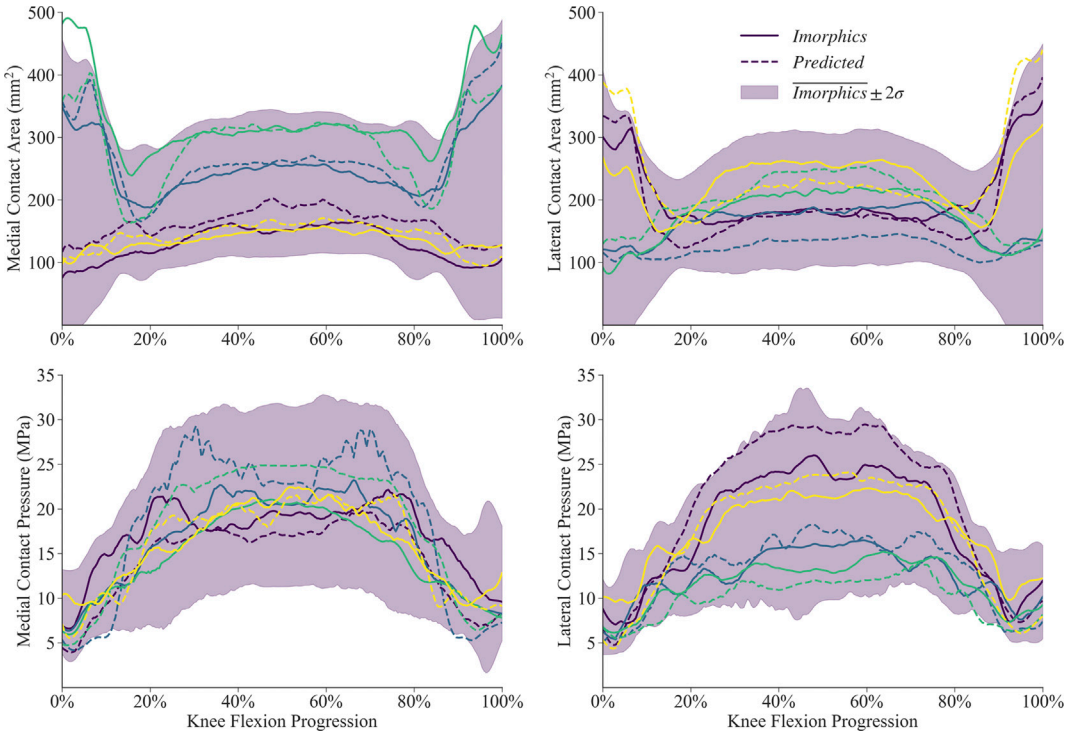

FIGURE 9
Contact mechanics data generated by 24 sets of segmentation labels provided with the Imorphics dataset and those predicted by a neural network. The predicted meshes tendsed to underestimate compressive pressure—and overestimate contact area—while the knee was nearly extended. Agreement throughout the middle 60% of the flexion cycle was excellent except for an overestimated medial contact pressure. Manual and predicted results for four representative simulations are shown for comparison.

pressure and area results deviate by less than 22%, and that most of the error occurs while the knee is extended. Our current CNN may not be suitable for studying contact mechanics during activities at lower flexion angles. Researchers should be mindful that errors introduced at the segmentation stage compound while traveling through the pipeline, altering soft-tissue attachments, for example.

While the primary focus of the current study was the development of an algorithm that could be used to generate robust finite element meshes for large-cohort populations, the finite element simulation that we have used to demonstrate the implementation of our algorithm is relatively simple, and as such, has a series of limitations and assumptions that should be noted. In order to run the

hundreds of simulations required for this analysis in a computationally efficient manner, we did not allow for material deformation of the cartilage tissues, instead using linear pressure-overclosure definitions to compensate for rigid cartilage representations (Halloran et al., 2005; Fitzpatrick et al., 2010; Hume et al., 2020). The computational cost of these rigid body simulations was an order of magnitude faster than their deformable counterparts. If cartilage stresses or strains are of interest to the user, a deformable cartilage representation would be necessary. However, this change to the finite element simulation is compatible with the segmentation and meshing workflow we have implemented. Similarly, our models did not include meniscal structures. Instead, we used the soft-tissue constraints of the tibiofemoral joint calibrated to match overall joint laxity measured in a cadaveric study—that is, researchers calibrated these ligament properties to compensate for the lack of a meniscus (Harris et al., 2016). Finally, we only examined contact mechanics of the tibiofemoral joint, which have historically been sensitive to geometry (Fitzpatrick et al., 2012, 2011; Navacchia et al., 2016; Gibbons et al., 2019). While this model provided us with numerical comparisons between the manual and automatic segmentations, additional experimental data is necessary to validate the resulting joint mechanics predictions. Additionally, further analysis is required to assess the sensitivity of joint kinematics, ligament mechanics, and joint loads to predicted labels and to quantify the effects of more sophisticated deep learning algorithms on FE simulation accuracy.

In combination with further advancements in deep learning, this framework represents a major advance in the study of natural knee biomechanics, and presents a feasible way to produce *population* sized finite element studies of the natural knee. The time required to produce quality hexahedral meshes has been reduced from a full workday of person-hours to 2 min. Additionally, we found that even the segmentation labels from our intermediate CNN models were useful during our bone segmentation process; manually correcting a percentage of suboptimal (DSC ~65%) segmentation labels proved much faster than starting from scratch. Future researchers should not underestimate the time savings made possible by even a simple predictive model, and semi-supervised methods make it possible to train such models with limited data (Burton et al., 2020).

We've designed our *alpha-build* framework such that it may be adapted to any laminar structure approximated by a planar or cylindrical surface. Few modifications are necessary for other "hinge" joints, and the hip joint would only require the addition of a spherical coordinate raytracing function. The pipeline presented here has potential to improve our statistical shape and function models of the knee joint by better capturing population-based variation through inclusion of large-volume patient datasets. Integrating this pipeline with longitudinal patient datasets like the Osteoarthritis Initiative allows us to develop libraries of patient-specific models to quantitatively investigate relationships between anatomy, joint loading and longitudinal joint degeneration.

Data availability statement

The raw data supporting the conclusions of this article will be made available by the authors, without undue reservation.

Ethics statement

Ethical review and approval was not required for the study on human participants in accordance with the local legislation and institutional requirements. Written informed consent for participation was not required for this study in accordance with the national legislation and the institutional requirements.

Author contributions

KG contributed to the design of the study, improved robustness of the CNN algorithm and ported to a single platform, developed the meshing algorithm, interpreted results and wrote the initial manuscript draft. VM developed the ligament attachment code, performed all finite element simulations and postprocessing of results, and contributed to writing of the manuscript. OA developed the initial version of the CNN. CF contributed to conception and design of the study, interpretation of results and editing of the manuscript.

Funding

This material is based upon work supported by the National Science Foundation under Grant No. 1944180 and National Science Foundation Graduate Research Fellowship under Grant No. 1946726, and the Center of Excellence in Biomedical Research through the Institutional Development Award (IDeA) from the National Institute of General Medical Sciences of the National Institutes of Health under Grant Nos. P20GM109095 and P20GM103408.

Acknowledgments

The authors would like to acknowledge the foundational work of Rodriguez-Vila et al. (2017), who graciously host an open source version of their software for download at https://im.engr.uconn.edu/downloads.php. Data and/or research tools used in the preparation of this manuscript were obtained and analyzed from the controlled access datasets distributed from the Osteoarthritis Initiative (OAI), a data repository housed within the NIMH Data Archive (NDA). OAI is a collaborative informatics system created by the National Institute of Mental Health and the National Institute of Arthritis, Musculoskeletal and Skin Diseases (NIAMS) to provide a worldwide resource to quicken the pace of biomarker identification, scientific investigation and OA drug development. Dataset identifier(s): 1200285; 1200816.

Conflict of interest

The authors declare that the research was conducted in the absence of any commercial or financial relationships that could be construed as a potential conflict of interest.

Publisher's note

All claims expressed in this article are solely those of the authors and do not necessarily represent those of their affiliated organizations, or those of the publisher, the editors and the reviewers. Any product that may be evaluated in this article, or claim that may be made by its manufacturer, is not guaranteed or endorsed by the publisher.

References

Almouahed, S., Hamitouche, C., Poignet, P., and Stindel, E. (2017). "Battery-free force sensor for instrumented knee implant," in Proceedings of the 2022 IEEE Healthcare Innovations and Point of Care Technologies (HI-POCT), Houston, TX, USA, 10-11 March 2022 (IEEE), 1–4. doi:10.1109/HIC.2017.8227570

Ambellan, F., Tack, A., Ehlke, M., and Zachow, S. (2019). Automated segmentation of knee bone and cartilage combining statistical shape knowledge and convolutional neural networks: Data from the Osteoarthritis Initiative. *Med. Image Anal.* 52, 109–118. doi:10.1016/j.media.2018.11.009

Attene, M. (2010). A lightweight approach to repairing digitized polygon meshes. *Vis. Comput.* 26, 1393–1406. doi:10.1007/s00371-010-0416-3

Baldwin, M. A., Langenderfer, J. E., Rullkoetter, P. J., and Laz, P. J. (2010). Development of subject-specific and statistical shape models of the knee using an efficient segmentation and mesh-morphing approach. *Comput. Methods Programs Biomed.* 97, 232–240. doi:10.1016/j.cmpb.2009.07.005

Bolcos, P. O., Mononen, M. E., Mohammadi, A., Ebrahimi, M., Tanaka, M. S., Samaan, M. A., et al. (2018). Comparison between kinetic and kinetic-kinematic driven knee joint finite element models. *Sci. Rep.* 8, 17351. doi:10.1038/s41598-018-35628-5

Bryan, R., Surya Mohan, P., Hopkins, A., Galloway, F., Taylor, M., and Nair, P. B. (2010). Statistical modelling of the whole human femur incorporating geometric and material properties. *Med. Eng. Phys.* 32, 57–65. doi:10.1016/j.medengphy.2009.10.008

Burton, W., Myers, C., and Rullkoetter, P. (2020). Semi-supervised learning for automatic segmentation of the knee from MRI with convolutional neural networks. *Comput. Methods Programs Biomed.* 189, 105328. doi:10.1016/j.cmpb.2020.105328

Chen, Y., and Medioni, G. (1992). Object modelling by registration of multiple range images. *Image Vis. comput.* 10, 145–155. doi:10.1016/0262-8856(92)90066-C

Colwell, C. W., Chen, P. C., and D'Lima, D. (2011). Extensor malalignment arising from femoral component malrotation in knee arthroplasty: Effect of rotating–bearing. *Clin. Biomech. (Bristol, Avon).* 26, 52–57. doi:10.1016/j.clinbiomech.2010.08.009

Cooper, R. J., Wilcox, R. K., and Jones, A. C. (2019). Finite element models of the tibiofemoral joint: A review of validation approaches and modelling challenges. *Med. Eng. Phys.* 74, 1–12. doi:10.1016/j.medengphy.2019.08.002

Cui, A., Li, H., Wang, D., Zhong, J., Chen, Y., and Lu, H. (2020). Global, regional prevalence, incidence and risk factors of knee osteoarthritis in population-based studies. *eClinicalMedicine* 29, 100587. doi:10.1016/j.eclinm.2020.100587

Dell'Isola, A., Allan, R., Smith, S. L., Marreiros, S. S. P., and Steultjens, M. (2016). Identification of clinical phenotypes in knee osteoarthritis: A systematic review of the literature. *BMC Musculoskelet. Disord.* 17, 425. doi:10.1186/s12891-016-1286-2

DesJardins, J. D., Walker, P. S., Haider, H., and Perry, J. (2000). The use of a force-controlled dynamic knee simulator to quantify the mechanical performance of total knee replacement designs during functional activity. *J. Biomechanics* 33, 1231–1242. doi:10.1016/S0021-9290(00)00094-4

Ebrahimkhani, S., Jaward, M. H., Cicuttini, F. M., Dharmaratne, A., Wang, Y., and de Herrera, A. G. S. (2020). A review on segmentation of knee articular cartilage: From conventional methods towards deep learning. *Artif. Intell. Med. (2017).* 106, 101851. doi:10.1016/j.artmed.2020.101851

Fitzpatrick, C. K., Baldwin, M. A., and Rullkoetter, P. J. (2010). Computationally efficient finite element evaluation of natural patellofemoral mechanics. *J. Biomech. Eng.* 132, 121013. doi:10.1115/1.4002854

Fitzpatrick, C. K., Baldwin, M. A., Rullkoetter, P. J., and Laz, P. J. (2011). Combined probabilistic and principal component analysis approach for multivariate sensitivity evaluation and application to implanted patellofemoral mechanics. *J. Biomech.* 44, 13–21. doi:10.1016/j.jbiomech.2010.08.016

Fitzpatrick, C. K., Clary, C. W., and Rullkoetter, P. J. (2012). The role of patient, surgical, and implant design variation in total knee replacement performance. *J. Biomech.* 45, 2092–2102. doi:10.1016/j.jbiomech.2012.05.035

Fitzpatrick, C. K., and Rullkoetter, P. J. (2014). Estimating total knee replacement joint load ratios from kinematics. *J. Biomech.* 47, 3003–3011. doi:10.1016/j.jbiomech.2014.07.002

Fitzpatrick, C. K., and Rullkoetter, P. J. (2012). Influence of patellofemoral articular geometry and material on mechanics of the unresurfaced patella. *J. Biomech.* 45, 1909–1915. doi:10.1016/j.jbiomech.2012.05.028

Gatti, A. A., and Maly, M. R. (2021). Automatic knee cartilage and bone segmentation using multi-stage convolutional neural networks: Data from the osteoarthritis initiative. *Magn. Reson. Mat. Phy.* 34, 859–875. doi:10.1007/s10334-021-00934-z

Gibbons, K. D., Clary, C. W., Rullkoetter, P. J., and Fitzpatrick, C. K. (2019). Development of a statistical shape-function model of the implanted knee for real-time prediction of joint mechanics. *J. Biomech.* 88, 55–63. doi:10.1016/j.jbiomech.2019.03.010

Gregson, J., Sheffer, A., and Zhang, E. (2011). All-Hex mesh generation via volumetric PolyCube deformation. *Comput. Graph. Forum* 30, 1407–1416. doi:10.1111/j.1467-8659.2011.02015.x

Guan, B., Lin, S., Wang, R., Zhou, F., Luo, X., and Zheng, Y. (2020). Voxel-based quadrilateral mesh generation from point cloud. *Multimed. Tools Appl.* 79, 20561–20578. doi:10.1007/s11042-020-08923-5

Halloran, J. P., Easley, S. K., Petrella, A. J., and Rullkoetter, P. J. (2005). Comparison of deformable and elastic foundation finite element simulations for predicting knee replacement mechanics. *J. Biomech. Eng.* 127 (5), 813–818. doi:10.1115/1.1992522

Harris, M. D., Cyr, A. J., Ali, A. A., Fitzpatrick, C. K., Rullkoetter, P. J., Maletsky, L. P., et al. (2016). A combined experimental and computational approach to subject-specific analysis of knee joint laxity. *J. Biomech. Eng.* 138 (8), 0810041–0810048. doi:10.1115/1.4033882

Heinlein, B., Graichen, F., Bender, A., Rohlmann, A., and Bergmann, G. (2007). Design, calibration and pre-clinical testing of an instrumented tibial tray. *J. Biomech.* 40, S4–S10. doi:10.1016/j.jbiomech.2007.02.014

Hoppe, H., DeRose, T., Duchamp, T., McDonald, J., and Stuetzle, W. (1993). "Mesh optimization," in Proceedings of the 20th Annual Conference on Computer

Graphics and Interactive Techniques, Anaheim ca, August 2 - 6, 1993 (Association for Computing Machinery), 19–26. doi:10.1145/166117.166119

Hume, D. R., Rullkoetter, P. J., and Shelburne, K. B. (2020). ReadySim : A computational framework for building explicit finite element musculoskeletal simulations directly from motion laboratory data. *Int. J. Numer. Method. Biomed. Eng.* 36, e3396. doi:10.1002/cnm.3396

Ito, Y., Shih, A. M., and Soni, B. K. (2009). Octree-based reasonable-quality hexahedral mesh generation using a new set of refinement templates. *Int. J. Numer. Methods Eng.* 77, 1809–1833. doi:10.1002/nme.2470

Ivester, J. C., Cyr, A. J., Harris, M. D., Kulis, M. J., Rullkoetter, P. J., and Shelburne, K. B. (2015). A reconfigurable high-speed stereo-radiography system for sub-millimeter measurement of *in vivo* joint kinematics. *J. Med. Device.* 9, 041009. doi:10.1115/1.4030778

Kutzner, I., Heinlein, B., Graichen, F., Bender, A., Rohlmann, A., Halder, A., et al. (2010). Loading of the knee joint during activities of daily living measured *in vivo* in five subjects. *J. Biomech.* 43, 2164–2173. doi:10.1016/j.jbiomech.2010.03.046

Lane, N. E., Brandt, K., Hawker, G., Peeva, E., Schreyer, E., Tsuji, W., et al. (2011). OARSI-FDA initiative: Defining the disease state of osteoarthritis. *Osteoarthr. Cartil.* 19, 478–482. doi:10.1016/j.joca.2010.09.013

Livesu, M., Pietroni, N., Puppo, E., Sheffer, A., and Cignoni, P. (2020). *LoopyCuts*: Practical feature-preserving block decomposition for strongly hex-dominant meshing. *ACM Trans. Graph.* 39 (4), 121:1–121:17. doi:10.1145/3386569.3392472

Livesu, M., Vining, N., Sheffer, A., Gregson, J., and Scateni, R. (2013). PolyCut: Monotone graph-cuts for PolyCube base-complex construction. *ACM Trans. Graph.* 32, 1–12. doi:10.1145/2508363.2508388

Lorensen, W. E., and Cline, H. E. (1987). Marching cubes: A high resolution 3D surface construction algorithm. *SIGGRAPH Comput. Graph.* 21, 163–169. doi:10.1145/37402.37422

Malbouby, V., Gibbons, K. D., and Fitzpatrick, C. K. (2022). "An automated pipeline to generate soft-tissue attachments of the knee for finite element simulations," in *ORS 2022 annual meeting paper No. 2250. Presented at the orthopaedic research society annual meetup* (Rosemont, Illinois: Orthopaedic Research Society), 1.

Maletsky, L. P., and Hillberry, B. M. (2005). Simulating dynamic activities using a five-Axis knee simulator. *J. Biomech. Eng.* 127, 123–133. doi:10.1115/1.1846070

National Institute of Arthritis and Musculoskeletal and Skin Diseases (NIAMS) (2004). *Osteoarthritis initiative (OAI): A knee Health study (clinical trial registration No. NCT00080171)*. Bethesda, Maryland: U. S national library of medicine.

Navacchia, A., Rullkoetter, P. J., Schütz, P., List, R. B., Fitzpatrick, C. K., and Shelburne, K. B. (2016). Subject-specific modeling of muscle force and knee contact in total knee arthroplasty: Modeling of knee contact in total knee arthroplasty. *J. Orthop. Res.* 34, 1576–1587. doi:10.1002/jor.23171

O'Neill, T. W., McCabe, P. S., and McBeth, J. (2018). Update on the epidemiology, risk factors and disease outcomes of osteoarthritis. *Best Pract. Res. Clin. Rheumatology* 32, 312–326. doi:10.1016/j.berh.2018.10.007

Paproki, A., Engstrom, C., Chandra, S. S., Neubert, A., Fripp, J., and Crozier, S. (2014). Automated segmentation and analysis of normal and osteoarthritic knee menisci from magnetic resonance images – data from the Osteoarthritis Initiative. *Osteoarthr. Cartil.* 22, 1259–1270. doi:10.1016/j.joca.2014.06.029

Paz, A., Orozco, G. A., Korhonen, R. K., García, J. J., and Mononen, M. E. (2021). Expediting finite element analyses for subject-specific studies of knee osteoarthritis: A literature review. *Appl. Sci. (Basel).* 11, 11440. doi:10.3390/app112311440

Ramos, A., and Simões, J. A. (2006). Tetrahedral versus hexahedral finite elements in numerical modelling of the proximal femur. *Med. Eng. Phys.* 28, 916–924. doi:10.1016/j.medengphy.2005.12.006

Rao, C., Fitzpatrick, C. K., Rullkoetter, P. J., Maletsky, L. P., Kim, R. H., and Laz, P. J. (2013). A statistical finite element model of the knee accounting for shape and alignment variability. *Med. Eng. Phys.* 35, 1450–1456. doi:10.1016/j.medengphy.2013.03.021

Rodriguez-Vila, B., Sánchez-González, P., Oropesa, I., Gomez, E. J., and Pierce, D. M. (2017). Automated hexahedral meshing of knee cartilage structures – application to data from the osteoarthritis initiative. *Comput. Methods Biomech. Biomed. Engin.* 20, 1543–1553. doi:10.1080/10255842.2017.1383984

Ronneberger, O., Fischer, P., and Brox, T., 2015. U-Net: Convolutional networks for biomedical image segmentation. ArXiv150504597 Cs.

Savitzky, A., and Golay, M. J. E. (1964). Smoothing and differentiation of data by simplified least squares procedures. *Anal. Chem.* 36, 1627–1639. doi:10.1021/ac60214a047

Schroeder, W., Martin, K., and Lorensen, B. (2006). *The visualization toolkit: An object-oriented approach to 3D graphics*. Clifton Park, NY: Kitware.

Sullivan, C. B., and Kaszynski, A. A. (2019). PyVista: 3D plotting and mesh analysis through a streamlined interface for the visualization toolkit (VTK). *J. Open Source Softw.* 4, 1450. doi:10.21105/joss.01450

Ta, M. (2019). *Development and implementation of a computational surgical planning model for pre-operative planning and post-operative assessment and analysis of total hip arthroplasty*. United States: The university of tennessee.

Tack, A., Mukhopadhyay, A., and Zachow, S. (2018). Knee menisci segmentation using convolutional neural networks: Data from the osteoarthritis initiative. *Osteoarthr. Cartil.* 26, 680–688. doi:10.1016/j.joca.2018.02.907

Tadepalli, S. C., Erdemir, A., and Cavanagh, P. R. (2011). Comparison of hexahedral and tetrahedral elements in finite element analysis of the foot and footwear. *J. Biomech.* 44, 2337–2343. doi:10.1016/j.jbiomech.2011.05.006

Taha, A. A., and Hanbury, A. (2015). Metrics for evaluating 3D medical image segmentation: Analysis, selection, and tool. *BMC Med. Imaging* 15, 29. doi:10.1186/s12880-015-0068-x

Torry, M. R., Shelburne, K. B., Peterson, D. S., Giphart, J. E., Krong, J. P., Myers, C., et al. (2011). Knee kinematic profiles during drop landings: A biplane fluoroscopy study. *Med. Sci. Sports Exerc.* 43, 533–541. doi:10.1249/MSS.0b013e3181f1e491

Valette, S., Chassery, J. M., and Prost, R. (2008). Generic remeshing of 3D triangular meshes with metric-dependent discrete voronoi diagrams. *IEEE Trans. Vis. Comput. Graph.* 14, 369–381. doi:10.1109/TVCG.2007.70430

Varadarajan, K. M., Harry, R. E., Johnson, T., and Li, G. (2009). Can *in vitro* systems capture the characteristic differences between the flexion–extension kinematics of the healthy and TKA knee? *Med. Eng. Phys.* 31, 899–906. doi:10.1016/j.medengphy.2009.06.005

Wang, H., Koff, M. F., Potter, H. G., Warren, R. F., Rodeo, S. A., and Maher, S. A. (2015). An MRI-compatible loading device to assess knee joint cartilage deformation: Effect of preloading and inter-test repeatability. *J. Biomech.* 48, 2934–2940. doi:10.1016/j.jbiomech.2015.08.006

Zhou, Q.-Y., Park, J., and Koltun, V., 2018. Open3D: A modern library for 3D data processing, ArXiv 1801.09847.

frontiers | Frontiers in Bioengineering and Biotechnology

TYPE Original Research
PUBLISHED 12 January 2023
DOI 10.3389/fbioe.2022.1078800

OPEN ACCESS

EDITED BY
Eiji Tanaka,
Tokushima University, Japan

REVIEWED BY
Uwe Wolfram,
Heriot-Watt University, United Kingdom
Josh Williams contributed to the review of Dr. Uwe Wolfram
María Jesús Lamela Rey,
University of Oviedo, Spain

*CORRESPONDENCE
Shireen Elhabian,
shireen@sci.utah.edu

SPECIALTY SECTION
This article was submitted to Biomechanics, a section of the journal Frontiers in Bioengineering and Biotechnology

RECEIVED 24 October 2022
ACCEPTED 28 December 2022
PUBLISHED 12 January 2023

CITATION
Iyer K, Morris A, Zenger B, Karanth K, Khan N, Orkild BA, Korshak O and Elhabian S (2023), Statistical shape modeling of multi-organ anatomies with shared boundaries.
Front. Bioeng. Biotechnol. 10:1078800.
doi: 10.3389/fbioe.2022.1078800

Statistical shape modeling of multi-organ anatomies with shared boundaries

Krithika Iyer[1,2], Alan Morris[2], Brian Zenger[2,3], Karthik Karanth[1,2], Nawazish Khan[1,2], Benjamin A. Orkild[2,4], Oleksandre Korshak[1,2] and Shireen Elhabian[1,2]*

[1]University of Utah, School of Computing, Salt Lake City, UT, United States, [2]University of Utah, Scientific Computing and Imaging Institute, Salt Lake City, UT, United States, [3]University of Utah School of Medicine, Salt Lake City, UT, United States, [4]University of Utah, Department of Biomedical Engineering, Salt Lake City, UT, United States

Introduction: Statistical shape modeling (SSM) is a valuable and powerful tool to generate a detailed representation of complex anatomy that enables quantitative analysis of shapes and their variations. SSM applies mathematics, statistics, and computing to parse the shape into some quantitative representation (such as correspondence points or landmarks) which can be used to study the covariance patterns of the shapes and answer various questions about the anatomical variations across the population. Complex anatomical structures have many diverse parts with varying interactions or intricate architecture. For example, the heart is a four-chambered organ with several shared boundaries between chambers. Subtle shape changes within the shared boundaries of the heart can indicate potential pathologic changes such as right ventricular overload. Early detection and robust quantification could provide insight into ideal treatment techniques and intervention timing. However, existing SSM methods do not explicitly handle shared boundaries which aid in a better understanding of the anatomy of interest. If shared boundaries are not explicitly modeled, it restricts the capability of the shape model to identify the pathological shape changes occurring at the shared boundary. Hence, this paper presents a general and flexible data-driven approach for building statistical shape models of multi-organ anatomies with shared boundaries that explicitly model contact surfaces.

Methods: This work focuses on particle-based shape modeling (PSM), a state-of-art SSM approach for building shape models by optimizing the position of correspondence particles. The proposed PSM strategy for handling shared boundaries entails (a) detecting and extracting the shared boundary surface and contour (outline of the surface mesh/isoline) of the meshes of the two organs, (b) followed by a formulation for a correspondence-based optimization algorithm to build a multi-organ anatomy statistical shape model that captures morphological and alignment changes of individual organs and their shared boundary surfaces throughout the population.

Results: We demonstrate the shared boundary pipeline using a toy dataset of parameterized shapes and a clinical dataset of the biventricular heart models. The shared boundary model for the cardiac biventricular data achieves consistent parameterization of the shared surface (interventricular septum) and identifies the curvature of the interventricular septum as pathological shape differences.

KEYWORDS

statistical shape modeling, biventricular cardiac MRI, particle-based shape modeling, interventricular septum, shared boundaries

1 Introduction

It has long been recognized in the anatomical sciences that the human body exhibits various morphological patterns and configurations, referred to as *anatomical variation*. Variations are prevalent throughout the body and may cause or be a factor resulting in a significant medical condition. To carry out a wide range of surgical and other medical procedures and therapeutic modalities, it is essential to have a thorough understanding of natural anatomical variation (Smith, 2021). Primitively, the morphometric variations of anatomies were commonly reported through observational studies that inspect large numbers of cadavers, and medical images (Alraddadi, 2021). By permitting in-depth, non-invasive investigation of the human body, recent advancements in medical imaging, such as Magnetic Resonance Imaging (MRI) and computed tomography (CT) scans, have significantly increased the understanding of the complexity of human anatomy. Owing to the growing interest in studying anatomical variations, statistical shape modeling (SSM) has emerged as an essential computational tool that discovers significant shape parameters directly from medical data (such as MRI and CT scans) that can fully quantitatively describe complex anatomy in the context of a population.

Statistical shape models are used to perform wide range of tasks in biomedical research ranging from visualizing organs (Orkild et al., 2022), bones (Lenz et al., 2021), and tumors (Krol et al., 2013), to aiding surgical planning (Borghi et al., 2020), monitoring disease progression (Uetani et al., 2015; Faber et al., 2020), and implant design (Goparaju et al., 2022). Shapes can be represented using an implicit (deformation fields (Durrleman et al., 2014), level set methods (Samson et al., 2000)) or explicit (set of ordered landmarks/points) representation. For explicit representations, points of the same anatomical position must be established consistently across shape populations to enable shape comparisons and obtain population-level shape statistics in an ensemble of shapes. These points are called *correspondences*. Explicit parameterization, such as correspondence points, is one of the most popular techniques used to represent shapes because of their simplicity and ability to represent multiple objects easily (Cerrolaza et al., 2019). Hence, in this work, we focus on point distribution models (PDM), which are a dense set of correspondences for shape representation. Multiple methods for correspondence generation have been proposed, which include non-optimized landmark estimation, parametric and non-parametric correspondence optimization. Non-optimized methods entail manually annotating the reference shape and warping the annotated landmarks on the population data using image-based or shape-based registration (McInerney and Terzopoulos, 1996; Paulsen et al., 2002; Heitz et al., 2005). Such non-optimized methods employ hard surface constraints to distribute points on a shape. Parametric methods use fixed geometrical basis (e.g., spheres (Styner et al., 2006)) to parameterize objects and generate correspondences. Correspondence models obtained using manual or parametric techniques are not optimal and can be incapable of handling complex shapes as the expressivity of the models is limited by choice of the fixed geometrical basis or template. On the other hand, non-parametric automatic methods provide a robust and general framework as they generate PDMs without relying on a specific geometric basis. Methods that follow a group-wise non-parametric approach find the correspondence by considering the variability of the entire cohort in the optimization process (e.g., particle-based optimization (Cates et al., 2017) and Minimum Description Length - MDL (Davies, 2002)).

Traditional SSM methods started by creating single-organ anatomy models particular to an organ or disease. However, the human body comprises intricate organs and systems that are physically, functionally, and spatially interrelated (Sanfilippo et al., 1990; Cates et al., 2014; Marrouche et al., 2014). For example, the hip joint is a ball and socket joint, with articular cartilage covering the articulating surfaces of the femur and pelvis. Similarly, the sacroiliac joint is a diarthrodial auricular joint between the sacrum and the ilium that allows bipedal movement. Due to the nature of these joints, subject-specific bone and cartilage anatomy drive the contact mechanics of the joint. Even subtle variations in anatomy may result in abnormal cartilage contact mechanics and lead to osteoarthritis (Dreyfuss et al., 2004; Andriacchi et al., 2009). Simultaneous quantification of the shape of the cartilage surface and the shared subchondral bone surface may help elucidate the joint's complex, dynamic articulation and diagnose biomechanical pathologies (Li et al., 2013; Jesse et al., 2017; Postacchini et al., 2017). Another example of interconnected anatomy is the heart, a four-chambered organ with several shared boundaries between chambers. Coordinated and efficient contraction of the chambers of the heart is necessary to adequately perfuse end organs throughout the body. Subtle shape changes within these shared boundaries of the heart can indicate potential pathological changes that lead to uncoordinated contraction and poor end-organ perfusion. Thorough examination and understanding of various interconnected organ systems are paramount to diagnosing and providing prompt therapeutic support (Bartsch et al., 2015). Hence, the attention of recent computational anatomy research has shifted from single-organ to multi-organ models (Cerrolaza et al., 2019). Multi-organ shape models perform joint statistical shape analysis to quantify meaningful shape variations and contextual information when studying the group differences and identifying the shape differences occurring due to a particular pathology affecting multiple interacting organs.

The group-wise SSM approaches mentioned previously have been extended to model multi-organ anatomies. These approaches either parameterize each object separately, sacrificing anatomical integrity (Cerrolaza et al., 2019), or minimize the combined cost function to generate correspondences assuming a global statistical model (Cates et al., 2008; Durrleman et al., 2014). However, these multi-organ models often fail to incorporate nuanced interactions such as shared surfaces (cartilage of the hip joint or the sacroiliac joint or interventricular septum of the heart) between multiple anatomies that can reveal critical features that might not be observable when the individual organs are modeled independently.

To address this issue, we propose a new shape modeling workflow that entails a method for extracting shared boundary surfaces and a correspondence-based optimization scheme to parameterize multi-organ anatomies and their shared surfaces consistently. We demonstrate the entire workflow using a cardiac biventricular

dataset, where we model the right ventricle (RV), left ventricle wall (LVW), and interventricular septum (IVS). We build upon the group-wise, non-parametric particle-based optimization method proposed by Cates et al., (Cates et al., 2007; Cates et al., 2008; Cates et al., 2017), to generate PDM and modify the framework to support multi-organ anatomies with shared boundaries.

The preliminary results of this work have been published in a workshop paper (Iyer et al., 2022). Here we significantly expand this work as follows.

1. Detailed experiments to convey the proof-of-concept with a synthetically generated parameterized set of shapes (the peanut dataset).
2. Study the necessity and effectiveness of modeling the shared boundary by comparing the modes of variations and group differences inferred using the shared boundary model of the biventricular anatomy with multi-organ shape models without explicitly shared boundary parameterization.
3. Perform multi-level analysis for the multi-organ shape models to disentangle pose from shape variations.
4. Perform ablation experiments to study the effect of class imbalance on the shape model generation process.

2 Methods

With a PDM, a shape can be represented as a vector that contains the coordinates of all of its surface correspondences. This concept can be broadened to encompass an ensemble of shapes, allowing for the representation of all shapes in a high-dimensional vector space, the shape space, and aiding in the investigation of how shapes are distributed to identify geometric variation patterns between the structures of interest. Statistical shape models are, in their most basic form, concise mathematical representations of objects that successfully parameterize every shape in the shape space. Herein we leverage the particle-based shape modeling (PSM) approach (Cates et al., 2007; Cates et al., 2017) for automatically constructing PDMs by optimizing point (or particle) distributions over a cohort of shapes using an entropy-based optimization method.

There are two essential considerations for modeling interconnected anatomical structures with surface openings and shared boundaries. First, it is necessary to explicitly characterize the statistics of the exterior (contour) and the interior of the shared surface to build statistical shape models that are aware of the interactions of the organs. This requires a consistent point distribution on the shared boundary across the multi-organ anatomies. To meet these needs, we develop methods for detecting and extracting shared boundaries and their edges (i.e., contour information) from multi-organ anatomies (see Section 2.2). Second, we need to optimize a PDM that includes joint statistics of the multi-organ anatomies, shared boundary interior, and contour. The PSM method proposed by Cates et al., which forms the foundation of our proposed method, uses a system of interacting particles with mutually repelling forces that learn the most compact statistical descriptors of the anatomy (Cates et al., 2008; Cates et al., 2017). For consistent parameterization on the shared boundary, we modify the surface sampling objective of the PSM method to accommodate the interaction between the anatomies and the shared surface. A brief overview of the PSM entropy optimization method for single anatomy is provided in Section 2.1 and the proposed surface cost function modifications for multi-organ anatomies with shared boundary surfaces is provided in Section 2.3.

2.1 Background: Particle-based shape modeling (PSM)

PDMs offer a framework for quantifying statistical relations between several factors representing the morphology of anatomy (Cootes et al., 1995). Using principal component analysis (PCA) on PDMs, it is possible to quantify population-level morphological variations. Therefore, an anatomical mapping across all anatomical (shape) samples in the given cohort should be established to obtain meaningful statistical shape variations. PSM offers a data-driven approach to establishing such mapping by establishing dense surface correspondences without needing an initial atlas or template. PSM learns the shape parameters by optimizing the position of a system of interacting particles such that the shape model can completely describe the variability of the population using the most compact statistical model that still preserves geometrical accuracy. In this section, we briefly describe the PSM method proposed by Cates et al., (Cates et al., 2007; Cates et al., 2008), that will be later modified in Section 2.3 to capture meaningful and consistent shape models for multi-organ anatomies with shared boundaries.

Consider a cohort of shapes $\mathcal{S} = \{\mathbf{z}_1, \mathbf{z}_2, \ldots, \mathbf{z}_N\}$ of N surfaces, each with its set of M corresponding particles $\mathbf{z}_n = [\mathbf{x}_1, \mathbf{x}_2, \ldots, \mathbf{x}_M] \in \mathbb{R}^{dM}$ where each particle $\mathbf{x}_m \in \mathbb{R}^d$ lives in d–dimensional Cartesian (i.e., configuration) space. This work uses surface meshes where $d = 3$. The ordering of the particles implies correspondence among shapes. Each correspondence particle is constrained to lie on the shape's surface. Collectively, the set of M particles is known as the *configuration*, and the space of all possible configurations is known as the *configuration space*. The particle positions are samples (i.e., realizations) of a random variable $\mathbf{X} \in \mathbb{R}^d$ in the configuration space with an associated probability distribution function (PDF) $p\ (\mathbf{X} = \mathbf{x})$. Each configuration of M particles can be mapped to a single point in dM–dimensional *shape space* by concatenating the correspondence coordinate positions into a single vector $\mathbf{z}_n$. The vector $\mathbf{z}_n$ is modeled as an instance of random variable $\mathbf{Z}$ in the shape space with PDF $p\ (\mathbf{Z} = \mathbf{z})$ assuming shapes are Gaussian distributed in the shape space, i.e., $\mathbf{Z} \sim \mathcal{N}(\boldsymbol{\mu}, \boldsymbol{\Sigma})$. The optimization proposed by Cates et al., (Cates et al., 2007; Cates et al., 2017), to establish correspondence minimizes the energy function

$$Q = H(\mathbf{Z}) - \sum_{n=1}^{N} H(\mathbf{X}_n) \tag{1}$$

where H is an estimation of differential entropy. The differential entropy of $p(\mathbf{X})$ is given as

$$H(\mathbf{X}) = -\int_S p(\mathbf{X}) \log p(\mathbf{X}) dx = -E\{\log p(\mathbf{X})\} \approx -\frac{1}{M} \sum_{m=1}^{M} \log p(\mathbf{x}_m) \tag{2}$$

where $H(\mathbf{X})$ is by calculating by estimating the density function $p(\mathbf{X})$ using a nonparametric, Parzen windowing estimation method with the help of the particles. The entropy in the shape space for the Gaussian

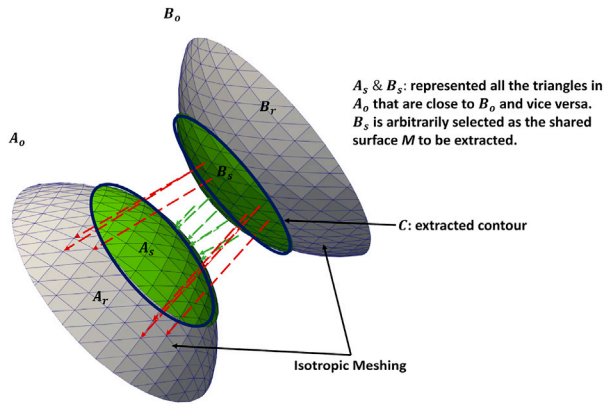

FIGURE 1
Extracting shared boundary between two meshes. The regions in green have Euclidean distances that fall within the threshold and are extracted as a shared boundary as per step 2. The green arrows show the distances within the threshold for the vertices included in the shared boundary. The red arrows show distances greater than the threshold for the vertices excluded from the shared boundary. The contour is extracted from the green region as per step 4. Note: the meshes are farther apart, and the threshold is larger for visualization purposes.

distribution is calculated as $H(\mathbf{Z}) = \frac{1}{2}\log|\mathbf{\Sigma}|$. More details regarding entropy terms can be found in (Cates et al., 2007; Cates et al., 2017). Gradient descent is used to minimize the cost function Q. Minimization of the first term in Q from Eq 1 produces a compact distribution of samples in shape space and encourages particles to be in correspondence across shapes. The second term seeks uniformly-distributed correspondence positions on the shape surfaces for a geometrically accurate shape representation (Cates et al., 2007; Cates et al., 2017). The negative gradient $-\frac{\partial H(Z)}{\partial Z}$ provides an update vector for the entire particle system, which is computed once per iteration, i.e., assuming lagging shape statistics for optimization stability. The individual shape-based updates $\frac{\partial H(X_n)}{\partial X_n}$ are combined with the negative gradient term to provide the update for each particle. Further details regarding the optimization and gradient updates can be found in (Cates et al., 2007; Cates et al., 2017).

A common coordinate system must be used to perform statistical analysis of the PDMs. Hence, the PDMs are built by factoring out global scaling, rotation, and translation. Typically the input shape data (volume segmentations or surface meshes) are aligned as a pre-processing step using iterative closed point alignment (Arun et al., 1987; Besl and McKay, 1992) that registers the shapes to an unbiased coordinate system by iteratively minimizing the pairwise least squares difference between the individual shapes and a reference shape. Once the similarity transformations have been removed, the statistical shape model can be easily constructed and analyzed.

2.2 Shared boundary extraction

To demonstrate the shared boundary extraction pipeline, consider two adjoining organs A and B, with a shared boundary (Figure 1). The steps for shared boundary extraction entail the following.

1. **Isotropic Explicit Re-meshing:** This generates a new mesh triangulation that conforms to the original data but contains more uniformly sized triangles. Re-meshing improves the quality of the mesh while preserving the original geometrical features. Re-meshing also has the benefit of ensuring equivalent average edge lengths across the two shapes, which is useful in ensuing steps (Valette et al., 2008).
2. **Extracting Shared Boundary:** In this step, we pass the two adjacent organs to the extraction tool that then outputs three new shapes, two of which correspond to the original shapes (without the shared boundary surface) and one for the shared boundary. To look into the overview of the algorithmic steps involved in the extraction tool, let us designate the original meshes of the adjoining organs as A_o and B_o (Figures 2A, B) then:

a. Find all the triangles in A_o that are close to B_o and construct a mesh with these triangles called A_s. A triangle with vertices (v_0, v_1, v_2) is considered close to another mesh if the shortest Euclidean distance between all three vertices and the other mesh is less than a specific threshold. The threshold must be experimentally tuned for the data to ensure the extracted shared surfaces are clinically relevant.
b. We similarly find all the triangles in B_o that are close to A_o and designate this mesh as B_s.
c. Find the remainder of the mesh in A_o after removing the triangles in A_s and designate this as A_r. Similarly, we designate the remainder of the mesh in B_o after removing the triangles in B_s as B_r.
d. Since, $A_s = B_s$, we arbitrarily designate B_s as the shared surface M
e. Copy all the points on the boundary loop of A_r to the boundary loop of M and return three new shapes A_r, M, and B_r (Figure 2C).

3. **Laplacian Smoothing:** At this point, the resulting triangulation typically contains jagged edges. We apply Laplacian smoothing to correct for this (Field, 1988). Laplacian smoothing reduces noisy edges/artifacts found on the mesh surface with minimal changes to its shape. This results in cells with better shapes and evenly distributed vertices.
4. **Extract Contour:** The boundary loop of the shared surface M is computed using LibIGL *boundary_loop* tool (Jacobson and Panozzo, 2018) and designate this contour as C (Figure 2D).

The input consisting of two adjoining organs A_o and B_o with a shared surface has been converted into input with four separate parts, the organs A_r and B_r, the shared surface M, and the contour C using the pipeline (Figure 2D; Figure 1).

2.3 Particle-based shape modeling with shared boundaries

A shape model built for multi-organ anatomies with shared boundaries requires a shape model that faithfully captures the joint statistics of all the interacting organs while consistently representing the individual organs. In order to capture the joint statistics of the multi-organ system, particle-based optimization should be capable of handling multi-organ anatomies. The optimization set up in Eq 1 was extended for multiple organs in (Cates et al., 2008). From the PSM formulation for single anatomies mentioned in the Section 2.1, it is important to note that $p(\mathbf{x}_m)$ in Eq 2 was estimated from the particle position using non-parametric kernel density estimation method (Cates et al., 2007; Cates et al., 2017). This results in a set of points on the surface that repel each other with Gaussian-weighted forces.

10.3389/fbioe.2022.1078800

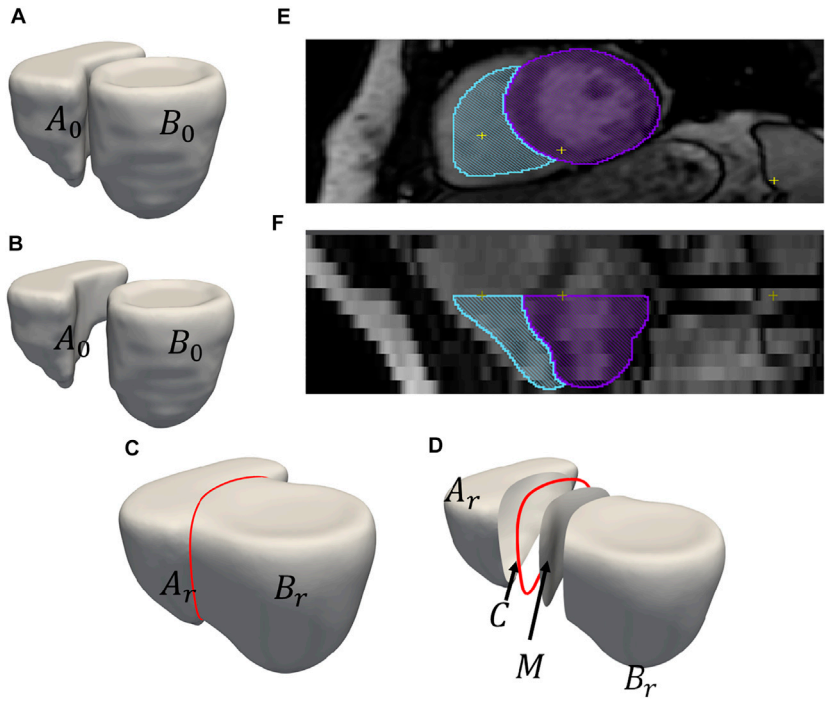

FIGURE 2
An example of output obtained after shared boundary extraction. Meshes representing **(A)** RV and LVW show that they have a shared boundary surface, and **(B)** RV and LVW meshes are pried apart. The meshes and contour obtained after shared boundary extraction **(C)** RV, LVW, shared surface and contour **(D)** all outputs pried apart for visualization. The red color indicates the contour. The image shows 2D slices of the endocardial segmentation for the RV (blue) and epicardial segmentation for the LV (violet) at end-diastole in the **(E)** axial view and **(F)** coronal view.

For multi-organ anatomy, the optimization is extended so that if one organ has a distinct unconnected surface, the spatial interactions between particles on different organs are decoupled, and particles are constrained to lie on a single organ (surface). This is enforced by considering the entropy of the correspondences in the configuration space (second term in Eq. 1) of each organ of each anatomy separately. This separation ensures that the particles are uniformly distributed on each organ independently. At the same time, the covariance $\mathbf{\Sigma}$ of the random variable $\mathbf{Z}$ in the space includes all particle positions across the multiple organs. This ensures the optimization takes place on the multi-organ shape space and the shape statistics remain coupled (Cates et al., 2008) resulting in an overall compact model and particles in correspondence on all organs and across anatomies. For K organs in anatomy, the cost function as in (10) is

$$Q = H(\mathbf{Z}) - \sum_{k=1}^{K}\left[\sum_{n=1}^{N} H\left(\mathbf{X}_n^k\right)\right] \tag{3}$$

where $\mathbf{X}_n^k$ represents the particle random variable associated with the n^{th} anatomy (or subject) and the k^{th} organ.

From Eq. 3, the second term, representing the sampling objective, is summed over all the shape samples. The sampling is restricted to the particles within the individual organs. As a result, when two organs have a shared boundary and sampling is done independently, it raises concerns about the statistics captured for the shared boundary surface using two particle systems. As there is no explicit representation of the common shared boundary, when the statistical analysis is performed for anatomies with shared boundaries, there is no mechanism to prevent the particles from penetrating other organs while studying the modes of variations. Such shape models with poorly parameterized anatomies and their interactions lead to a clinically incorrect statistical representation of morphological variations and observation. Hence, the shared boundary has to be explicitly parameterized into two parts - the interior (shared boundary surface) and exterior (shared boundary contour) of the surface. The extracted shared boundary has to be modeled as a separate entity from the two organs to avoid capturing the same statistics from multiple particle systems of the multi-organ anatomy. Another important consideration is that we need to ensure that the particles do not clutter around the edges of the organs and the shared boundary surface and contour. Hence, the interaction between the organs and the extracted shared boundary surface and contour has to be introduced during the optimization process. The sampling objective needs to be modified to introduce the interaction so that the particles on the shared boundary contour repel the particles of other organs to present each organ faithfully. This will result in a buffer distance between particles of the multiple organs leading to a uniform correspondence model and discouraging particles from moving into other organs during the representation of morphological variations.

The proposed objective function is:

$$Q = H(\mathbf{Z}) - \left[\sum_{k\in(A_r,M,B_r)}\sum_{n=1}^{N} H\begin{pmatrix}\mathbf{X}_n^k\\ \mathbf{X}_n^C\end{pmatrix} + \sum_{n=1}^{N} H\left(\mathbf{X}_n^C\right)\right] \tag{4}$$

where $\mathbf{X}^C$ is the matrix of particle positions located in the contour. Effectively, this means that all the particles on the A_r, M and B_r are

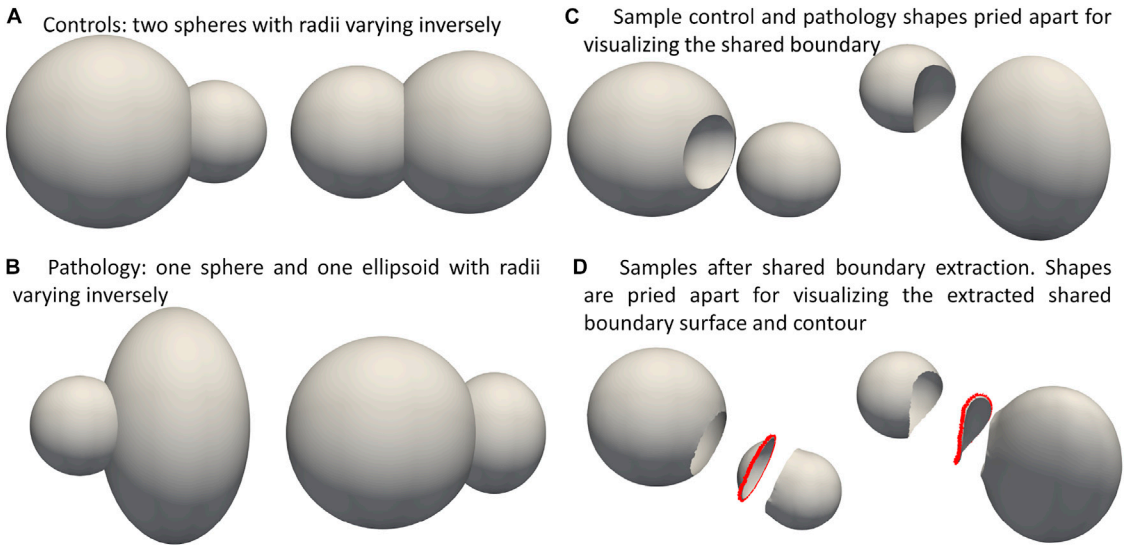

FIGURE 3
Synthetic Peanut Dataset: Surface meshes representing the two groups included in the peanut dataset- **(A)** Controls group: two spheres with varying radii, **(B)** pathalogical changes are emulated by changing one of the spheres to ellipsoid. **(C)** Samples from the controls and pathalogy groups show casing the shared boundary surface, **(D)** sample outputs obtained after extracting the shared boundary surface and contour. The meshes are pried apart for visualization.

repelled by particles on the contour C. Similar to the original PSM formulation mentioned in Section 2.1, the cost function Q from Eq 4 is minimized using gradient descent. As a general assumption, the surface area and circumference of the shared boundary surface are smaller than the anatomy's individual organs. The number of particles required to describe the shared boundary and contour is much lower than the number of particles required to describe the organs. Hence, we do not change the sampling objective for the contour ($\sum_{n=1}^{N} H(\mathbf{X}_n^C)$ term in Eq 4. This is because the large magnitude of gradients from more particles of the meshes could cause the particles on the contour to swap places. Since there is only one degree of freedom on a contour, it is almost impossible to recover from this situation.

3 Dataset and shape modeling

3.1 Synthetic peanut dataset

We demonstrate the proposed pipeline for shared boundary extraction and optimization of models with shared surfaces by considering a synthetic peanut dataset. Each sample in this dataset consists of surface meshes of two spheres, but one of the spheres is subtracted from the other. There exists a shared surface between the two spheres (Figure 3C). The radii of the two spheres vary inversely, i.e., as one gets bigger, the other gets smaller (Figure 3A). Pathological shape changes are emulated by converting one of the spheres to ellipsoids where the radii in the y and z direction are varied (Figure 3B). The dataset is balanced and consists of 15 controls (i.e., where both the shapes are spheres) and 15 pathology (i.e., where one of the shapes is an ellipsoid.) All the shapes are alignment and are centered at $[0, 0, 0]$ during the data generation process.

3.2 Cardiac biventricular dataset

We evaluated our method on a real world cardiac biventricular dataset, comparing how well the resulting correspondence model captures variability in shape for cardiovascular clinic patients and healthy volunteer groups. The dataset consists of MRIs of six healthy volunteers and 23 patients treated at a cardiovascular clinic. In the patient group, tricuspid regurgitation was secondary to pulmonary hypertension in one patient; congestive heart failure (CHF) in 10 patients; and other causes (atrial fibrillation, pacemaker lead injury, pacemaker implantation, congenital heart disease) in 12 patients. The healthy volunteers had no diagnosis of cardiac disease and no cardiovascular risk factors. The 23 patients were retrospectively identified from the University of Utah medical data warehouse after verification of the patient charts. Healthy volunteer images were obtained during a previous study at Weill-Cornell Medical College, after IRB approval (Orkild et al., 2022). These studies involving human participants were reviewed and approved by the University of Utah Internal Review Board committee.

RV and LVW shapes were generated from manual segmentations performed on reconstructed 3D image volumes from end-diastole CINE MRI. From each CINE short axis time stack, an image of the heart at end diastole was extracted to create a 3D volume image stack. Image extraction was performed using a custom MATLAB image processing code. The volume stacks were then segmented using the open-source Seg3D software (SCI Institute, University of Utah, SLC UT). The volume stack was segmented semi-automatically by inserting seed points along the edge of each slice. After that, the segmentation was manually modified to remove any flaws or artifacts. A binary mask volume of the completed segmentation was exported for further analysis. The segmentations were then isotropically resampled and converted to meshes using the open software ShapeWorks. In order to align the shapes, the meshes were

10.3389/fbioe.2022.1078800

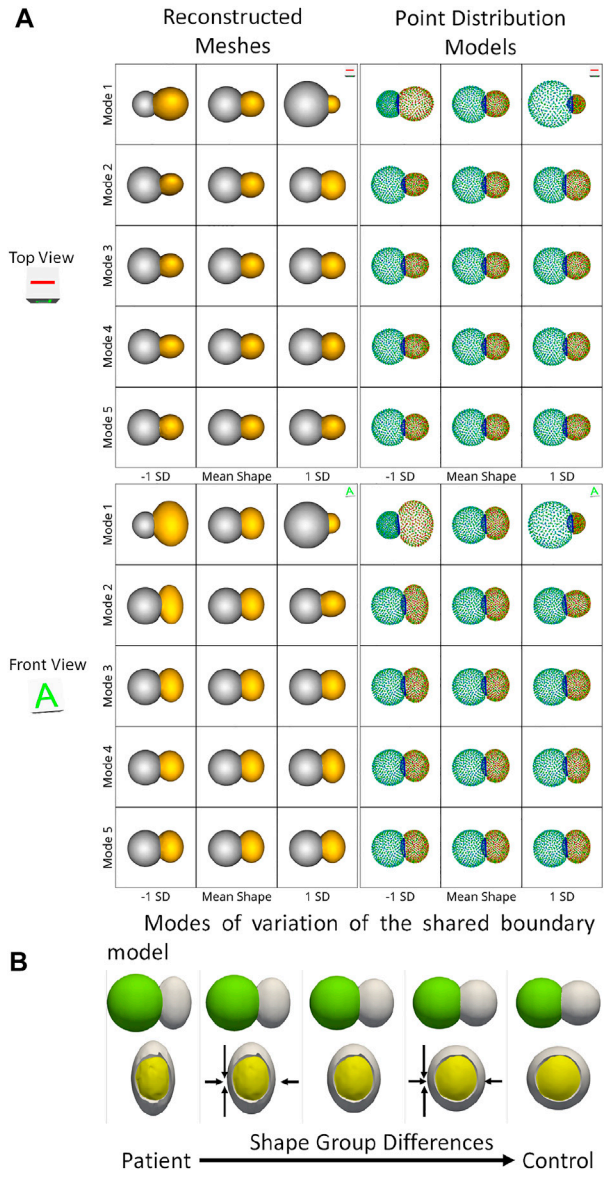

FIGURE 4
(A) Two viewpoints of the point distribution models and the reconstructed meshes of the modes of variations of the peanut dataset discovered by the shared boundary model. **(B)** Group-level shape differences observed by the shared boundary shape model. The arrows indicate the direction of shape change, the yellow mesh represents the extracted shared boundary, and the white represents one of the shapes of the peanut.

centered and rigidly aligned to a representative reference sample selected from the population. The reference sample is selected by first computing the mean (average) mesh, then selecting the sample closest to that mean (i.e., medoid). The rigid alignment was done by calculating the transformations only using the RV meshes of the population due to their complex shapes. These transformations were then applied to the RV and the LVW meshes. The average edge length (given as mean ± std in mm) of the right ventricle meshes was .8224 ± .3987, left ventricle wall meshes was .9438 ± .3399, the IVS meshes .5196 ± .4047, and the contours 21.469 ± 26.205.

3.3 Shape model construction

We used ShapeWorks, an open-source software that implements the particle-based entropy optimization (Cates et al., 2007; Cates et al., 2017) described in Section 2.1. We modified the optimization with the proposed cost function (Eq. 4) to support multi-organ anatomies with shared boundaries. First, the shared boundary surface and contour were extracted for both the datasets before building shape models using the tool described in Section 2.2. During the extraction process, Laplacian smoothing was performed as per step 3 mentioned in Section 2.2 for 30 iterations with relaxation parameter set to 1. Figure 2 shows an example output for one sample of the cardiac biventricular dataset and Figure 3D shows example output for the peanut dataset. For the peanut dataset, a shape model was built using 512 particles for each shape (sphere and ellipsoid), and 64 particles each for the shared boundary surface and contour. For the cardiac dataset, a shape model was built using 512 particles for the RV and LVW, and 64 particles were used for the IVS surface and contour. We also generated a multi-organ anatomy shape model for the cardiac dataset without performing the shared boundary extraction and optimization as a baseline model for comparison. This shape model was generated using the optimization cost function specified in Eq 3 (already a part of ShapeWorks) and will be referred to as the multiple-domain shape model.

4 Results and discussions

4.1 Synthetic peanut dataset

We use the peanut dataset as proof of concept. Figures 3C, D show the extracted shared boundary and contour for a control sample with two spheres and a patient sample with a sphere and ellipsoid. A shape model was then generated using the proposed optimization. We use PCA to simplify the complexity of the high-dimensional correspondence model while identifying the patterns learned by the PSM. Using PCA, we rank the independent modes of shape variation according to the proportion of variance that is explained (measured by eigenvalues) to the overall variance. The modes that account for the most form variability are called the dominant modes. The generated shape model was used to identify the group-level shape differences shown in Figures 4A, B. The shape model correctly identified the relative increase and decrease in size as modes of variation while appropriately representing the shared boundary surface and contour. It can be seen from the particle distribution models shown in Figure 4A that the proposed shared boundary optimization ensures that the particles from one object do not penetrate other objects while visualizing the modes of variations. From Figure 4B, we can see that the shared boundary models correctly identified partial ellipsoids as the shared surface in the case of pathology samples and partial spheres in the case of control samples as group-level shape difference. The observations made using the synthetic peanut dataset shared boundary model have successfully showcased the proof of concept and the feasibility of implementing the proposed tools.

10.3389/fbioe.2022.1078800

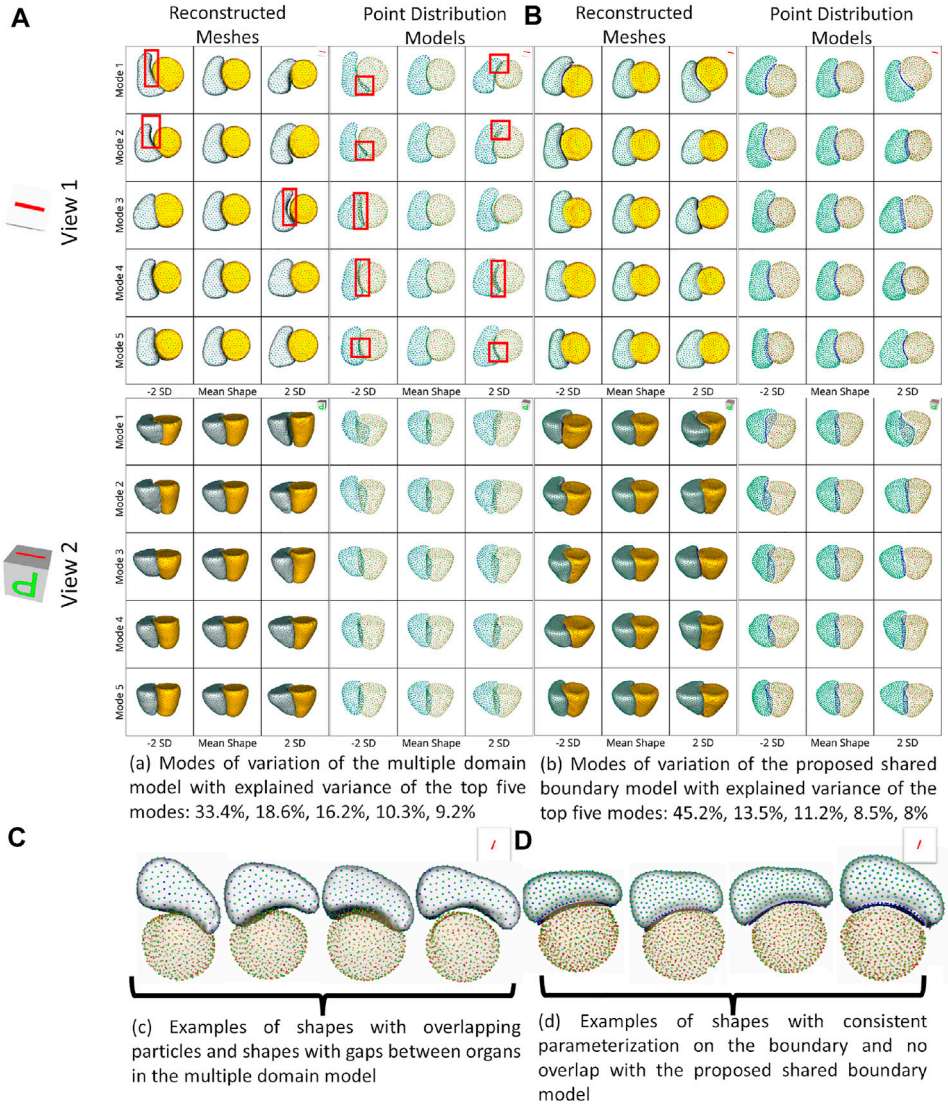

FIGURE 5
Two different views of the same reconstructed meshes and the point distribution models of the modes of variations discovered by **(A)** multiple domains model and **(B)** the proposed shared boundary model. The red boxes indicate shape modeling inconsistencies of multiple domain model - particle overlap and gaps between organs. **(C)** Examples of shapes with overlapping particles and shapes with gaps between organs in the multiple domains model and **(D)** examples of shapes with consistent parameterization in the proposed shared boundary model.

4.2 Cardiac biventricular dataset

For the cardiac biventricular dataset, we compare the following two models - shared boundary and multiple domains. Both shape models are assessed on their capability to identify the underlying morphometric variations. Like the peanut dataset, PCA was used to identify the modes of variations identified by the shape models. Figure 5 shows the five dominant modes of variation discovered by the multiple domains and shared boundary model for the cardiac dataset. As multiple domain models lack the explicit parameterization of the shared boundary surface between the LVW and RV, the modes of variations show anatomical inconsistencies visible in Figures 5A, C. The particles penetrate the adjacent organs (indicated with red boxes) in the identified modes of variations rendering the learned statistics of the data clinically irrelevant. On the other hand, the shared boundary model produces clinically useful modes of variation with a consistent representation of the IVS, i.e., the shared boundary surface. The multiple domain model also generated modes of variations with that introduced gaps between the LVW and RV. This anatomical inconsistency is seen with the multiple domains shape model because the model does not consider the interactions between the two organs and fails to account for the joint statistics of the shared surface in the optimization process. In contrast, the proposed method directly models the joint statistics.

We also compared the performance of the shared boundary model and the multiple domain model for the cardiac dataset to identify the group-level differences between pathology and controls. Figure 6A shows the group differences identified by the shared boundary model, and Figure 6B shows multiple domains. There is a marked difference in the curvature of IVS of the healthy group as compared to the patient group as identified by the shared boundary model in the first row of Figure 6A. Multiple domain model group differences show anatomical inconsistencies as the shared surface is not explicitly modeled. The

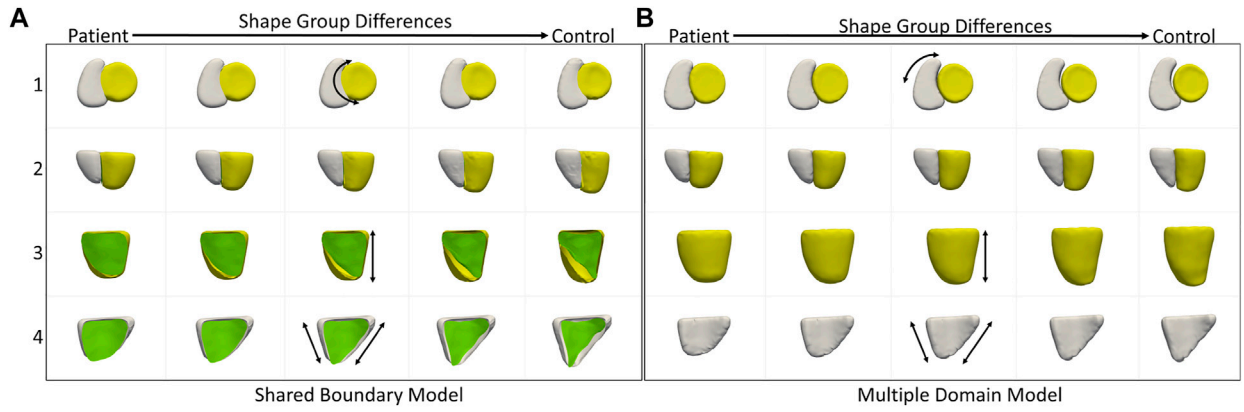

FIGURE 6
Group shape differences identified by **(A)** the proposed shared boundary and **(B)** the multiple domains model. Each row shows the samples from a different view to visualize the differences. The black arrows indicate the direction of the variation of shape.

anatomical inconsistencies are in the form of a gap introduced between the two organs, which is visible in the first row of Figure 6. The shared boundary removed the anatomical inconsistencies and correctly identified the shape difference describing the pathology and control group. In contrast, the multiple domains model identifies size differences correctly but fails to model the curvature of the IVS as there is no explicit representation of the IVS in the model.

4.3 Multi-level analysis of morphology and alignment

Statistical shape modeling aims to identify subtle variations within a population. The data acquisition process plays an essential role in determining data quality. Due to manual and system errors, the image acquisition process can introduce pose variations that result in the variation of the relative position of the organs in the anatomy. Most modeling pipelines rely on iterative closed point alignment (Arun et al., 1987; Besl and McKay, 1992) to rigidly align the cohort of shapes in the population. However, these alignment techniques cannot robustly eliminate variations in the relative pose. Therefore, we need tools that identify the pose variations and separate them from clinically relevant shape variations of the multi-organ anatomy.

The cardiac biventricular dataset is challenging as it contains some misalignments that could not be resolved by using rigid alignment in the pre-processing step. Hence, the modes of variation identified by using PCA for the shared boundary shape model and multiple domain model include variations in alignment and shape entangled together. The entangled observations can be seen in the first mode shown in Figures 5A, B where the right ventricle moves around the left ventricle wall. Such observations render the learned statistics clinically insignificant as these variations do not naturally occur in the anatomy. In order to mitigate the problem of entangled mode of variations, we use the multi-level component analysis (MLCA) technique (Timmerman, 2006). MLCA is an extension to PCA, where the analysis is done at different levels in which the data is observed. PCA is done on the joint shape space for the shape model having multiple organs under consideration. MLCA, on the other hand, applies PCA to capture the individual subspace of each organ under consideration that encodes the within-organ shape variations across the population and the between-organ subspace capturing the relative alignment variations across the population. Thus, applying this multi-level analysis technique helps disentangle the mode of variations into shape variations and pose (relative positioning of the organs) variations, which was not seen otherwise using PCA only. Figure 7 shows the top four dominant modes of pose variations where the arrows indicate the direction of the movement of the organs. Figure 8 shows the top four dominant modes of shape variations discovered by multi-level analysis. Comparing the disentangled shape variations in Figure 8 with the PCA modes of variations in Figure 5B, we can see that the two organs no longer showcase translation or rotation with respect to each other.

4.4 Data imbalance

In order to study statistically significant geometric group differences learned by the shared boundary model, we performed linear discrimination of variation. The linear discrimination between the two groups is defined as the difference vector between the particle-wise mean shapes of the two groups. The shape of each subject is then mapped/projected onto this difference vector by taking the dot product between the subject-specific shape representation (the particle correspondences) and this difference vector. The mapping results in a single scalar value (or a "shape-based score") that places subject-specific anatomy on a group-based shape difference that is statistically derived from the shape population. The particle-wise mean shape for the cardiac patients is set as -1, and controls are set as 1. The mappings of all the other subjects are then similarly normalized relative to these values, giving a shape distribution of individual members of the population relative to the mean shapes of their respective groups. A univariate Gaussian distribution is then fitted to the normalized mapping of each group to define the probability density function of the shape scores for each group.

Since the number of samples in the patient group and control group are not the same, we performed hypothesis testing to identify if the shape-based score assigned to each sample is statistically significant and agnostic to the data imbalance. We generated the shape-based scores for each sample by building a shared boundary shape model with six randomly selected samples from the patient group and all six control group samples and use these samples to generate the particle wise mean shapes and the

10.3389/fbioe.2022.1078800

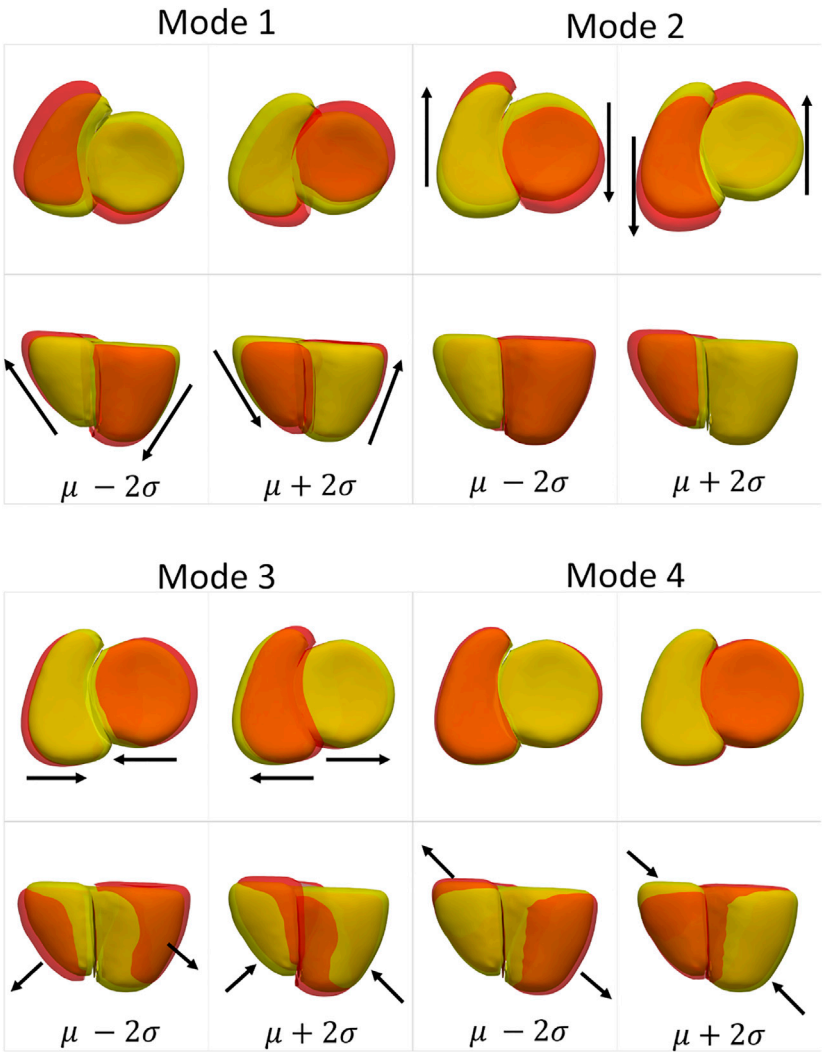

FIGURE 7
Alignment variations identified using multi-level component analysis for the cardiac dataset. The surface meshes in yellow represent the mean reconstructed shape, and the surface meshes in red represent the shapes at μ+2σ and μ–2σ. The black arrows indicate the direction of the variation of the pose.

difference vector. We then used this model to predict the particle position on the remaining samples without optimizing the shape model again. The predicted particle positions for all samples are then mapped to the difference vector to generate the shape based scores. This experiment was repeated ten times, and a shape-based score was generated for all the samples for each experiment. The shape-based scores from the experiment were then compared to those shape-based scores generated by using the shape model built with the complete dataset. We use a *t*-test to test for the null hypothesis that the expected value (mean) of a sample of independent observations from the ten trials equals the given population mean, i.e., the scores generated using the complete dataset. Figure 9 shows the box-and-whisker plot of the distribution of scores of each sample obtained from the experiment, and the table above the color indicates the *p*-values. We select the alpha value to be .01. Hence, if the *p*-values are smaller than .01, the null hypothesis holds (shown in green), and if the *p*-value is greater than .01, we can reject the null hypothesis and assume that the scores are affected by the imbalance (shown in red). As mentioned previously, the cardiac biventricular dataset is challenging and the misalignments could not be resolved with rigid alignments and the variability in scale is also high. Due to these conditions, the shape-based score for the samples are not centered around the means of patients and controls set at -1 and 1. Although it can be seen from box-whisker plots of Figure 9 that the imbalance does not affect the shape-based scores, the study of group shape differences and pathological changes can benefit from the addition of more samples and better shape alignment strategies for the biventricular database.

4.5 Clinical importance of shared boundary SSM

The observations from the shared boundary model confirm what has been observed in the cardiology literature: a decrease in interventricular septal curvature during prolonged right ventricular dysfunction (Marcu et al., 2006; Kochav et al., 2015; Addetia et al., 2018; Mauger et al., 2019). A healthy heart has a significant pressure gradient between the right and left ventricles (Dawes et al., 2017; Morgan et al., 2018). However, in many cardiac diseases, the pressure

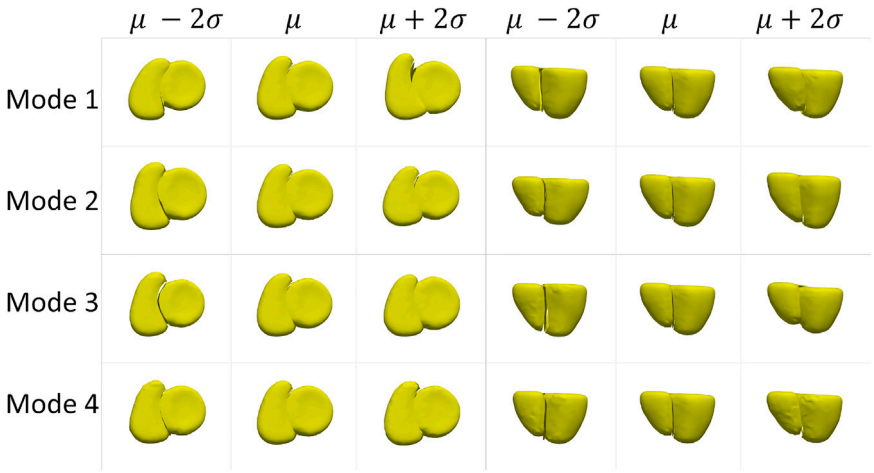

FIGURE 8
Shape variations identified using multi-level analysis for the cardiac dataset visualized from two different views.

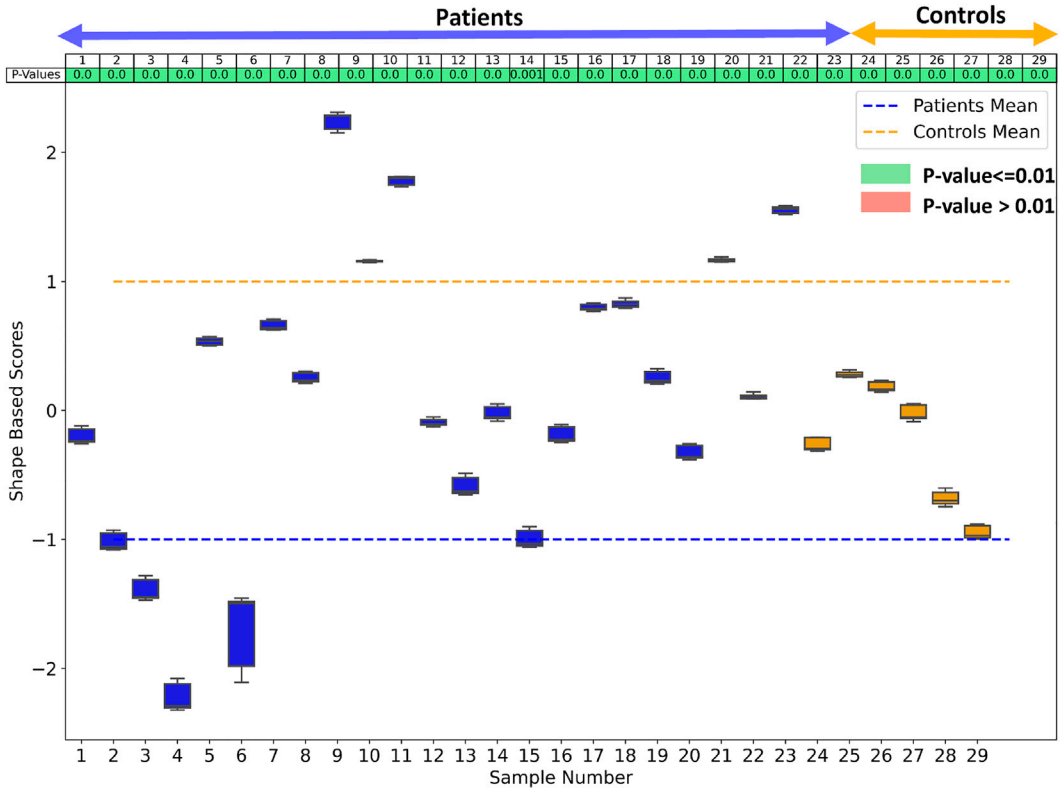

FIGURE 9
The box whisker plot shows the distribution of the shape-based scores for each sample from ten different shape models generated to study the effect of data imbalance. The table at the top of the plot shows the *p*-values of the shape-based scores.

gradient dissipates because right ventricular pressure increases (Kochav et al., 2015). As the pressure increases, a distortion occurs at the interventricular septum, and the original septal curvature matching the left ventricular becomes flattened. This signifies the structural remodeling that occurs with severe cardiac pathologies (Farrar et al., 2016; Addetia et al., 2018).

4.6 Limitations

For the shared boundary extraction tool from Section 2.2, the threshold used in step 2 needs to be tuned for all the samples with high variability in the dataset. As the threshold is changed, the shape of the shared surface changes. Hence, the shared boundary extraction

mechanism of the proposed tool has to be robust and needs to be improved such that the extraction is carried out based on the statistics of the entire population rather than operating on a sample level. The extracted shared boundary surfaces and contours can also showcase a very high level of variability compared to the rest of the organs, making it challenging to produce a stable shape model with meaningful modes of variations. Hence, we cannot rely on the Gaussian assumption for generating compact PDMs. In the future, the proposed PSM optimization method from Section 2.3 could be modified to incorporate non-linear shape variations for a compact and generalizable model.

5 Conclusion

We demonstrated that our approach preserves the integrity of the multiple-organ PDM while offering a reliable and consistent representation of the shared boundary. The unique shape changes of the IVS that are not captured when modeling the ventricles alone were demonstrated using our method on a cardiac biventricular dataset. The initial structural changes of the heart are an adaptation to overcome changes in cardiac physiology secondary to various pathologies. Prolonged exposure to these pathological changes results in chronic maladaptations that increase morbidity, and mortality (Leary et al., 2012). Patients often do not have symptoms of cardiac disease, such as shortness of breath or decreased exercise tolerance, at this stage because of the initially compensatory changes in cardiac function (Dreyfuss et al., 2004). However, structural changes, such as the IVS curvature change, are frequently visible and simple to spot. Therefore, IVS curvature changes could be used as an early identification tool to detect abnormalities before the patient develops symptoms. Shape analysis also has other clinical advantages, including being non-invasive. The current gold standard approach for assessing cardiac pressure differences is *via* invasive cardiac catheterization, which puts the patient at significant procedural risk for a diagnostic test. In conclusion, our novel approach for extracting and generating shape models of multi-organ anatomy with shared boundaries could pave the way for using statistical shape modeling from non-invasive imaging as a powerful diagnostic tool.

Data availability statement

The datasets presented in this article are not readily available because Patient data cannot be shared. Requests to access the datasets should be directed to krithika.iyer@utah.edu.

Ethics statement

These studies involving human participants were reviewed and approved by the University of Utah Internal Review Board committee was HIPAA compliant.

Author contributions

KI ran data processing (alignment) steps, shared boundary extraction, and developed the shape model for the toy and biventricular dataset. KI also ran all experiments and performed the statistical analysis, including PCA and MLCA, LDA, testing, and verification of statistical methods, along with writing the manuscript. AM assisted in shape model development and manuscript review. AM also developed and maintained shared boundary tools and ShapeWorks. BZ headed clinical oversight of the problem and provided clinical input on the manuscript and data collection. KK implemented the shared boundary extraction tool and modified the optimization of ShapeWorks. NK implemented MLCA and helped with MLCA conclusions. BO headed the MRI image processing and MATLAB tool development. OK added support for mesh-based optimization to ShapeWorks. SE headed project origination and oversight, supervised statistical analysis and manuscript preparation, and is the senior author.

Funding

This work was supported by the National Institutes of Health under grant numbers NIBIB-U24EB029011, NIAMS R01AR076120, NHLBI-R01HL135568, NIBIB-R01EB016701, NIGMS-P41GM103545, NIGMS-R24GM136986. (MacLeod), and NHLBI-F30HL149327 (Zenger).

Acknowledgments

We thank the University of Utah Division of Cardiovascular Medicine and the ShapeWorks team. A preliminary version of this work was accepted at the Statistical Atlases and Computational Modeling of the Heart (STACOM) workshop at MICCAI 2022 (print yet to appear). The workshop version of the accepted paper is available on archive (Iyer et al., 2022).

Conflict of interest

AM has equity interest in Marrek, Inc.

The authors declare that the research was conducted in the absence of any commercial or financial relationships that could be construed as a potential conflict of interest.

Publisher's note

References

Addetia, K., Maffessanti, F., Muraru, D., Singh, A., Surkova, E., Mor-Avi, V., et al. (2018). Morphologic analysis of the normal right ventricle using three-dimensional echocardiography–derived curvature indices. *J. Am. Soc. Echocardiogr.* 31, 614–623. doi:10.1016/j.echo.2017.12.009

Alraddadi, A. (2021). Literature review of anatomical variations: Clinical significance, identification approach, and teaching strategies. *Cureus* 13, e14451. doi:10.7759/cureus.14451

Andriacchi, T. P., Koo, S., and Scanlan, S. F. (2009). Gait mechanics influence healthy cartilage morphology and osteoarthritis of the knee. *J. Bone Jt. Surg. Am. volume* 91, 95–101. doi:10.2106/jbjs.h.01408

Arun, K. S., Huang, T. S., and Blostein, S. D. (1987). "Least-squares fitting of two 3-d point sets," in *IEEE Transactions on pattern analysis and machine intelligence*, 698–700. doi:10.1109/tpami.1987.4767965

Bartsch, R. P., Liu, K. K., Bashan, A., and Ivanov, P. C. (2015). Network physiology: How organ systems dynamically interact. *PloS one* 10, e0142143. doi:10.1371/journal.pone.0142143

Besl, P. J., and McKay, N. D. (1992). "Method for registration of 3-d shapes," in *Sensor fusion IV: Control paradigms and data structures* (Boston, MA: United States), 1611, 586–606.

Borghi, A., Rodriguez Florez, N., Ruggiero, F., James, G., O'Hara, J., Ong, J., et al. (2020). A population-specific material model for sagittal craniosynostosis to predict surgical shape outcomes. *Biomechanics Model. Mechanobiol.* 19, 1319–1329. doi:10.1007/s10237-019-01229-y

Cates, J., Bieging, E., Morris, A., Gardner, G., Akoum, N., Kholmovski, E., et al. (2014). Computational shape models characterize shape change of the left atrium in atrial fibrillation. *Clin. Med. Insights Cardiol.* 8, 15710. CMC–S15710. doi:10.4137/cmc.s15710

Cates, J., Elhabian, S., and Whitaker, R. (2017). "Shapeworks: Particle-based shape correspondence and visualization software," in *Statistical shape and deformation analysis* (Elsevier), 257–298.

Cates, J., Fletcher, P. T., Styner, M., Hazlett, H. C., and Whitaker, R. (2008). "Particle-based shape analysis of multi-object complexes," in *International conference on medical image computing and computer-assisted intervention* (Springer), 477–485.

Cates, J., Fletcher, P. T., Styner, M., Shenton, M., and Whitaker, R. (2007). "Shape modeling and analysis with entropy-based particle systems," in *Biennial international conference on information processing in medical imaging* (Springer), 333–345.

Cerrolaza, J. J., Picazo, M. L., Humbert, L., Sato, Y., Rueckert, D., Ballester, M. Á. G., et al. (2019). Computational anatomy for multi-organ analysis in medical imaging: A review. *Med. Image Anal.* 56, 44–67. doi:10.1016/j.media.2019.04.002

Cootes, T. F., Taylor, C. J., Cooper, D. H., and Graham, J. (1995). Active shape models-their training and application. *Comput. Vis. image Underst.* 61, 38–59. doi:10.1006/cviu.1995.1004

Davies, R. H. (2002). *Learning shape: Optimal models for analysing natural variability*. The University of Manchester United Kingdom.

Dawes, T. J. W., de Marvao, A., Shi, W., Fletcher, T., Watson, G. M. J., Wharton, J., et al. (2017). Machine learning of three-dimensional right ventricular motion enables outcome prediction in pulmonary hypertension: A cardiac mr imaging study. *Radiology* 283, 381–390. doi:10.1148/radiol.2016161315

Dreyfuss, P., Dreyer, S. J., Cole, A., and Mayo, K. (2004). Sacroiliac joint pain. *JAAOS-Journal Am. Acad. Orthop. Surg.* 12, 255–265. doi:10.5435/00124635-200407000-00006

Durrleman, S., Prastawa, M., Charon, N., Korenberg, J. R., Joshi, S., Gerig, G., et al. (2014). Morphometry of anatomical shape complexes with dense deformations and sparse parameters. *NeuroImage* 101, 35–49. doi:10.1016/j.neuroimage.2014.06.043

Faber, B. G., Bredbenner, T., Baird, D., Gregory, J., Saunders, F., Giuraniuc, C., et al. (2020). Subregional statistical shape modelling identifies lesser trochanter size as a possible risk factor for radiographic hip osteoarthritis, a cross-sectional analysis from the osteoporotic fractures in men study. *Osteoarthr. Cartil.* 28, 1071–1078. doi:10.1016/j.joca.2020.04.011

Farrar, G., Suinesiaputra, A., Gilbert, K., Perry, J. C., Hegde, S., Marsden, A., et al. (2016). Atlas-based ventricular shape analysis for understanding congenital heart disease. *Prog. Pediatr. Cardiol.* 43, 61–69. doi:10.1016/j.ppedcard.2016.07.010

Field, D. A. (1988). Laplacian smoothing and delaunay triangulations. *Commun. Appl. Numer. methods* 4, 709–712. doi:10.1002/cnm.1630040603

Goparaju, A., Iyer, K., Bone, A., Hu, N., Henninger, H. B., Anderson, A. E., et al. (2022). Benchmarking off-the-shelf statistical shape modeling tools in clinical applications. *Med. Image Anal.* 76, 102271. doi:10.1016/j.media.2021.102271

Heitz, G., Rohlfing, T., and Maurer, C. R., Jr (2005). "Statistical shape model generation using nonrigid deformation of a template mesh," in *Medical imaging 2005: Image processing* (San Diego, CA: United States), 5747, 1411–1421.

Iyer, K., Morris, A., Zenger, B., Karnath, K., Orkild, B. A., Korshak, O., et al. (2022). *Statistical shape modeling of biventricular anatomy with shared boundaries*. arXiv preprint arXiv:2209.02706.

Jacobson, A., and Panozzo, D. (2018). *libigl: A simple C++ geometry processing library*. Available at: https://libigl.github.io/.

Jesse, M. K., Kleck, C., Williams, A., Petersen, B., Glueck, D., Lind, K., et al. (2017). 3d morphometric analysis of normal sacroiliac joints: A new classification of surface shape variation and the potential implications in pain syndromes. *Pain Physician* 20, E701–E709.

Kochav, J., Simprini, L., and Weinsaft, J. W. (2015). Imaging of the right heart—Ct and cmr. *Echocardiography* 32, S53–S68. doi:10.1111/echo.12212

Krol, Z., Skadlubowicz, P., Hefti, F., and Krieg, A. H. (2013). Virtual reconstruction of pelvic tumor defects based on a gender-specific statistical shape model. *Comput. aided Surg.* 18, 142–153. doi:10.3109/10929088.2013.777973

Leary, P. J., Kurtz, C. E., Hough, C. L., Waiss, M.-P., Ralph, D. D., and Sheehan, F. H. (2012). Three-dimensional analysis of right ventricular shape and function in pulmonary hypertension. *Pulm. Circ.* 2, 34–40. doi:10.4103/2045-8932.94828

Lenz, A. L., Krähenbühl, N., Peterson, A. C., Lisonbee, R. J., Hintermann, B., Saltzman, C. L., et al. (2021). Statistical shape modeling of the talocrural joint using a hybrid multi-articulation joint approach. *Sci. Rep.* 11, 7314–14. doi:10.1038/s41598-021-86567-7

Li, G., Yin, J., Gao, J., Cheng, T. S., Pavlos, N. J., Zhang, C., et al. (2013). Subchondral bone in osteoarthritis: Insight into risk factors and microstructural changes. *Arthritis Res. Ther.* 15, 223–312. doi:10.1186/ar4405

Marcu, C. B., Beek, A. M., and Rossum, A. C. V. (2006). Cardiovascular magnetic resonance imaging for the assessment of right heart involvement in cardiac and pulmonary disease. *Heart, Lung Circulation* 15, 362–370. doi:10.1016/j.hlc.2006.08.003

Marrouche, N. F., Wilber, D., Hindricks, G., Jais, P., Akoum, N., Marchlinski, F., et al. (2014). Association of atrial tissue fibrosis identified by delayed enhancement mri and atrial fibrillation catheter ablation: The decaaf study. *Jama* 311, 498–506. doi:10.1001/jama.2014.3

Mauger, C., Gilbert, K., Lee, A. M., Sanghvi, M. M., Aung, N., Fung, K., et al. (2019). Right ventricular shape and function: Cardiovascular magnetic resonance reference morphology and biventricular risk factor morphometrics in UK biobank. *J. Cardiovasc. Magnetic Reson.* 21, 41–13. doi:10.1186/s12968-019-0551-6

McInerney, T., and Terzopoulos, D. (1996). "Deformable models in medical image analysis," in *Proceedings of the workshop on mathematical methods in biomedical image analysis* (IEEE), 171–180.

Morgan, A. E., Zhang, Y., Tartibi, M., Goldburg, S., Kim, J. J., Nguyen, T. D., et al. (2018). Ischemic mitral regurgitation: Abnormal strain overestimates nonviable myocardium. *Ann. Thorac. Surg.* 105, 1754–1761. doi:10.1016/j.athoracsur.2018.01.00510.1016/j.athoracsur.2018.01.005

Orkild, B. A., Zenger, B., Iyer, K., Rupp, L. C., Ibrahim, M. M., Khashani, A. G., et al. (2022). All roads lead to rome: Diverse etiologies of tricuspid regurgitation create a predictable constellation of right ventricular shape changes. *Front. Physiology* 13, 908552. doi:10.3389/fphys.2022.908552

Paulsen, R., Larsen, R., Nielsen, C., Laugesen, S., and Ersbøll, B. (2002). "Building and testing a statistical shape model of the human ear canal," in *International conference on medical image computing and computer-assisted intervention* (Springer), 373–380.

Postacchini, R., Trasimeni, G., Ripani, F., Sessa, P., Perotti, S., and Postacchini, F. (2017). Morphometric anatomical and ct study of the human adult sacroiliac region. *Surg. Radiologic Anat.* 39, 85–94. doi:10.1007/s00276-016-1703-0

Samson, C., Blanc-Féraud, L., Aubert, G., and Zerubia, J. (2000). A level set model for image classification. *Int. J. Comput. Vis.* 40, 187–197. doi:10.1023/a:1008183109594

Sanfilippo, A. J., Abascal, V. M., Sheehan, M., Oertel, L. B., Harrigan, P., Hughes, R. A., et al. (1990). Atrial enlargement as a consequence of atrial fibrillation. a prospective echocardiographic study. *Circulation* 82, 792–797. doi:10.1161/01.cir.82.3.792

Smith, H. (2021). Anatomical variation and clinical diagnosis. *diagnostics* 11, 247. doi:10.3390/diagnostics11020247

Styner, M., Oguz, I., Xu, S., Brechbühler, C., Pantazis, D., Levitt, J. J., et al. (2006). Framework for the statistical shape analysis of brain structures using spharm-pdm. *insight J.* 242, 242–250. doi:10.54294/owxzil

Timmerman, M. E. (2006). Multilevel component analysis. *Br. J. Math. Stat. Psychol.* 59, 301–320. doi:10.1348/000711005x67599

Uetani, M., Tateyama, T., Kohara, S., Tanaka, H., Han, X.-H., Kanasaki, S., et al. (2015). Statistical shape model of the liver and its application to computer-aided diagnosis of liver cirrhosis. *Electr. Eng. Jpn.* 190, 37–45. doi:10.1002/eej.22668

Valette, S., Chassery, J. M., and Prost, R. (2008). Generic remeshing of 3d triangular meshes with metric-dependent discrete voronoi diagrams. *IEEE Trans. Vis. Comput. Graph.* 14, 369–381. doi:10.1109/tvcg.2007.70430

frontiers | Frontiers in Bioengineering and Biotechnology

TYPE Original Research
PUBLISHED 27 January 2023
DOI 10.3389/fbioe.2023.1086234

OPEN ACCESS

EDITED BY
Hao Gao,
University of Glasgow, United Kingdom

REVIEWED BY
Debao Guan,
University of Glasgow, United Kingdom
Scott Richardson,
University of Glasgow, United Kingdom

*CORRESPONDENCE
Jadie Adams,
jadie@sci.utah.edu
Nawazish Khan,
nawazish.khan@sci.utah.edu
Shireen Elhabian,
shireen@sci.utah.edu

†These authors have contributed equally to this work and share first authorship

SPECIALTY SECTION
This article was submitted to Biomechanics, a section of the journal Frontiers in Bioengineering and Biotechnology

RECEIVED 01 November 2022
ACCEPTED 16 January 2023
PUBLISHED 27 January 2023

CITATION
Adams J, Khan N, Morris A and Elhabian S (2023), Learning spatiotemporal statistical shape models for non-linear dynamic anatomies.
Front. Bioeng. Biotechnol. 11:1086234.
doi: 10.3389/fbioe.2023.1086234

Learning spatiotemporal statistical shape models for non-linear dynamic anatomies

Jadie Adams[1,2*†], Nawazish Khan[1,2*†], Alan Morris[1,2] and Shireen Elhabian[1,2*]

[1]School of Computing, University of Utah, Salt Lake City, UT, United States, [2]Scientific Computing and Imaging Institute, University of Utah, Salt Lake City, UT, United States

Numerous clinical investigations require understanding changes in anatomical shape over time, such as in dynamic organ cycle characterization or longitudinal analyses (e.g., for disease progression). Spatiotemporal statistical shape modeling (SSM) allows for quantifying and evaluating dynamic shape variation with respect to a cohort or population of interest. Existing data-driven SSM approaches leverage information theory to capture population-level shape variations by learning correspondence-based (landmark) representations of shapes directly from data using entropy-based optimization schemes. These approaches assume sample independence and thus are unsuitable for sequential dynamic shape observations. Previous methods for adapting entropy-based SSM optimization schemes for the spatiotemporal case either utilize a cross-sectional design (ignoring within-subject correlation) or impose other limiting assumptions, such as the linearity of shape dynamics. Here, we present a principled approach to spatiotemporal SSM that relaxes these assumptions to correctly capture population-level shape variation over time. We propose to incorporate modeling the underlying time dependency into correspondence optimization *via* a regularized principal component polynomial regression. This approach is flexible enough to capture non-linear temporal dynamics while encoding population-specific spatial regularity. We demonstrate our method's efficacy on synthetic data and left atrium segmented from cardiac MRI scans. Our approach better captures the population modes of variation and a statistically significant time dependency than existing methods.

KEYWORDS

statistical shape modeling, spatiotemporal modeling, cardiac motion, nonlinear dynamics, population morphology analysis

1 Introduction

Statistical shape models (SSMs) provide a compact representation of shape in relation to a population. SSM is a valuable tool in clinical research because it allows for quantifying and analyzing anatomical shape variation with respect to a cohort of interest. SSM has been effectively used to quantify group differences (for example, between healthy and disease-specific populations) and in downstream tasks such as pathology detection and disease diagnosis (Bhalodia et al. (2020); Harris et al. (2013); Atkins et al. (2017); Gaffney et al. (2019)). Many clinical investigations require *spatiotemporal* evaluation, i.e., analysis of anatomical shape change over time. Such is the case for studies of *dynamic* motion that involve dense observations over short time intervals (such as organ cycles), as well as for *longitudinal* studies that involve sparse observations over extended periods (such as in disease staging and intervention analysis). Traditional SSM methods are incapable of representing spatiotemporal data and can only be

applied in a time-agnostic manner by assuming a *cross-sectional* study design. Here individual subject correlation across time is ignored, and each time point is incorrectly assumed to be an independent observation, i.e., a different subject. Disregarding the inherent correlation of shapes from the same sequence can confound the resulting population statistics and subsequent analyses (Gerig et al. (2016); Fitzmaurice and Ravichandran (2008)). Spatiotemporal SSM captures the time-based trajectory of shapes across patient sequences (intra-subject variation) and the population (inter-subject variation).

In SSM, a shape can be represented explicitly or implicitly. The explicit representation comprises of sets of landmark or correspondence points, i.e., geometrically consistent points defined on each anatomical surface in the shape population. The implicit representation takes the form of deformation fields or coordinate transformations in relation to a predefined shape atlas (Miller et al. (2014); Cootes et al. (2004)). Explicit correspondence-based SSM is one of the most popular techniques due to the simplicity and interpretability of the shape representation (Cerrolaza et al. (2019)). Correspondence points can be easily interpreted and visualized by clinicians. Additionally, this approach does not require the formulation of an atlas, which is non-trivial to define. For these reasons, we focus on correspondence-based SSM in this work. Historically, correspondence points were defined manually by domain experts to capture biologically relevant features (Bookstein (1996); Dryden and Mardia (2016)). However, such manual annotation was burdensome, subjective, and sparse—potentially missing clinically relevant shape attributes. More recently, computational methods have been utilized automatically define dense sets of correspondence points, or *point distribution models* (PDMs), to represent shape. A small example of a PDM can be seen in Figure 1.

Automatic PDM construction is computationally derived by formulating point placement as an optimization problem. Parametric optimization schemes have been formulated which utilize a geometric basis, i.e., spherical harmonics (assuming a template sphere) (Styner et al. (2006)), wavelet-based (Nain et al. (2007)), and functional maps (Ovsjanikov et al. (2012)). Optimization schemes that do not rely on parameterization but rather utilize a point-based representation have also been formulated using metrics such as entropy (Cates et al. (2007)) and minimum description length (Davies et al. (2002)). These approaches avoid complex parameterization construction steps and the limitations inherent in parametric representations, such as restriction to specific topologies and bias resulting from the choice of basis or template. The non-parametric techniques have been shown to produce more robust and compact models that better retain clinically relevant shape characteristics (Goparaju et al. (2018); Goparaju et al. (2022)). In this work, we utilize the entropy-based approach to PDM optimization formulated in Cates et al. (2007), a. k.a. particle-based shape modeling, as it is a data-driven approach that does not require any form of atlas. Correspondence point, or *particle*, positions are optimized directly from shape data to capture population-level shape variations. This formulation is implemented in the open source software, ShapeWorks (Cates et al. (2017)), and explained in detail in Section 2.2.1. ShapeWorks SSM has been proven to be state-of-the-art (Goparaju et al. (2018)) and has been successfully used in a variety of medical applications, including downstream tasks such as pathology detection and disease diagnosis (Bhalodia et al. (2020); Harris et al. (2013); Atkins et al. (2017)).

ShapeWorks cannot be directly applied to spatiotemporal data without assuming a cross-sectional design, where instances from a temporal sequence are treated independently. Adams et al. (2022) proposed adapting the entropy-based PDM optimization objective to disentangle subject and time dependencies. This disentangled technique (explained further in Section 2.2.2) outperforms an image-based approach that was originally proposed in Morris et al. (2020) for estimating organ segmentation and functional measurements over time. Adams et al. (2022) adapted this image-based approach for spatiotemporal SSM by first generating a PDM for a single, corresponding time point across subjects, then independently propagating the correspondence points across individual time sequences using image-based deformable registration. The disentangled entropy formulation provided an improvement over this image-based method, both in terms of capturing shape variation and the underlying time dependency. However, this approach still assumes a Gaussian distribution to approximate subject-wise entropy across time, hence violating the independence assumption. Furthermore, it does not explicitly parameterize the time dependency and requires consistent, identical time points for every subject in the cohort, limiting its utility in practical medical settings.

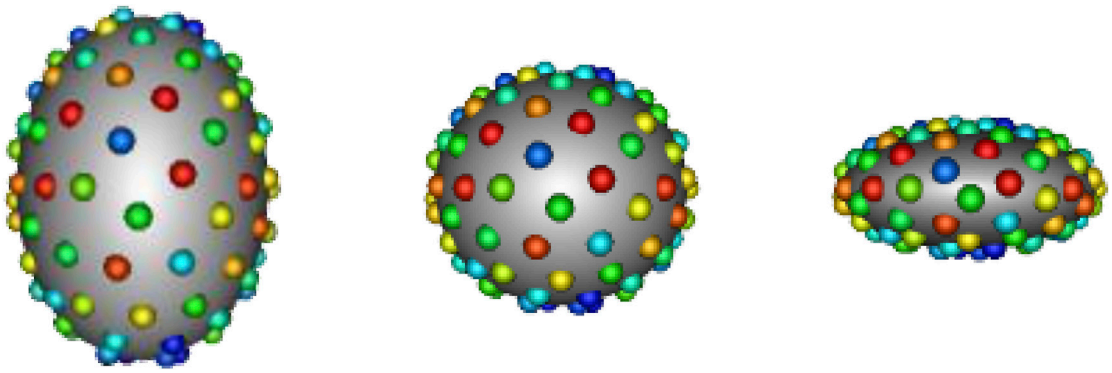

FIGURE 1
Example PDM: An example of a PDM with 128 particles on three ellipsoid shapes, where color denotes correspondence. The particle color pattern matches across shapes, indicating geometrically consistent particle placement.

Datar et al. (2009) proposed incorporating regression analysis in the process of optimizing correspondences. The details of this approach are explained in Section 2.2.3. Linear regression allowed for directly modeling the time-dependency and including partial sequences; however, it is limited to cases of linear shape dynamics. This technique may be applicable to specific studies of developmental modeling that involve linear growth, but it is not applicable to the general, much more common case of non-linear shape dynamics or longitudinal changes. The motion of the left atrium, for example, is an instance of highly non-linear dynamics as the volume increases and decreases cyclically. Datar et al. (2012) proposed using linear mixed effect modeling rather than simple regression in spatiotemporal PDM optimization. This hierarchical model allowed for capturing the global population trend as a fixed effect and individual trends as random effects. However, it is still limited to the case of linear longitudinal changes. Both the linear regression and mixed effects methods further suffered from the limitation of not handling spatial correlations between points on a shape (i.e., spatial regularity). In these methods, each particle coordinate is regressed independently without providing smoothness constraints.

In this paper, we introduce a novel approach to spatiotemporal SSM that combines entropy-based PDM optimization with non-linear regression to model the time dependency. Specifically, we extend the method presented by Cates et al. (2007) to incorporate regularized polynomial regression analysis in particle optimization. This regression is fit in the principal component subspace that best explains the data span to leverage population-specific statistics for capturing the spatial regularity of shape dynamics across time. The benefits of our proposed approach to spatiotemporal PDM optimization can be outlined as follows.

- It provides both inter-subject shape correspondence across the population and temporal intra-subject correspondence across time points without incorrect independence assumptions.
- It directly models the time-dependency in a manner that is not only flexible and non-linear, but also regularized to be generalizable and to reflect population-specific statistics.
- It does not require temporal sequences to be consistent across subjects. Thus subjects with partial observations or missing time points can be included in PDMs generated *via* the proposed approach.

The proposed method is capable of modeling any case of dynamic or longitudinal shape, surpassing the limitations of existing, aforementioned spatiotemporal SSM methods and increasing the potential for SSM to provide medical insight. The code will be released to magnify the scientific impact and clinical utility of the proposed method. Section 2, provides the details of the method as well as an explanation of three baseline methods used for comparison: the cross-sectional PDM formulation presented in Cates et al. (2007), the disentangled intra- and inter-subject entropy approach presented in Adams et al. (2022), and the linear regression approach presented in Datar et al. (2009). In Section 3, we first utilize a synthetic dataset to provide evidence of the theoretical motivation for the proposed method, then demonstrate its efficacy on a real dataset. We utilize a population of left atrium sequences over the cardiac cycle from CINE magnetic resonance imaging (MRI) scans to demonstrate the benefits of our approach over the comparison methods in capturing non-linear shape dynamics. The left atrium is an example of dynamic motion; however, our method also applies to longitudinal studies. We employ quantitative and qualitative metrics to verify the superiority of the proposed method.

2 Methods

2.1 Notation

For spatiotemporal SSM, we define a dataset of N subjects each with a consistent time-sequence of T − shapes, each represented as a set of d − dimensional correspondence points (or particles). In this work, shape is segmented from volumetric images, so $d = 3$. To optimize particle position, we define two forms of random variables: configuration and shape space variables. These two spaces are illustrated in Figure 2.

The configuration space variable captures sample-specific geometry. It is denoted $\mathbf{X}_{n,t}$, representing the particle position on the n − th subject at the t − th time point, where $n \in [1, N]$ and $t \in [1, T]$. M − realizations of this random variable defines the point set (or PDM) of the n, t − shape: $\mathbf{x}_{n,t} = [\mathbf{x}^1_{n,t}, \mathbf{x}^2_{n,t}, \ldots, \mathbf{x}^M_{n,t}] \in \mathbb{R}^{dM}$, where a single particle $\mathbf{x}^m_{n,t} \in \mathbb{R}^d$. Here $\mathbf{x}^m_{n,t}$ is the vector of three coordinates of the m − th particle. The shape space variable describes population-level shape statistics, and is denoted as $\mathbf{Z}$. As explained in later sections, this variable is used differently in the proposed and comparison methods. In general, a single random variable $\mathbf{Z} \in \mathbb{R}^{dM}$ is used to denote the vector form of the PDM for a subject at a specific time point, where coordinates from all particles are concatenated in a single vector.

2.2 Baseline methods

2.2.1 Cross-sectional

Cross-sectional denotes the vanilla PDM optimization approach formulated for non-temporal modeling introduced in Cates et al. (2007), Cates et al. (2017). This is applied to spatiotemporal SSM by treating each time point as an independent observation, ignoring inter-subject correlation. We consider this baseline to showcase the impact of the sample independence assumption to model study designs with repeated measurements. Shape can be represented either as mesh or binary image volume, and the structure of the shape representation can vary across the cohort. Particle positions are constrained to shape surfaces and optimized by minimizing the following entropy-based objective.

$$\mathcal{Q}_{cross-sectional} = \alpha H(\mathbf{Z}) - \sum_{n=1}^{N} \sum_{t=1}^{T} H(\mathbf{X}_{n,t}) \tag{1}$$

where α is a relative weighting parameter and H is the differential entropy. Minimizing this objective balances two terms. The first encourages a compact distribution of samples in the shape space, ensuring maximal correspondence between particles across shapes (i.e., lower model complexity). Minimizing this term alone would cause the particles to collapse to a single location on all shapes, providing the most compact model possible. The second encourages the maximal uniformly-distributed spread of points across individual shapes so that the shape is faithfully represented (i.e., better geometric accuracy). Intuitively the second term causes the

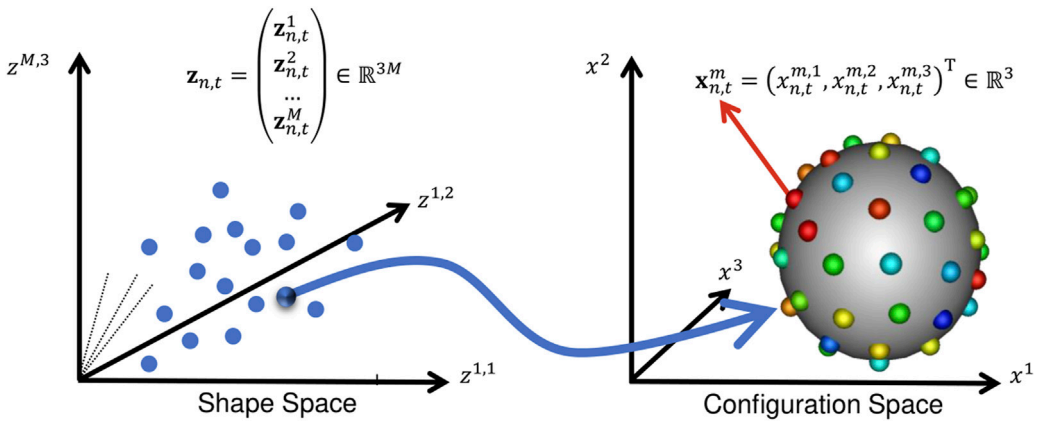

FIGURE 2
Configuration Space vs. Shape Space: This illustration aids in understanding the notation in Section 2. A point in shape space corresponds to a particle set in configuration space.

particles on a given shape to repel each other and spread out. The combination of the two entropy terms encourages particles to spread uniformly across each shape while retaining geometrically consistent locations across shapes.

Eq. (1) is optimized *via* gradient descent. This requires taking the derivative of $H(\mathbf{Z})$ with respect to particle positions. Differential entropy is defined as:

$$H(\mathbf{Z}) = -\int_{\mathcal{Z}} p(\mathbf{z}) \log p(\mathbf{z}) d\mathbf{z} = -\mathbb{E}[\log p(\mathbf{Z})]. \tag{2}$$

To make this tractable, $p(\mathbf{Z})$ is modeled parametrically as a Gaussian distribution with a population-specific mean $\boldsymbol{\mu}$ and covariance matrix $\boldsymbol{\Sigma}$. Assuming the shape space is Gaussian distributed introduces a generative statistical model:

$$\mathbf{z} = \boldsymbol{\mu} + \boldsymbol{\epsilon}, \boldsymbol{\epsilon} \sim \mathcal{N}(0, \boldsymbol{\Sigma}) \tag{3}$$

where $\boldsymbol{\epsilon}$ is a normally-distributed error. The entropy can then be estimated by:

$$H(\mathbf{Z}) \approx \frac{1}{2} \log \boldsymbol{\Sigma} = \frac{1}{2} \sum_{i=1}^{dM} \log \lambda_i \tag{4}$$

where λ_i are the eignevalues of $\boldsymbol{\Sigma}$. The covariance is estimated from the data and found to be:

$$\frac{\partial H(\mathbf{Z})}{\partial \mathbf{X}} \approx \mathbf{Y}\left(\mathbf{Y}^{\top}\mathbf{Y} + \alpha \mathbf{I}\right)^{-1} \tag{5}$$

where $\mathbf{Y}$ denotes the matrix of points minus the sample mean $\boldsymbol{\mu}$ of the ensemble, and the regularization term, α, accounts for the possibility of diminishing gradients (see Cates et al. (2007) for more detail). We get an update for each point by combining Eq. (5) with the shape-based updates explained in Cates et al. (2007). By intermittently fitting $\mathcal{N}(\boldsymbol{\mu}, \boldsymbol{\Sigma})$ to $\mathbf{Z}$ and updating the particle positions to decrease $\boldsymbol{\Sigma}$ (*via* Eq. (5)), $H(\mathbf{Z})$ is minimized producing correspondence.

2.2.2 Disentangled

Disentangled denotes the spatiotemporal SSM method proposed in Adams et al. (2022). This approach uses an adjusted optimization objective that disentangles the shape space entropy for $\mathbf{Z}_t$ and $\mathbf{Z}_n$, where $\mathbf{Z}_t$ represents shapes across subjects at a specific time point t (i.e., inter-subject variable) and $\mathbf{Z}_n$ represents shape across time for a specific subject n (i.e., intra-subject variable):

$$\mathcal{Q}_{disentangled} = \alpha\left(\sum_{t=1}^{T} H(\mathbf{Z}_t) + \sum_{n=1}^{N} H(\mathbf{Z}_n)\right) - \sum_{n=1}^{N}\sum_{t=1}^{T} H(\mathbf{X}_{n,t}) \tag{6}$$

The first term encourages intra-subject correspondence across time points, the second promotes inter-subject correspondence across sequences, and the third retains geometric accuracy across subjects and time points. The particle updates are found in the same manner as in the cross-sectional formulation, except $p(\mathbf{Z}_t)$ and $p(\mathbf{Z}_n)$ are modeled as separate Gaussian distributions with covariance matrices $\boldsymbol{\Sigma}_t$ and $\boldsymbol{\Sigma}_n$, respectively. Thus the gradient has multiple terms that follow the form of Eq. (5). Given that the Gaussian distributions are fit using overlapping samples, simultaneously minimizing $H(\mathbf{Z}_t)$ and $H(\mathbf{Z}_n)$ encourages correspondence across all subjects and time points. In this approach, the inter- and intra-subject variability are disentangled. However, by assuming $p(\mathbf{Z}_t)$ is Gaussian, the independence assumption is violated, and the temporal trajectory is diminished.

2.2.3 Linear regression

Linear regression denotes the approach to spatiotemporal SSM presented in Datar et al. (2009) where regression analysis is incorporated into in the optimization process. This approach utilizes the same cross-sectional optimization objective (Eq. (1)) but optimizes correspondence with regression against an explanatory variable, t. This is done by replacing $\boldsymbol{\mu}$ in the generative model of Eq. (3) with a function of t. The linear regression generative model can be written as:

$$\mathbf{z} = f(t) + \tilde{\boldsymbol{\epsilon}}, \tilde{\boldsymbol{\epsilon}} \sim \mathcal{N}\left(0, \tilde{\boldsymbol{\Sigma}}\right) \tag{7}$$

where

$$f(t) = \mathbf{a} + \mathbf{b}t. \tag{8}$$

and $\mathbf{a} \in \mathbb{R}^{dM}$ are fit intercepts and $\mathbf{b} \in \mathbb{R}^{dM}$ are fit slopes. In the cross-sectional formulation, minimizing $H(\mathbf{Z})$ decreases the entropy associated with $\boldsymbol{\epsilon}$, which is the difference from the mean. Here, minimizing $H(\mathbf{Z})$ decreases the entropy associated with $\tilde{\boldsymbol{\epsilon}}$, which is

the residual from the linear regression model, $f(t)$. Minimizing the residual has a similar effect to minimizing $H(\mathbf{Z}_t)$ in the disentangled approach. Intuitively, we can think of $f(t)$ as defining the mean of each $p(\mathbf{Z}_t)$ distribution. By moving particles closer to $f(t)$, we encourage inter-subject correspondence. However, unlike the disentangled approach, $f(t)$ expresses linear time-dependency rather than diminishing intra-subject trajectory.

The linear parameters $\mathbf{a}$ and $\mathbf{b}$ are estimated by minimizing the sum of squared error (SSE) (Charnes et al. (1976)). Let k be an index for a shape of a specific subject at a specific time, then for shape $\mathbf{z}_k \in \mathbb{R}^{dM}$, let $t_k \in \mathbb{R}^1$ denote the time. The SSE is then defined as:

$$SSE = \sum_k \left(\mathbf{z}_k - f(t_k)\right)^2 \tag{9}$$

Estimating *via* a least-squares fit to the correspondence data,

$$\text{argmin}_{\mathbf{a},\mathbf{b}} E(\mathbf{a},\mathbf{b}) = \sum_k [(\mathbf{a}+\mathbf{b}t_k) - \mathbf{z}_k]^\top \tilde{\mathbf{\Sigma}}^{-1} [(\mathbf{a}+\mathbf{b}t_k) - \mathbf{z}_k]. \tag{10}$$

The regression parameters are found to be:

$$\mathbf{a} = \frac{1}{M}\left(\sum_k \mathbf{z}_k - \sum_k \mathbf{b}t_k\right) \tag{11}$$

$$\mathbf{b} = \frac{\sum_k t_k \mathbf{z}_k - \sum_k t_k \sum_k \mathbf{z}_k}{\sum_k t_k^2 - \left(\sum_k t_k\right)^2} \tag{12}$$

The regression optimization algorithm is then carried out as follows. Initial correspondences are optimized using the cross-sectional approach, and initial estimates for $\mathbf{a}$ and $\mathbf{b}$ are computed. Then correspondence positions are updated by replacing $\mathbf{\Sigma}$ from the cross-sectional formulation with $\tilde{\mathbf{\Sigma}}$, the covariance of the underlying residual relative to the generative model. The two estimation problems are then interleaved and the parameters $\mathbf{a}$ and $\mathbf{b}$ are re-estimated after each iteration of the gradient descent on the particle positions.

2.3 Proposed method: Regularized principal component polynomial regression

We propose to capture the trajectory of shape across time (from 1 to T) using polynomial regression. This could be accomplished similarly to the linear regression formulation by replacing the function $f(t)$ in Eq. (7) with a polynomial. However, the spatial relationship between the particle coordinates is ignored in the linear regression approach. Each value of the dM-dimensional parameters $\mathbf{a}$ and $\mathbf{b}$ are fit separately without utilizing spatial correlations between points on a shape. This is fundamentally equivalent to fitting dM individual functions, one for each particle coordinate. There is no smoothness constraint that reflects the natural spatial regularity prior for anatomies, where the regression models for neighboring particles should be encouraged to vary smoothly over anatomical surfaces. This can lead to particle miscorrespondences across time and increases the risk of individual regression models overfitting the data noise.

To address this issue, we propose performing principal component analysis (PCA) (Abdi and Williams (2010)) on the set of shape space variables, then fitting a regularized polynomial in the principal subspace that represents the data span. PCA provides an orthogonal projection of the high dimensional particle sets, $\mathbf{z}_k \in \mathbb{R}^{dM}$, onto a lower dimensional linear space, $\mathbb{R}^{NT}$, such that the variance of the projected data is maximized. By formulation, the dimensions of the principal subspace are independent and uncorrelated; thus, defining separate polynomial functions for each principal component is justified. The principal subspace is parameterized by mean vector (denoted $\boldsymbol{\mu} \in \mathbb{R}^{dM}$), a diagonal matrix of eigenvalues (denoted $\mathbf{\Delta} \in \mathbb{R}^{NT\times NT}$), and a matrix of eigenvectors (denoted $\mathbf{U} \in \mathbb{R}^{dM\times NT}$). Note we are modeling the full data span by considering $NT-1$ eigenvectors, such that all shape variability is preserved. The projection of an instance $\mathbf{z}_k$ is defined as $\mathbf{q}_k = \mathbf{U}^\top(\mathbf{z}_k - \boldsymbol{\mu})$. These projected representations, or PCA scores, can be mapped back to shape space as follows: $\mathbf{z}_k = \mathbf{U}\mathbf{q}_k + \boldsymbol{\mu}$.

We propose to define the generative model as:

$$\mathbf{z}_k = g(t_k) + \tilde{\boldsymbol{\epsilon}}_k, \tilde{\boldsymbol{\epsilon}} \sim \mathcal{N}\left(0, \tilde{\mathbf{\Sigma}}\right) \tag{13}$$

where

$$g(t_k) = \mathbf{U}h(t_k) + \boldsymbol{\mu} \tag{14}$$

$g(t_k)$ maps a time value to a particle set, $g(t_k)$: $\mathbb{R}^1 \to \mathbb{R}^{dM}$, and $h(t_k)$ is a polynomial of degree P. $h(t_k)$: $\mathbb{R}^1 \to \mathbb{R}^{NT}$ models the shape trajectory in the principal subspace over time and is defined as:

$$h(t_k) = \boldsymbol{\beta}_0 + \boldsymbol{\beta}_1 t_k + \boldsymbol{\beta}_2 (t_k)^2 + \ldots \boldsymbol{\beta}_P (t_k)^P = \boldsymbol{\beta}_0 + \sum_{p=1}^{P} \boldsymbol{\beta}_p (t_k)^p \tag{15}$$

where $\boldsymbol{\beta}_0 \in \mathbb{R}^{NT}$ is the intercept and $\boldsymbol{\beta}_p \in \mathbb{R}^{NT}$ (where $p \in [1, P]$) are the coefficients of the polynomial. This formulation requires selecting the degree of the polynomial, $P \in [1, T-1]$. If $p = 1$ then $h(t_k)$ is linear, and if $P = T-1$ or greater, then the curve will polynomially interpolate all of the points, meaning if $N = 1$, it would perfectly fit with a residual of zero. Selecting $P = T-1$ would allow the polynomial to be maximally expressive or flexible, reducing residuals. However, there is a risk of over-fitting. Cross validation could be used to directly tune P, however this is computationally expensive. Thus to ensure model generalizability, we add regularization that biases $\boldsymbol{\beta}$ values to be small and sparse. We employ elastic net regularization (Zou and Hastie (2005)), which adds an L_1 and L_2 penalty on coefficients to the SSE cost function:

$$\sum_k \left(\mathbf{q}_k - h(t_k)\right)^2 + r_1 \sum_p \|\boldsymbol{\beta}_p\|_1 + r_2 \sum_p \|\boldsymbol{\beta}_p\|_2^2 \tag{16}$$

where r_1 and r_2 are parameters that control the weight of the regularization terms. The L_1 penalty imposes a sparsity prior on the coefficients and the L_2 penalty encourages the coefficients to have small magnitude. This allows us to set $P = T-1$ and fit only relevant coefficients while keeping the rest close to zero, also known as variable selection. Regularization is necessary for robust, generalizable polynomial regression. It prevents the $h(t_k)$ from over-fitting to lesser components in the principal subspace that capture mostly noise so that false time dependency is not incorporated into the particle updates. We utilize 5-fold cross validation to select the optimal values for the r_1 and r_2 weights each time Eq. (16) is fit.

Optimization is carried out using a similar alternating process as in the linear regression approach. First initial correspondences are fit using the cross-sectional formulation. Next the polynomial coefficients $\{\boldsymbol{\beta}_0, \boldsymbol{\beta}_1, \ldots \boldsymbol{\beta}_{T-1}\}$ are fit using Eq. (16) on the PCA scores of the initial correspondence points. Then correspondence positions are updated by replacing $\mathbf{\Sigma}$ from the cross-sectional formulation with $\tilde{\mathbf{\Sigma}}$, the covariance of the underlying residual relative to $g(t_k)$. The two estimation problems are then interleaved.

PCA is performed (updating $\mathbf{U}$ and $\boldsymbol{\mu}$) and $\boldsymbol{\beta}$-values are re-estimated after each iteration of the gradient descent on the particle positions.

The particle density is a parameter that depends on the complexity of the shape cohort. Simple, smooth shapes can be described by fewer particles than more complex, variable shapes. ShapeWorks utilizes a particle splitting strategy in optimization. Particles are added in a multi-step fashion by splitting each particle to produce a new, nearby particle at each step until the desired number of particles is reached. This coarse-to-fine optimization scheme speeds up convergence to an acceptable local minimum Cates et al. (2017). It also allows for selecting the number of particles empirically, by adding particles until the representation is deemed to capture enough details for the given application.

2.4 Evaluation metrics

2.4.1 Population variation analysis

In a PDM shape model, particle positions capture the modes of variation present in the population. Principal component analysis (PCA) is commonly utilized in SSM analysis to reduce the complexity of high dimensional shape models. PCA enables visualization and interpretation of the population-level shape variation while preserving the information captured by the PDM. We can identify the dominant modes of variation in the population as the PCA modes that account for a large portion of the overall variance. We can then visualize these modes by computing the mean of the correspondences and deforming the mean along the dominant modes to plus or minus one standard deviation. Meshes are created for such visualizations by first finding the warp transform between particles of shape with a known mesh and the particles of interest, then applying that transform to the mesh to create a new mesh that provides a denser representation of the particles of interest. In the case of spatiotemporal SSM, we would expect that the dominant modes of variation shift smoothly over time.

2.4.2 Time dependency analysis

Analysis of spatiotemporal SSM also requires evaluating how well the PDM captures the underlying time dependency. If we know the true form of the underlying time dependency function f, then we can perform regression on the particles and analyze the R^2 value:

$$R^2 = \frac{\sum_k \left(f\left(t_k\right) - \bar{\mathbf{z}}\right)}{\sum_k \left(\mathbf{z}_k - \bar{\mathbf{z}}\right)} \tag{17}$$

The best possible R^2 score is one, indicating the regression equation explains all of the variability of the data. A constant model $f(t)$ that always predicts the average of the particles, disregarding input time t, would get and R_2 score of zero. If form of the underlying time dependency is unknown, we can utilize statistical tests to analyze the significance of the shape dynamics captured by the PDM.

3 Results

This section provides experiments that illustrate and validate the proposed method. First, we validate the method with synthetically generated *ellipsoids* (3D surfaces for which all plane cross sections are either ellipses or circles). Next, we present an application of real dynamic motion; the left atrium over the cardiac cycle. An overview of these datasets is provided in Table 1. ShapeWorks Cates et al. (2017) was used for cross-sectional optimization and as a starting point for implementing the proposed and other comparison methods.

3.1 Synthetic experiment

3.1.1 Ellipsoid data generation

Synthetic shapes are useful in analyzing the performance of spatiotemporal PDM generation because the shape dynamics are formulated in a known way. We select to use a cohort of axis-aligned ellipsoids with differing x- and y-diameter values and a population consistent z-diameter value. The x-diameter represents a subject-dependent parameter that varies between subjects but not across time. The y-diameter represents a time-dependent parameter that varies across time in the same way for each subject. The x-diameter is randomly sampled for each subject from the following normal Gaussian distribution:

$$x - \text{diameter} \sim \mathcal{N}\left(0.6, 0.1\overline{3}\right) \tag{18}$$

This results in x-diameters with a high probability (99.7%) of being in the range (0.2, 1). The y-diameter is defined to vary sinusoidal over time to mimic non-linear dynamics encountered in organ cycles. For each time point, t, the y-diameter is defined as follows for all ellipsoids in the cohort:

$$y - \text{diameter}\left(t\right) = 0.6 + 0.4\sin\left(\frac{2\pi}{T}t\right) \tag{19}$$

This results in y-diameter values that vary cyclically between 0.2 and 1. We select the period and total time points to be $T = 8$. The z-diameter is fixed to be 1 across subjects and time for simplicity and 2D visualization purposes. These constraints result in ellipsoids with x, y, and z-diameters ≤ 1; thus all shapes fit within a unit cube. This scaling allows us to interpret SSE as relative SSE. Figure 3 displays plots of Eqs 18 and 19 as well as two examples of ellipsoid shape sequences.

3.1.2 Ellipsoid results

We chose to use 128 particles in generating the PDM; this is sufficient for representing the simple ellipsoid shapes (see Figure 1).

3.1.2.1 Modes of variation

As explained in Section 2.4.1, PCA is used to analyze and visualize the modes of variation captured by a PDM. Based on the construction of the ellipsoid cohort, a successful spatiotemporal shape model needs to meet the following requirements:

1. Overall variation should be described by two modes: the x and y-diameter.
2. For any given subject, inter-subject variation should be described by a single mode: the x-diameter.
3. At any given time point, intra-subject variation should be described by a single mode: the y-diameter.

The proposed method results in a PDM that meets all of these requirements. A visualization of the significant mode of variation at each time point is provided in Figure 4.

3.1.2.2 Time dependency analysis

A spatiotemporal PDM should correctly capture the shape dynamics or underlying time dependency. In the case of the ellipsoid data, the

TABLE 1 Overview of shape cohorts used in experiments.

Dataset	Number of subjects	Time points per subject	Number of particles	Optimization iterations	Covariance calculation frequency
Ellipsoid	30	8	128	1000	Every iteration
Left Atrium	28	25	1024	1000	Every 3rd iteration

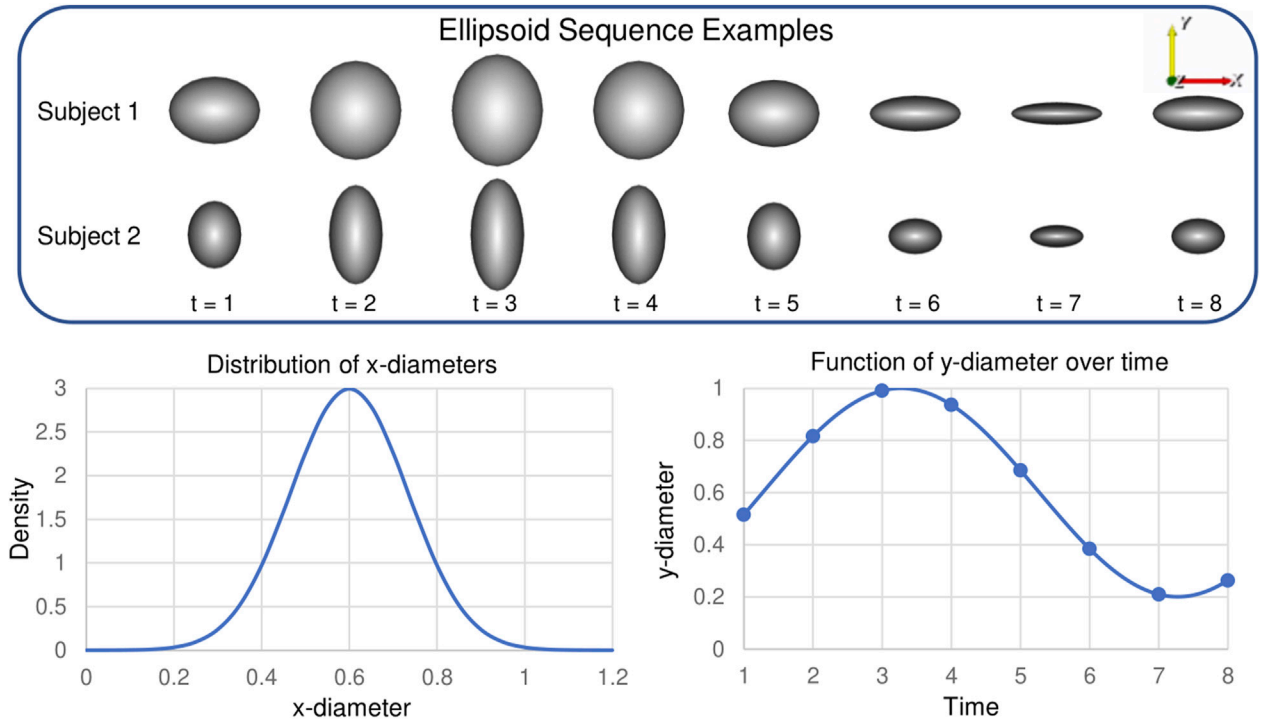

FIGURE 3
Synthetic Ellipsoid Data: Two example ellipsoids shape sequences are provided. Plots illustrate the distribution of subject-dependent *x*-diameters (Eq. 18) and the function for time-dependent *y*-diameters (Eq. 19).

dynamics are parameterized by a known sine function (Eq. (19)). Thus an ideal PDM could be expressed *via* a sine function for each subject. To test this, we use sinusoidal regression to fit subject-wise functions to the PDMs resulting from the proposed method and then quantify the residual error or SSE with respect to the fit functions. The general sine function:

$$s(t) = o + A\sin(2\pi f t) \tag{20}$$

is fit by estimating the parameters {o (offset), A (amplitude), and $2\pi f$ (period)} using least squares. The SSE resulting from subject-wise sinusoidal regression was 1.176e − 3 ± 2.468e − 3. The R^2, value (Eq. (17)) was found to be **0.999**, suggesting the proposed approach captured the time dependency very well.

3.2 Left atrium experiment

3.2.1 4D left atrium data

The left atrium shape cohort originated from 3D LGE and stacked CINE CMR scans of 28 patients presenting with atrial fibrillation between 2019 and 2020. The average patient age was 64.9 years, with 15 male and 13 female patients in the cohort. The scans for each patient used in this work were captured before a cardiac RF ablation procedure. Each CINE scan contained 25-time points covering the cardiac cycle (between R wave peaks). The temporal dimension was normalized at the time of acquisition to cover one heartbeat for each patient. Thus the number of milliseconds covered varies patient-wise. The 3D LGE images were manually segmented by a cardiac imaging expert, and this segmentation was matched to the closest CINE time-point based on CMR trigger time. The segmentation was then transformed to each time point through pairwise deformable registrations to create a full 3D segmentation for each time point Morris et al. (2020). This technique reduces the manual burden and has been shown to produce segmentations with a reasonable error when compared to fully manual segmentation Parikh et al. (2019). An example of one subject left atrium mesh sequence is provided in Figure 5.

We selected this dataset to demonstrate how the proposed approach can correctly capture highly non-linear dynamic motion.

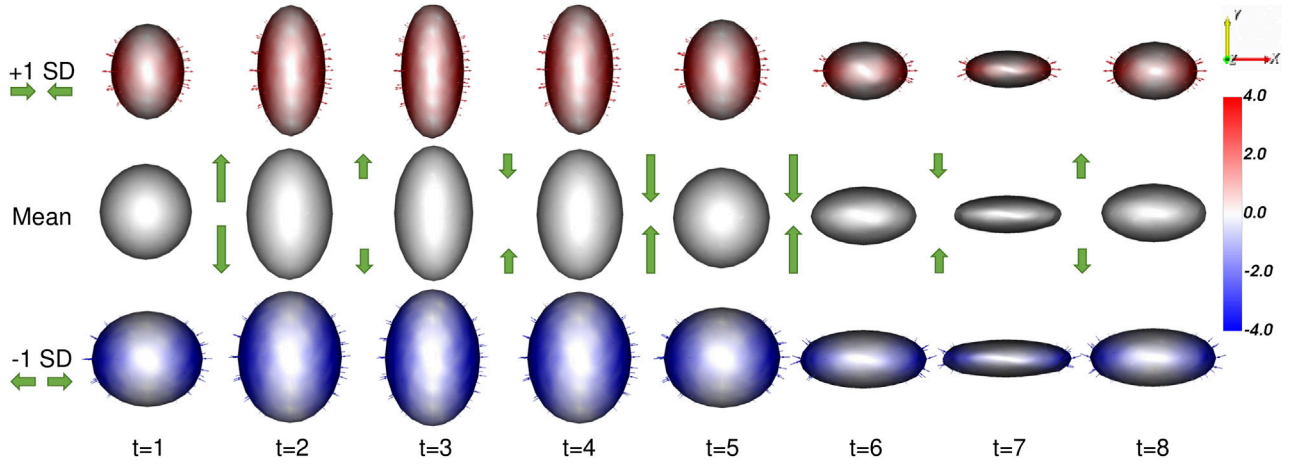

FIGURE 4
Ellipsoid Mode of Variation: The primary mode of variation from the proposed shape model is shown at each time point *via* the mean shape and ±1 standard deviations. The heat map and vectors show the difference to the associated mean. The subject-dependent *x*-diameter variation is correctly captured by the primary mode at each time point. The difference in the mean shapes across time correctly captures the time-dependent *y*-diameter. Green arrow annotations are provided to illustrate these dynamics.

The left atrium shape varies greatly across patients (see Figure 6), and atrial fibrillation affects the non-linear dynamics in differing ways. These challenges help demonstrate the robustness of the proposed spatiotemporal modeling approach.

3.2.2 Left atrium results

We built a PDM using the proposed method as well as the cross-sectional, disentangled, and linear regression comparison methods. We used 1024 particles in each left atrium PDM, which is sufficient to capture the details of the shapes. Examples of the PDM resulting from the proposed method are provided in Figure 7. Particle correspondence was maintained across both time points and subjects.

Each left atrium shape sequence covers one heartbeat, from the peak of 1 R wave to the peak of the next R wave. The spread of the volumes of the left atrium meshes across time is visualized *via* box plots in Figure 8. Here we can see the three key left atrium functions: reservoir or filling (where the volume increases), conduit or passive emptying (where volume decreases slowly in a decelerating manner), and pump or active emptying (where volume decreases quickly). Figure 9 shows the mean shapes resulting from the proposed PDM at five-time points. Heat maps show the difference to the next time point mean, where red indicates expansion and blue indicates contraction. Here we can see that the mean shapes correctly expand during the reservoir, slightly contract during the conduit, and further contract during the pump. This demonstrates that the proposed method correctly captures the non-linear dynamics of the left atrium across the cardiac cycle.

3.2.2.1 Modes of variation

As with the synthetic data experiment, we utilize PCA to analyze and visualize the modes of variation captured by the PDMs. We are interested in whether the PDM correctly captures the primary mode of variation at each time point. This primary mode is expected to be overall size or *sphericity* given the large spread of left atrium volume across subjects (Figure 8). Sphericity is calculated as $\frac{\pi^{1/3}(6*\text{Volume})^{2/3}}{\text{Surface Area}}$ where a higher value indicates the shape is closer to a sphere (for a perfect sphere, sphericity = 1). In Figure 10, we display the primary mode captured by the disentangled and proposed approaches across time from top and anterior view.

3.2.2.2 Time dependency analysis

For this experiment, we do not know the parametric form of the underlying time dependency as we did for the synthetic ellipsoid. Thus in order to analyze if the shape models are capturing the underlying time dependency, we must measure the statistical significance of the relationship between particle positions and time. Here we employ a *repeated measures ANOVA* test, which is used to determine whether or not there is a statistically significant difference between the means of multiple groups in which the same subjects show up in each group (Girden (1992)). In this case, the null hypothesis is that there is no difference in the mean particle positions at each time point. Rejecting this hypothesis means that at least one time-point mean is different from the rest, thus the PDM is capturing some time dependency. To conduct this test, we utilized the repeated measures function *RM()* from the R package MANOVA. RM (Friedrich et al. (2018)) with significance level 0.05, specifying both time and particle coordinate index as within-subject factors. For computational memory purposes, a consistent randomly selected subset of 100 particle coordinates is used. The *RM()* function calculates the modified ANOVA-type statistic (Friedrich and Pauly (2018)) for repeated measure designs with metric data. The assumptions of the multivariate repeated measures ANOVA test are met as follows:

- Random Samples: The subject that comprises the left atrium cohort are assumed to be a random sample from the population of interest.
- Independent Observations: The subject sequences in the left atrium cohort are independent of each other. Note that while shape sequences are assumed to be independent, shapes within a given sequence are not, they are considered repeated measures.
- Multivariate Normality: There are normally distributed population values for each particle position at each time

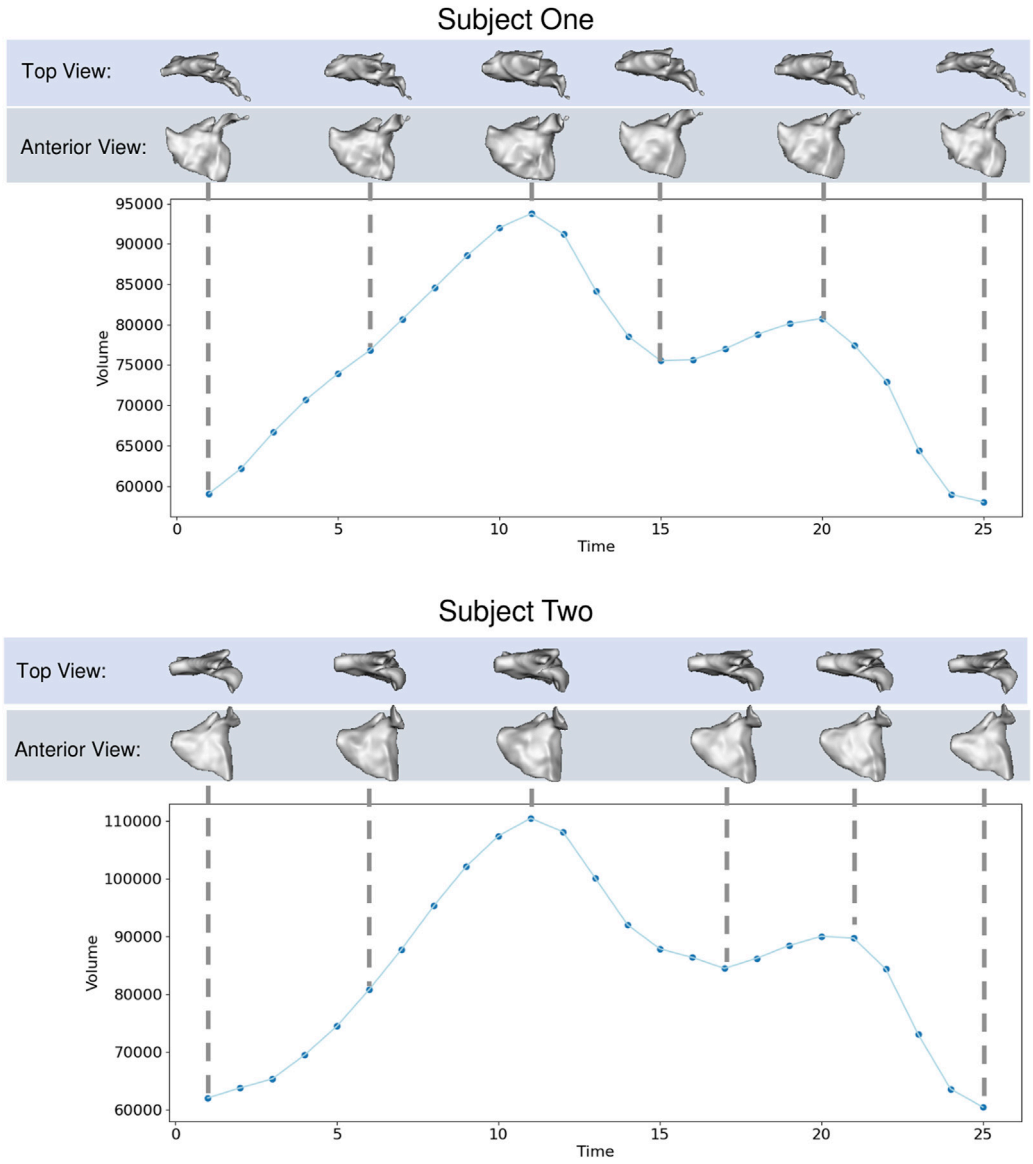

FIGURE 5
Left Atrium Examples: Left atrium volume is plotted over time for two subjects with meshes shown at selected time points from top and anterior view.

point. This was verified using the Shapiro-Wilk test, which provided p-values greater than 0.05 in all cases.

- Sphericity: As we are performing a repeated measures ANOVA factor with two levels (time and particle coordinate), the sphericity assumption is automatically met.

In Table 2, we report the test statistics and corresponding p-values for the PDM resulting from each of the optimization approaches.

3.3 Discussion

The synthetic ellipsoid experiment provides a proof-of-concept, demonstrating the efficacy of our proposed method. The resulting PDM correctly captured the inter-subject variation as the x-diameter (Figure 4) and the intra-subject variation as the y-diameter. Additionally, the resulting PDM captured the known time dependency very well (with R^2 = 0.999). The left atrium dataset served as a real use case of dynamic organ motion. Each left atrium sequence was comprised of 25 time points which covered the span of one cardiac cycle, including the reservoir, conduit, and pump phases The time dependency underlying left atrium dynamics is not parameterized by a known function. However, it is known that throughout the cardiac cycle, the amount of blood contained by the left atrium changes, resulting in a change in volume and sphericity (Figure 8). Figure 9 shows that the changes in the mean shapes resulting from the proposed approach correctly capture this underlying mechanism. In mode visualization (Figure 10), we selected not to compare against the cross-sectional and linear regression approaches as these approaches are ill-suited to capture the non-linear dynamics (as is evident by the subsequent time dependency analysis). Both the PDM generated by disentangled

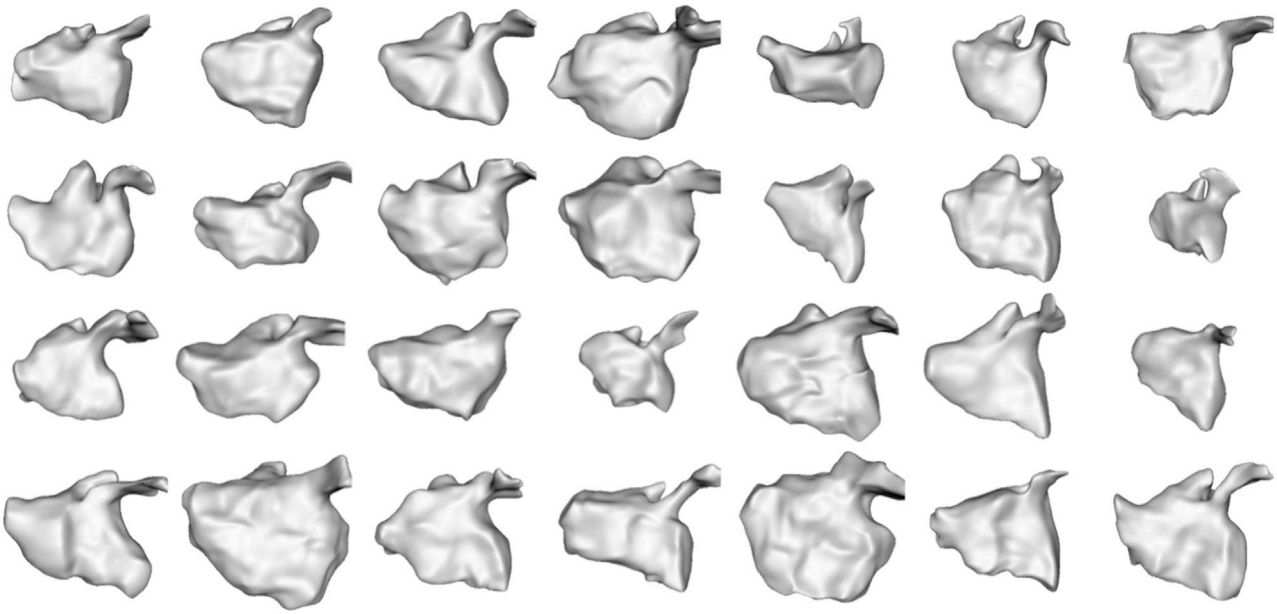

FIGURE 6
Left Atrium Subjects: The first time point mesh for all 28 subjects in the left atrium cohort is displayed from the anterior view. The left atrium shape is highly variable across subjects.

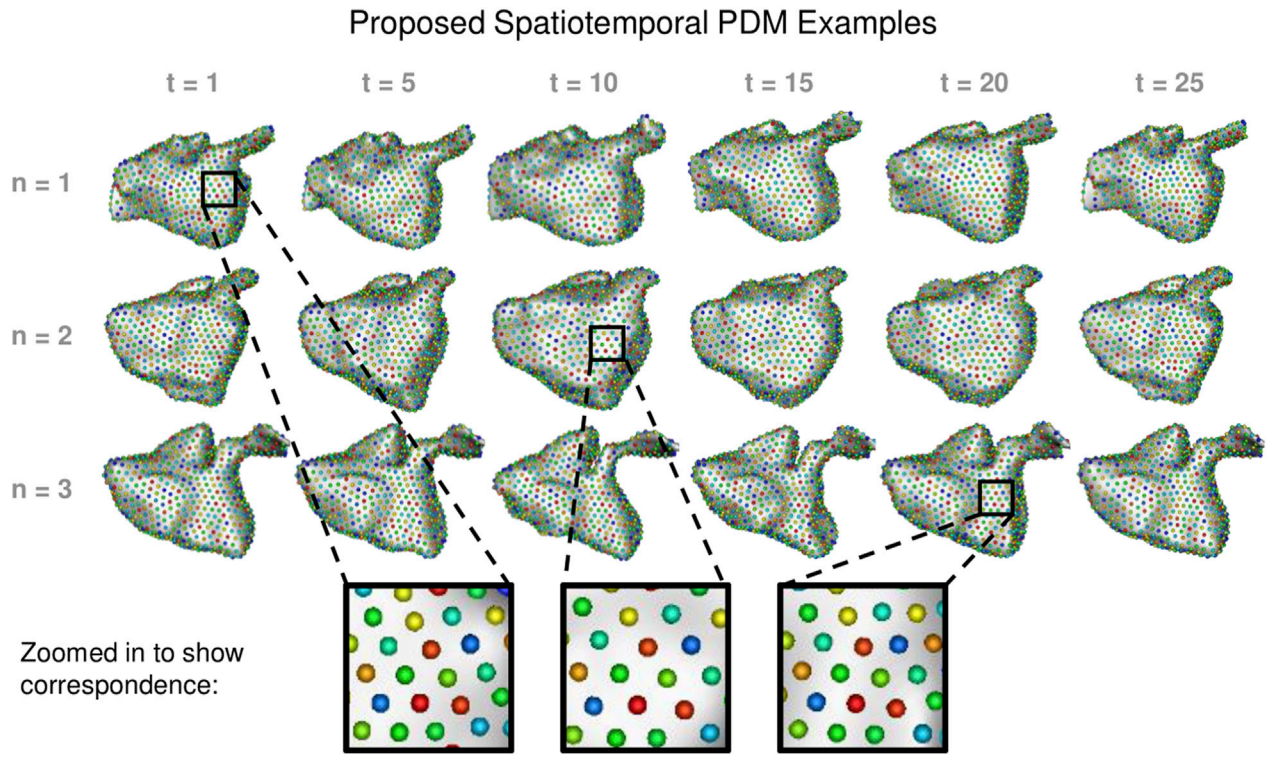

FIGURE 7
Proposed Spatiotemporal PDM Examples: Particles from the proposed approach are shown at selected time points for three different subjects. Zoomed-in boxes illustrate that particle correspondence (denoted by color) is maintained across subjects and time.

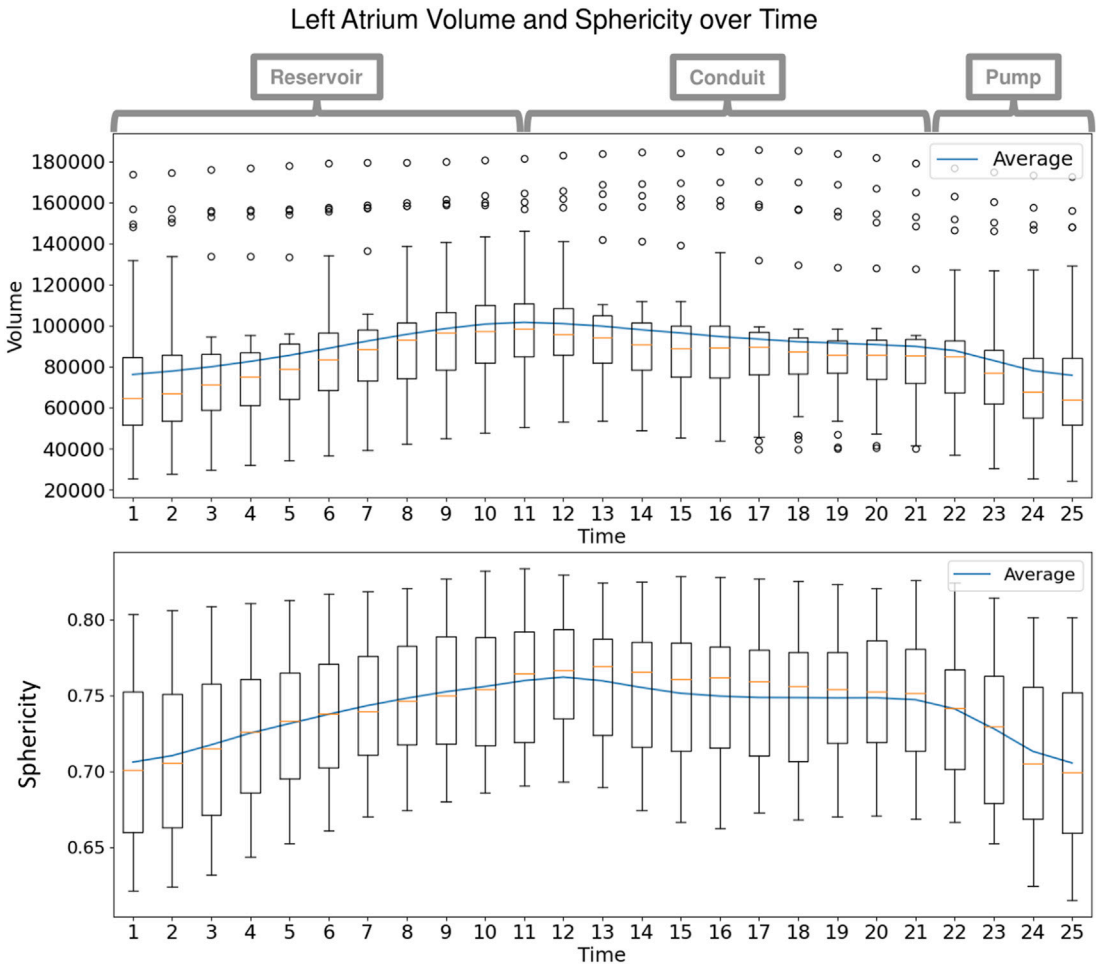

FIGURE 8
Left Atrium Volume over Time: Box plots display the spread in volume of the ground truth left atrium meshes across the subjects at each time point in the cardiac cycle. The mean volume is plotted as a blue line across time. Annotations at the top show the intervals of the three left atrium functions: reservoir during ventricular systole, conduit during early diastole, and pump during end diastole.

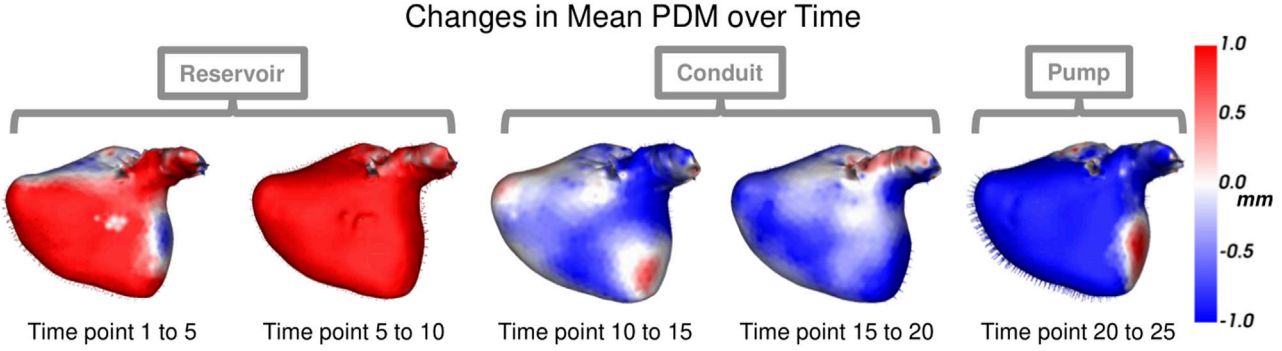

FIGURE 9
Mean Shape Dynamics: The mean shape from the proposed PDM is shown from the anterior view at a subset of time points. Heat maps show the change in shape to the next displayed time point mean shape. Here red denotes expansion, and blue denotes contraction. The mean shape dynamics correctly match the mean volume over time (Figure 8) and three left atrium function intervals: reservoir, conduit, and pump.

10.3389/fbioe.2023.1086234

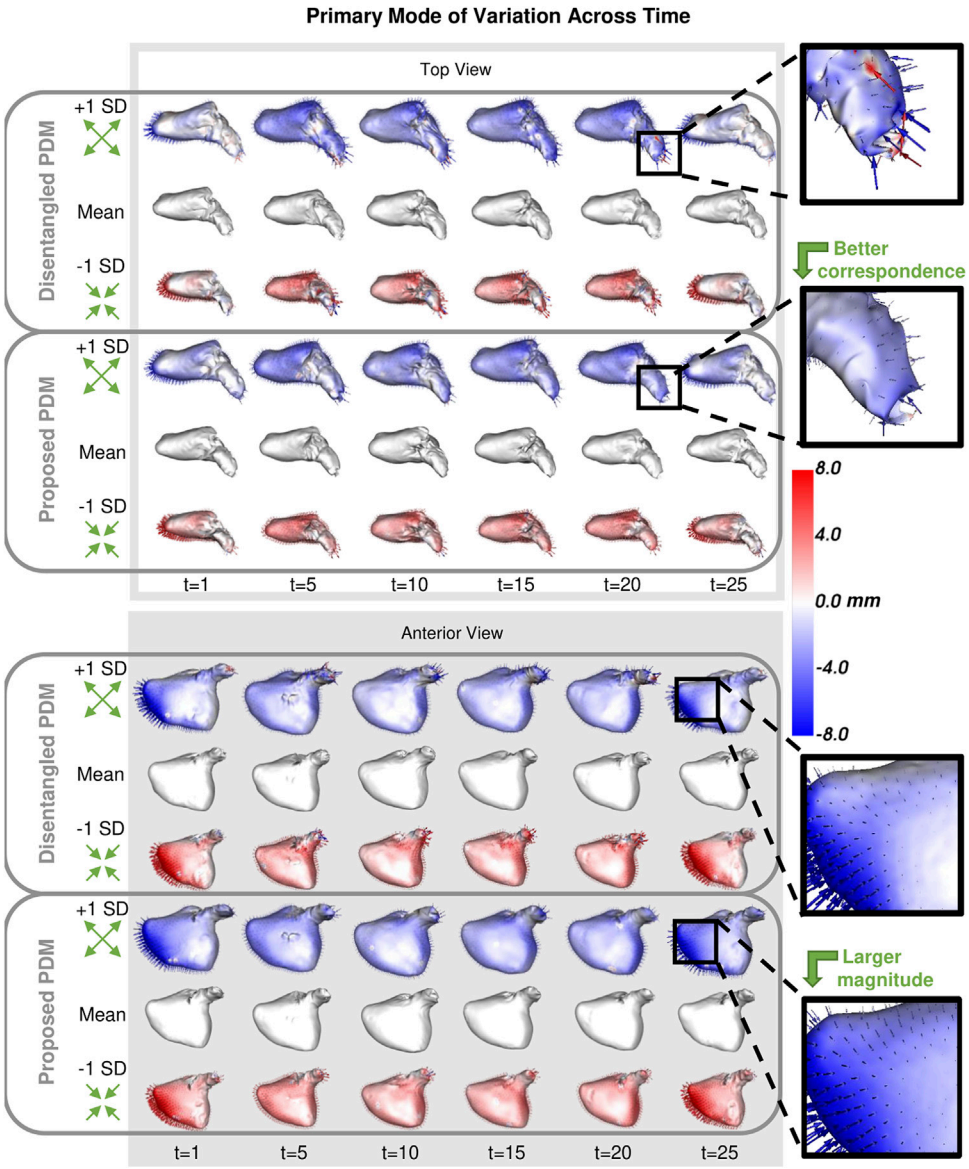

FIGURE 10
Primary Mode of Variation over Time: The primary mode of variation shown at a subset of time points for the disentangled PDM and proposed PDM shown from the top and anterior view. The heat map and vectors show the difference to the associated mean. Green arrow annotations are provided to note the change, and zoomed-in boxes on the left help illustrate some of the differences.

TABLE 2 Repeated measures ANOVA-type test statistic (larger is better, in bold) and corresponding *p*-value (smaller is better, in bold).

	Test statistic	*p*-value
Cross-Sectional	2.272	0.114
Disentangled	4.368	0.019
Linear Regression	2.568	0.090
Proposed	**9.186**	< **0.001**

optimization and the proposed optimization correctly capture the primary mode as size. However, the primary mode from the proposed approach is more consistent across time and demonstrates better correspondence. This is evident by the smooth deformation from the mean to ±1 standard deviation at each time point. The primary mode from the proposed approach also explains a larger proportion of the overall population variability than the cross-sectional, indicating a superior, more compact model.

The statistical test demonstrated that the proposed approach captured the underlying time dependency better than the baseline methods (Table 2). In the case of the cross-sectional and linear regression models, the *p*-values are greater than 0.05; thus, we accept the null hypothesis that there is no difference in the mean particle positions at each time point. The cross-sectional and linear regression approaches do not provide a PDM that captures the time dependency. The disentangled and proposed models, in contrast, provide enough evidence to reject the null hypothesis, suggesting that they are capturing the time dependency. Furthermore, the proposed PDM resulted in a larger test statistic and a *p*-value that

is an order of magnitude smaller than the disentangled PDM. This suggests the time dependency is more strongly captured by the proposed model. These experiments validate the efficacy of the proposed approach in modeling non-linear dynamic shape and surpassing the limitations of existing spatiotemporal SSM methods.

3.3.1 Limitations

The proposed approach and baseline comparison methods inherit the limitations of particle-based shape modeling. One such limitation is defining correspondence with respect to topological changes within a shape population. The proposed approach assumes that shapes within the cohort have similar features across time and subjects. Addressing anomalies or sub-groups with the cohort would require additional methodology that is out of the scope of this work. An additional limitation is this approach is not generative. While partial shape sequences can be use in PDM optimization, this model is not capable of inferring the missing time points of a subjects sequence.

3.3.2 Future work

In future work, this formulation could be extended to utilize regularized non-linear mixed effect modeling in the principal subspace rather than regression. This hierarchical approach would provide the benefit of characterizing both individual subject trends and an overall population trend. Alternatively, we could utilize a time-series generative statistical model for modeling the shape projections, such as the linear dynamical system. This generative approach would allow for inferring shapes for missing time points in subject sequences.

4 Conclusion

We presented a principled approach for statistical shape modeling of non-linear dynamic anatomies. By incorporating regularized principal component polynomial regression into the PDM optimization scheme, we are able to capture the underlying non-linear shape trajectories in a smooth, generalizable manner. We demonstrated our approach on synthetic ellipsoids as a proof-of-concept and verified that it outperforms existing methods of spatiotemporal SSM on a real cohort of left atrium over the cardiac cycle. Our approach results in SSM with inter and intra-subject correspondence that correctly captures a statistically significant underlying time dependency. Additionally, our approach does not require temporal sequences to be consistent across subjects, allowing for the use of partial observations or missing time points. Alleviating the requirement of complete sequences makes the approach more viable as medical shape data is typically scarce. Spatiotemporal SSM has great potential to inform clinical research regarding dynamic anatomy and longitudinal shape changes. Our approach provides a principled solution for capturing non-linear shape trajectories, greatly increasing the potential for SSM utilization in clinical studies.

Data availability statement

The data analyzed in this study is subject to the following licenses/restrictions: The left atrium dataset was provided by the University of Utah Division of Cardiovascular Medicine and is not publically available. Requests to access these datasets should be directed to AM, alan.morris@utah.edu.

Author contributions

JA derived the theoretical formulation, ran evaluation and statistical tests, and wrote the manuscript. NK implemented the proposed and comparison methods and ran the PDM optimization experiments. JA and NK contributed equally to this work. AM prepared the left atrium data and provided cardiac expertise and ShapeWorks guidance. SE provided the scientific guidance on the project as the senior author and helped with the ideation and conceptualization of the method. All authors assisted with interpreting results and manuscript review.

Funding

This work was supported by the National Institutes of Health under grant numbers NIBIB-U24EB029011, NIAMS-R01AR076120, NHLBI-R01HL135568, and NIBIB-R01EB016701.

Acknowledgments

The authors thank the National Institutes of Health for supporting this work. The content is solely the responsibility of the authors and does not necessarily represent the official views of the National Institutes of Health. The authors also thank the ShapeWorks team and the University of Utah Division of Cardiovascular Medicine for providing the left atrium data.

Conflict of interest

The authors declare that the research was conducted in the absence of any commercial or financial relationships that could be construed as a potential conflict of interest.

Publisher's note

References

Abdi, H., and Williams, L. J. (2010). Principal component analysis. *Wiley Interdiscip. Rev. Comput. Stat.* 2, 433–459. doi:10.1002/wics.101

Adams, J., Khan, N., Morris, A., and Elhabian, S. (2022). Spatiotemporal cardiac statistical shape modeling: A data-driven approach. *arXiv preprint arXiv:2209.02736*

Atkins, P. R., Elhabian, S. Y., Agrawal, P., Harris, M. D., Whitaker, R. T., Weiss, J. A., et al. (2017). Quantitative comparison of cortical bone thickness using correspondence-based shape modeling in patients with cam femoroacetabular impingement. *J. Orthop. Res.* 35, 1743–1753. doi:10.1002/jor.23468

Bhalodia, R., Dvoracek, L. A., Ayyash, A. M., Kavan, L., Whitaker, R., and Goldstein, J. A. (2020). Quantifying the severity of metopic craniosynostosis: A pilot study application of machine learning in craniofacial surgery. *J. Craniofacial Surg.* 31, 697–701. doi:10.1097/scs.0000000000006215

Bookstein, F. L. (1996). Biometrics, biomathematics and the morphometric synthesis. *Bull. Math. Biol.* 58, 313–365. doi:10.1007/bf02458311

Cates, J., Elhabian, S., and Whitaker, R. (2017). "Shapeworks: Particle-based shape correspondence and visualization software," in *Statistical shape and deformation analysis* (Elsevier), 257–298.

Cates, J., Fletcher, P. T., Styner, M., Shenton, M., and Whitaker, R. (2007). "Shape modeling and analysis with entropy-based particle systems," in *Ipmi* (Springer), 333–345.

Cerrolaza, J. J., Picazo, M. L., Humbert, L., Sato, Y., Rueckert, D., Ballester, M. Á. G., et al. (2019). Computational anatomy for multi-organ analysis in medical imaging: A review. *Med. Image Anal.* 56, 44–67. doi:10.1016/j.media.2019.04.002

Charnes, A., Frome, E. L., and Yu, P. L. (1976). The equivalence of generalized least squares and maximum likelihood estimates in the exponential family. *J. Am. Stat. Assoc.* 71, 169–171. doi:10.1080/01621459.1976.10481508

Cootes, T. F., Twining, C. J., and Taylor, C. J. (2004). "Diffeomorphic statistical shape models," in BMVC *(citeseer)*, 1–10.

Datar, M., Cates, J., Fletcher, P. T., Gouttard, S., Gerig, G., and Whitaker, R. (2009). "Particle based shape regression of open surfaces with applications to developmental neuroimaging," in International Conference on Medical Image Computing and Computer-Assisted Intervention. Springer, 167–174.

Datar, M., Muralidharan, P., Kumar, A., Gouttard, S., Piven, J., Gerig, G., et al. (2012). "Mixed-effects shape models for estimating longitudinal changes in anatomy," in *International workshop on spatio-temporal image analysis for longitudinal and time-series image data* (Springer), 76–87.

Davies, R. H., Twining, C. J., Cootes, T. F., Waterton, J. C., and Taylor, C. J. (2002). A minimum description length approach to statistical shape modeling. *IEEE Trans. Med. imaging* 21, 525–537. doi:10.1109/tmi.2002.1009388

Dryden, I. L., and Mardia, K. V. (2016). *Statistical shape analysis: With applications in R*, 995. John Wiley & Sons.

Fitzmaurice, G. M., and Ravichandran, C. (2008). A primer in longitudinal data analysis. *Circulation* 118, 2005–2010. doi:10.1161/circulationaha.107.714618

Friedrich, S., Konietschke, F., and Pauly, M. (2018). Analysis of multivariate data and repeated measures designs with the r package manova.rm. *arXiv preprint arXiv:1801.08002*

Friedrich, S., and Pauly, M. (2018). Mats: Inference for potentially singular and heteroscedastic manova. *J. Multivar. Analysis* 165, 166–179. doi:10.1016/j.jmva.2017.12.008

Gaffney, B. M., Hillen, T. J., Nepple, J. J., Clohisy, J. C., and Harris, M. D. (2019). Statistical shape modeling of femur shape variability in female patients with hip dysplasia. *J. Orthop. Research®* 37, 665–673. doi:10.1002/jor.24214

Gerig, G., Fishbaugh, J., and Sadeghi, N. (2016). Longitudinal modeling of appearance and shape and its potential for clinical use. *Med. Image Anal.* 33, 114–121. doi:10.16/j.media.2016.06.014

Girden, E. R. (1992). *Anova: Repeated measures*, 84. Newbury Park, CA: sage.

Goparaju, A., Csecs, I., Morris, A., Kholmovski, E., Marrouche, N., Whitaker, R., et al. (2018). "On the evaluation and validation of off-the-shelf statistical shape modeling tools: A clinical application," in *International workshop on shape in medical imaging* (Springer), 14–27.

Goparaju, A., Iyer, K., Bone, A., Hu, N., Henninger, H. B., Anderson, A. E., et al. (2022). Benchmarking off-the-shelf statistical shape modeling tools in clinical applications. *Med. Image Anal.* 76, 102271. doi:10.1016/j.media.2021.102271

Harris, M. D., Datar, M., Whitaker, R. T., Jurrus, E. R., Peters, C. L., and Anderson, A. E. (2013). Statistical shape modeling of cam femoroacetabular impingement. *J. Orthop. Res.* 31, 1620–1626. doi:10.1002/jor.22389

Miller, M. I., Younes, L., and Trouvé, A. (2014). Diffeomorphometry and geodesic positioning systems for human anatomy. *Technology* 2, 36–43. doi:10.1142/s2339547814500010

Morris, A., Kholmovski, E., Marrouche, N., Cates, J., and Elhabian, S. (2020), An image-based approach for 3d left atrium functional measurements. *2020 computing in cardiology*. IEEE, 1–4.

Nain, D., Styner, M., Niethammer, M., Levitt, J. J., Shenton, M. E., Gerig, G., et al. (2007). "Statistical shape analysis of brain structures using spherical wavelets," in 2007 4th IEEE International Symposium on Biomedical Imaging: From Nano to Macro (IEEE), 209–212.

Ovsjanikov, M., Ben-Chen, M., Solomon, J., Butscher, A., and Guibas, L. (2012). Functional maps: A flexible representation of maps between shapes. *ACM Trans. Graph. (ToG)* 31, 1–11. doi:10.1145/2185520.2185526

Parikh, S., Goparaju, A., Bhalodia, R., Loveless, B., Morris, A., Cates, J., et al. (2019), Efficient segmentation pipeline using diffeomorphic image registration: A validation study. *2019 computing in cardiology (CinC)*. IEEE, 1–4.

Styner, M., Oguz, I., Xu, S., Brechbuehler, C., Pantazis, D., Levitt, J., et al. (2006). Framework for the statistical shape analysis of brain structures using spharm-pdm. *Insight J.* 2006 (1071), 242–250.

Zou, H., and Hastie, T. (2005). Regularization and variable selection via the elastic net. *J. R. Stat. Soc. Ser. B Stat. Methodol.* 67, 301–320. doi:10.1111/j.1467-9868.2005.00503.x

frontiers | Frontiers in Bioengineering and Biotechnology

TYPE Original Research
PUBLISHED 16 February 2023
DOI 10.3389/fbioe.2023.1089113

OPEN ACCESS

EDITED BY
Mario Rothbauer,
Medical University of Vienna, Austria

REVIEWED BY
Seungik Baek,
Michigan State University, United States
Peter Laz,
University of Denver, United States

*CORRESPONDENCE
Nawazish Khan,
nawazish.khan@sci.utah.edu

SPECIALTY SECTION
This article was submitted to Biomechanics, a section of the journal Frontiers in Bioengineering and Biotechnology

RECEIVED 03 November 2022
ACCEPTED 06 February 2023
PUBLISHED 16 February 2023

CITATION
Khan N, Peterson AC, Aubert B, Morris A, Atkins PR, Lenz AL, Anderson AE and Elhabian SY (2023), Statistical multi-level shape models for scalable modeling of multi-organ anatomies.
Front. Bioeng. Biotechnol. 11:1089113.
doi: 10.3389/fbioe.2023.1089113

Statistical multi-level shape models for scalable modeling of multi-organ anatomies

Nawazish Khan[1,2]*, Andrew C. Peterson[3], Benjamin Aubert[4], Alan Morris[1], Penny R. Atkins[1,3], Amy L. Lenz[3], Andrew E. Anderson[1,3] and Shireen Y. Elhabian[1,2]

[1]Scientific Computing and Imaging Institute, University of Utah, Salt Lake City, UT, United States, [2]School of Computing, University of Utah, Salt Lake City, UT, United States, [3]Department of Orthopaedics, School of Medicine, University of Utah, Salt Lake City, UT, United States, [4]EOS Imaging Inc., Montreal, QC, Canada

Statistical shape modeling is an indispensable tool in the quantitative analysis of anatomies. Particle-based shape modeling (PSM) is a state-of-the-art approach that enables the learning of population-level shape representation from medical imaging data (e.g., CT, MRI) and the associated 3D models of anatomy generated from them. PSM optimizes the placement of a dense set of landmarks (i.e., correspondence points) on a given shape cohort. PSM supports multi-organ modeling as a particular case of the conventional single-organ framework *via* a global statistical model, where multi-structure anatomy is considered as a single structure. However, global multi-organ models are not scalable for many organs, induce anatomical inconsistencies, and result in entangled shape statistics where modes of shape variation reflect both within- and between-organ variations. Hence, there is a need for an efficient modeling approach that can capture the inter-organ relations (i.e., pose variations) of the complex anatomy while simultaneously optimizing the morphological changes of each organ and capturing the population-level statistics. This paper leverages the PSM approach and proposes a new approach for correspondence-point optimization of multiple organs that overcomes these limitations. The central idea of multilevel component analysis, is that the shape statistics consists of two mutually orthogonal subspaces: the within-organ subspace and the between-organ subspace. We formulate the correspondence optimization objective using this generative model. We evaluate the proposed method using synthetic shape data and clinical data for articulated joint structures of the spine, foot and ankle, and hip joint.

KEYWORDS

computational anatomy, hierarchical statistical models, statistical shape modeling, computational morphometrics, shape and relative pose models, vertebra, foot and ankle, hip and pelvis

1 Introduction

Human anatomy is spatially and hierarchically organized into complex, interrelated, and interacting organs with definite shapes (i.e., forms) tied to their function. These shapes vary substantially across populations Cerrolaza et al. (2019). Form and function can also adapt in response to many biological processes, including morphogenesis, injury, disease, and death Costafreda et al. (2011), Lindberg et al. (2012), Carriere et al. (2014), Zhang et al. (2009), and Sciancalepore et al. (2012). Statistical shape modeling

(SSM) is an enabling quantitative tool in medical and biological sciences to study form and function. SSM parses the anatomy into a quantitative representation that facilitates testing of biologically relevant hypotheses by defining an *anatomical mapping across a population* of 3D models of anatomy generated from medical imaging data (e.g., CT, MRI). Studying multiple organs together, especially for complex anatomical structures like that of the subcortical brain or articulated joints, can reveal crucial insights, which can help explore links between changes in anatomy due to pathology and the underlying biological process. Thus, most clinical applications encourage statistical shape modeling of multiple organs together instead of single organ structures outside their multi-organ context Gorczowski et al. (2007). Unlike a single-organ model, a multi-organ shape model should capture both organ-specific variability and inter-organ relations to accurately represent complex anatomies and derive quantitative metrics on mechanisms and progression of biological processes. Inter-organ relations can also provide contextual information for expert-driven and automated interpretation of medical images in applications such as radiotherapy planning, diagnosis, and treatment planning Fritscher et al. (2014) and Si and Heng (2017). Furthermore, multi-organ models can advantageously introduce statistical priors for complex periodic multi-structures, such as the spine, to apply non-rigid or poly-rigid image registration in intraoperative guidance imaging Drobny et al. (2020). However, inter-organ relations are either user-defined (e.g., Cerrolaza et al. (2013) and Cerrolaza et al. (2011), limited by their generality and practicality for an arbitrary number of organs, or usually estimated in isolation by learning intra-organ variability, resulting in sub-optimal models Cerrolaza et al. (2019). Moreover, hierarchical models such as Lecron et al. (2012) rely on pre-built shape models that were constructed independently, for further statistical analyses, sacrificing anatomical integrity and inducing anatomical inconsistencies Cerrolaza et al. (2019).

Anatomical mappings can be represented implicitly using deformation fields or explicitly using a set of landmarks (or point correspondences) that are defined consistently across the population. Implicit representations hold promise, but finding the transformation that quantifies differences among shapes is challenging. Explicit representations, which are the focus of this work, provide more interpretable results for statistical analyses and visualization Zachow (2015). These mappings should be learned from the study population in a data-driven manner to capture the underlying population-specific morphological variability Kulis et al. (2013). Approaches for establishing such mappings that rely on pairwise comparisons (e.g., Styner et al. (2006) and Jenkinson et al. (2012)] typically require a predefined atlas for initialization, leading to biased and suboptimal models Goparaju et al. (2022). Group-wise approaches [e.g., Durrleman et al. (2014) and Cates et al. (2017a)], on the other hand, observe the entire population to quantify the quality of shape correspondences, and hence better reflect the underlying population variability Goparaju et al. (2022). Particle-based shape modeling (PSM) Cates et al. (2007) and Cates et al. (2017a), in particular, is a state-of-the-art computational approach for constructing point distribution models (PDM) *via* automatically placing a dense set of corresponding landmarks on a set of shapes. The scientific and clinical utility of PSM have been demonstrated in image and shape analysis [e.g., Bhalodia et al. (2021) and Shigwan et al. (2020)], neuroscience [e.g., Sultana et al. (2019) and Audette et al. (2017)], biological phenotyping [e.g., Jones et al. (2013) and Cates et al. (2017b)], cardiology [e.g., Bieging et al. (2018) and Goparaju et al. (2022)], and orthopaedics [e.g., Lenz et al. (2021), Goparaju et al. (2022), Krähenbühl et al. (2020), Jacxsens et al. (2020), Atkins et al. (2017a), Atkins et al. (2019), Atkins et al. (2017b), and Atkins et al. (2022)].

PSM supports multi-organ modeling using a global statistical model, similar to other landmarks-based models [e.g., Picazo et al. (2018), Kokko et al. (2021), and Li et al. (2016)]. This is due to its computational simplicity and benefits over single-organ models Wilms et al. (2017). In this modeling scheme, the multi-structure anatomy is considered a single structure and landmarks positions are optimized in the full shared shape space Cates et al. (2008) and Agrawal et al. (2020). However, global multi-organ models suffer from anatomical inconsistencies (e.g., overlapping neighboring organs) and make subtle morphological differences within each organ less obvious Cerrolaza et al. (2019). Global shape models are not computationally and statistically scalable to an arbitrarily large number of organs, with each represented by many landmarks to describe their shapes accurately. Thus, substantially large sample sizes are indispensable for global shape models to have sufficient statistical power and this being reinforced by higher dimensionality of the number of landmarks, leads to a significant memory footprint for correlations computation Cerrolaza et al. (2019) and Jung and Marron (2009). Furthermore, optimizing in the shared shape space of multi-organ structures does not separate shape from pose variations and entangles both intra- and inter-organ modes of variation, making the interpretation of the articulated shape models challenging to relate to clinically relevant insights necessary for the diagnosis of joint misalignment, pathological deformity, and bone abnormalities. On the other hand, the individual modeling approach for multi-organ complexes independently builds the statistical model of each organ. These models fail to capture the inter-organ anatomical patterns completely Yao et al. (2016).

In this paper, we propose a multi-level statistical shape modeling approach that overcomes the limitations of the global shape modeling scheme. We disentangle the shared shape space used in the global shape modeling technique into within-organ and between-organs subspaces to model the intra-organ shape and inter-organ pose variabilities. We formulate the training objective to optimize the point correspondences across the ensemble of multi-organ anatomies in the disentangled shape space, which makes it easily scalable to model multiple organs together without generating anatomical inconsistencies. We demonstrate that the Point Distribution Model (PDM) generated from the proposed shape modeling technique effectively captures the shape variation of each organ while simultaneously reflecting the relative pose variations between the organs in the shape complex. We use synthetic data for proof of concept and real clinical data with downstream validation tasks to demonstrate the efficacy of the proposed method for

articulated structures. The proposed shape modeling technique is referred to as the Multi-Level Multi-Organ (MLMO) shape modeling technique.

2 Methodology

2.1 Background—Particle-based shape modeling for single-organ anatomy

We define the shape surface for an organ structure as a smooth manifold of codimension one, which is a subset of $\mathbb{R}^d$. We have $d = 3$ in this work as the shapes are segmented from 3D volumetric images. The particle-based shape modeling (PSM) approach optimizes population-specific shape representations by sampling each surface in a consistently ordered fashion. Each surface $\mathcal{S} \subset \mathbb{R}^d$ can be sampled using a discrete set of M points $\{\mathbf{x}^m \in \mathbb{R}^d\}_{m=1}^M$ that define the configuration space to capture the geometry for each sample. The particle positions $\mathbf{z} = (\mathbf{x}^1, \mathbf{x}^2, \ldots \mathbf{x}^M)$ are the realizations of the random variable $\mathbf{X}$ for configuration space associated with its probability density function $p(\mathbf{X} = \mathbf{x})$. Consider an ensemble $\mathcal{E}$ that consists of shape surfaces defined for N subjects as $\mathcal{E} = \{\mathbf{z}_1, \mathbf{z}_2, \ldots, \mathbf{z}_N\}$ such that each surface has its own set of particles after factoring out global transformations that are irrelevant to modeling shape variations. This defines the shape space such that the vector of M particle positions for each surface in the configuration space is mapped to a single point in dM − dimensional shape space. Each surface $\mathbf{z}_n$ of the ensemble is an instance of the shape space random variable $\mathbf{Z}$ associated with its probability density function $p(\mathbf{Z} = \mathbf{z})$. PSM assumes that the shape space is modeled by a Gaussian distribution as $\mathbf{Z} \sim (\boldsymbol{\mu}, \boldsymbol{\Sigma})$. Correspondences across the ensemble are established by minimizing an entropy-based objective function that is a combined cost function $\mathcal{Q}$ for shape correspondence and surface sampling defined as:

$$\mathcal{Q} = H(\mathbf{Z}) - \sum_{n=1}^{N} H(\mathbf{X}_n) \tag{1}$$

where $H(.)$ denotes the estimation of the entropy function. The differential entropy of $p(\mathbf{X})$ is given as

$$\begin{aligned} H(\mathbf{X}) &= -\int_{\mathcal{E}} p(\mathbf{X}) \log p(\mathbf{X}) dx \\ &= -E\{\log p(\mathbf{X})\} \approx -\frac{1}{M} \sum_{m=1}^{M} \log p(\mathbf{x}_m) \end{aligned} \tag{2}$$

The cost function Q is minimized using a gradient descent algorithm. The first term in Eq. 1 encourages a compact distribution of the samples in the shape space such that particles are in good correspondence across the shapes. The second term favors uniformly-distributed correspondence positions on the shape surfaces to accurately capture the geometric details of the shape. For a stable optimization of these terms, shape statistics $\boldsymbol{\mu}$ and $\boldsymbol{\Sigma}$ are allowed to lag when particle positions are updated and the negative gradient update $-\frac{\partial H(\mathbf{Z})}{\partial \mathbf{Z}}$ in the shape space is computed once per optimization iteration. The individual shape-based updates in configuration space $\frac{\partial H(\mathbf{X}_n)}{\partial \mathbf{X}_n}$ are then combined to provide the update for each particle. More details related to the optimization technique and gradient updates can be found in Cates et al. (2007) and Cates et al. (2017a).

2.2 Multi-organ shape modeling—Problem formulation

A multi-organ (or multi-object) shape complex is defined as a set of solid shapes, each representing a single and connected biological structure, assembled together within a common coordinate frame. This shape complex contains the shape, scale, and positional information for each organ structure, thereby containing the relative pose and orientation between different organ structures in the shape complex. Multi-organ shape structures have alignment variations between the organs that reflect subject-wise anatomical variations relevant to how the organs are relatively positioned and aligned with respect to each other. These alignment variations should not be factored out by the initial rigid alignment techniques that are usually performed prior to the shape modeling process. These geometric relationships between the organs are of significant importance, especially in biomechanics-based shape modeling Agrawal et al. (2020), Zhang et al. (2016), and Kainmueller et al. (2009).

Here, we define the notations for the multi-organ shape modeling problem that will be used in the following sections. Given an ensemble $\mathcal{E}$ of N subjects such that each subject has 3D surfaces defined for K organs. Thus, the ensemble is defined as $\mathcal{E} = \{\{\mathbf{z}_{n,k}\}_{k=1}^K\}_{n=1}^N$. Each surface (or shape) is represented by a set of M_k correspondence particles, where each particle is d − dimensional[1] such that $M = \sum_{k=1}^K M_k$ is the total number of particles representing a multi-organ shape sample. $\mathbf{x}_{n,k}$ is the realization of the configuration space random variable $\mathbf{X}_{n,k}$ for the n − th subject and k − th organ and the corresponding shape space variable is $\mathbf{Z}_{n,k}$ such that its realization is $\mathbf{z}_{n,k} = [\mathbf{x}_{n,k}^1, \mathbf{x}_{n,k}^2, \ldots, \mathbf{x}_{n,k}^{M_k}] \in \mathbb{R}^{dM_k}$.

2.3 Global shape modeling for multi-object complexes

To capture shape statistics in multi-organ anatomies, Cates et al. (2008) extended the concept of particle-based shape modeling for single objects as described in Section 2.1, and presented an optimization scheme where multiple organs are treated as a single structure. Here, the shape space variable $\mathbf{Z} \in \mathbb{R}^{dM}$ is the concatenation of the random variables defined for each organ $\mathbf{Z}_{n,k} \in \mathbb{R}^{dM_k}$. The optimization objective here is the combined ensemble and shape cost function which is defined as:

$$\mathcal{Q} = \alpha H(\mathbf{Z}) - \sum_{k=1}^{K} \sum_{n=1}^{N} H(\mathbf{X}_{n,k}) \tag{3}$$

where H is the differential entropy of the corresponding random variable and α is the relative weighting parameter. The first term in

1 $d = 3$ in this work, however PSM and the proposed approach is flexible to model any dimension.

Eq. 3 represents the ensemble entropy in shape space $\mathbf{Z}$ and minimizing this produces a compact representation of the model, and hence lowers the complexity of the shape model. The second term in Eq. 3 represents the surface entropy in the configuration space $\mathbf{X}$, which on maximizing gives a uniform distribution of correspondence particles across shape surfaces. This formulation assumes that object-level correspondence of each organ is known a priori. This formulation decouples the spatial interaction between the particles on different organs by constraining each particle to stay on the shape surface of a single organ, but the ensemble entropy is minimized in a shared shape space by modeling the entire multi-organ shape sample $\mathbf{z} \in \mathbb{R}^{dM}$ as an instance of the random variable $\mathbf{Z}$ that is assumed to be Gaussian-distributed and follows a generative model described as,

$$\mathbf{z} = \boldsymbol{\mu} + \boldsymbol{\epsilon}, \boldsymbol{\epsilon} \sim \mathcal{N}(\mathbf{0}, \boldsymbol{\Sigma}) \tag{4}$$

The covariance matrix $\boldsymbol{\Sigma}$ includes all particle positions across the entire multi-organ shape, forcing the optimization to take place in the shared shape space of all organs. Minimizing the entropy of this distribution favors high spatial correlations between corresponding samples of the entire multi-organ shape complex across the population without incorporating how these organs interact with each other across the population. Treating the multi-organ complex as a single object, leads to the oversimplification of the complex human anatomy and fails to capture the variabilities within the organ and the interactions between the organ. To produce a compact statistical representation of the shape complex as a whole, the global shape modeling technique might not capture the individual morphological changes of each organ and their interactions correctly by placing correspondence particles that are anatomically inconsistent.

2.4 Multi-level component analysis

One of the widely used approaches to characterize the variability of shapes represented by a point distribution model (PDM) is the Principal Component Analysis (PCA) that allow both visualization and dimensionality reduction. The basis vectors defined by PCA are optimal in the least squares sense as each basis vector is chosen to minimize the sum-of-squares (SSQ) residual error in data. The basis vectors describe the independent modes of variation by accounting for the correlations among the correspondence positions of the particles.

The Multilevel Component Analysis (MLCA) Timmerman (2006), an extension of PCA, is used to analyze hierarchical structures in multi-object models. More specifically, the correspondence particle $\mathbf{z}^m_{n,k} \in \mathbb{R}^d$ is observed at two levels—a local within level, where shape variation is identified in each individual organ, and at a global level, where the relative pose of each organ is observed in the multi-organ shape complex. Using this model, the generative model of a particle can be formulated as follows:

$$\mathbf{z}^m_{n,k} = \underbrace{\bar{\mathbf{z}}_n}_{\text{offset}} + \underbrace{\left(\mathbf{z}^m_{n,k} - \bar{\mathbf{z}}_{n,k}\right)}_{\text{within-organ}} + \underbrace{\left(\bar{\mathbf{z}}_{n,k} - \bar{\mathbf{z}}_n\right)}_{\text{between-organs}}, \tag{5}$$

where $\bar{\mathbf{z}}_n = \frac{1}{M}\sum_{k=1}^{K}\sum_{m=1}^{M_k}\mathbf{z}^m_{n,k}$ is the offset term representing the global centroid of the multi-organ shape complex and $\bar{\mathbf{z}}_{n,k} = \frac{1}{M_k}\sum_{m=1}^{M_k}\mathbf{z}^m_{n,k}$ is the centroid of the $k-$ th organ. The second term of Eq. 5 encodes within shape organ variations, which is the deviation of the correspondence particle of each organ from its own centroid. The last term of Eq. 5 encodes the between organs pose variations, which is the relative pose changes of each organ in the multi-organ shape complex from the global centroid of the shape complex.

MLCA uses the notion of Analysis of Variance (ANOVA) to split the total sum of squares into components that are related to the effects used in the model. For Eq.5, we can write SSQ residual errors as:

$$\underbrace{\sum_{m,n,k}\left(\mathbf{z}^m_{n,k}\right)^2}_{ssq_{total}} = \underbrace{\sum_{m,n,k}\left(\mathbf{z}^m_{n,k} - \bar{\mathbf{z}}_{n,k}\right)^2}_{ssq_{within}} + \underbrace{\sum_{n,k}\left(\bar{\mathbf{z}}_{n,k} - \bar{\mathbf{z}}_n\right)^2}_{ssq_{between}} \tag{6}$$

In Component Analysis (CA) models such as PCA, the main goal is to approximate the data in the best possible manner in the least-squares sense. By Eq. 6, the total sum of squares for correspondence particle data can be split into two levels—within and between, then it is natural to explain the best possible sum of squares at each level by building a two-level component model. Thus, MLCA gives a general formulation of such a two-level component model. Here, we build the component model at each level—in the within subspace for each organ and in the between subspace for all the organs together. This gives us $K + 1$ mutually orthogonal subspaces and we assume each of these subspaces can be modeled by a Gaussian distribution. Thus, analogous to PCA, the shape vector describing each organ $\mathbf{z}_k \in \mathbb{R}^{dM_k}$ can be expressed by a linear combination of the basis vectors of the within subspace and between subspace as follows:

$$\mathbf{z}_k = \boldsymbol{\mu} + \mathbf{U}^W_k\boldsymbol{\alpha}^W_k + \mathbf{U}^B_k\boldsymbol{\alpha}^B_k \tag{7}$$

where $\boldsymbol{\mu} \in \mathbb{R}^{dM_k}$ is the consolidated mean of the within and between subspace and the offset, $\mathbf{U}^W_k \in \mathbb{R}^{dM_k \times N}$ is the matrix of principal components of the within subspace of organ k and $\mathbf{U}^B_k \in \mathbb{R}^{dM_k \times N}$ is the sub-matrix of principal components of between subspace that belongs to organ k. The coefficient vectors $\boldsymbol{\alpha}^W_k \in \mathbb{R}^N$ of the within subspace are distributed according to $\mathcal{N}(\mathbf{0}, \boldsymbol{\Sigma}^W_k)$ and the coefficient vectors $\boldsymbol{\alpha}^B \in \mathbb{R}^N$ are distributed according to $\mathcal{N}(\mathbf{0}, \boldsymbol{\Sigma}^B)$ where $\boldsymbol{\Sigma}^\star$ denotes the covariance matrix of the within subspaces of each organ and the between subspace defined respectively by the within and between terms of Eq. 5. This formulation of MLCA, gives us an analysis technique by which we can probe the configuration variations of articulated joints or other multi-organ anatomies separately from the morphological or shape variations.

2.5 Proposed shape modeling approach—multi-level multi-organ shape modeling

We propose a novel optimization scheme for multi-organ shape complexes that disentangles the shared shape space of the multiple organs into relevant subspaces. We build our hypothesis from the generative model in Eq. 7 of multi-level component analysis. The shared shape space for the multi-organ structure can be split into individual subspaces for each organ, which models the shape variability within each organ, and a common subspace, which

accounts for the relative pose variability between the organs in the shape sample. The random variable $\mathbf{Z}$ is replaced by a sequence of random variables $\mathbf{Z}_k^W$, which models the shape variability of each organ, and another random variable $\mathbf{Z}^B$ for the interactions between each organ across the population. The shape morphology variations for each organ k and their relative alignment in the multi-organ complex are encoded in the within vectors for each organ $\mathbf{z}_k^W$ and a between vector $\mathbf{z}^B$ by splitting the particles in the shape vector $\mathbf{z}$ in terms of the deviation of the centroid of each organ and centroid of the multi-organ complex according to within and between terms of Eq. 5. We propose a new cost function that minimizes the entropy of each individual within subspaces and between subspace as follows.

$$\mathcal{Q} = \alpha_W \sum_{k=1}^{K} H\left(\mathbf{Z}_k^W\right) + \alpha_B H\left(\mathbf{Z}^B\right) - \sum_{k=1}^{K} \sum_{n=1}^{N} H\left(\mathbf{X}_{n,k}\right) \tag{8}$$

where H is the differential entropy function; α_W and α_B are the relative weighting parameters for the within and between subspaces, respectively, that define the contribution of the correspondence objective of that subspace to the particle optimization process. The within subspaces for each organ and the between subspace are modeled as Gaussian distributions $p(\mathbf{Z}_k^W)$ and $p\ (\mathbf{Z}^B)$ with covariances $\mathbf{\Sigma}_k^W$ and $\mathbf{\Sigma}^B$, respectively. We estimate these covariance matrices directly from the data using the within and between parts of Eq. 5. The objective function Q in the above Eq. 8 is minimized in such a way that correspondence particle updates for the within and between subspaces are made in an alternating fashion. We first make particle updates by computing the gradient in the within subspace for each organ and then make changes in the relative alignment in each organ by computing the gradient updates in the between subspace. In this way, we disentangle the shape from pose in the optimization process, while simultaneously preserving the anatomical correctness of the articulation of the joint. The entropy terms for the within and between subspace in Eq. 8 are given by:

$$H\left(\mathbf{Z}_k^W\right) \approx \frac{1}{2}\log \mathbf{\Sigma}_k^W = \frac{1}{2}\sum_{i=1}^{dM_k} \log \lambda_{k,i}^W \tag{9}$$

$$H\left(\mathbf{Z}^B\right) \approx \frac{1}{2}\log \mathbf{\Sigma}^B = \frac{1}{2}\sum_{i=1}^{dK} \log \lambda_i^B \tag{10}$$

where $\lambda_{k,i}^W$ and λ_i^B denotes the eigenvalues of $\mathbf{\Sigma}_k^W$ and $\mathbf{\Sigma}^B$ respectively. The gradient updates of each subspace is computed as:

$$\frac{-\partial H\left(\mathbf{Z}^{\bigstar}\right)}{\partial \mathbf{X}} \approx \mathbf{Y}^{\bigstar}\left(\mathbf{Y}^{\bigstar\top}\mathbf{Y}^{\bigstar} + \alpha\mathbf{I}\right)^{-1} \tag{11}$$

where $\mathbf{Z}^{\bigstar}$ denotes the subspace and $\mathbf{Y}^{\bigstar}$ denotes the mean centered matrix of that subspace. Here, $\bigstar$ can be W or B representing the within and between subspace, respectively. The dimensionality of the particle correlation matrices in these disentangled within and between subspaces $\mathbf{\Sigma}_k^W$ and $\mathbf{\Sigma}^B$ are $dM_k \times dM_k$ and $dK \times dK$, respectively, which is much lower than the dimensionality of the correlation matrix in global shape modeling approach which is $dM \times dM$. This disentangled formulation in the proposed MLMO method gives relief in computational burden as it leads to faster eigenvalue decomposition of the correlation matrix of significantly lower dimension used for entropy computations (Eqs. 9, 10) and consequently, faster optimization as compared to the global shape modeling approach. Moreover, this makes the MLMO model more flexible and less constrained, demonstrating its better statistical power under high dimensional and low sample-size settings which is more predominant in multi-object shape modeling scenarios.

2.6 Evaluation metrics

In this section, we describe different quantitative and qualitative metrics used to systematically evaluate the results produced by the underlying PSM method and the associated shape correspondence performance.

2.6.1 Qualitative metrics

We use mean and modes of variation to qualitatively assess the shape model. PCA is a linear transformation of data into new coordinate space, in which each coordinate axis represents decreasing amount of variability in the data. In MLCA, this transformation is done at different levels in which the data is observed. The point correspondences generated by the respective PSM technique is subjected to PCA in the shared subspace and MLCA in the within-organ and between-organs subspaces. This provides a ranking of the uncorrelated modes of variation based on the amount of variance explained relative to the total variance. When PCA is performed in the shared shape space, the modes of variation for the morphology and relative pose of the multi-organ shape structure remain entangled. This limits the ability of the shape model to discover hidden patterns in the shape class of interest that can be clinically relevant. MLCA disentangles shape morphology and alignment variations in multi-organ shape complexes. This helps in factoring out significant variations of how the shape morphology of each organ changes across the population and also how the relative alignment of multi-organ shape varies across the population. We visualize and describe these qualitative modes for the clinical data in Section 3 by examining the anatomical correctness and integrity of the mean shape and its associated modes.

2.6.2 Quantitative evaluation metrics

We use the quantitative metrics of compactness, generalization, and specificity Davies (2002) to assess the shape-correspondence performances with respect to the PDM construction. These measures are defined under the assumption that the shape model is inherently built using a PCA generative process. We extend these metrics for MLCA by defining these evaluation measures for within-organ and between-organs subspaces for the multi-organ shape model. These measures collectively quantify the quality of the shape model constructed from correspondence particles and are defined as a function of number of modes P under consideration.

2.6.2.1 Compactness

Multi-organ shape models inherently have high dimensionality but this high dimensional shape space can be parameterized by a low-dimensional subspace (shared, within and between) in terms of eigenvectors and associated eigenvalues. *Compactness* is the evaluation metric that quantifies the amount of variance of the underlying shape model. For a given subspace S, compactness is

computed as sum of the eigenvalues λ_p^S up to the $P-$ th mode as $C(P) = \sum_{p=1}^{P} \lambda_p^S$, where S can be G, W or B denoting the global shared, within or between subspaces, respectively. A shape model with higher compactness measure is better as it can explain the shape and/or pose variability with fewer modes of variation.

2.6.2.2 Generalization

Generalization is defined as the ability of the shape model to represent unseen shapes of the structure modeled. It is quantified as an approximation error using the leave-one-out cross validation approach where a testing shape vector is left out from N shape vectors and the shape model is obtained from the remaining $N-1$ shape vectors. The approximation error is then calculated in terms of Euclidean distance (in *mm*) between the held-out shape instance and its reconstruction from the shape model. For a multi-organ shape model, we compute this metric in different subspaces—shared, within and between, which quantifies how well the shape model can generalize shape vectors from that subspace. Generalization is thus quantified as $Generalization(P) = \frac{1}{N}\sum_{n=1}^{N} \mathcal{E}_n(P)$ where, $\mathcal{E}_n(P) = \|\mathbf{z}_n^S(P) - \mathbf{z}_n^S\|^2$ is the approximation error between shape vector $\mathbf{z}_n^S(P)$ reconstructed using P modes, $\mathbf{z}_n^S$ is the held out shape vector, and S can be either G, W or B denoting the global shared, within or between subspaces respectively. The shape vector reconstruction for the shared subspace follows the PCA generative Eq. 4 and the reconstruction for the within and between subspace follows the MLCA generative Eq. 7. For two shape models built using the same training data, the model having a lower value of generalization error indicates a more efficient shape model that can better represent unseen shape structures. By computing generalization in these different subspaces, we can assess how well a shape model can learn the characteristics of the multi-organ shape and it's relative alignment modeled from a limited training set. If the multi-organ shape model is over-fitted to the training data, it will not be able to generalize well to unseen examples and this would be highlighted by a higher generalization error. A lower generalization error in the within subspace denotes that the shape model can easily generalize the morphological changes of a particular organ and similarly a lower generalization error in the between subspace indicates that the shape model can easily generalize the relative pose of the multi-organ shape complex (denoted by the centroid of each organ).

2.6.2.3 Specificity

Specificity quantifies the ability of the shape model to generate new plausible instances of the shapes by constraining the variability in the shape space using the learned population-specific shape statistics. To compute this metric, we randomly sample a large number of vectors (1,000 in our experiments) from the subspace and then compute the approximation error (Euclidean distance, in *mm*) between the randomly sampled shape vector and nearest training sample. Specificity is defined as a function of number of modes P considered and computed as $Specificity(P) = \frac{1}{T}\sum_{t=1}^{T} \|\mathbf{z}_t^S(P) - \mathbf{z}_t^S\|^2$, where T is the large number of shape vectors randomly generated, $\mathbf{z}_t^S(P)$ is the shape vector randomly sampled from the subspace, $\mathbf{z}_t^S$ is the closest training sample and S can be either G, W or B denoting shared, within or between subspaces respectively. The randomly sampled vectors for shared subspace are generated using the PCA generative Eq. 4 and the randomly sampled vectors for the within and between subspace are generated using the MLCA Eq. 7. For two shape models, a model with lower value of specificity is better and more specific. A lower specificity value in the within subspace denotes that the shape model is more specific to the morphological changes in the shape model and similarly a lower specificity in the between subspace indicates that the shape model is more specific to the relative pose variations of the multi-object shape complex.

3 Experiments and results

We used synthetic and real medical data to demonstrate that the proposed shape modeling approach generates optimal shape models for complex multi-organ anatomical structures. We use the global shape modeling approach described in Section 2.3 as a baseline method for comparison. Shape models can also be created by the individual modeling approach (Section 2.1), where shape models are built separately for each organ in the multi-organ structure. If we model each organ separately, we sacrifice the inter-structural shape and pose correlations, which are of significant interest in many clinical contexts. The main emphasis of this paper is to efficiently bring in these inter-organ relations in the shape model for multi-organ structure. Therefore, in this work, we restrict our comparison only to the joint shape modeling approach. We employed ShapeWorks Cates et al. (2017a) and Cates et al. (2007), an open-source software implementation of the particle-based shape modeling method to build shape models for the clinical and synthetic data. We implemented the baseline method of global shape modeling approach using the optimization scheme already given by ShapeWorks. We modified the objective function to implement our proposed optimization scheme described in Section 2.5. ShapeWorks utilizes an iterative, particle-splitting strategy, in which the full set of particles is initialized in a multiscale fashion such that in every step each particle is split to produce a new nearby particle until the desired number of particles is attained. This mechanism is a self-tuning system of particles that distribute themselves across the shape surface using repulsive forces to achieve optimal point distributions that cover each surface. The number of particles for a particular anatomical shape surface depends on its size, curvature, and morphological variations such that smooth and small shapes require less number of particles as compared to complex and highly variable shapes. In our experiments on different datasets, the number of particles for given anatomy is chosen empirically by utilizing this coarse-to-fine particle splitting strategy until the resulting particle representation is deemed to capture sufficiently good detail for the given anatomy depending on its size and curvature.

3.1 Proof of concept experiment

To illustrate and assess the proposed MLMO shape modeling approach, we devised a proof-of-concept experiment using synthetic shapes. We created synthetic data simulating multi-organ structures using supershapes, which are a family of parameterized shapes Gielis (2003). Each object in the multi-object synthetic shape is modeled by a supershape with different number of lobes and shape parameters

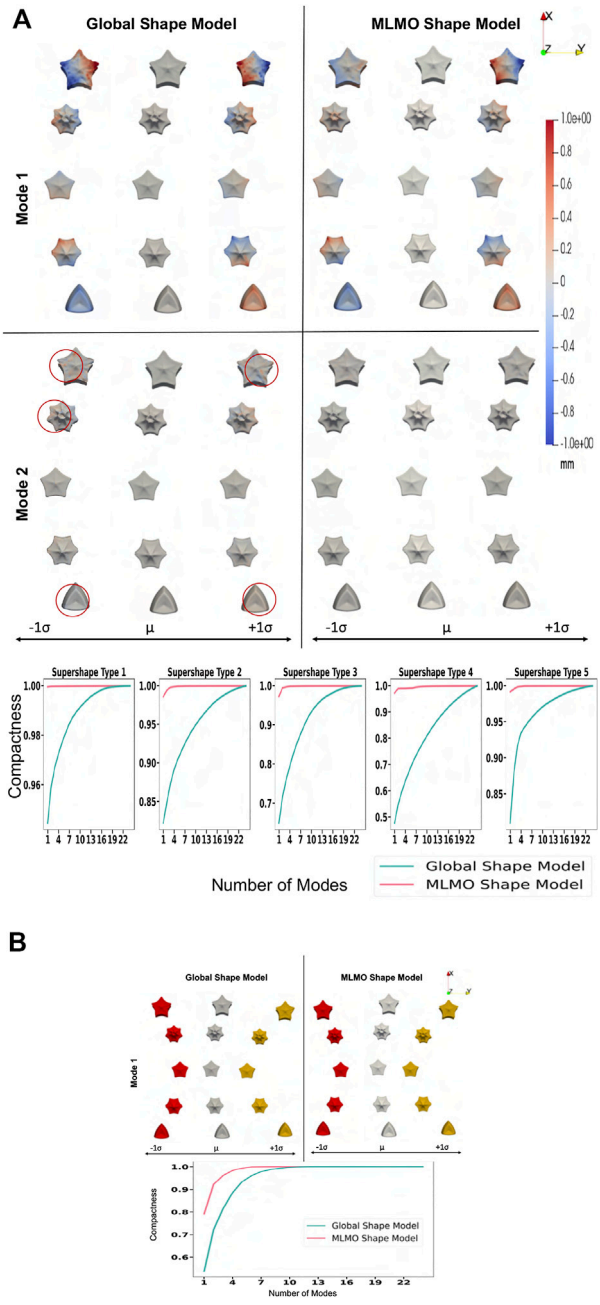

FIGURE 1
Proof of concept experiment results—Modes of variation and compactness metric. **(A)** Within-object subspace. **(B)** Between-objects subspace.

randomly drawn from a χ^2 distribution which reflects the morphological changes in each supershape. The relative alignment of supershapes in the multi-object shape complex is modeled by a parabolic curve $y = ax^2$, where $a \sim \mathcal{U}(0, 0.001)$ for each x coordinate of the individual supershape. This results in shape variations in the supershape reflected by the change in one parameter of supershape and the alignment variations of the multi-object shape complex changing from concave to convex. Thus, the synthetic dataset helps us evaluate the shape modeling technique as these shape and pose variations have been incorporated in a known way, and the underlying PSM technique should correctly model these variations.

We build the shape models using 512 correspondence points for each supershape object in the multi-object shape complex. To evaluate the shape model, we use MLCA to visualize the patterns of shape and pose variability across the population. The dominant modes of the shape model should correctly reflect these variabilities, which are known to be only two for the synthetic dataset. Figure 1A shows the within-object morphology variations with the compactness measure for each supershape and Figure 1B shows the between-objects alignment variations and its compactness measure. For the MLMO shape model, there is only one mode of variation in the within-object subspace that shows the shape variability of each supershape and there is only one mode of variation in the between subspace which shows the changes in the alignment of the entire shape structure going from concave to convex. Therefore, it can be concluded that the proposed shape modeling technique correctly disentangled the shape and pose variations and explained the total variability for within and between subspaces with just one mode. On the other hand, although the global shape model correctly identifies the pose variation in the between subspace, it adds shape variations in the secondary within-object modes, which does not truly reflect the shape variations in the actual synthetic dataset. This underpins our hypothesis that optimizing the shape model in the shared shape subspace of a multi-object structure without disentangling the shape from alignment might bring in those variations in morphology or pose that are not anatomically accurate.

3.2 Spinal column

3.2.1 Dataset

Publicly available labeled and segmented data for human vertebrae by the vertebrae segmentation challenge (VerSe) Sekuboyina et al. (2021) is used to build shape models. Although this database is large-scale, the number of patients that have the entire spine segmented is limited. A subset of subjects from VerSe is selected such that the number of vertebrae covered in the multi-organ structure of each subject is maximized. 30 patients having complete 17 vertebrae present in the thoracolumbar vertebral region - thoracic (T1 to T12), and lumbar (L1 to L5) were selected. The shape cohort comprises of healthy subjects and the subjects having multiple pathologies related the spinal column, in the age range of 60 ± 17 years. We build the shape model with 8,704 correspondence particles on the whole spine such that 512 particles are placed on each vertebra.

3.2.2 Qualitative results

Figure 2 shows the modes of variation for PCA done in shared shape space. We can see that for both the shape modeling approaches, the modes depicting morphological changes of vertebrae and their relative pose are entangled. The primary mode of variation shows variation in the spinal length with some changes in the morphology of each vertebra. Both pose and local shape changes are inter-twined across these variations. The second and third modes show a variation of kyphosis and lordosis

10.3389/fbioe.2023.1089113

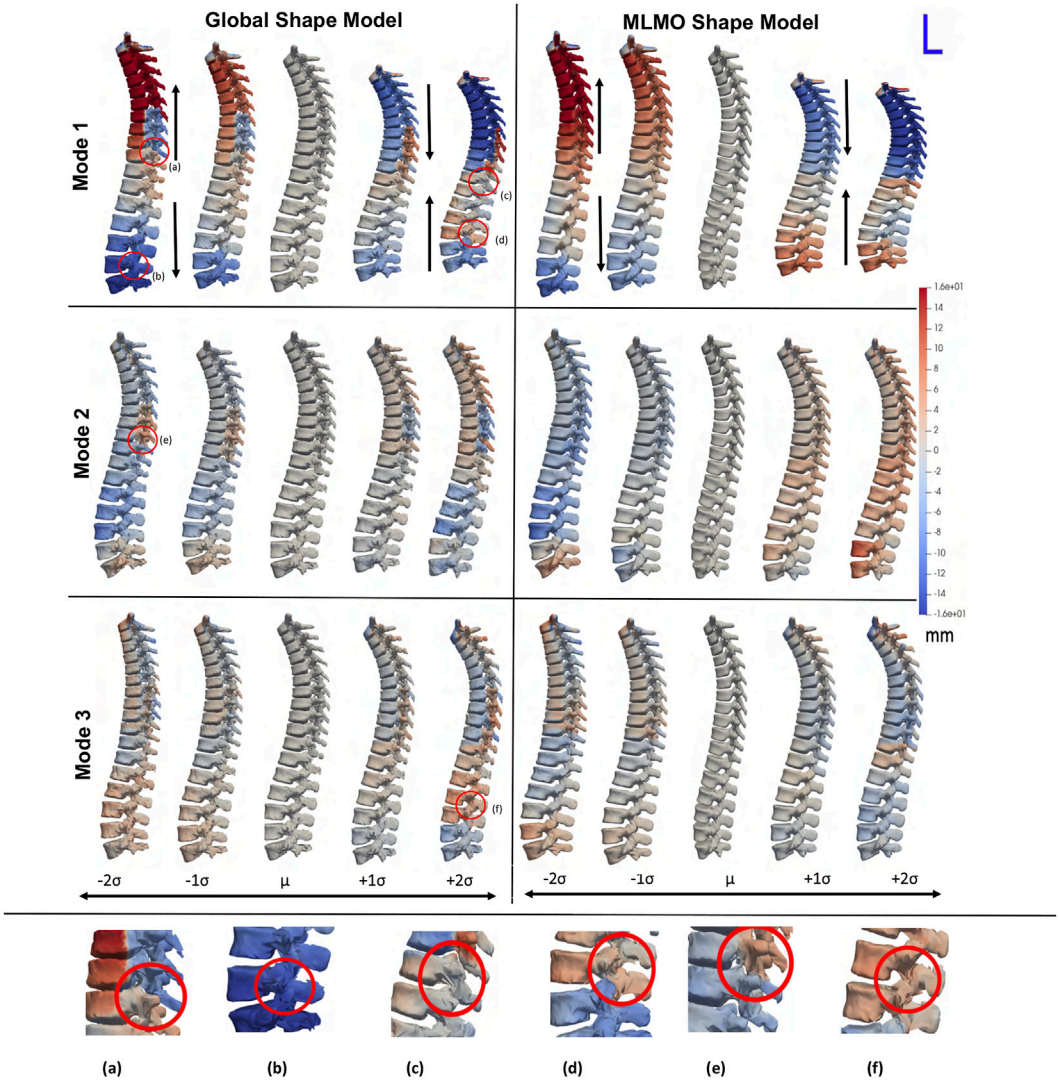

FIGURE 2
PCA modes of variation computed in the shared subspace for the spinal column dataset. The color map shows the distance of each mode from the mean shape. Some of the anatomical inconsistencies are highlighted in red circles labeled from **(A–F)**.

curvatures in the sagittal plane. The particles are in better correspondence with the proposed MLMO shape modeling approach as this is indicated by the smooth reconstructed shapes from the generated particles that are more faithful to the original training shape. The modes of variation for the global shape model show anatomical inconsistencies in regions where the vertebrae come close to each other.

Figure 3 shows the within-organ modes of variation highlighting only morphological changes in each vertebra. For both shape modeling approaches, we can see that the primary mode captures the change in scale. The secondary mode shows significant changes in the size of the vertebral body and spinous process, especially in the lower thoracic-lumbar regions. The third mode shows a similar change in the vertebral body and spinous process in the lumbar region but the changes are more clearly seen in the MLMO shape model. The particles are in good correspondence and the shape reconstructions are smooth, preserving the anatomical correctness of the vertebrae for the proposed MLMO shape model as compared to the global shape model. The global shape model has inconsistencies in particle correspondence, denoted by jagged shape reconstruction, especially in the posterior arch of the vertebrae, and also weaker correspondence is seen in regions where the lower end of vertebrae comes in close to each other.

Figure 4 shows the between-organs mode of variation illustrating the relative alignment variations of the spine. Similar modes were observed for both shape models. The between modes explain the global shape of the spinal curve passing through the vertebral body centers. The primary mode of variation is the elongation and compression of the entire vertebra column which depicts the change in inter-vertebral spaces. However, more penetration of bones is seen in the middle arch of the vertebrae column for the global shape model as compared to the proposed MLMO shape model. The secondary mode captures the curvatures of the thoracolumbar spine segments. It well reproduces the natural

10.3389/fbioe.2023.1089113

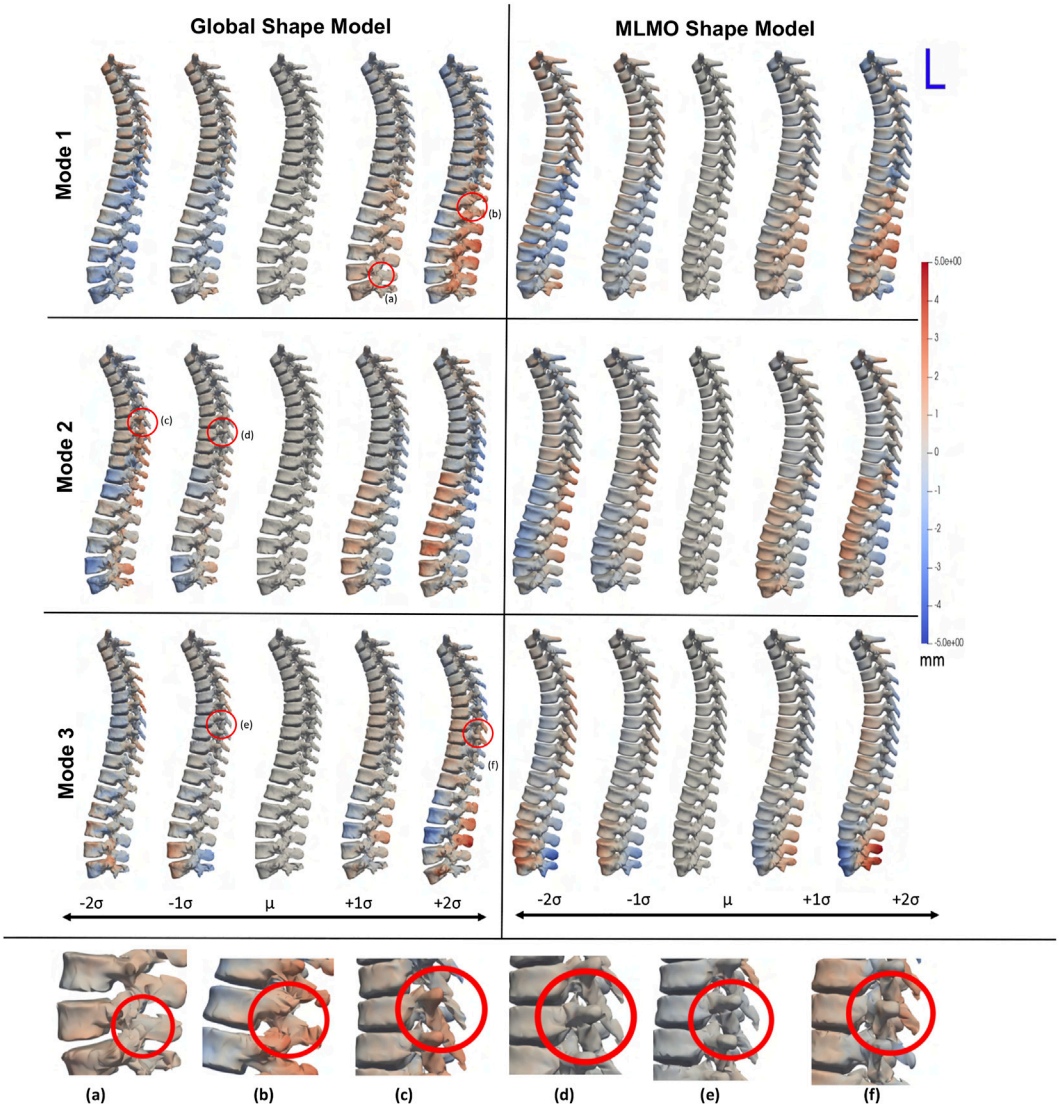

FIGURE 3
Within-organ modes of variation showing morphological changes in each vertebra. The color map shows the distance of each mode from the mean shape. Some of the anatomical inconsistencies are highlighted in red circles labeled from **(A–F)**.

variations in the spine when the lumbar segment curvature (lordosis) compensates for the thoracic segment curvature (kyphosis). The third mode captures the variations in the upper-thoracic segment curvature. To see some clinically relevant modes, we can fix one of the vertebrae and observe alignment variations around that vertebra. One such mode is observed when we fix L3 as the origin referential frame, a spine kyphosis variation from hyper-kyphosis (an adult spine deformity pathology where the spine curvature is important), passing to asymptomatic kyphosis for the mean model (moderated natural angle), towards hypo-kyphosis (straight spine, also pathological).

3.2.3 Quantitative results

The evaluation metrics described in Section 2.6.2 are used to quantitatively assess the proposed shape modeling approach and compare it to the baseline method of the global shape modeling approach. Figure 5A shows the within-organ compactness for each individual vertebra from T1 to L5. We observe that the proposed MLMO shape model gives a compact shape model in the within-organ subspace better than the joint shape model. The shape variations of each vertebra can be explained by less number of modes for the MLMO shape model as compared to the global shape model. To explain 99% of variance, MLMO shape models need 15 modes as compared to more than 20 modes needed by the global shape model. Figures 5B, C show the compactness in the between-organ subspace and in the shared shape space and we can see that the compactness measure is nearly the same for both the approaches.

Figure 6A shows the within-organ generalization error for each individual vertebra in the multi-organ structure. On average, the MLMO shape model has a generalization error of 1.5 mm and 2.5 mm in the thoracic and lumbar regions, whereas, the global shape model has a generalization error of 3.0 mm and 4.5 mm for

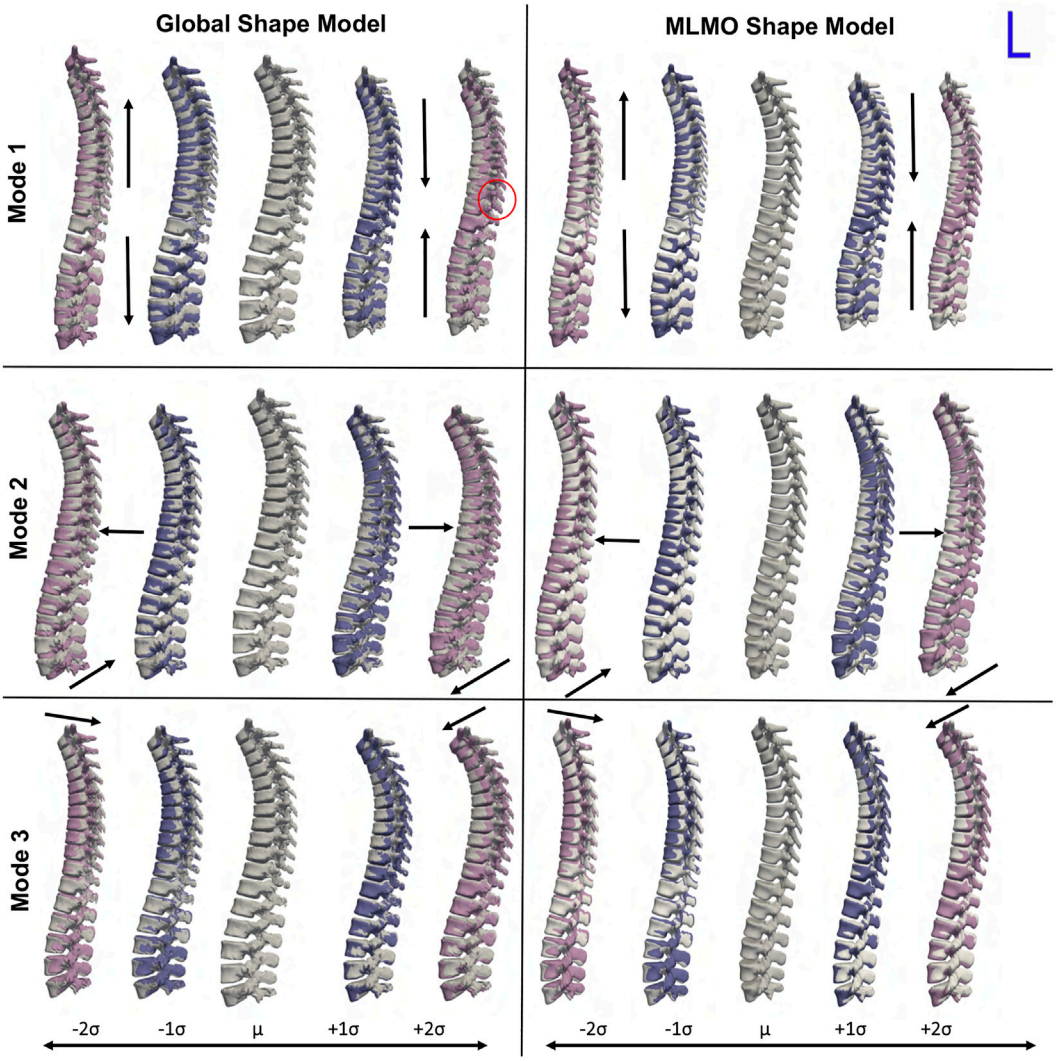

FIGURE 4
Between-organ modes of variation showing relative pose variations in the spinal column. The mean shape is grey in color with $\pm 1\sigma$ modes shown in blue and $\pm 2\sigma$ modes shown in pink color. Some of the anatomical inconsistencies are highlighted in red circles and significant pose variations are annotated using arrows.

the thoracic and lumbar regions, respectively. MLMO shape model consistently improves the generalization on the held-out samples for each vertebra as compared to the global shape model. This implies that the shape morphological variations of each bone are generalized well by the proposed shape modeling technique. Figure 6B shows the generalization error in the between-organs subspace and we can see that the proposed MLMO approach can generalize well for unseen relative alignment of the bones in the multi-organ model of the vertebra as compared to the global approach where the relative pose is not optimized during the shape modeling. Thus, it can be seen that by optimizing the shape and relative pose subspace separately, we can get a shape model which can generalize well to unseen morphological changes of each vertebra and also to their unseen relative alignment. From Figure 6C, it can be seen that the proposed modeling approach gives a lower generalization error in the shared PCA subspace. Figure 7 shows the specificity measures in different subspaces. The MLMO shape model is more specific in the shared, within, and between subspaces.

3.2.4 Validation results

To investigate the relevance of our proposed shape modeling approach, we experimented to use the resulting shape descriptors as a predictor in a regression task. Therefore, an experiment is formulated to compare the predicted patient age by the shape model versus the ground-truth age. Correspondence particles of a statistical shape model have the potential to produce additional diagnostic, predictive, and prognostic information beyond what is visually perceptive and hence can be used for various downstream tasks which are clinically relevant Goparaju et al. (2018). Several clinical studies have shown age-related morphological and alignment changes in the vertebra. Osteophyte formation involves an increase in the vertebral endplate dimensions, and

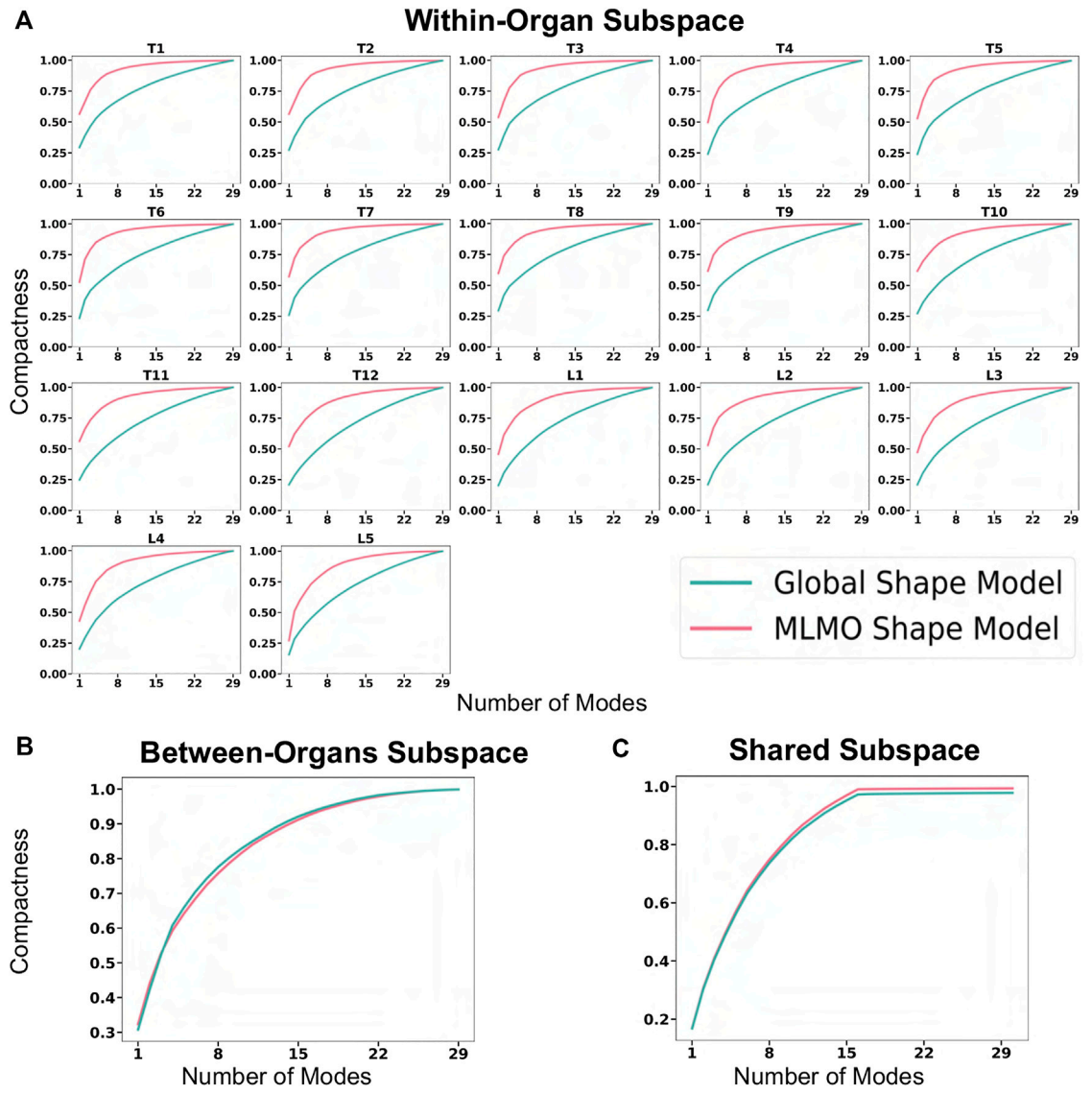

FIGURE 5
Compactness metric for spinal column data—**(A)** within-organ subspace. **(B)** Between-organs subspace. **(C)** Shared subspace.

activity-induced lifelong periosteal growth Junno et al. (2015) and Whitmarsh et al. (2012) or due to some other underlying pathological condition. This validation task aims to study which shape modeling technique's correspondence particles are more predictive of the patient's age and is based on the hypothesis that due to the temporal features of age progression, the correspondence particles generated by the shape model can also display a sequential pattern of low-dimensional distribution of age progression. With the age regression on the shape descriptors, we aim to corroborate that the proposed model efficiently captures the morphological changes related to normal aging evolution. These aging variations of the spinal column are typically related to the narrowing of the spinal canal, increase in endplate size and convexity, decrease in vertebral body height, and increase in pedicle diameters Whitmarsh et al. (2012). The idea is to compare both model regressions (MLMO and global shape Model) to see if the MLMO shape model has more prediction power (better R^2 metric). A regression model is built using the correspondence particles generated by the shape model to predict the age of the same shape cohort of 30 subjects as described in Section 3.2 having mean age of 60 ± 17 years. We applied random sampling and selected 30% of subjects to be used as a testing dataset which is held out from the initial analysis. Feature vectors for the regression model were generated by projecting the correspondence particles to the shared PCA subspace for the global shape modeling approach and the MLCA subspace for the proposed MLMO shape modeling approach. For both approaches, we select features up to the number of modes that can explain 97% variability across the population. We used Least Absolute Shrinkage and Selection Operator (LASSO) as the regression model for our experiment Friedman et al. (2010). The independent variable is the subject's age and the dependent variables are the correspondence particles of the training set which are the shape descriptors in the PCA and MLCA

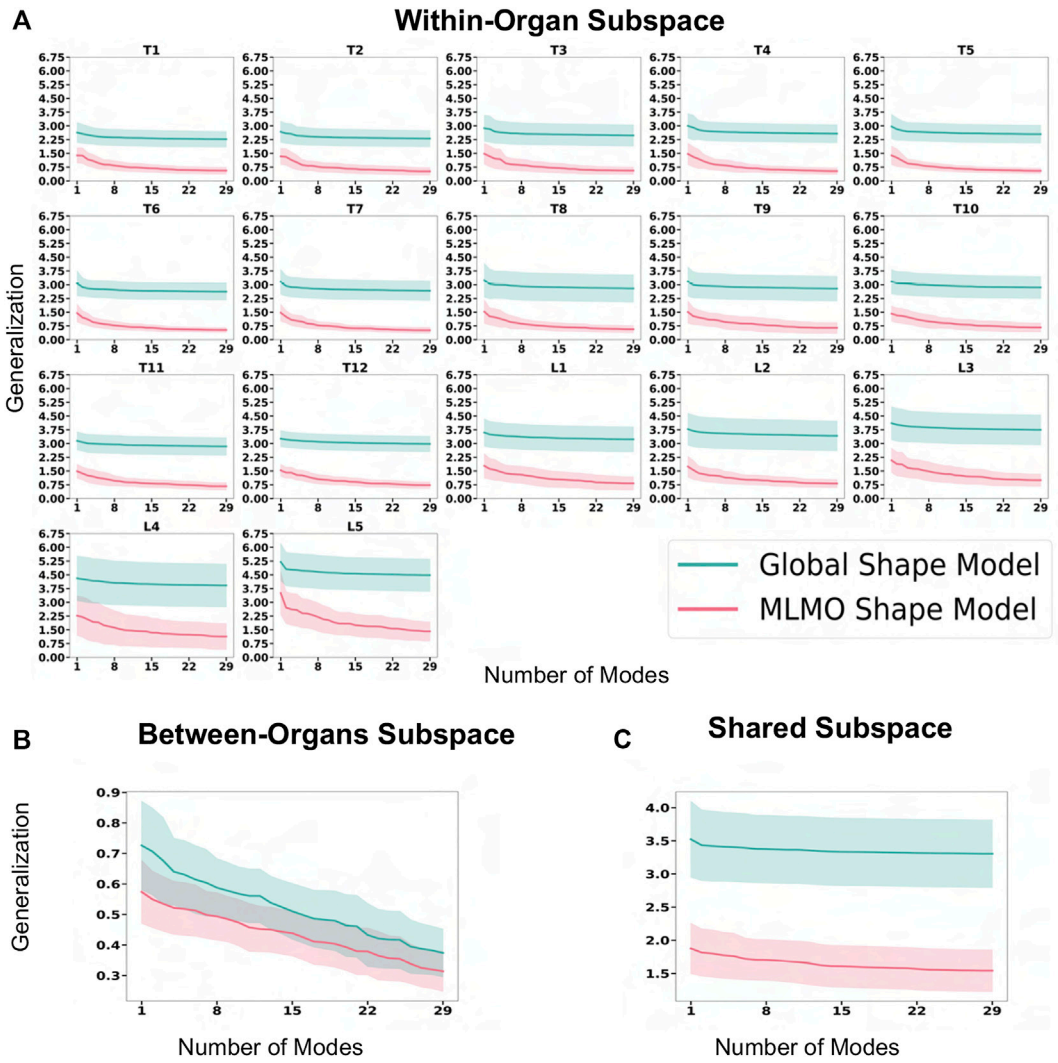

FIGURE 6
Generalization error (in *mm*) for spinal column data—**(A)** within-organ subspace. **(B)** Between-organs subspace. **(C)** Shared subspace.

subspaces, respectively for the two shape models. The coefficient of determination R^2 is computed to assess the two trained regression models. This metric is related to the regression residuals and is defined as:

$$R^2 = 1 - \frac{\sum_{i=1}^{T} (y_i - \tilde{y}_i)^2}{\sum_{i=1}^{T} (y_i - \bar{y})^2} \tag{12}$$

where T is the number of test subjects, y_i is the actual patient age and $\tilde{y}_i$ is the patient age predicted from the shape model and $\bar{y}$ is the mean patient age. The regression model was tuned using a five-fold cross-validation approach to get optimal regularization weight for the curve fit. The R^2 metric was then calculated on the testing dataset. The age regression curve fitted for the MLMO shape modeling approach has an R^2 value of 0.62 with a mean predicted age of 63 ± 8 years and for the global shape modeling approach, the R^2 value is 0.20 with a mean predicted age of 46 ± 15 years. As we have a drawback of having a small number of samples in the regression model, we studied the influence of sample number on the regression model. We repeated this experiment by training it on a specific percentage of subjects coming from the training data and then increasing the percentage of training shapes. The R^2 metric values coming from these experiments are then interpolated using a power law curve. Under the power law curve assumption, we should see a significant improvement in accuracy if we increase the training data size. This helps in getting an estimate of the evaluation metric value at a point when we have a sufficient number of training shapes available. The results from this experiment are shown in Figure 14A and we observe that there is an improvement in the R^2 score for both the shape models. The R^2 value for the regression model built for the MLMO shape model increases to 0.81 and the R^2 score increases up to 0.31 for the global shape model if we have a training dataset of size 1.2 times the current size. These results suggest that the correspondence particles generated from the MLMO shape modeling approach are more predictive in capturing the morphological and relative alignment variations of the vertebra column which arise due to changes in age. We hypothesize that as the proposed MLMO shape model optimizes particle correspondences separately on the within-organ and

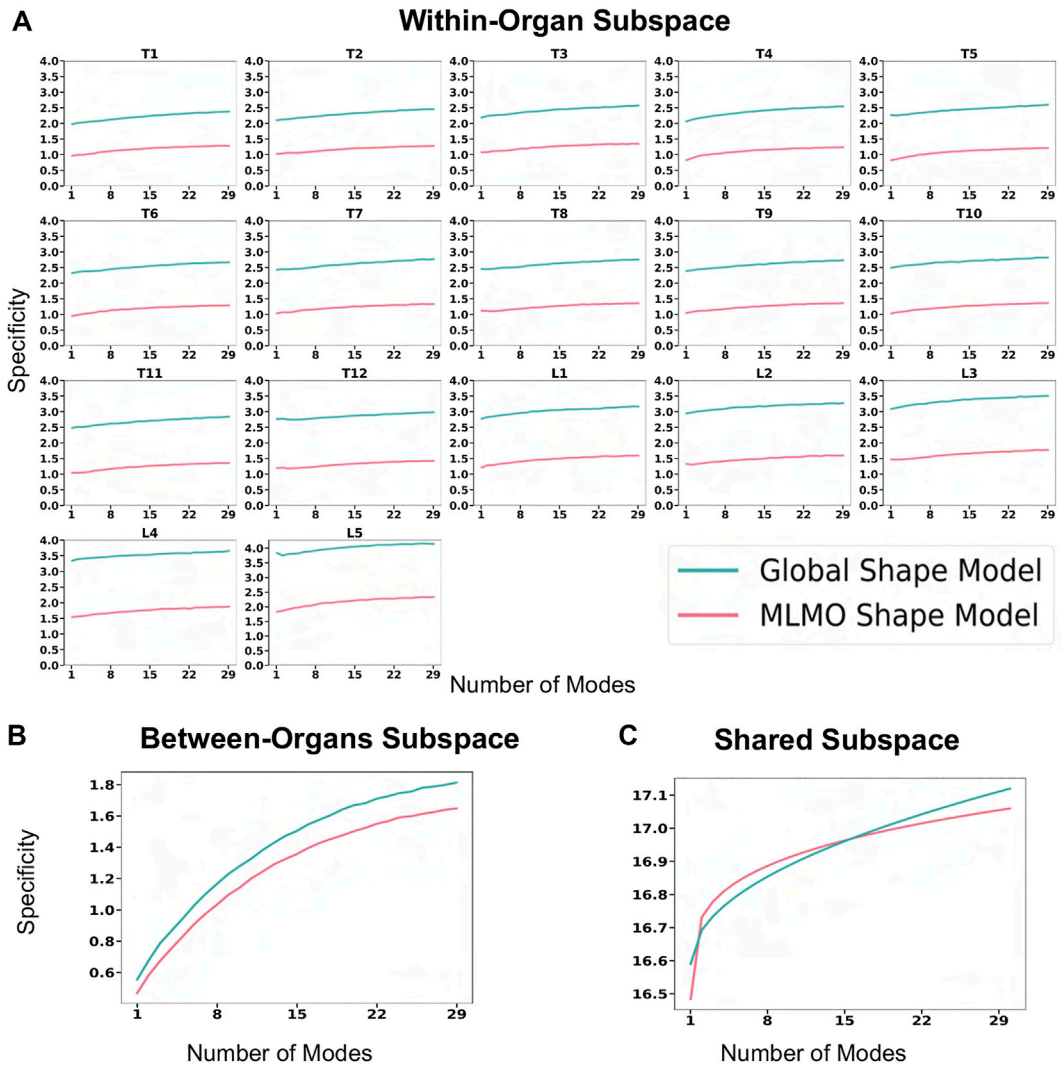

FIGURE 7
Specificity (in *mm*) for spinal column data—**(A)** within-organ subspace. **(B)** Between-organs subspace. **(C)** Shared subspace.

between-organs subspaces, it can better capture the feature changes of the vertebra both morphology as well as configuration-wise. However, this validation task has certain limitations that warrant consideration. The results are shown on a very small dataset and the gender of the subjects is not taken into consideration. However, there seems to be a correlation between gender and vertebral pathology, which limits the generalizability of the validation results.

3.3 Foot and ankle

3.3.1 Dataset

Dataset comprising images from weightbearing CT (WBCT) scans (Planmed Verity - 0.4 × 0.4 × 0.4 mm voxels) for the foot and ankle of twenty-seven asymptomatic participants is used to build shape models. The subjects' age was in the range of 50.0 ± 7.3 years, with height and BMI in the range of 169.4 ± 6.4 cm and 25.3 ± 3.8 kg/m^2, respectively. The bones of interest (namely, the calcaneus, talus, navicular, and cuboid), make up the hindfoot and part of the midfoot, which is comprised of the subtalar, talonavicular, and calcaneocuboid joints. Due to the complex morphology and joint relationships within these four bones, current 2D radiographic measurements fail to quantify the 3D morphology and joint relationships properly. Computationally modeling these morphologies and joint relations could yield increased clinical understanding of pathologies, improved surgical planning, and advanced implant design. The WBCT scans were subjected to segmentation, decimation, and smoothing to generate 3D surface models of the talus, calcaneus, navicular, and cuboid. We build shape models using 1,024 correspondences for the talus, 2048 for the calcaneus, and 512 for both the navicular and cuboid bones.

3.3.2 Qualitative results

Figure 8A shows the modes of variation for PCA in the shared subspace of all the bones. Both the shape modeling techniques give similar morphological and configurational modes while maintaining

10.3389/fbioe.2023.1089113

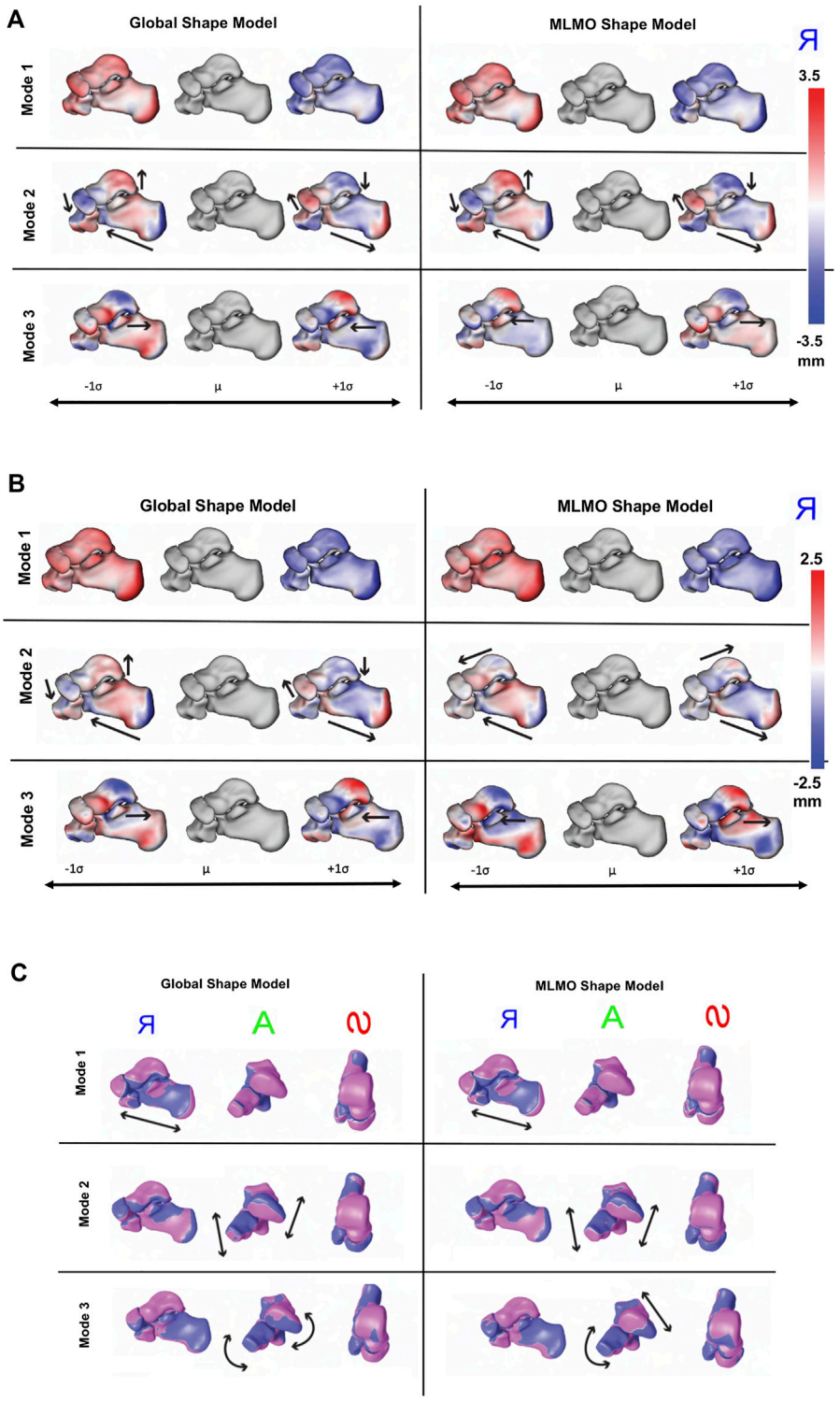

FIGURE 8
Qualitative results for foot and ankle data. **(A)** PCA modes of variation. The color map shows the distance of each mode from the mean shape. mean shape. The arrows denote the direction along which significant shape changes take place. **(B)** Within-organ modes of variation. The color map shows the distance of each mode from the mean shape. The arrows denote the direction along which significant shape changes take place. **(C)** Between-organs modes of variation—Medial, Anterior and Superior View. The mean shape is grey in color with +1 σ modes shown in blue and −1 σ modes shown in pink color.

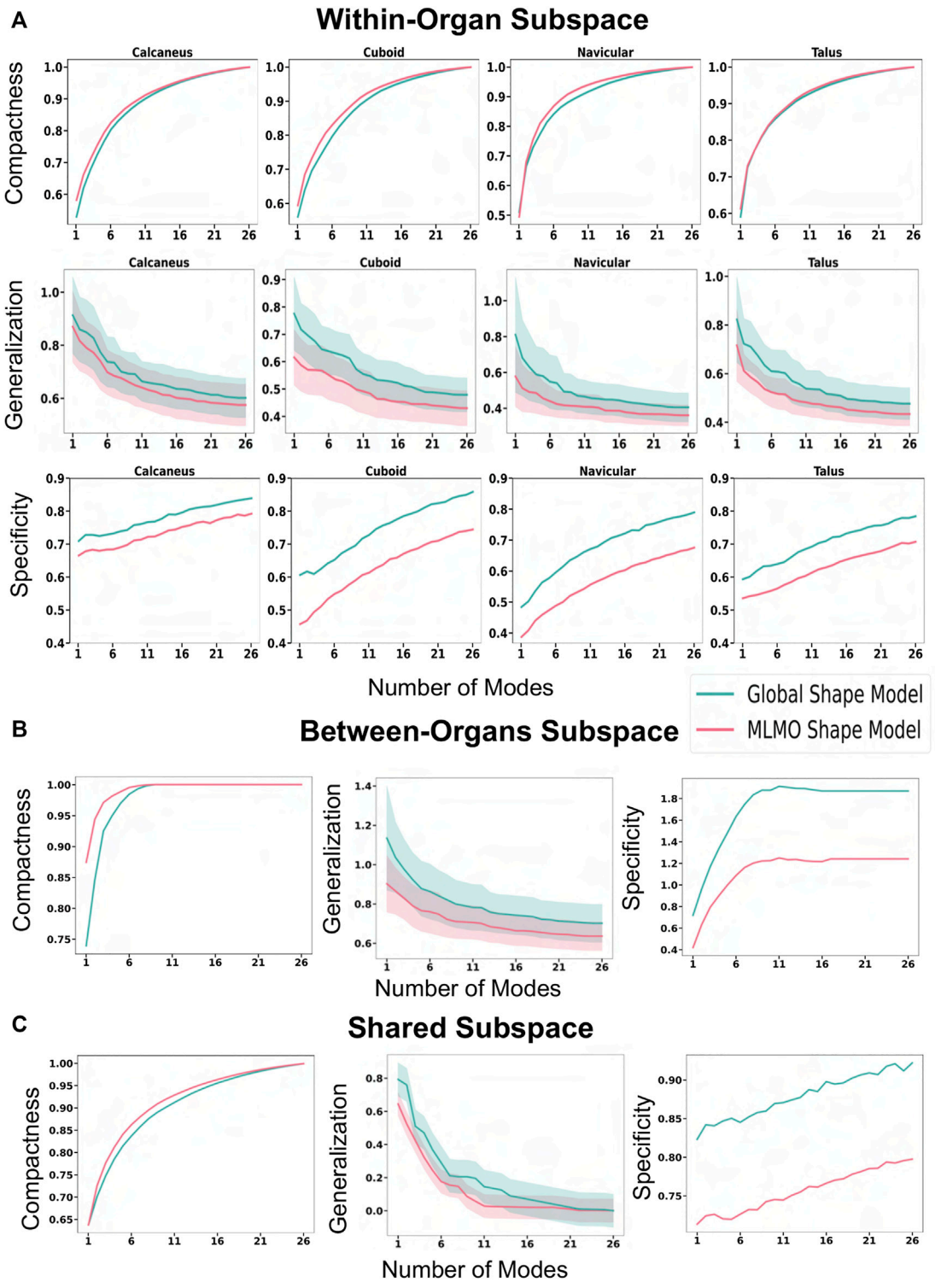

FIGURE 9
Quantitative Evaluation metrics (compactness, generalization (in *mm*), and specificity (in *mm*)) for the foot and ankle dataset in **(A)** within-organ **(B)** between-organs **(C)** shared subspaces.

the joint articular relationships. The primary mode highlights the overall growth and shrinkage of all four bones simultaneously. The secondary PCA modes remain entangled in terms of alignment and morphology and there is an inverse relationship between the calcaneus and talus. As the calcaneus lengthens, the posterior facet's slope decreases and when the two bones are analyzed together simultaneously, we see that when the talar dome heightens, the posterior process diminishes and the calcaneus

shortens with the posterior facet's slope increasing. Moreover, as the talar dome heightens, we see that the navicular and cuboid slide inferiorly with very less rotation around the anterior-posterior axis. The third PCA mode shows variation in the anteromedial facet such that it moves from the anterior to posterior direction as we move along different standard deviations of modes.

Figure 8B shows the within-organ modes of variation. We observe identical morphological modes for both shape modeling techniques. The primary mode here as well highlights the change in scale and shows each bone increasing and shrinking in size individually. The secondary mode shows the lengthening of the calcaneus with a simultaneously decreasing posterior facet slope. We can still observe modest talar dome, navicular and cuboid changes, but they are not as dominant as the PCA modes discussed above. The third mode emphasizes a similar anterior/posterior anteromedial facet variation but this is accompanied by a rotational component. We also see that the anteromedial facet's slope changes as we move along the standard deviations from a steep slope to a more flattened slope.

Figure 8C shows the between-organ modes of variation. We notice similar modes for both shape modeling techniques, highlighting significant variations in the overall configuration of the articulated joint while preserving the mean morphology, which was not seen directly in the PCA modes. The primary mode of variation is an overall outward and inward movement between the bones which effectively increases and decreases the joint space distance. The secondary mode primarily emphasizes the superior and inferior motion of the four bones such that as the talus moves along the superior direction, the calcaneus, cuboid, and navicular move along the inferior direction. The third mode reflects the medial, and lateral movement of the talus and calcaneus such that as the talus moves along the medial axis, the calcaneus moves laterally. Moreover, we see as the talus moves in the medial direction, the navicular rotates along the superior and lateral axis, and the cuboid rotates in an inferior and medial direction.

3.3.3 Quantitative results

Figure 9 shows the quantitative evaluation metric results. The compactness measure for the MLMO shape model is higher as compared to the global shape model, although the difference is not very pronounced. The MLMO shape model gives lower generalization and specificity errors in each subspace (within, between, shared), which indicates that it can generalize well to unseen morphological and pose variations of the ankle joint, either combined or separately.

3.3.4 Validation results

Joint level measurements serve as an important tool to better understand the joint level morphology and alignment variations and to improve ankle joint pathological diagnosis and operative procedures. To validate the proposed shape modeling technique, we used the shape model to predict the joint coverage area of the articulating region of the subtalar joint which is the joint between two of the tarsal bones (the talus and calcaneus) in the foot. Coverage area can be used to gain useful insight and quantify the morphological variations, like osteoarthritis development and alignment variation, such as joint subluxation Schaefer et al. (2012) and Louie et al. (2014).

TABLE 1 Coverage area measurements ($\mu \pm \sigma$ in mm^2) of the subtalar joint.

	Talus	Calcaneus
Ground truth	1527.87 ± 201.30	1439.94 ± 186.78
Global shape model	1503.08 ± 164.38	1413.19 ± 141.92
MLMO shape model	1481.22 ± 165.38	1391.91 ± 140.33

Samples from the entire dataset were randomly sampled into train-test splits with seventy percent of samples selected for the training of the shape models using the proposed and the global shape modeling approach. Each test shape sample is then orthogonally projected onto the PCA subspace for the global shape modeling approach and onto the within-organ and between-organs subspaces for the proposed MLMO shape modeling approach, and then reconstructed back following the generative equations of PCA and MLCA as described in Eqs 4, 7. We then compare the coverage of the subtalar joint for the reconstructed sample to the ground truth coverage measurements of that subject. To calculate the coverage area between two bones we use normal vectors from each face of one of the bones and identify which faces those vectors intersect with on the opposing bone. We consider that normal vector to be within coverage only if it intersects with an opposing face and the surface area was calculated on that identified region. To measure the error in coverage area between the ground-truth and reconstructed shape samples, we use relative error ϵ as an evaluation metric which is defined as

$$\epsilon = \frac{|\tilde{a} - a|}{a} \tag{13}$$

where $\tilde{a}$ is the predicted coverage area of the subtalar joint measured from the reconstructed shape complex and a is the coverage area of the subtalar joint for that particular subject computed on ground-truth meshes. We repeated this experiment using five-fold cross-validation. Figure 14B shows the box plot for the relative errors. We can see that the relative error for the proposed MLMO shape model is comparatively smaller than the global shape model, although this difference is small. The mean relative coverage area error of calcaneus and talus is 4.0% and 3.6%, respectively, for the proposed MLMO shape modeling approach. For the global shape modeling approach, the errors are 4.4% and 3.8% for the calcaneus and talus, respectively. In Table 1, we report the population level coverage area measurements of the subtalar joint for the five-fold cross-validation experiments from each of the optimization approaches along with the ground truth coverage measurements. These results suggest that the MLMO shape modeling technique is better at preserving the true anatomical correctness of the articulated joint (indicated here by coverage area) while simultaneously building a compact model.

3.4 Hip joint

3.4.1 Dataset

We used a dataset of 51 hemi-pelvis and proximal femur pairs of the hip joint. The shape cohort comprised of 24 control subjects, six patients with cam femoroacetabular impingement (FAI), 10 patients

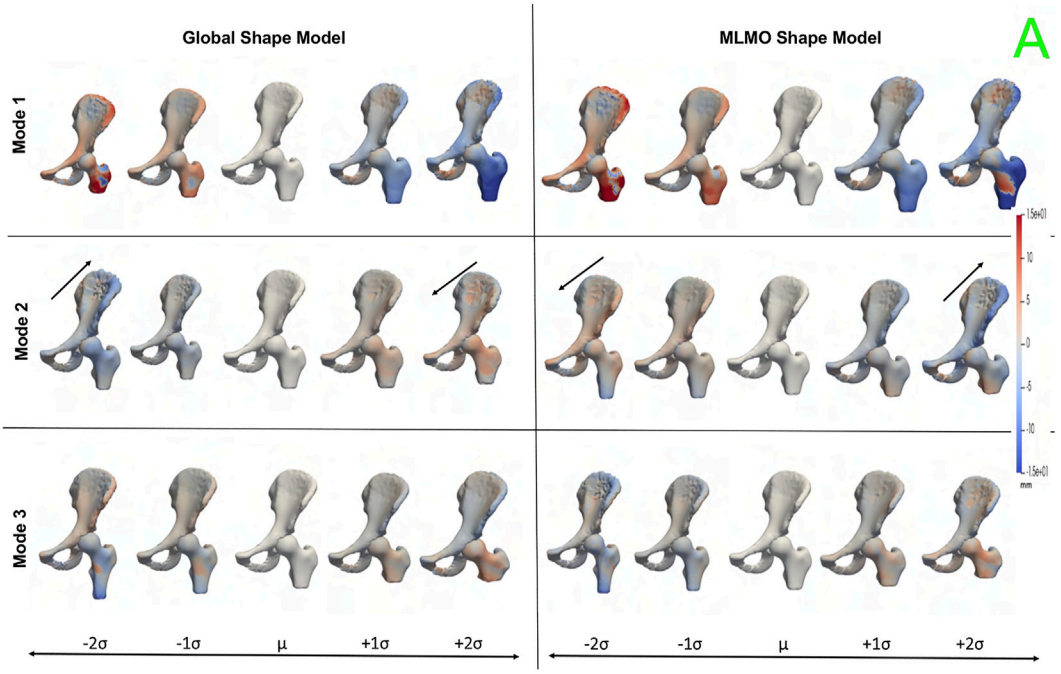

FIGURE 10
PCA modes of variation in the shared subspace for the hip joint dataset. The color map shows the distance of each mode from the mean shape. The arrows denote the direction along which major shape variations take place.

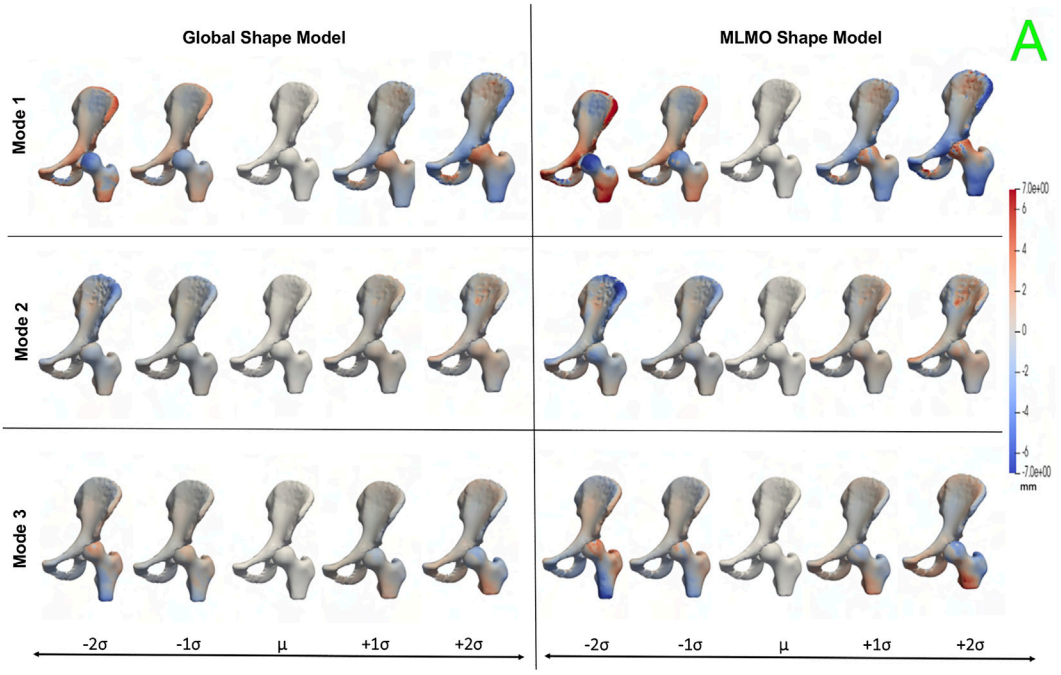

FIGURE 11
Within-organ modes of variation showing morphological changes in each bone for the hip joint dataset. The color map shows the distance of each mode from the mean shape.

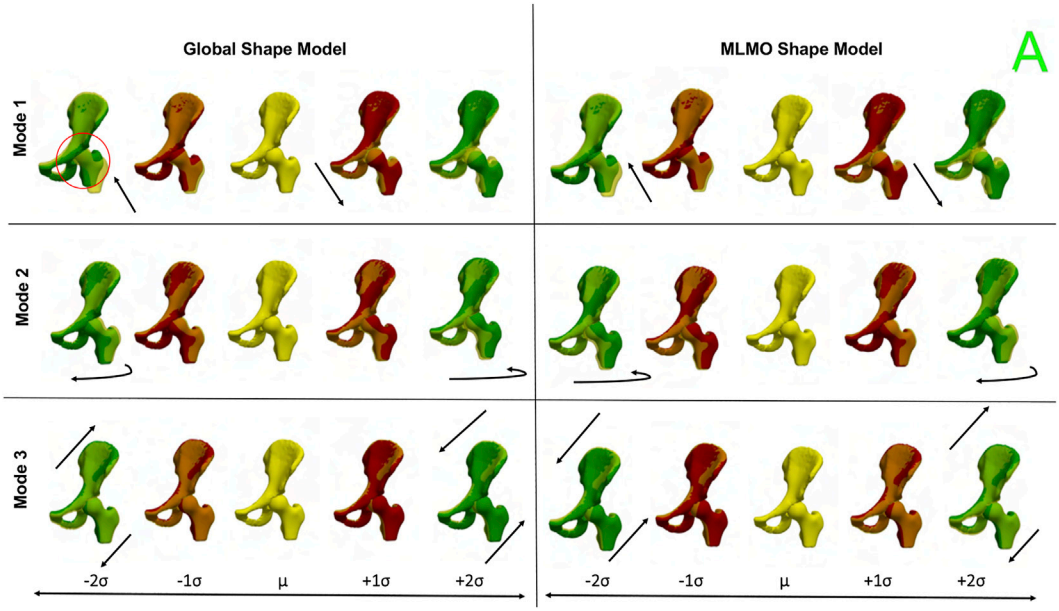

FIGURE 12
Between-organs modes of variation showing relative pose variations for the hip joint dataset. The mean shape is yellow in color with $\pm 1\sigma$ modes shown in red and $\pm 2\sigma$ modes shown in green color. The arrows denote the direction along which significant pose variations take place.

with acetabular dysplasia and 10 patients with pelvic retroversion. The shape models were built using 2048 correspondences on the pelvis and 512 on the femur, using the two shape modeling approaches.

3.4.2 Qualitative results

Figure 10 shows the PCA modes of variation in the shared subspace. We observe similar modes for both the shape models with a difference in magnitude, with the global shape model having reduced magnitude of variation. The primary mode highlights the shape variation associated with overall growth and shrinkage in size, along with an asphericity of the femoral head likely attributed to some of the subjects having cam FAI morphology. The second mode highlights anterior-posterior pelvic tilt entangled with shape variations on the femoral head and the ilium. The third mode shows elongation and shortening of the femoral shaft attributed to the field of view of the imaging, as well as changes in the curvature of the ilium.

Figure 11 shows the within-organ modes of variation highlighting morphological changes of pelvis and hip. The primary mode shows the changes in scale as growth and shrinkage variations. There are some morphological changes on the femoral head as well. The secondary mode shows the morphological changes of the ilium with minimal shape variation for femur. The third mode shows the shape variations in femoral head and shaft. The shape variation capture by the modes of the proposed MLMO shape model are of higher magnitude as compared to the global shape model.

Figure 12 shows the between-organ modes of variation depicting the relative alignment variations of the hip joint while simultaneously preserving the mean shape. In the primary mode, we observe the increased and decreased space between the femoral head and the acetabulum. This observation may be unique to this dataset, as the images were acquired with the hip in traction to widen the intra-articular joint space for visualization of the separated cartilage layers during CT image acquisition. The variability in the amount of traction applied cannot be factored out by the initial rigid alignment process. However, we notice that the non-physiological penetration of femoral head into the acetabulum is more pronounced in the modes discovered by the global shape model. The second mode shows the femoral head tilting towards the posterior direction with the pelvis fixed, representing variation in flexion-extension of the hip joint. The third mode shows minor alignment shift between the pelvis and femur in the opposite direction, such that when pelvis shifts laterally the femur shifts medially and vice versa.

3.4.3 Quantitative results

Figure 13 shows the quantitative evaluation metric results. The compactness measure for the shape models, both baseline and proposed are very close to each other. The MLMO shape model has lower generalization and specificity errors as compared to the global shape model in the between and within subspaces but has similar errors in the shared subspace. The specificity measure is lower for the MLMO shape model in each subspace. In the within subspace, the generalization and specificity metrics are higher for the pelvis than the femur for both shape models.

3.4.4 Validation results

Statistical shape models can be employed to automate the inference of patient-specific anatomical morphometrics. For the validation task using the hip joint data, we estimated the patient-specific anatomical landmarks for the pelvis and femur anatomies. The estimation of landmarks is an important task as landmarks are

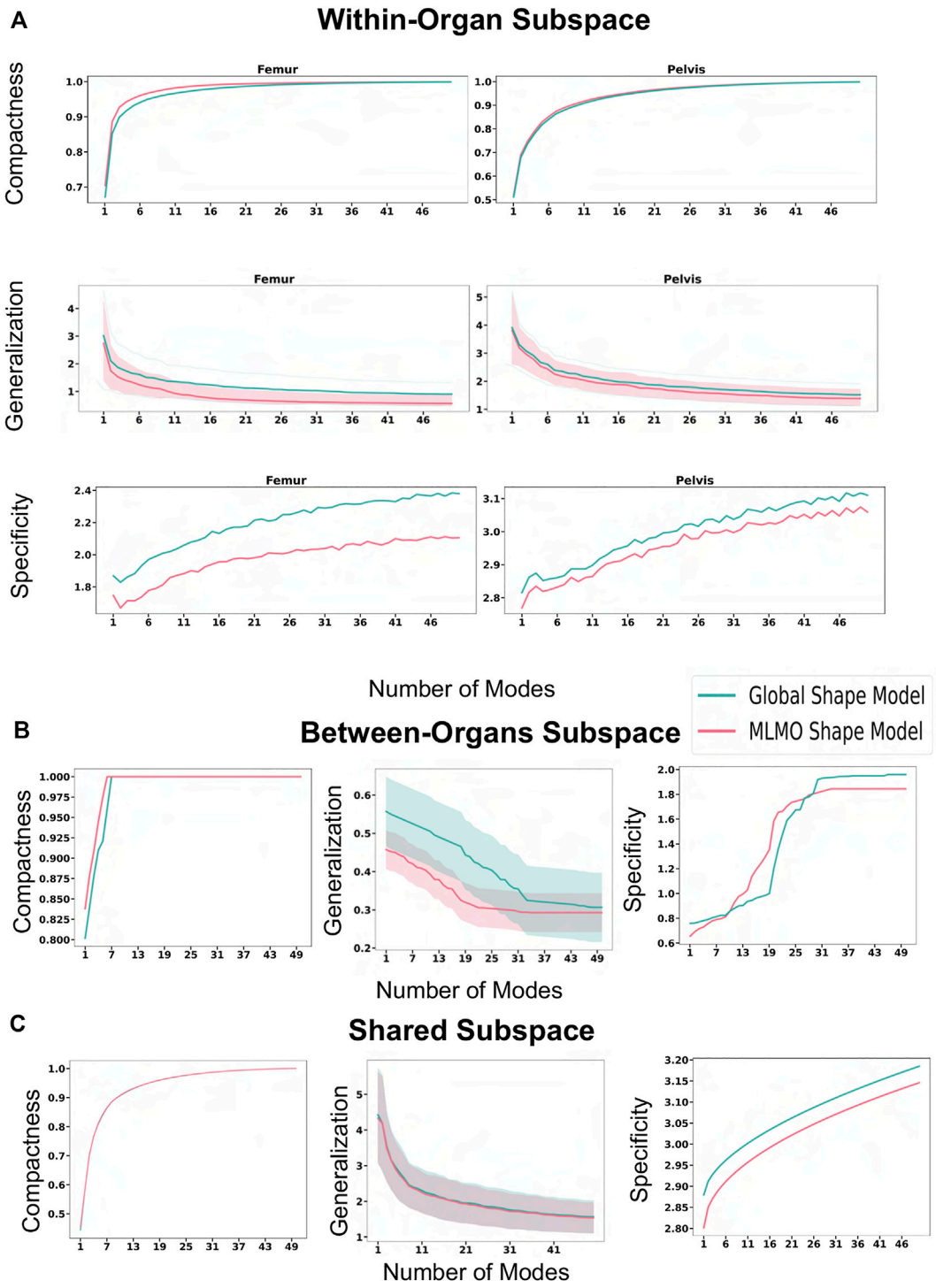

FIGURE 13
Quantitative Evaluation metrics (compactness, generalization (in *mm*), and specificity (in *mm*)) for the hip joint dataset computed in **(A)** within-organ **(B)** between-organs **(C)** shared subspaces.

used for a variety of clinical and research applications, like motion tracking or coordinate system identification for surgical planning or robotic surgery. The given dataset was randomly sampled into train-test split with 30% of subjects held out as testing dataset. The shape model was generated on the training dataset using the baseline and proposed methodology. Ground-truth landmarks were manually annotated by an expert using first and second principal curvature of the surfaces for guidance. We chose five landmarks for the hip joint in our validation task as shown in Figure 14C. Three landmarks were defined on the pelvis, including the anterior superior iliac spine

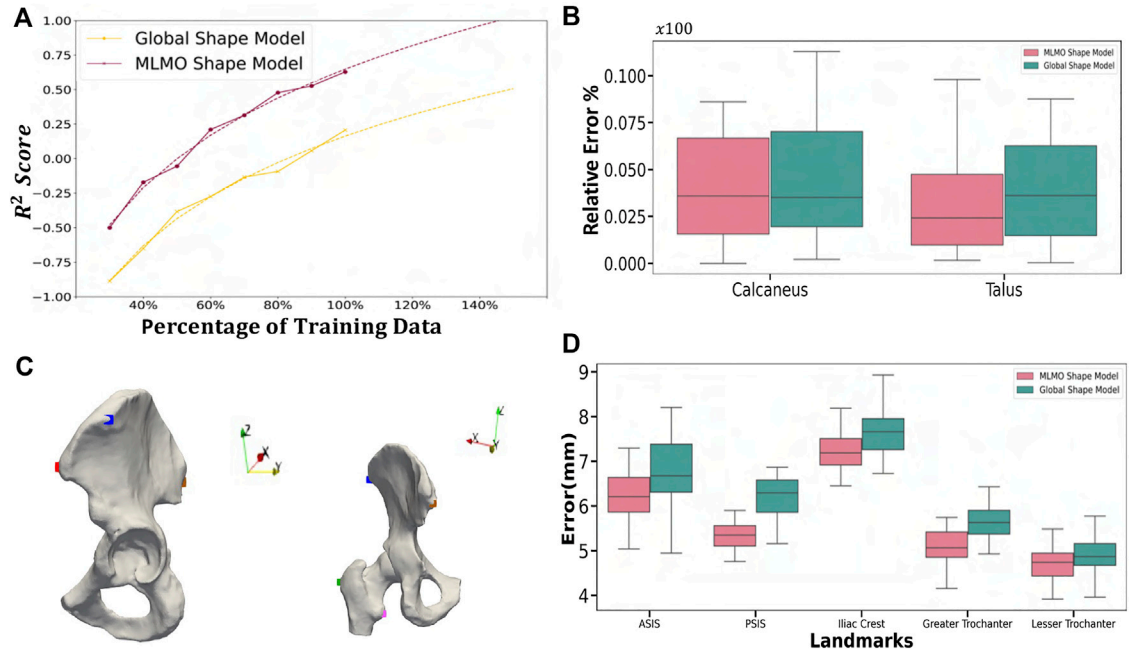

FIGURE 14
Validation Results—**(A)** Power law interpolation for R^2 metric computed at different training data sizes of spinal column data. **(B)** Box-plot for the relative error of coverage area for calcaneus and talus. **(C)** Anatomical landmarks for femur and pelvis used for landmark inference - iliac crest (blue), ASIS (red), PSIS (brown), lesser trochanter (pink) and greater trochanter (green). **(D)** Box-plot for Euclidean distance error computed for the landmark inference validation task done on the hip joint.

(ASIS), posterior superior iliac spine (PSIS) and iliac crest, as are commonly used in motion capture and for the development of a pelvic coordinate system. Two landmarks were defined on the femur, including the greater trochanter and lesser trochanter. The point correspondences for each test subject were then generated using the shape model of the training data. The subject-specific landmarks were then warped from the subject space to the mean space of the shape model using thin plate splines (TPS) Bookstein (1989). This was followed by constructing a TPS warp using correspondences of the mean shape and the subject-specific anatomy as reference points, which served as a mapping between the mean and subject spaces. Finally, the mean landmarks were warped back to subject space to obtain subject-specific landmarks which were the predicted points from the SSM. We then computed the Euclidean distances between the predicted landmarks and the ground-truth values. We repeated this process five times on different train-test splits to get five-fold cross-validation metrics for the euclidean distance error. Figure 14D shows the box-plot for the Euclidean distance error in mm for the proposed and baseline methods. The landmarks predicted by the proposed MLMO shape model had comparatively lower errors as compared the ones predicted by global shape model. The errors for the landmarks placed on femur (greater and lesser trochanter) are lower in magnitude as compared to the errors for landmarks on pelvis. The highest errors were observed for the iliac crest landmark, which was placed on the most prominent feature of the iliac crest, a location which is variable across subjects and difficult to identify through palpation of bony prominences for motion capture. From these results, we infer that due to the disentangled approach to build the shape model, the proposed MLMO shape model had particle correspondences which reflected the true morphology of the individual bone (femur or pelvis) which were anatomically correct. A promising direction for the future application of the MLMO shape model motivated by this validation experiment is to calculate joint angle measurements in a relevant clinical/anatomical coordinate system from the surface reconstructions provided by the MLMO shape models. With the MLMO shape model, landmarks that are necessary to define a coordinate system could be based on their spatial relationship to the underlying correspondence particles, which can then be used to calculate pose automatically in a clinically relevant anatomic coordinate system. This work can improve the clinical interpretation of articulated joint data from statistical shape models. We also see the potential of tying the correspondence model to associated biomechanics measurements to quantify form-function relationships. For instance, we can show that patients with more severe cases of hip dysplasia (which can be measured by MLMO) also exhibit more pronounced hip instability (as measured by motion capture).

4 Conclusion

In this paper, we proposed a new shape modeling approach for multi-organ anatomies by separating shape from pose and building a shape model by optimizing the mutually orthogonal subspaces of each organ and their relative pose. The proposed method efficiently uses the available, typically limited, 3D models of anatomy to capture subtle, clinically relevant morphological intra- and inter-structural

correlations. The method also provides a scalable approach for modeling anatomies with more organs compared to the current global shape modeling scheme that can get prohibitive with increased number of correspondence points and more organs. This offers a practical solution for a wider range of problems in the multi-organ shape acquisition and modeling relative to the work in the literature. We showed from experiments that the MLMO shape modeling technique outperforms the global PSM method by accurately capturing the morphological and configuration variations for multi-object structures. Our model mitigates the problem of overestimation of variance which is the case with global shape models, where PCA in the shared shape space leads to anatomical inconsistencies. The proposed MLMO modeling technique is scalable as the generative model is built individually for each organ and also for their relative pose, thereby leading to covariance matrices of much lower dimension than the joint models. The shape models generated by the proposed PSM method are more compact, specific, and generalizable as compared to the global shape models in high dimensional, low sample size settings. Due to the generative nature of the proposed MLMO shape modeling technique, this method is orthogonal to and can be extended to various posterior inference techniques that are applied to traditional statistical shape models Albrecht et al. (2013). An intriguing direction for a future work application using the MLMO shape modeling technique could be to infer the shape and pose relations when some organ shapes are known a priori, and the objective is to model the posterior distribution of the entire multi-organ shape given the known partial parts. The additional benefit of learning conditional distribution using MLMO shape models for articulated joints will be that it can be used to reconstruct and understand the healthy morphology of the shape with simultaneously restoring the native joint biomechanics as the shape and relative pose subspaces remain disentangled in the proposed approach.

Our work comes with some limitations. The proposed MLMO shape modeling technique builds from the idea that configuration variations in the pose can be learned by modeling the distance of the centroid of each object from the global centroid. This enables us to disentangle the shape from its relative pose and gives us a simple way to learn the relative alignment of structures in the multi-organ shape complex, along with the morphological changes in each object. Although this linear assumption that a Gaussian distribution can model each subspace helps us to bring anatomical correlations in terms of relative pose between joint structures in multi-organ settings to the shape modeling process, however, these relative pose variations cannot be entirely linear, and might have some non-linear variations across the shape and pose features. A direction for future work can be to incorporate a more robust generative model that can learn linear and non-linear embeddings of the high-dimensional shape and pose spaces in low-dimensional space in a fully probabilistic manner for multi-organ anatomies. This will improve the capability of the multi-organ shape models to handle complex inter-object pose relations better to build shape models of complex anatomies as realistically as possible.

Data availability statement

The raw data supporting the conclusion of this article will be made available by the authors, without undue reservation.

Ethics statement

The studies involving human participants were reviewed and approved by University of Utah Internal Review Board. The patients/participants provided their written informed consent to participate in this study.

Author contributions

NK and SE conceptualized, designed the study, derived the proposed shape modeling approach, and wrote initial versions of the work. NK drafted the manuscript and developed parts of software routines used for optimization and shape analysis of the proposed approach. AM developed parts of software routines used for optimization and shape analysis of the baseline approach. AL and AP provided the image data for foot and ankle shape model, analyzed and provided its joint coverage analysis. BA analyzed the vertebra shape model and provided classification of deformities according to age. PA and AA provided the image data for the hip joint. PA analyzed the hip shape model and provided anatomical landmarks its validation. All authors contributed to the article and reviewed the manuscript.

Funding

This work was supported by the National Institutes of Health under grant numbers NIBIB-U24EB029011, NIAMS R01AR076120, NIBIB-R01EB016701, and NHLBI-R01HL135568.

Acknowledgments

The authors thank the National Institutes of Health for supporting this work. The content is solely the responsibility of the authors and does not necessarily represent the official views of the National Institutes of Health. The authors also thank the ShapeWorks team and the the University of Utah Department of Orthopaedics.

Conflict of interest

Author BA was employed by EOS Imaging Inc.

The remaining authors declare that the research was conducted in the absence of any commercial or financial relationships that could be construed as a potential conflict of interest.

Publisher's note

References

Agrawal, P., Mozingo, J. D., Elhabian, S. Y., Anderson, A. E., and Whitaker, R. T. (2020). "Combined estimation of shape and pose for statistical analysis of articulating joints," in Shape in Medical Imaging: International Workshop, ShapeMI 2020, Held in Conjunction with MICCAI 2020, Lima, Peru, October 4, 2020 (Springer), 111–121.

Albrecht, T., Lüthi, M., Gerig, T., and Vetter, T. (2013). Posterior shape models. *Med. image Anal.* 17, 959–973.

Atkins, P. R., Agrawal, P., Mozingo, J. D., Uemura, K., Tokunaga, K., Peters, C. L., et al. (2022). Prediction of femoral head coverage from articulated statistical shape models of patients with developmental dysplasia of the hip. *J. Orthop. Research®* 40, 2113–2126. doi:10.1002/jor.25227

Atkins, P. R., Aoki, S. K., Whitaker, R. T., Weiss, J. A., Peters, C. L., and Anderson, A. E. (2017a). Does removal of subchondral cortical bone provide sufficient resection depth for treatment of cam femoroacetabular impingement? *Clin. Orthop. Relat. Research®* 475, 1977–1986. doi:10.1007/s11999-017-5326-5

Atkins, P. R., Elhabian, S. Y., Agrawal, P., Harris, M. D., Whitaker, R. T., Weiss, J. A., et al. (2017b). Quantitative comparison of cortical bone thickness using correspondence-based shape modeling in patients with cam femoroacetabular impingement. *J. Orthop. Res.* 35, 1743–1753. doi:10.1002/jor.23468

Atkins, P. R., Shin, Y., Agrawal, P., Elhabian, S. Y., Whitaker, R. T., Weiss, J. A., et al. (2019). Which two-dimensional radiographic measurements of cam femoroacetabular impingement best describe the three-dimensional shape of the proximal femur? *Clin. Orthop. Relat. Res.* 477, 242–253. doi:10.1097/corr.0000000000000462

Audette, M. A., Rashid, T., Ghosh, S., Patel, N., and Sultana, S. (2017). "Towards an anatomical modeling pipeline for simulation and accurate navigation for brain and spine surgery," in Proceedings of the Summer Simulation Multi-Conference, Bellevue, Washington (San Diego, CA: Society for Computer Simulation International), 1–12.

Bhalodia, R., Elhabian, S., Kavan, L., and Whitaker, R. (2021). Leveraging unsupervised image registration for discovery of landmark shape descriptor. *Med. Image Anal.* 73, 102157. doi:10.1016/j.media.2021.102157

Bieging, E. T., Morris, A., Wilson, B. D., McGann, C. J., Marrouche, N. F., and Cates, J. (2018). Left atrial shape predicts recurrence after atrial fibrillation catheter ablation. *J. Cardiovasc. Electrophysiol.* 29, 966–972. doi:10.1111/jce.13641

Bookstein, F. L. (1989). Principal warps: Thin-plate splines and the decomposition of deformations. *IEEE Trans. pattern analysis Mach. Intell.* 11, 567–585. doi:10.1109/34.24792

Carriere, N., Besson, P., Dujardin, K., Duhamel, A., Defebvre, L., Delmaire, C., et al. (2014). Apathy in Parkinson's disease is associated with nucleus accumbens atrophy: A magnetic resonance imaging shape analysis. *Mov. Disord.* 29, 897–903. doi:10.1002/mds.25904

Cates, J., Elhabian, S., and Whitaker, R. (2017a). "Shapeworks: Particle-based shape correspondence and visualization software," in *Statistical shape and deformation analysis* (Elsevier), 257–298.

Cates, J., Fletcher, P. T., Styner, M., Hazlett, H. C., and Whitaker, R. (2008). "Particle-based shape analysis of multi-object complexes," in International conference on medical image computing and computer-assisted intervention (Springer), 477–485.

Cates, J., Fletcher, P. T., Styner, M., Shenton, M., and Whitaker, R. (2007). "Shape modeling and analysis with entropy-based particle systems," in *Ipmi* (Springer), 333–345.

Cates, J., Nevell, L., Prajapati, S. I., Nelon, L. D., Chang, J. Y., Randolph, M. E., et al. (2017b). Shape analysis of the basioccipital bone in pax7-deficient mice. *Sci. Rep.* 7, 17955. doi:10.1038/s41598-017-18199-9

Cerrolaza, J. J., Herrezuelo, N. C., Villanueva, A., Cabeza, R., González Ballester, M. A., and Linguraru, M. G. (2013). "Multiresolution hierarchical shape models in 3d subcortical brain structures," in International conference on medical image computing and computer-assisted intervention (Springer), 641–648.

Cerrolaza, J. J., Picazo, M. L., Humbert, L., Sato, Y., Rueckert, D., Ballester, M. Á. G., et al. (2019). Computational anatomy for multi-organ analysis in medical imaging: A review. *Med. Image Anal.* 56, 44–67. doi:10.1016/j.media.2019.04.002

Cerrolaza, J. J., Villanueva, A., and Cabeza, R. (2011). Hierarchical statistical shape models of multiobject anatomical structures: Application to brain mri. *IEEE Trans. Med. Imaging* 31, 713–724. doi:10.1109/tmi.2011.2175940

Costafreda, S. G., Dinov, I. D., Tu, Z., Shi, Y., Liu, C.-Y., Kloszewska, I., et al. (2011). Automated hippocampal shape analysis predicts the onset of dementia in mild cognitive impairment. *Neuroimage* 56, 212–219. doi:10.1016/j.neuroimage.2011.01.050

Davies, R. H. (2002). *Learning shape: Optimal models for analysing natural variability*. United Kingdom: The University of Manchester.

Drobny, D., Ranzini, M., Isaac, A., Vercauteren, T., Ourselin, S., Choi, D., et al. (2020). "Towards automated spine mobility quantification: A locally rigid ct to x-ray registration framework," in *Biomedical image registration*. Editors Ž. Špiclin, J. McClelland, J. Kybic, and O. Goksel (Cham: Springer International Publishing), 67–77.

Durrleman, S., Prastawa, M., Charon, N., Korenberg, J. R., Joshi, S., Gerig, G., et al. (2014). Morphometry of anatomical shape complexes with dense deformations and sparse parameters. *NeuroImage* 101, 35–49. doi:10.1016/j.neuroimage.2014.06.043

Friedman, J., Hastie, T., and Tibshirani, R. (2010). Regularization paths for generalized linear models via coordinate descent. *J. Stat. Softw.* 33, 1–22. doi:10.18637/jss.v033.i01

Fritscher, K. D., Peroni, M., Zaffino, P., Spadea, M. F., Schubert, R., and Sharp, G. (2014). Automatic segmentation of head and neck ct images for radiotherapy treatment planning using multiple atlases, statistical appearance models, and geodesic active contours. *Med. Phys.* 41, 051910. doi:10.1118/1.4871623

Gielis, J. (2003). A generic geometric transformation that unifies a wide range of natural and abstract shapes. *Am. J. Bot.* 90, 333–338. doi:10.3732/ajb.90.3.333

Goparaju, A., Csecs, I., Morris, A., Kholmovski, E., Marrouche, N., Whitaker, R., et al. (2018). "On the evaluation and validation of off-the-shelf statistical shape modeling tools: A clinical application," in *International workshop on shape in medical imaging* (Springer), 14–27.

Goparaju, A., Iyer, K., Bône, A., Hu, N., Henninger, H. B., Anderson, A. E., et al. (2022). Benchmarking off-the-shelf statistical shape modeling tools in clinical applications. *Med. Image Anal.* 76, 102271. doi:10.1016/j.media.2021.102271

Gorczowski, K., Styner, M., Jeong, J.-Y., Marron, J., Piven, J., Hazlett, H. C., et al. (2007). "Statistical shape analysis of multi-object complexes," in 2007 IEEE conference on computer vision and pattern recognition (IEEE), 1–8.

Jacxsens, M., Elhabian, S. Y., Brady, S. E., Chalmers, P. N., Mueller, A. M., Tashjian, R. Z., et al. (2020). Thinking outside the glenohumeral box: Hierarchical shape variation of the periarticular anatomy of the scapula using statistical shape modeling. *J. Orthop. Research®* 38, 2272–2279. doi:10.1002/jor.24589

Jenkinson, M., Beckmann, C. F., Behrens, T. E., Woolrich, M. W., and Smith, S. M. (2012). Fsl. *Neuroimage* 62, 782–790. doi:10.1016/j.neuroimage.2011.09.015

Jones, K. B., Datar, M., Ravichandran, S., Jin, H., Jurrus, E., Whitaker, R., et al. (2013). Toward an understanding of the short bone phenotype associated with multiple osteochondromas. *J. Orthop. Res.* 31, 651–657. doi:10.1002/jor.22280

Jung, S., and Marron, J. S. (2009). Pca consistency in high dimension, low sample size context. *Ann. Statistics* 37, 4104–4130. doi:10.1214/09-aos709

Junno, J.-A., Paananen, M., Karppinen, J., Niinimäki, J., Niskanen, M., Maijanen, H., et al. (2015). Age-related trends in vertebral dimensions. *J. Anat.* 226, 434–439. doi:10.1111/joa.12295

Kainmueller, D., Lamecker, H., Zachow, S., and Hege, H.-C. (2009). "An articulated statistical shape model for accurate hip joint segmentation," in 2009 annual international conference of the IEEE engineering in medicine and biology society (IEEE), 6345–6351.

Kokko, M. A., Seigne, J. D., Van Citters, D. W., and Halter, R. J. (2021). "Multi-body statistical shape representation of anatomy for navigation in robot-assisted laparoscopic partial nephrectomy," in *Medical imaging 2021: Image-guided procedures, robotic interventions, and modeling* (Bellingham, WA: International Society for Optics and Photonics), 1159808.

Krähenbühl, N., Lenz, A. L., Lisonbee, R. J., Peterson, A. C., Atkins, P. R., Hintermann, B., et al. (2020). Morphologic analysis of the subtalar joint using statistical shape modeling. *J. Orthop. Research®* 38, 2625–2633. doi:10.1002/jor.24831

Kulis, B. (2013). Metric learning: A survey. *Found. Trends® Mach. Learn.* 5, 287–364. doi:10.1561/2200000019

Lecron, F., Boisvert, J., Benjelloun, M., Labelle, H., and Mahmoudi, S. (2012). "Multilevel statistical shape models: A new framework for modeling hierarchical structures," in 2012 9th IEEE international symposium on biomedical imaging (ISBI) (IEEE), 1284–1287.

Lenz, A. L., Krähenbühl, N., Peterson, A. C., Lisonbee, R. J., Hintermann, B., Saltzman, C. L., et al. (2021). Statistical shape modeling of the talocrural joint using a hybrid multi-articulation joint approach. *Sci. Rep.* 11, 7314–14. doi:10.1038/s41598-021-86567-7

Li, D., Zang, P., Chai, X., Cui, Y., Li, R., and Xing, L. (2016). Automatic multiorgan segmentation in ct images of the male pelvis using region-specific hierarchical appearance cluster models. *Med. Phys.* 43, 5426–5436. doi:10.1118/1.4962468

Lindberg, O., Walterfang, M., Looi, J. C., Malykhin, N., Östberg, P., Zandbelt, B., et al. (2012). Hippocampal shape analysis in alzheimer's disease and frontotemporal lobar degeneration subtypes. *J. Alzheimer's Dis.* 30, 355–365. doi:10.3233/jad-2012-112210

Louie, P. K., Sangeorzan, B. J., Fassbind, M. J., and Ledoux, W. R. (2014). Talonavicular joint coverage and bone morphology between different foot types. *J. Orthop. Res.* 32, 958–966. doi:10.1002/jor.22612

Picazo, M. L., Baro, A. M., Barquero, L. M. D. R., Di Gregorio, S., Martelli, Y., Romera, J., et al. (2018). 3-d subject-specific shape and density estimation of the lumbar spine from a single anteroposterior dxa image including assessment of cortical and trabecular bone. *IEEE Trans. Med. imaging* 37, 2651–2662. doi:10.1109/tmi.2018.2845909

Schaefer, K. L., Sangeorzan, B. J., Fassbind, M. J., and Ledoux, W. R. (2012). The comparative morphology of idiopathic ankle osteoarthritis. *JBJS* 94, 1–6. e181. doi:10.2106/jbjs.l.00063

Sciancalepore, M. A., Maffessanti, F., Patel, A. R., Gomberg-Maitland, M., Chandra, S., Freed, B. H., et al. (2012). Three-dimensional analysis of interventricular septal curvature from cardiac magnetic resonance images for the evaluation of patients with pulmonary hypertension. *Int. J. Cardiovasc. imaging* 28, 1073–1085. doi:10.1007/s10554-011-9913-3

Sekuboyina, A., Husseini, M. E., Bayat, A., Loffler, M., Liebl, H., Li, H., et al. (2021). Verse: A vertebrae labelling and segmentation benchmark for multi-detector ct images. *Med. Image Anal.* 73, 102166. doi:10.1016/j.media.2021.102166

Shigwan, S. J., Gaikwad, A. V., and Awate, S. P. (2020). "Object segmentation with deep neural nets coupled with a shape prior, when learning from a training set of limited quality and small size," in 2020 IEEE 17th international symposium on biomedical imaging (ISBI) (IEEE), 1149–1153.

Si, W., and Heng, P.-A. (2017). Point-based visuo-haptic simulation of multi-organ for virtual surgery. *Digit. Med.* 3, 18. doi:10.4103/digm.digm_7_17

Styner, M., Oguz, I., Xu, S., Brechbühler, C., Pantazis, D., Levitt, J. J., et al. (2006). Framework for the statistical shape analysis of brain structures using spharm-pdm. *insight J.* 1071, 242–250. doi:10.54294/owxzil

Sultana, S., Agrawal, P., Elhabian, S., Whitaker, R., Blatt, J. E., Gilles, B., et al. (2019). Medial axis segmentation of cranial nerves using shape statistics-aware discrete deformable models. *Int. J. Comput. Assisted Radiology Surg.* 14, 1955–1967. doi:10.1007/s11548-019-02014-z

Timmerman, M. E. (2006). Multilevel component analysis. *Br. J. Math. Stat. Psychol.* 59, 301–320. doi:10.1348/000711005x67599

Whitmarsh, T., Río Barquero, L. M. D., Gregorio, S. D., Sierra, J. M., Humbert, L., and Frangi, A. F. (2012). "Age-related changes in vertebral morphometry by statistical shape analysis," in *Workshop on mesh processing in medical image analysis* (Springer), 30–39.

Wilms, M., Handels, H., and Ehrhardt, J. (2017). Multi-resolution multi-object statistical shape models based on the locality assumption. *Med. image Anal.* 38, 17–29. doi:10.1016/j.media.2017.02.003

Yao, J., Burns, J. E., Forsberg, D., Seitel, A., Rasoulian, A., Abolmaesumi, P., et al. (2016). A multi-center milestone study of clinical vertebral ct segmentation. *Comput. Med. Imaging Graph.* 49, 16–28. doi:10.1016/j.compmedimag.2015.12.006

Zachow, S. (2015). Computational planning in facial surgery. *Facial Plast. Surg.* 31, 446–462. doi:10.1055/s-0035-1564717

Zhang, H., Wahle, A., Johnson, R. K., Scholz, T. D., and Sonka, M. (2009). 4-d cardiac mr image analysis: Left and right ventricular morphology and function. *IEEE Trans. Med. imaging* 29, 350–364. doi:10.1109/TMI.2009.2030799

Zhang, J., Fernandez, J., Hislop-Jambrich, J., and Besier, T. F. (2016). Lower limb estimation from sparse landmarks using an articulated shape model. *J. biomechanics* 49, 3875–3881. doi:10.1016/j.jbiomech.2016.10.021

frontiers | Frontiers in Bioengineering and Biotechnology

TYPE Original Research
PUBLISHED 08 March 2023
DOI 10.3389/fbioe.2023.1055860

OPEN ACCESS

EDITED BY
Ajay Seth,
Delft University of Technology,
Netherlands

REVIEWED BY
Lorenzo Grassi,
Lund University, Sweden
Elisabetta M. Zanetti,
University of Perugia, Italy
Mariska Wesseling,
Delft University of Technology,
Netherlands

*CORRESPONDENCE
E. Audenaert,
emmanuel.audenaert@ugent.be

SPECIALTY SECTION
This article was submitted to Biomechanics, a section of the journal Frontiers in Bioengineering and Biotechnology

RECEIVED 28 September 2022
ACCEPTED 21 February 2023
PUBLISHED 08 March 2023

CITATION
Van Oevelen A, Duquesne K, Peiffer M, Grammens J, Burssens A, Chevalier A, Steenackers G, Victor J and Audenaert E (2023), Personalized statistical modeling of soft tissue structures in the knee. *Front. Bioeng. Biotechnol.* 11:1055860. doi: 10.3389/fbioe.2023.1055860

Personalized statistical modeling of soft tissue structures in the knee

A. Van Oevelen[1,2,3], K. Duquesne[1,2], M. Peiffer[1,2], J. Grammens[4,5], A. Burssens[1,2], A. Chevalier[6], G. Steenackers[3], J. Victor[1,2] and E. Audenaert[1,2,3,7]*

[1]Department of Orthopedic Surgery and Traumatology, Ghent University Hospital, Ghent, Belgium, [2]Department of Human Structure and Repair, Ghent University, Ghent, Belgium, [3]InViLab research group, Department of Electromechanics, University of Antwerp, Antwerp, Belgium, [4]Antwerp Surgical Training, Anatomy and Research Centre (ASTARC), University of Antwerp, Wilrijk, Belgium, [5]Imec-VisionLab, Department of Physics, University of Antwerp, Antwerp, Belgium, [6]Cosys-Lab research group, Department of Electromechanics, University of Antwerp, Antwerp, Belgium, [7]Department of Trauma and Orthopedics, Addenbrooke's Hospital, Cambridge University Hospitals NHS Foundation Trust, Cambridge, United Kingdom

Background and Objective: As *in vivo* measurements of knee joint contact forces remain challenging, computational musculoskeletal modeling has been popularized as an encouraging solution for non-invasive estimation of joint mechanical loading. Computational musculoskeletal modeling typically relies on laborious manual segmentation as it requires reliable osseous and soft tissue geometry. To improve on feasibility and accuracy of patient-specific geometry predictions, a generic computational approach that can easily be scaled, morphed and fitted to patient-specific knee joint anatomy is presented.

Methods: A personalized prediction algorithm was established to derive soft tissue geometry of the knee, originating solely from skeletal anatomy. Based on a MRI dataset (n = 53), manual identification of soft-tissue anatomy and landmarks served as input for our model by use of geometric morphometrics. Topographic distance maps were generated for cartilage thickness predictions. Meniscal modeling relied on wrapping a triangular geometry with varying height and width from the anterior to the posterior root. Elastic mesh wrapping was applied for ligamentous and patellar tendon path modeling. Leave-one-out validation experiments were conducted for accuracy assessment.

Results: The Root Mean Square Error (RMSE) for the cartilage layers of the medial tibial plateau, the lateral tibial plateau, the femur and the patella equaled respectively 0.32 mm (range 0.14–0.48), 0.35 mm (range 0.16–0.53), 0.39 mm (range 0.15–0.80) and 0.75 mm (range 0.16–1.11). Similarly, the RMSE equaled respectively 1.16 mm (range 0.99–1.59), 0.91 mm (0.75–1.33), 2.93 mm (range 1.85–4.66) and 2.04 mm (1.88–3.29), calculated over the course of the anterior cruciate ligament, posterior cruciate ligament, the medial and the lateral meniscus.

Conclusion: A methodological workflow is presented for patient-specific, morphological knee joint modeling that avoids laborious segmentation. By allowing to accurately predict personalized geometry this method has the potential for generating large (virtual) sample sizes applicable for biomechanical research and improving personalized, computer-assisted medicine.

KEYWORDS

statistical shape modeling, soft-tissue modeling, computational modeling, personalized medicine, knee joint

1 Introduction

Osteoarthritis (OA) affects almost one out of 4 people globally and represents one of the fastest growing socio-economic burdens in the world (Hunter et al., 2020; Boer et al., 2021). Knee OA constitutes 83% of the global disease burden for OA (Vos et al., 2012). Although highly prevalent, researchers are only at dawn of unravelling the complex interaction between both biomechanical and systemic factors triggering disease onset and progression (Sharma et al., 2010).

Methodologies to accurately measure *in vivo* joint contact forces acting on the knee and to analyze soft tissue functioning are currently lacking and hamper research progression. A valuable approach that is increasingly being adopted, involves computational musculoskeletal modeling to indirectly estimate joint mechanics. This method allows for non-invasive estimation of joint loading distribution while improving insight in intersubjective anatomical variance when repeatedly performed. While it has been previously shown that the results of these models rely strongly on accurate anatomical information, generation of such input structures is generally deducted from manual segmentation of Computed Tomography (CT) and/or Magnetic Resonance Imaging (MRI) (Marra et al., 2015; Kang et al., 2017). However, repeated laborious manual segmentations remain a substantial bottleneck of the personalized musculoskeletal modeling workflow. In addition, manual segmentations contribute to a higher rate of observer-related inaccuracies (Seim et al., 2008; Bae et al., 2009). Furthermore, the frequent use of MRI is complicated by a high cost and a low availability (Bae et al., 2009). To date, these limitations impede the bench to bedside translation and routine use in clinical practice.

An emerging approach to mitigate this problem is the combination of computational musculoskeletal modeling with statical shape analysis (van Houcke et al., 2020a; Pascoletti et al., 2021). Aiming to bypass the aforementioned restrictions, Audenaert and colleagues developed a validated pipeline for semi-automated shape model-based segmentation of the lower limb based on computed tomography (CT) imaging (van Haver et al., 2014a; Audenaert et al., 2019a). Next, Van Houcke and colleagues tackled the issue of personalized cartilage layer geometry prediction by the development of cartilage thickness maps based on a training MRI dataset and by building on the features of simplicity and anatomical correspondence of geometric morphometrics. Femoroacetabular cartilage geometry was thus estimated according to hip joint morphometrics, avoiding the manual segmentation inaccuracies and optimizing time-efficiency (van Houcke et al., 2020a). For the inclusion of muscle and tendon paths, Audenaert et al. overcame the hurdle of modeling deformable soft tissue utilizing discrete elements rigid body spring models, again relying on geometric morphometrics for the prediction of origin and insertion (Audenaert and Audenaert, 2008; Audenaert et al., 2019b).

The combined methodology to describe bone, cartilage and soft tissue at a population wide level was recently adopted for the ankle joint by (Peiffer et al., 2022a). In this study, the techniques described by Van Houcke et al. and Audenaert et al. were combined for estimation of cartilage topography of the tibiotalar joint and inclusion of the main ankle ligament paths (Audenaert et al., 2019b; van Houcke et al., 2020a; Peiffer et al., 2022a). However, no similar advancements have been made for the knee joint. Van Dijck and colleagues developed a statistical shape model (SSM) based on 524 knee joint MRI's to predict cartilage thickness and localization in the tibiofemoral joint. This model, however, lacks inclusion of patellar bone and cartilage layer as well as the menisci and the cruciate ligaments (van Dijck et al., 2018).

The recent introduction of SSM allows for efficient population-wide analysis of shape as variance is compactly modeled and is an established tool for medical image segmentation. Being able to simulate large populations, the use of SSM improves understanding of disease models and injury biomechanics. Furthermore, the use of SSM enables patient-specific modeling which facilitates the introduction of individualized medicine in the clinical practice (Nauwelaers et al., 2021). However, an inclusive, patient-specific computational knee joint model, minimally relying on manual segmentation is currently lacking.

The aim of this study is to develop a generic computational model that can easily be scaled, morphed and fitted to patient-specific knee joint anatomy, avoiding laborious segmentation tasks and improving accuracy of patient-specific geometry predictions. This study builds further on in-house available expertise regarding statistical shape modeling and soft tissue wrapping methodology (Audenaert et al., 2019b; van Houcke et al., 2020a; Peiffer et al., 2022a). The objectives of the current study are: 1. Patient-specific prediction of the cartilage layer of the tibiofemoral and the patellofemoral joint, 2. Prediction of the anatomy of the anterior and posterior cruciate ligament, main knee ligaments and patellar tendon, 3. Prediction of static meniscal anatomy, and 4. Validation of patient-specific soft tissue prediction.

2 Materials and methods

2.1 Data collection

Two distinct imaging databases were used for the shape modeling workflow. In particular, a first dataset consisted of CT images, adopted for the SSM development and the description of osteology, whereas soft tissue features were derived from a second dataset, consisting of MR images.

For the description and parameterization of the osseous structures, a total of 311 bilateral lower limb CT scans (training sample n = 622) were derived of 181 male and 130 female non-arthritic subjects. The average age of males and females was respectively 67.8 (±10.8) and 69 (±13.3) years. Each scan contained an average of 1864 slices with a pixel size 0.575 mm–0.975 mm. This imaging data were previously used in the development of an articulated skeletal SSM of the lower limb, including the knee joint (Audenaert et al., 2019a). A detailed description of the articulated skeletal SSM generation and

validation in terms of specificity, compactness, generalizability, accuracy and population coverage was previously published (Audenaert et al., 2019a).

For the description and parameterization of soft tissue structures, the extensive MRI database built by Van Hoecke et al. was used (Van Hoecke et al., 2020b). This database consisted of 53 young and healthy Caucasian men who underwent dedicated, high resolution series of hip, knee and ankle joints in an unloaded position. The dataset contained healthy Caucasian men aged between 17 and 25 years who were not overweight with a mean total body length of 181.79 cm. Dedicated hip, knee and ankle scans were taken using a Siemens® 3 Tesla MRI with a pixel size of 0.469 mm–0.469 mm and a slice thickness of 0.5 mm (van Houcke et al., 2020b; de Roeck et al., 2020). These dedicated scans were then stitched using Materialise's Interactive Medical Image Control System (Mimics® v21.0, Materialise, Leuven, Belgium) in the formation of an overview, full lower limb scan. Further details on data collection and imaging acquisition were previously published (van Houcke et al., 2020b).

Subjects included in both studies provided written informed consent. An ethics committee of the Ghent University Hospital (Belgium) approved both investigations.

2.2 MRI segmentation, landmark identification and definition of structural features

MR scan data were exported as Digital Imaging and Communications in Medicine (DICOM) files and subsequently imported in Mimics®. Osseous and cartilage anatomy was extracted from all 53 cases (see section 2.2.1 and 2.2.2). Identification of dedicated landmarks and structural features (e.g., thickness, height and width) used in ligament, patellar tendon and meniscal anatomy prediction was performed on 10 cases. The used cases were randomly selected from the complete dataset. All calculations were completed in Matlab by using both custom-made Matlab® scripts and the Matlab® plugin in the Mimics software, and performed on a Dell Precision 5560 Laptop (Intel Core i9 -11950H, 64 GB RAM, 64 bit).

2.2.1 Segmented osseous anatomy

The osseous anatomy was derived from the overviewing full lower limb MRI scans, relying on SSM-based semi-automated image segmentation. First, 300 points were manually determined, randomly distributed over the cortical edges of the structures for which segmentation is required (e.g., the femoral bone, the patellar bone and the combined tibial-fibular bone). Second, the SSM of the corresponding structure was fitted (van Haver et al., 2014a; van Haver et al., 2014b; Audenaert et al., 2019a). For fitting, a total of 50 principal components was retained, resulting in a cumulative explained variance of 99.55%, 96.60% and 99.19% for respectively the femur, the patella and the combined tibia-fibula. These target meshes were thus dense corresponding surface geometries provided by means of quasi-isometric triangulated meshes consisting out of 21097, 3825 and 39197 vertices and 42188, 7646 and 78386 faces for respectively the femur, the patella and the combined tibia with fibula. Uniformly distributing the total of vertices over the osseous structure, the average length of the triangle edges equaled respectively 1.77 mm, 1.05 mm and 1.24 mm for the femur, the patella and the combined tibia with fibula. Audenaert and colleagues evaluated the accuracy of SSM-based segmentation against manual segmentation based on the Average Surface Distance (ASD) and the Hausdorff Distance (HD). The ASD equaled 0.65 mm (SD 0.10 mm), 0.63 mm (SD 0.11 mm) and 0.76 mm (SD 0.18 mm) for respectively the femoral, tibial and fibular bone. The HD equaled respectively 4.79 mm (SD 2.39 mm), 4.07 mm (SD 2.15 mm) and 3.76 mm (SD 1.17 mm). Based on the proven generalizability of the model, accurate SSM-based segmentation was obtained (Audenaert et al., 2019a). From these triangulated meshes, the distal femur, the proximal tibia and the patella were isolated and imported for further use in the high resolution series of the knee in Mimics®.

2.2.2 Segmented cartilage anatomy

For all 53 cases, the cartilage layers of distal femur, proximal tibia and patella were manually segmented on the dedicated high resolution knee series. The contour editing tool in Mimics® was used to deform the uniform osseous meshes of the femur, the patella and the combined tibia-fibula, to no longer solely delineating the osseous cortex but additionally comprising the cartilage layer. The Mimics® contour editing tool applied a distance-based Gaussian deformation, a type of free-form deformation, to provide a smooth contour edit and to control locality. As such, it allowed for point correspondence between the osseous mesh and the deformed mesh comprising the cartilage layer (Yoshida et al., 2002).

2.2.3 Landmarks defining ligamentous and patellar tendon anatomy

Ligamentous and patellar tendon origin and insertion sites were manually selected. The selection was supported and guided by the anatomical reference of Laprade et al. (LaPrade and Engebretsen, 2007; James et al., 2015). To minimize the error related to manual landmark identification, landmarks were first localized on MRI in 10 cases. Subsequently, the location of the origin and insertion points was established in relation to the bony surfaces of femur, tibia and patella as nearest neighboring points were derived. Lastly, the average origin and insertion was determined and annotated on a reference template mesh. Non-rigid surface registration of the reference template towards the SSM allowed for indices-based landmark transfer within the osseous shape model while maintaining anatomical correspondence (van Haver et al., 2014b). Ligamentous thicknesses, later required for ligament modeling, were obtained from literature (Nomura et al., 2005; Wilson et al., 2012; Hedderwick et al., 2017; Ariel de Lima et al., 2019; Atkinson et al., 2022). The described ligaments included the Medial Patellofemoral Ligament (MPFL), the Lateral Patellofemoral Ligament (LPFL), the two strands of the superficial Medial Collateral Ligament (sMCL) (e.g., an anterior and posterior bundle), the Lateral Collateral Ligament (LCL), the Anterolateral Ligament (ALL), the Posterior Oblique Ligament (POL) and the Oblique Popliteal Ligament (OPL).

2.2.4 Landmarks and structural features defining cruciate ligament anatomy

Similarly, origin and insertion sites of the anterior (ACL) and posterior (PCL) cruciate ligament were manually selected, averaged

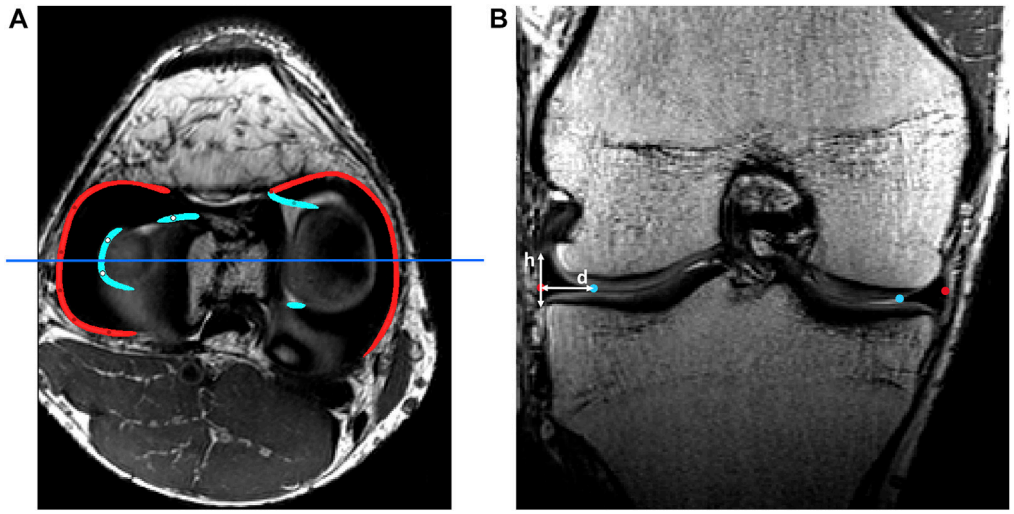

FIGURE 1
(A) Axial view of the knee joint on MRI with manually detected outer rims (red) and inner rims (light blue). The dark blue line represents the slice of the coronal view. **(B)** Coronal view of the knee joint on MRI. The height (h) and width (d) of the meniscus were measured as shown. This process was repeated over the course of the outer rim.

and annotated on a reference template mesh, allowing non rigid registration towards the SSM. Additionally, the thickness of the ACL and PCL over their respective course from origin to insertion was measured for every 10 slices on MRI, to describe local variation in their respective radius.

2.2.5 Landmarks and structural features defining meniscal anatomy

Similar to ligament and patellar tendon inclusion, the anterior and posterior root of the medial and lateral meniscus were subsequently manually selected, averaged and determined in relation to the tibia anatomy. Following, corresponding nearest indices values were derived to allow for landmark transfer within the shape model. An inner and outer rim was generated based on manually selected points on MRI, using the spline generation tool incorporated in Mimics®. The meniscal height and width was repeatedly measured from origin to insertion to describe the triangular geometry of the meniscus and local variation herein. For randomly selected points distributed over the outer rim, the meniscal height was measured and the meniscal width was defined as the Euclidean distance between the inner and outer meniscal rim. A detailed description of this process is described in Figure 1.

2.3 Workflow for subject-specific, soft tissue prediction

2.3.1 Cartilage thickness prediction

To determine the location of the cartilage layer, the previously developed meshes of the osseous structures and the ones including the cartilage layers were easily compared, as correspondence was maintained following Gaussian-based contour editing in Mimics®. A total of 2221 vertices, 872 vertices, 875 vertices and 1572 vertices were identified for respectively the distal femoral bone, the medial tibia plateau, the lateral tibia plateau and the patellar bone. For every case, the node-specific cartilage thickness was defined as the distance of the subchondral bone to the cartilage surface, along the surface normal. To smoothly attach the cartilage to the bone, the distances at the edge vertices were adjusted to zero. As such, 53 case-specific cartilage thickness maps were generated (Figure 2).

These thickness maps were averaged to develop a mean cartilage thickness map. The cartilage geometry of any new shape was then predicted by projecting the vertices, part of the articular surface, along the direction of their normal over their corresponding distance, extracted from the mean distance map. As previous research has already demonstrated the correlation between osseous size and thickness of the cartilage layers, the dedicated distance maps were scaled according to the femoral length to account for size differences between cases (Rissech et al., 2013; van Dijck et al., 2018; Schneider et al., 2022). Thus, the cartilage thickness does not solely depend on the morphology of the underlying bone.

2.3.2 Meniscal anatomy prediction

Both menisci were modeled as mobile, elastic structures accommodating to the shape of the femoral condyles and their variable position relative to the tibia. The geometry of both menisci was numerically simplified as triangular with varying height and width. The previously derived height and width measures were averaged and plotted against the relative outer length of the meniscus (Figure 1). Polynomial functions of increasing order were fitted and compared to the ground truth, an over-fitted 20th degree polynomial, by means of the Root Mean Square Error (RMSE). Evolution in the RMSE for increasing order of the polynomial enabled the detection of the optimal degree of polynomial fitting. Based on the coefficients extracted from the optimal degree polynomial function, meniscal

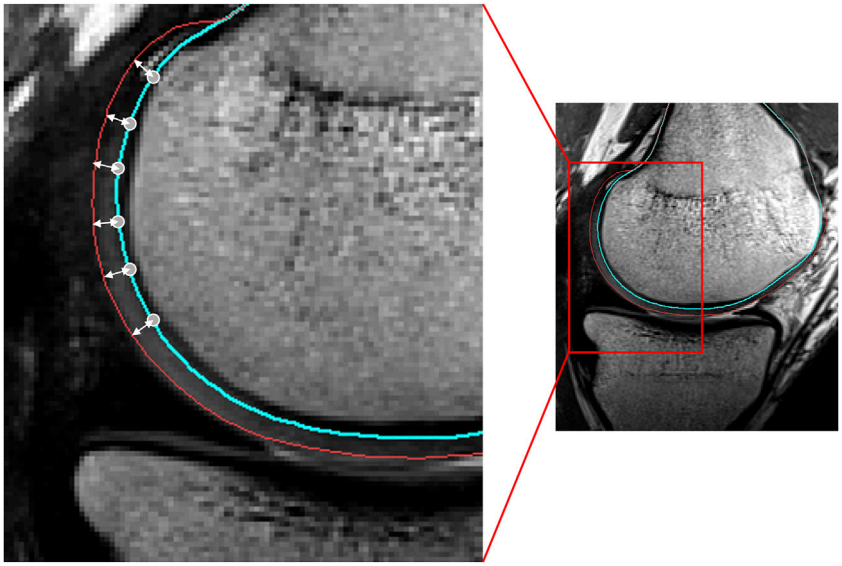

FIGURE 2
Sagittal view of the femoral condyle on MRI. The node-specific cartilage thickness was defined as the distance of the vertex (located on the blue line) to the cartilage surface (red), along the vertex normal.

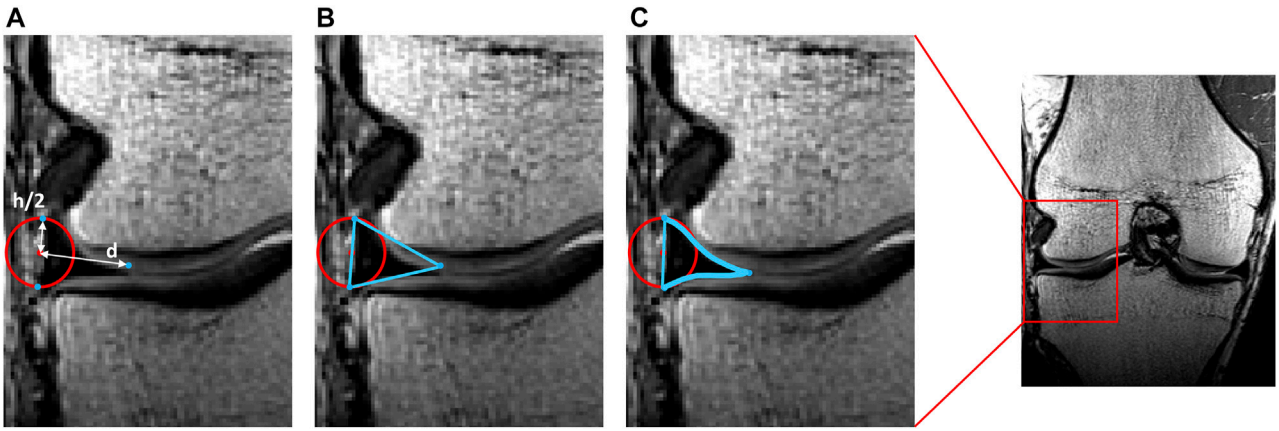

FIGURE 3
Representation of meniscal modeling. **(A)** A tube was wrapped elastically from the anterior to the posterior horn enforcing an offset of half the meniscal height (h/2). A varying distance (d) is extracted for every node. **(B)** Triangles are formed by interconnecting the three points per node. **(C)** Following correction for local penetration, the edges of the meniscus adapt to fit in between cartilage layers.

height and width were calculated over the course of the meniscus from anterior to posterior root. As such, this method allowed for description of regional variation in meniscal triangular geometry.

First and relying on previous work, a tube was elastically wrapped from the anterior to the posterior horn enforcing an offset equal to half the meniscal height. Tube formation, as described by Audenaert and colleagues, was based on a generalized cylinder model. Over the path of a spline, connecting the anterior to the posterior meniscal root, the point-dependent offset was imposed to avoid osseous and cartilage penetration and thus force the tube to wrap around the femoral condyle (Audenaert et al., 2009; Audenaert et al., 2019b; Peiffer et al., 2022a). Second, according to the calculated path and at equidistant interval, triangles were defined with height and width derived from the above described polynomial estimates, with the width projected towards the meniscal center and the height orthogonal to this. The triangles, generated by interconnecting the three projections per node were then logically arranged to form a 3D mesh. Third, to correct for local penetration and to fit meniscal geometry between femoral and tibial cartilage, local meniscal morphometry was adjusted by projecting penetrating meniscal nodes on the outer osseous–cartilage surface (Figures 3, 4).

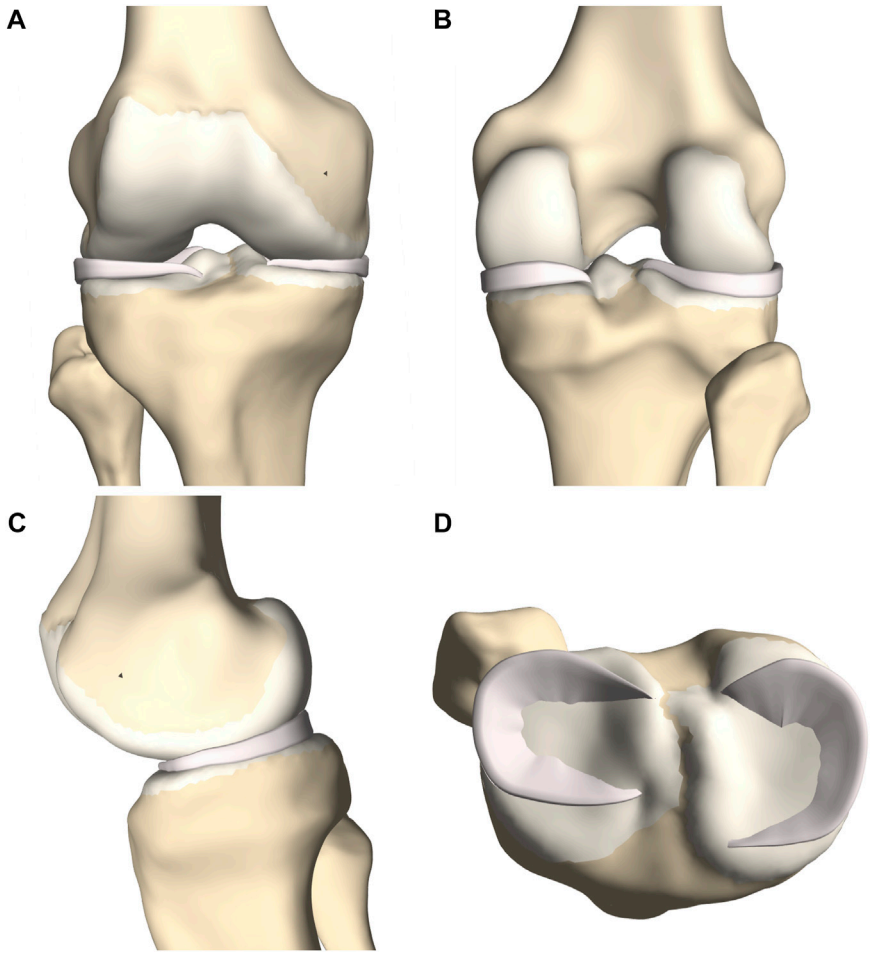

FIGURE 4
(A) Frontal, **(B)** posterior and **(C)** medial view of femoral and tibial bone (yellow) with predicted cartilage layers (white) and menisci (pink). **(D)** Axial view on the tibial plateau (yellow), with predicted cartilage layers (white) and menisci (pink).

2.3.3 Ligament and patellar tendon anatomy prediction

Ligament geometry and path prediction was based on a custom-made mesh wrapping algorithm as previously described by (Audenaert et al., 2009; Audenaert et al., 2019b; Peiffer et al., 2022a). This mesh wrapping algorithm was based on path prediction of the psoas anatomy as described by Audenaert et al. A finite number of springs formed an elastic membrane that was iteratively released to progressively minimize the potential energy while not permitting penetration of underlying structures (Audenaert et al., 2019b). Peiffer et al. converted this technique towards ligamentous modeling as elastic line segments rather than membranes connected ligamentous origins and insertions. Again, by progressively releasing the elastic segment, the potential energy was minimized without permitting penetration of adjacent structures. Penetrating nodes were returned to the closest point on the penetrated surface. Applying this technique for knee soft tissue modeling, knee ligaments were wrapped around the osseous-cartilage–meniscus meshes while surface penetration was impeded. Following, a flat mesh was formed by interconnecting the nodes (Peiffer et al., 2022a). Lastly, a volume was added to the ligament description by assigning a single, ligament-specific thickness over the course of the ligament. This thickness was based on previously published cadaveric studies and MRI measurements (Table 1) (Nomura et al., 2005; Wilson et al., 2012; Hedderwick et al., 2017; Ariel de Lima et al., 2019; Atkinson et al., 2022). The methodology was repeated for the different knee joint ligaments. A more elaborate description of the process details was previously provided by Audenaert et al. and Peiffer et al. (Audenaert et al., 2019b; Peiffer et al., 2022a).

Prediction and modeling of the patellar tendon is an exception on the above described technique. On both the

TABLE 1 The assigned ligament-specific mid-substance thickness (in millimeters), based on cadaveric studies and MRI measurements.

	MPFL	LPFL	sMCL	LCL	ALL	POL	OPL
Thickness (in mm)	2.90	1.80	2.10	2.20	1.50	1.00	1.44

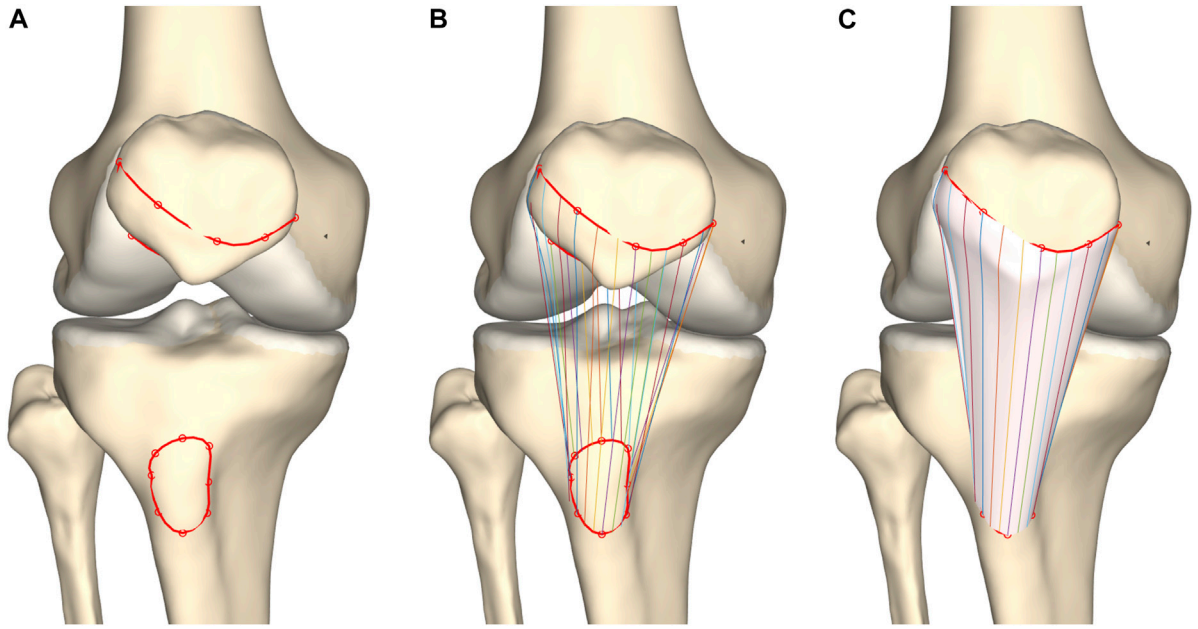

FIGURE 5
Frontal view of the knee joint. **(A)** Splines were formed interconnecting patellar origin and tibial insertion vertices. **(B)** Corresponding coordinates were connected. **(C)** Tendon modeling was based on a custom-made mesh wrapping algorithm.

origin and insertion site a spline was defined connecting the origin and insertion vertices respectively. Similarly as for ligamentous path prediction, corresponding coordinates were connected based on a custom-made mesh wrapping algorithm while any penetration of the combined osseous–cartilage–meniscus surface was corrected. As corresponding points on a closed spline were connected, the thickness of the ligament is inherent to the positioning of the vertices and is therefore not an assigned value (Figure 5).

2.3.4 Cruciate ligament anatomy prediction

The cruciate ligaments were modeled as curved tubes with variable radii in three dimensional space, based on estimating Frenet-Serret frames along a centerline. First, the centerline of the ACL was modeled from origin to insertion as a series of connected spring elements (n = 15) and its was position optimized based on a shortest path function, similar as for initial ligament modeling (Audenaert et al., 2009; Audenaert et al., 2019b). Connecting nodes between spring elements were spatially constrained to a minimal offset similar to the cruciate ligament width. Second, and contrary to previous ligamentous modeling, regional variation in ACL thickness was appraised by low degree polynomial functions, the degree of which was determined following a similar sensitivity analysis as conducted for meniscal height and width. Third, the ACL was comprised in the osseous–cartilage–meniscus–ligament model to function as a constraint for the course of the PCL. The PCL was similarly modeled and thus wrapped around the ACL in its course from origin to insertion (Figure 6).

A complete knee joint model was generated combining the modeled structures, described in section 2.3 (Figure 7).

2.4 Validation of soft tissue anatomy prediction

Validation of the predicted soft tissue anatomy relied on leave-one-out experiments. The predicted and manually detected anatomy was compared based on the Root Mean Square Error (RMSE, square root of the average of all absolute square distances), the Average Surface Distance (ASD, the average of all the distances) and the Hausdorff distance (HD, the maximum absolute distance).

2.4.1 Validation of cartilage thickness prediction

For all the cases, the predicted and manually segmented node-specific cartilage thicknesses were compared (n = 53).

2.4.2 Validation of ligament and patellar tendon anatomy prediction

2.4.2.1 Validation of ligamentous and patellar tendon landmark identification

Manually selected ligament and tendon origin and insertion surface areas were compared with the predicted surface areas (n = 10). The surface areas were delineated as curves on the osseous structure. Curves were formed using a spline generating tool to interconnect both the manually selected and the predicted vertices on origin and insertion site.

2.4.2.2 Validation of ligament and patellar tendon geometry prediction

Similar to the methodology described by Peiffer et al., the edges of the main knee ligaments and patellar tendon were manually identified on MR imaging (n = 10) (Peiffer et al., 2022b). A nearest

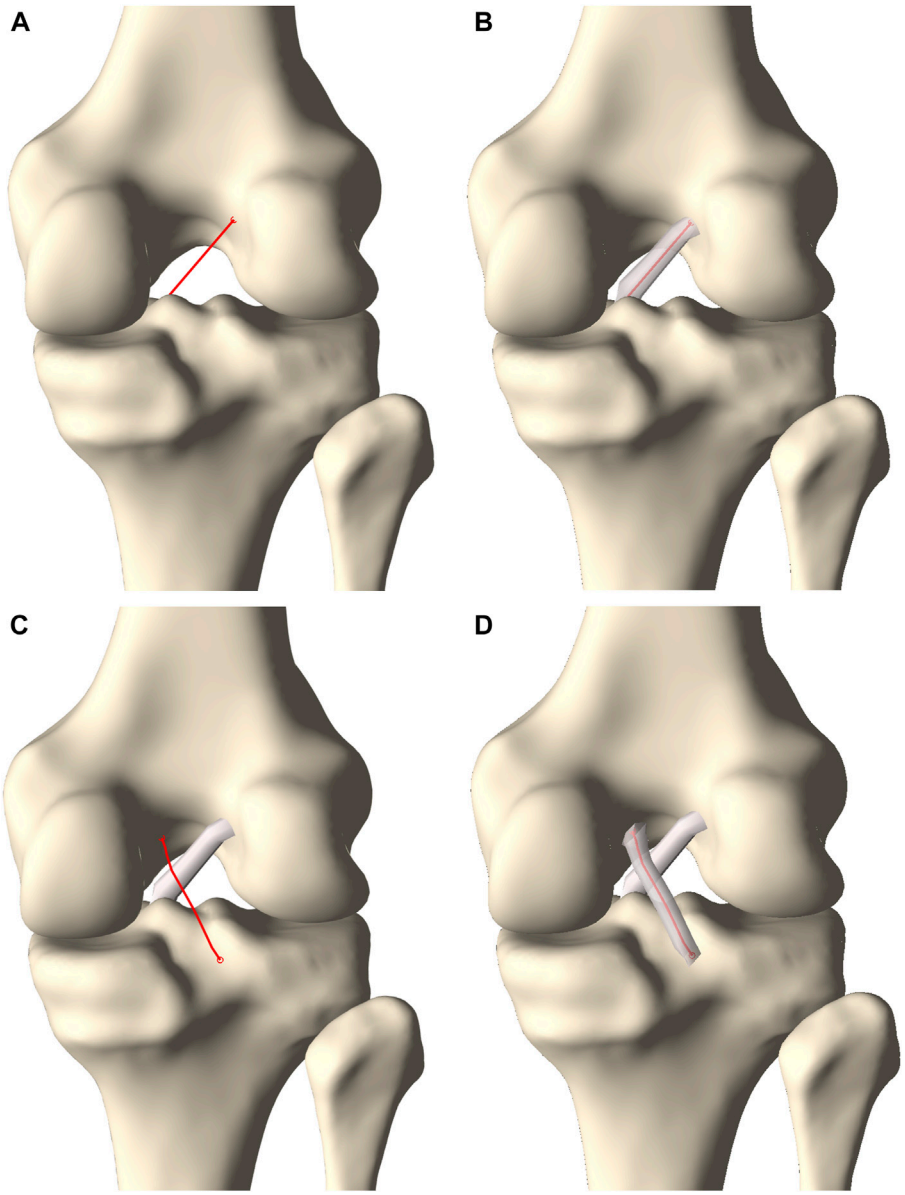

FIGURE 6
Posterior view on the knee. **(A)** A centerline was generated connecting the femoral ACL origin and the tibial ACL insertion. **(B)** A tube with varying radius was fitted around the centerline to model the ACL. **(C)** A second centerline was forced to wrap around the ACL when connecting the femoral PCL origin and the tibial PCL insertion. **(D)** A tube fitted around the centerline with a varying radius formed the PCL.

neighbor algorithm was used to compare manually detected edges with the edges of the predicted course.

2.4.2.3 Validation of cruciate ligament landmark identification

The manually selected origin and insertion of ACL and PCL were compared with the predicted origin and insertion (n = 10).

2.4.2.4 Validation of cruciate ligament geometry prediction

The edges of the cruciate ligaments were manually determined on MR imaging and a nearest neighbor algorithm was used to compare with the predicted ligamentous edges (n = 10).

2.4.3 Validation of meniscal anatomy prediction

2.4.3.1 Validation of meniscal landmark identification

The anterior and posterior root of the medial and lateral meniscus were manually selected on MR imaging and compared with the predicted anterior and posterior root (n = 10).

2.4.3.2 Validation of meniscal geometry prediction

Manually segmented medial and lateral menisci, unseen to the model, were compared to the predicted medial and lateral meniscus (n = 10) (Figure 8). The point-dependent error was averaged over the cases and plotted to identify regions that contained most variation.

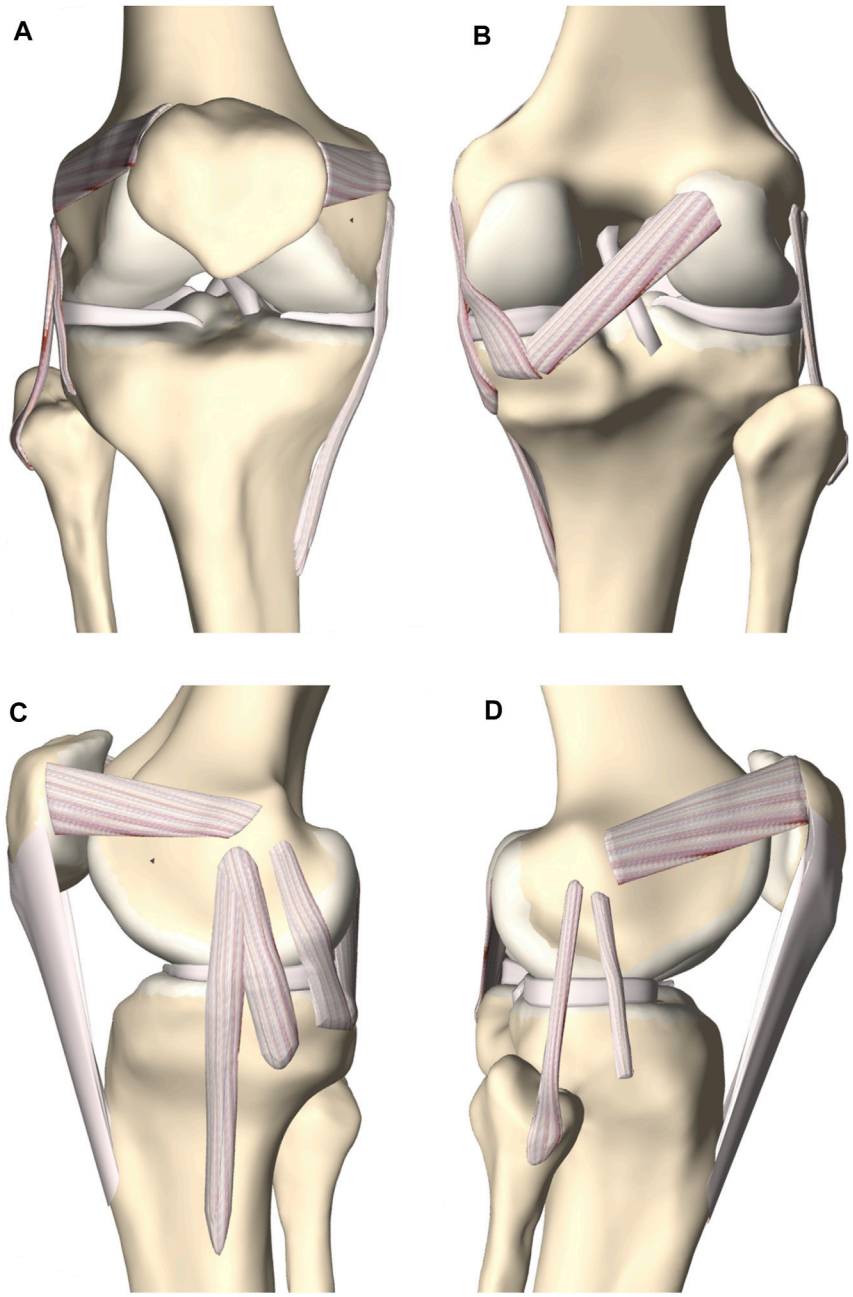

FIGURE 7
(A) Frontal, **(B)** posterior, **(C)** medial and **(D)** lateral view of the knee joint. The femoral, tibial and patellar bone were depicted including the predicted cartilage layer. The model contained the main knee ligaments, the patellar tendon (except in the frontal view), the medial and lateral meniscus and the anterior and posterior cruciate ligament.

3 Results

3.1 Mean cartilage thickness maps

The average femoral cartilage thickness totaled 1.41 mm (SD 0.37, range 0–3.08 mm), with local cartilage thickness maxima located at the patellofemoral joint surface and the posterior condyles. Similarly, the average cartilage thickness equaled 1.10 mm (SD 0.31, range 0–1.71 mm) and 1.19 mm (SD 0.34, range 0–1.89 mm) for respectively the medial and lateral tibial plateau. For the patella, the average cartilage thickness was 1.69 mm (SD 0.72, range 0–3.23 mm). Local variation is shown in Figure 9.

3.2 Validation of soft tissue anatomy prediction

3.2.1 Validation of cartilage thickness prediction

The largest error was observed for the prediction of the patellar cartilage thickness with a median RMSE of 0.75 mm (range

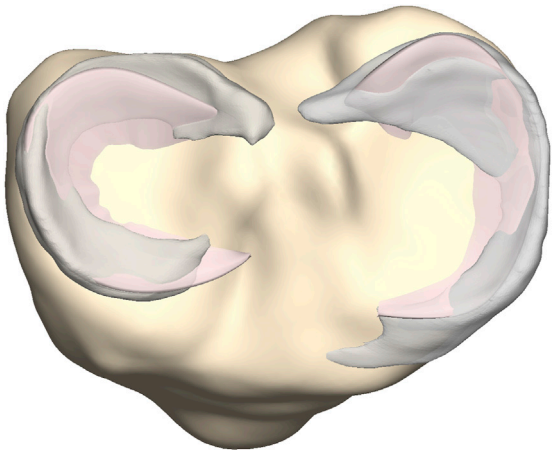

FIGURE 8
Axial view on the tibial plateau (yellow). The predicted medial and lateral menisci (pink) were superimposed on the manually segmented medial and lateral menisci (grey).

0.16–1.11 mm), a median ASD of 0.60 mm (range 0.13–0.89 mm) and a median HD of 2.05 mm (range 0.40–3.55 mm) (n = 53). Smaller errors and in the same order of magnitude were observed for prediction of tibial and femoral cartilage thickness prediction. The findings were summarized in Table 2.

To localize the sites with the largest error in cartilage thickness prediction, the point-dependent mean error is plotted relative to the point-dependent mean cartilage thickness (Figure 10).

3.2.2 Validation of ligament and patellar tendon prediction

3.2.2.1 Validation of ligamentous and patellar tendon landmark identification

Errors in predicting the osseous origin and insertion sites by landmark transfer were evaluated. The median RMSE ranged from 1.49 mm to 4.61 mm. The minimal and maximal error was described respectively for the femoral origin of the LCL and the tibial insertion of the anterior bundle of the sMCL. Detailed findings are presented in Table 3.

3.2.2.2 Validation of ligament and patellar tendon geometry prediction

The median RMSE in predicting the shape of the ligaments and patellar tendon ranged from 0.27 mm to 1.04 mm. The largest variation was observed in patellar tendon prediction with a median ASD of 0.80 mm (range 0.74–0.97 mm) and a median HD of 2.20 mm (range 1.64–2.84 mm). The smallest error was observed for the POL with a median ASD of 0.23 mm (range

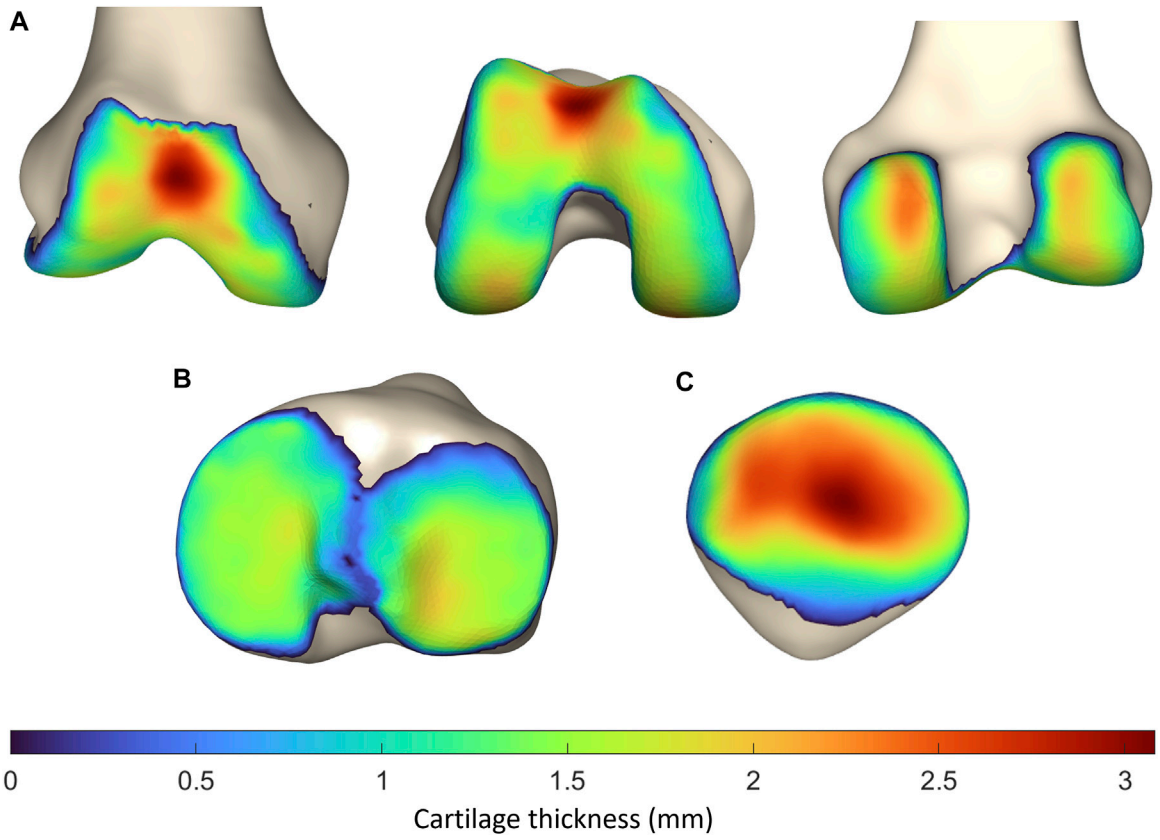

FIGURE 9
Representation of the vertex-specific cartilage thickness on **(A)** the mean femur, **(B)** the mean tibia and **(C)** the mean patella, extracted from the SSM. The average cartilage thickness ranges from 0 mm (blue) to 3.23 mm (red).

TABLE 2 Median RMSE, ASD and HD with range for tibial, femoral and patellar cartilage layer prediction.

	Tibial cartilage	Tibial cartilage	Femoral cartilage	Patellar cartilage
	Medial plateau	Lateral plateau		
RMSE (mm) (range)	0.32 (0.14–0.48)	0.35 (0.16–0.53)	0.39 (0.15–0.80)	0.75 (0.16–1.11)
ASD (mm) (range)	0.26 (0.11–0.38)	0.29 (0.13–0.43)	0.31 (0.12–0.67)	0.60 (0.13–0.89)
HD (mm) (range)	0.80 (0.34–2.06)	0.90 (0.32–1.81)	0.96 (0.35–2.66)	2.05 (0.40–3.55)

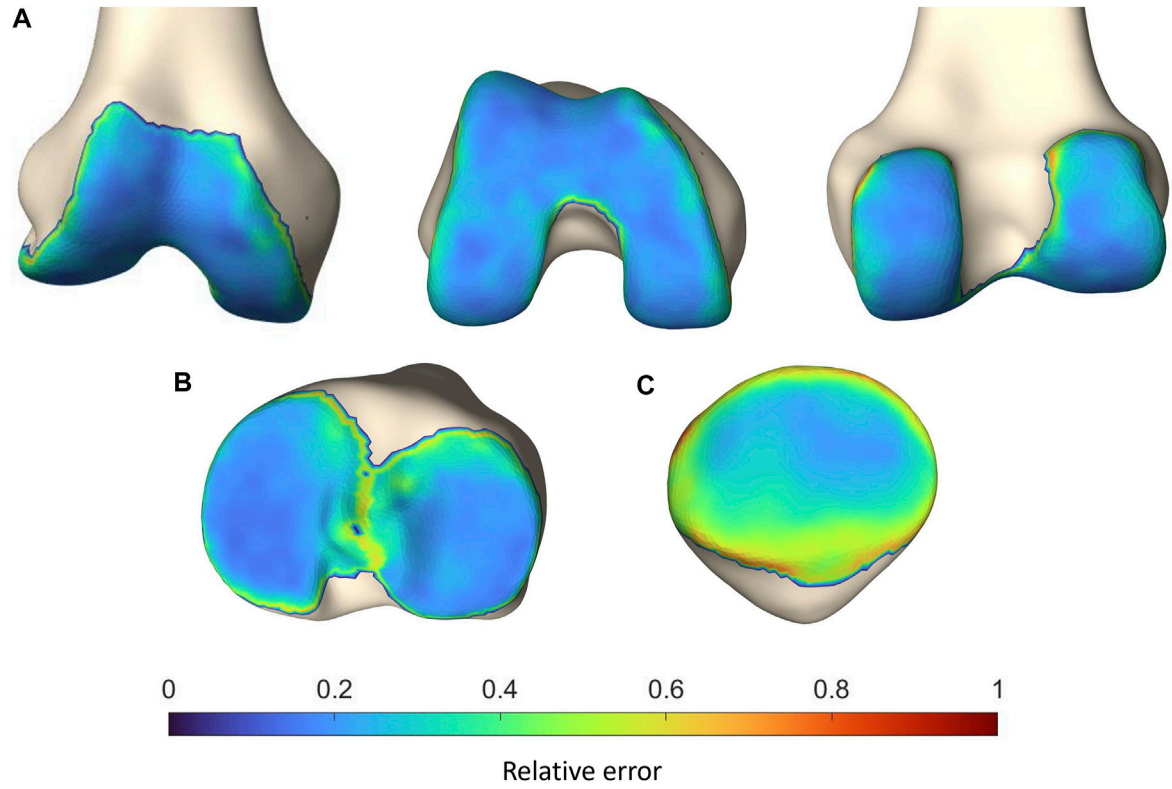

FIGURE 10
Representation of the vertex-specific relative error in cartilage thickness prediction on **(A)** the mean femur, **(B)** the mean tibia and **(C)** the mean patella, extracted from the SSM. Color-coding ranges from blue (absent error) to red (error equaling the point-dependent mean cartilage thickness).

0.14–0.36 mm) and a median HD of 0.49 (range 0.29–1.07). These and additional findings are summarized in Table 4.

3.2.2.3 Validation of cruciate ligament landmark identification

The largest error in predicting the osseous origin and insertion was observed for the tibial insertion of the ACL. The RMSE equaled 6.29 mm and the median error equaled respectively 5.65 mm (range 4.15–8.66 mm). Additional findings are summarized in Table 5.

3.2.2.4 Validation of cruciate ligament geometry prediction

Only small errors were observed in predicting cruciate ligament geometry. The RMSE equaled 1.16 mm (range 0.99–1.59) and 0.91 mm (range 0.75–1.33) for respectively the PCL (Table 6).

Based on a sensitivity study the degree of polynomial fitting for prediction of local variation in thicknesses from origin to insertion for both the ACL and the PCL was determined. The optimal polynomial fit was respectively a 2nd and 4th degree polynomial fit (Figure 11). The measured and predicted cruciate thickness was compared for validation purposes (Table 7).

3.2.3 Validation of meniscal anatomy prediction

3.2.3.1 Validation of meniscal landmark identification

The median RMSE in landmark prediction ranged from 2.71 mm to 3.75 mm. In general, a larger error was observed for prediction of the location of the anterior root in comparison to the prediction of the location of the posterior root. Detailed findings are described in Table 8.

TABLE 3 Median RMSE, ASD and HD with range for the main knee joint ligaments and patellar tendon origin and insertion.

Origin	MPFL (patella)	LPFL (patella)	sMCL anterior bundle (femur)	sMCL posterior bundle (femur)	LCL (femur)	ALL (femur)	POL (femur)	OPL (femur)	PT (patella)
RMSE (in mm) (range)	2.82 (0.35–5.16)	3.06 (2.92–7.12)	2.08 (1.05–4.14)	2.22 (1.00–3.93)	1.49 (1.17–2.78)	3.71 (3.63–4.61)	2.66 (1.12–7.37)	2.71 (2.03–4.69)	2.78 (0.86–4.39)
ASD (in mm) (range)	1.84 (0.20–4.79)	2.90 (2.35–5.87)	1.92 (0.70–4.09)	2.04 (0.72–3.52)	1.41 (1.13–2.61)	2.61 (2.02–2.70)	2.49 (1.03–7.33)	1.90 (1.49–4.31)	2.73 (0.77–3.76)
HD (in mm) (range)	6.44 (1.31–9.87)	5.94 (5.41–12.33)	3.86 (2.22–7.62)	3.59 (2.14–5.62)	1.89 (1.81–3.47)	12.18 (11.33–13.88)	3.51 (1.89–8.05)	7.57 (4.78–9.51)	4.17 (1.81–7.62)
Insertion	**MPFL (femur)**	**LPFL (femur)**	**sMCL anterior bundle (tibia)**	**sMCL posterior bundle (tibia)**	**LCL (fibula)**	**ALL (tibia)**	**POL (tibia)**	**OPL (tibia)**	**PT (tibia)**
RMSE (mm) (range)	2.82 (2.37–5.42)	4.44 (4.13–6.88)	4.61 (2.71–7.08)	3.22 (2.65–13.36)	1.57 (0.16–2.91)	2.49 (1.84–3.11)	1.72 (1.66–3.01)	1.63 (1.36–3.24)	2.67 (0.79–6.06)
ASD (in mm) (range)	2.37 (1.74–4.46)	4.42 (3.53–6.03)	3.49 (1.88–5.28)	2.56 (2.23–13.15)	1.45 (0.14–3.48)	2.39 (1.63–3.05)	1.55 (1.03–2.45)	1.46 (1.15–2.96)	1.80 (0.67–4.96)
HD (in mm) (range)	5.95 (3.84–10.14)	6.86 (5.04–10.53)	10.05 (6.21–15.10)	5.83 (4.76–15.10)	2.41 (0.23–3.48)	3.33 (2.65–4.12)	4.67 (3.25–6.57)	2.90 (2.49–5.53)	5.26 (1.44–9.56)

TABLE 4 Median RMSE, ASD and HD with range for the main knee joint ligaments and the patellar tendon course.

	MPFL	LPFL	sMCL anterior bundle	sMCL posterior bundle	LCL	ALL	POL	OPL	PT
RMSE (in mm) (range)	0.46 (0.24–1.05)	0.34 (0.19–0.57)	0.44 (0.26–0.59)	0.40 (0.37–0.53)	0.47 (0.27–1.29)	0.51 (0.40–0.91)	0.27 (0.17–0.47)	0.43 (0.24–0.72)	1.04 (0.85–1.13)
ASD (in mm) (range)	0.35 (0.23–0.84)	0.29 (0.17–0.40)	0.38 (0.25–0.57)	0.34 (0.30–0.44)	0.40 (0.25–1.03)	0.43 (0.34–0.68)	0.23 (0.14–0.36)	0.38 (0.21–0.57)	0.80 (0.74–0.97)
HD (in mm) (range)	0.60 (0.34–1.63)	0.69 (0.31–1.64)	0.80 (0.39–1.12)	0.75 (0.65–0.98)	0.79 (0.35–2.63)	0.70 (0.58–1.70)	0.49 (0.29–1.07)	0.70 (0.42–1.48)	2.20 (1.64–2.84)

TABLE 5 The RMSE and the median error with range from minimal to maximal error for the ACL and the PCL origin and insertion.

Origin	ACL (femur)	PCL (femur)	Insertion	ACL (tibia)	PCL (tibia)
RMSE (in mm)	2.70	2.25	**RMSE (in mm)**	6.29	2.97
Error (in mm) (range)	2.02 (0–3.84)	2.54 (0–3.14)	**Error (in mm) (range)**	5.65 (4.15–8.66)	2.69 (0–4.83)

TABLE 6 Median RMSE, ASD and HD with range for the ACL and PCL course.

	ACL	PCL
RMSE (in mm) (range)	1.16 (0.99–1.59)	0.91 (0.75–1.33)
ASD (in mm) (range)	1.15 (0.89–1.39)	0.87 (0.72–1.26)
HD (in mm) (range)	1.60 (1.41–2.61)	1.35 (0.95–2.15)

TABLE 7 Median RMSE, ASD and HD with range between predicted and measured thickness of the ACL and PCL.

	ACL	PCL
RMSE (mm) (range)	0.17 (0.06–0.48)	0.95 (0.64–1.42)
ASD (mm) (range)	0.14 (0.05–0.35)	0.88 (0.58–1.30)
HD (mm) (range)	0.27 (0.11–0.94)	1.36 (0.94–1.99)

3.2.3.2 Validation of meniscal geometry prediction

Comparable errors were observed for the medial and lateral meniscus. The median RMSE equaled respectively 2.93 mm (range 1.85–4.66) and 2.04 mm (range 1.88–3.29) (Table 9). The average point-dependent error ranged from 0 mm to 5 mm. The local variation in meniscal geometry prediction was largest for the inner rim of the lateral meniscus and the anterior root of the medial meniscus. The error was plotted in Figure 12.

Based on a sensitivity study the degree of polynomial fitting for prediction of meniscal height and width was determined. For the medial meniscus, height and width were plotted as respectively a 6th and 4th degree polynomial function. For the lateral meniscus, height and width were both plotted as a 4th degree polynomial function (Figure 13). The degree of polynomial fitting was validated comparing the measured and predicted meniscal height and width (Table 10).

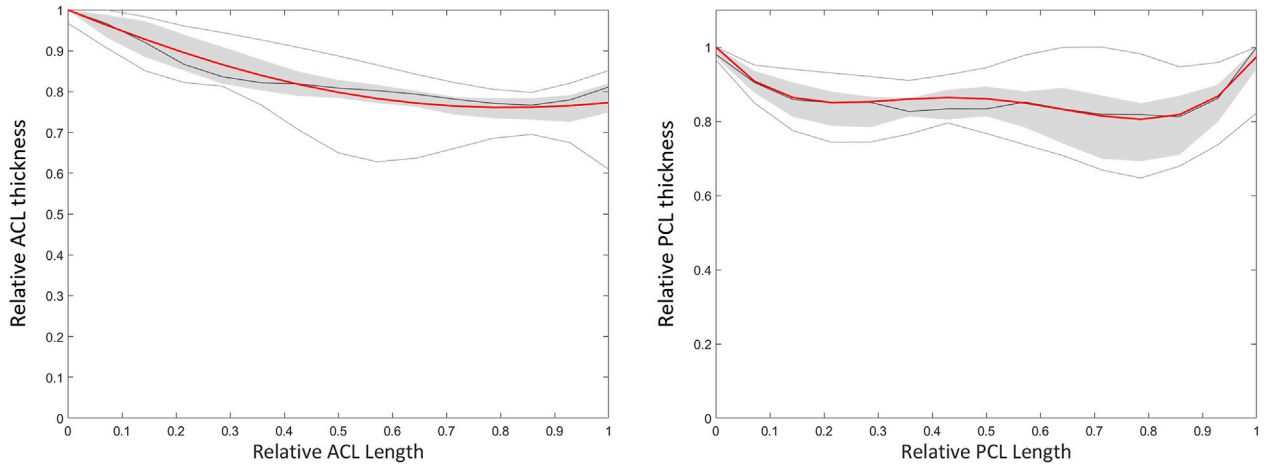

FIGURE 11
Polynomial fitting for ACL and PCL thickness prediction. The median thickness of the ACL (left) and PCL (right) is presented as the dark grey line. The grey zone represents the values between P25 and P75. The light grey lines represent minimal and maximal values. The red line represents the thickness based on a respectively 2nd and 4th degree polynomial function for the ACL and PCL.

TABLE 8 The RMSE and the median error with range from minimal to maximal error for medial and lateral meniscus anterior and posterior root.

Anterior root	Medial meniscus	Lateral meniscus	Posterior root	Medial meniscus	Lateral meniscus
RMSE (in mm)	3.51	3.75	**RMSE (in mm)**	2.71	2.82
Error (in mm) (range)	3.31 (1.37–5.10)	2.91 (1.49–5.29)	**Error (in mm) (range)**	1.78 (1.47–5.22)	2.45 (0–4.22)

TABLE 9 Median RMSE, ASD and HD with range for the medial and lateral meniscal course.

	Medial meniscus	Lateral meniscus
RMSE (range)	2.93 (1.85–4.66)	2.04 (1.88–3.29)
ASD (range)	1.84 (1.21–3.26)	1.49 (1.30–2.40)
HD (range)	11.64 (7.97–17.09)	9.79 (6.09–14.43)

4 Discussion

We present a methodological workflow for the development of a morphological knee model based on individual osseous morphology to automate the prediction of soft tissue anatomy. Computational models are on the rise for techniques to estimate joint kinetics, however soft tissue inclusion generally depends on laborious manual segmentation. For example, Dong et al. developed a three-dimensional knee joint model combining osseous elements with cartilage layers, cruciate and collateral ligaments, menisci and tendon insertions, solely based on manual segmentations (Dong et al., 2014). Similarly, Kang et al. generated a three-dimensional knee joint model in the development process of a finite element model to assess weight-bearing related deformation of the intra-articular cartilage contact area (Kang et al., 2015). As knee joint malalignment contributes to the onset and progression of joint OA, Mootanah et al. predicted knee joint contact forces and pressures depending on the amount of varus-valgus malalignment (Mootanah et al., 2014). Non-etheless, the model generation is very time-consuming and generalization to other cases and patient geometries is not straightforward.

Aiming to avoid manual segmentation and allow for patient specific analysis, we predict soft tissue anatomy relying solely on the underlying osseous morphology and capitalizing on the advantage of point correspondence and uniformly, isometrically distributed meshes when using SSM (Dong et al., 2014; Mootanah et al., 2014; Kang et al., 2015; Audenaert et al., 2019a). As a result, the extensive workload related to manual segmentation to obtain patient specific description of bony and soft tissue can be avoided (Audenaert et al., 2019a). Furthermore, as all computations originate from skeletal statistical shape modeling, and considering the generative power of these SSMs, large virtual cohorts can be defined for population-wide studies.

In analogy with a mesh node-specific cartilage thickness was allocated and averaged over the cohort in the development of a mean cartilage thickness map (van Houcke et al., 2020a). Previous research has already demonstrated the correlation between osseous size and cartilage layer thickness (van Dijck et al., 2018; Schneider et al., 2022). Proven to be an accurate estimator for total body length, we scaled the mean distance map by the femoral length (Hauser et al., 2005). To avoid small errors in underlying skeletal anatomy, possibly introduced by SSM-based automated image segmentation, to influence the validation process of cartilage thickness prediction, we

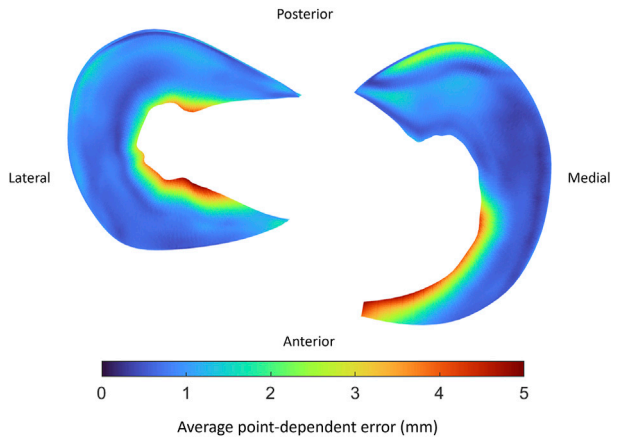

FIGURE 12
Visual representation of the average point-dependent error for the mean predicted lateral (left) and medial (right) meniscus. The mean error was color-coded ranging from blue towards red, equaling respectively an average point-dependent error of 0 mm and 5 mm.

compared the scaled, mean distance map to the case-specific calculated distance map instead of comparing the predicted and segmented cartilage surfaces (Seim et al., 2008; Bae et al., 2009). Of note, a small amount of variation in total length of the investigated population was observed, with a 95% confidence interval ranging from 180.1 to 183.5 cm. As a result, little variation was introduced in the imposed scaling factor.

The observed RMSE and ASD for femoral and tibial cartilage prediction was smaller than the MRI pixel size of 0.469 mm, on which our methodology was based. Although the prediction error for the patellar cartilage layer was slightly larger than the pixel size, it did not exceed 1.0 mm. Furthermore, when comparing to manual cartilage segmentation, considered the ground truth, the observed RMSE and ASD are in the same order of magnitude of previously published results. Manual segmentation itself is thus subject to intra- and inter-observer variation, inherent to the manual aspect of the technique. Part of the reported error in this study is therefore attributable to error related to manual segmentation (Cohen et al., 1999).

Since a relatively large HD of 2.05 mm was observed for patellar cartilage layer prediction, the zones with the largest errors were identified. Therefore, the obtained point-dependent mean error was then evaluated relative to the point-dependent mean cartilage thickness. The zones with the relatively largest local error are located near the edges of the cartilage layers and are rather small. Cartilage thickness prediction at the weight bearing sites, on the other hand, present a relatively small absolute error of approximately 0.6 mm, 0.36 mm and 0.6 mm for respectively the femoral bone, the tibial plateau and the patellar bone. In the absence of complete knee joint DEA modeling, the influence of cartilage thickness errors was evaluated for DEA modeling of the hip joint based on the available research. Niknafs and colleagues compared the relative decrease in peak contact stresses based on DEA modeling for different types of cartilage modeling following alignment optimization. For an acetabular cartilage thickness ranging between 1.24 and 1.95 mm a relative decrease of 39% was observed. For increased cartilage thickness, ranging from 1.29 mm to 2.87 mm, a greater relative decrease of 47% was observed. Thus, a thicker cartilage layer results in decreased peak stresses based on DEA modeling. Future research is however necessary to evaluate the impact of the variation in cartilage thickness on DEA-based stress calculations in the knee joint (Cohen et al., 1999).

Subsequently, we predicted meniscal anatomy as mobile, elastic structures connecting origin and insertion and being able to accommodate to the shape of the femoral condyles and their variable position relative to the tibia. As such, meniscal anatomy prediction was based on the underlying osseous geometry. Vrancken and colleagues manually segmented the medial meniscus with a 6 months' time period in between to evaluate the inter- and intra-observer variability. They report a relatively small RMSE of 0.29 and 0.27 for respectively the intra- and inter-observer reliability, in comparison with the reported errors in this study (Vrancken et al., 2014). However, the described error in meniscal course prediction when compared to manual segmentation is in the same order of magnitude as the findings of Tack and colleagues, who augmented their segmentation technique with the introduction of convolutional neural networks (Tack et al., 2018). Regarding meniscal origin and insertion prediction, we observe the largest prediction error to be present in the anterior root of the medial meniscus. This greater variation in anterior root error is explained as one out of the ten cases presents an extremely anterior insertion of the root. Variations in anterior root insertion of the medial meniscus are previously investigated by De Coninck and colleagues who identified three different bony insertion types on MRI. One of these types is described as an insertion anteriorly of the anterior tibial edge and is present in approximately 7% of the studied population (de Coninck et al., 2017). This specific anatomical variant was present in only one case of the cohort ($n = 10$) used for development of the meniscal model. The increased mean error positioned at the anterior root of the medial meniscus in the leave-one-out experiment can in part be attributed to this morphological variant. While currently not included in the present model, introduction of this variant in a probabilistic sense, is possible by simply changing the anterior root insertion reference (Figure 14). In large virtual population studies, different types of anterior root insertions can be included with the probability of a type I, II or III insertion linked to their respective population-wide prevalence.

Lastly, we included the cruciate ligaments, the main knee ligaments and the patellar tendon, again aiming to avoid manual segmentation and based on a fixed origin and insertion. To assess the accuracy of the main and cruciate ligamentous origin and insertion prediction, the described errors are evaluated against the available literature. Van der Merwe and colleagues reported MRI-based intra-observer agreements for manual femoral and tibial landmark identification. The intra-observer agreements ranged between 0.09 mm and 2.46 mm and between 0.06 mm and 2.69 mm for respectively the femoral and tibial bone (van der Merwe et al., 2019). Similarly, Esfandiarpour et al. studied the variability in landmark identification on the femoral condyles.

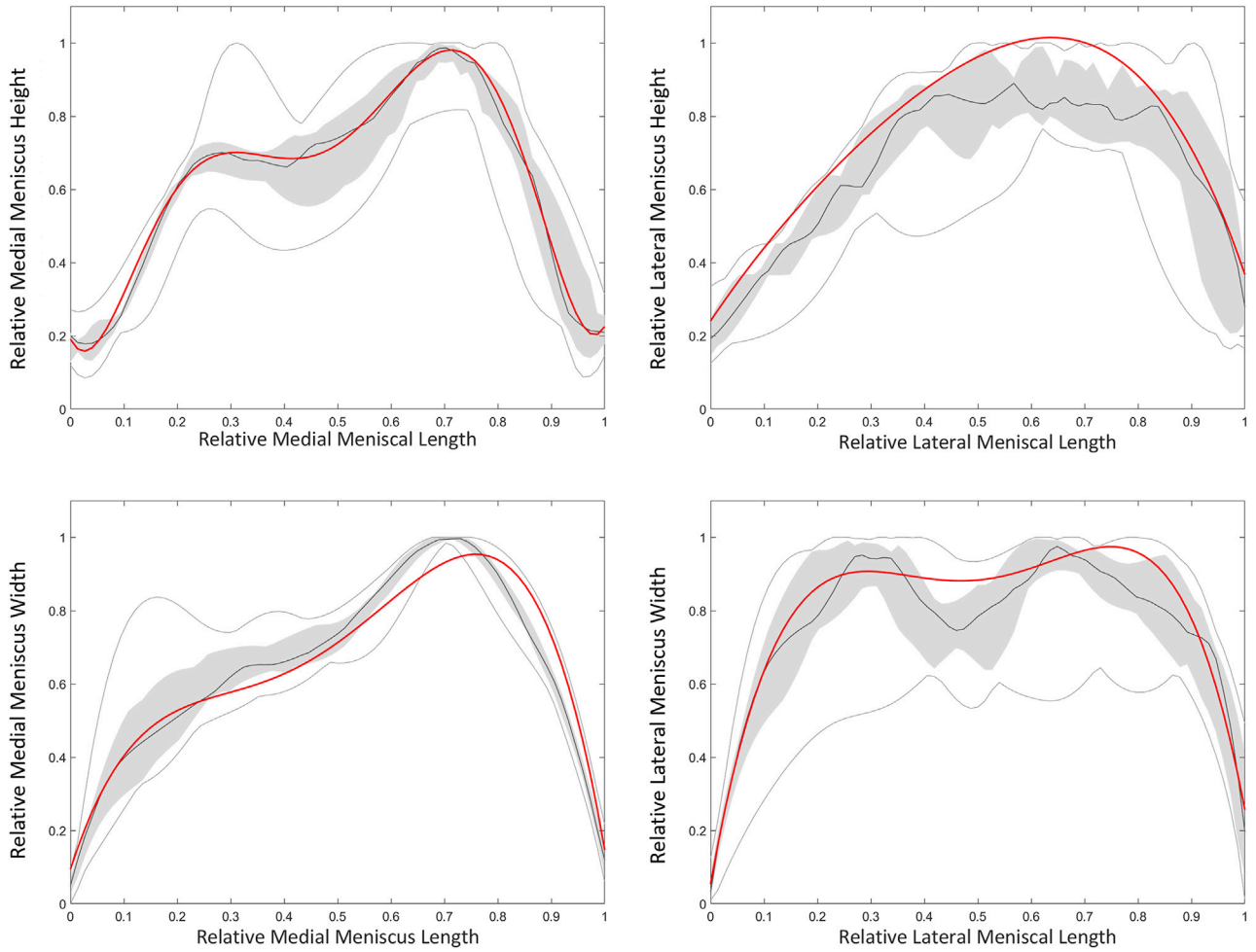

FIGURE 13
Polynomial fitting for medial and lateral meniscal height and width prediction. The median height and width of the medial (left) and lateral (right) meniscus is presented as the dark grey line. The grey zone represents the values between P25 and P75. The light grey lines represent minimal and maximal values. The red line represents height and width of respectively a 6th and 4th degree polynomial function for the medial meniscus. For the lateral meniscus, the red line represents twice a 4th degree polynomial fit.

TABLE 10 Median RMSE, ASD and HD with range between predicted and measured height and width of the medial meniscus (MM) and lateral meniscus (LM).

	Medial meniscus (height)	Lateral meniscus (height)	Medial meniscus (width)	Lateral meniscus (width)
RMSE (mm) (range)	3.88 (1.18–6.43)	2.96 (1.49–3.75)	2.77 (1.51–3.69)	2.27 (1.04–5.41)
ASD (mm) (range)	3.71 (0.97–6.06)	2.45 (1.17–3.27)	2.40 (1.27–3.20)	1.97 (0.89–4.28)
HD (mm) (range)	5.97 (2.44–9.47)	5.55 (3.63–7.12)	4.94 (2.68–7.33)	4.18 (1.91–10.78)

The standard error of measurement for medial and lateral epicondyle landmark identification ranged from 0.41 mm to 0.78 mm, from 1.35 mm to 3.43 mm and from 1.03 mm to 4.71 mm in respectively the mediolateral, the craniocaudal and the anteroposterior direction (Esfandiarpour et al., 2009). The observed errors in this study are in the same order of magnitude as the previously described variability in manual landmark identification. Furthermore, for future application in DEA modeling, the general direction of the ligamentous fibers is of greater importance than absolute errors in origin and insertion identification. For a ligamentous length of 5 cm, a 3 mm error changes the orientation of the ligament with only 3.4°. Thus, in the case of a prediction error in the order of magnitude of the reported average errors, the fiber orientation will change only minimally. However, we have to acknowledge that for greater prediction errors, as reported by the Hausdorff distance, changes in fiber orientation up to 20° are currently inevitable. The exact impact of larger changes in ligamentous orientation for DEA-

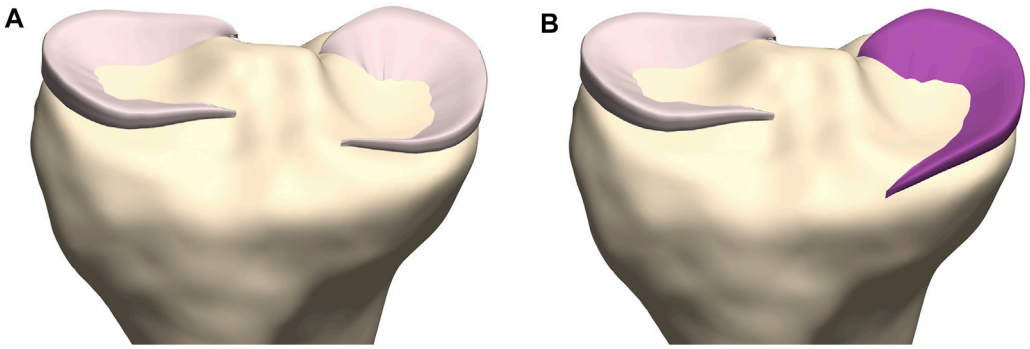

FIGURE 14
Coronal view on the tibial plateau (yellow). **(A)** Prediction of the medial meniscus according to the developed workflow demonstrates the type I insertion as described by De Coninck and colleagues. **(B)** By changing the anterior root insertion reference, a medial meniscus with a type III insertion is modeled (Mootanah et al., 2014).

based stress calculations in the knee joint is yet to be examined (Peña et al., 2006).

Besides ligament origin and insertion, ligamentous thickness over the course is imposed based on measurements from cadaveric studies, with the exception of the thickness of the cruciate ligaments. However, since soft tissue contains a substantial amount of water, measurements based on cadaveric specimens are possibly influenced by tissue dehydration (Haut et al., 1998). For the prediction of cruciate ligament geometry, a varying thickness is imposed based on MRI measurements. This matches the cadaveric findings of Triantafyllidi and colleagues, who described the thickness of the ACL varying from a small femoral attachment towards a broad tibial attachment whereas the PCL showed a large femoral and tibial attachment with a smaller mid-substance (Triantafyllidi et al., 2013). However, accurate assessment of ligamentous thickness and osseous insertions based on MRI imaging is challenging (Rachmat et al., 2014). Based on the results of the validation experiments, we are able to predict cruciate ligaments, main knee ligament and patellar tendon anatomy with a large accuracy.

4.1 Strengths

We present a novel methodology for personalized, static knee joint modelling, avoiding laborious manual segmentation tasks and improving generalizability. Being less time-consuming, it allows for easier applicability in a clinical setting. Starting from CT or MRI imaging, the osseous anatomy of the individual patient can easily be extracted, requiring only a few minutes to manually allocate the osseous edges on imaging data. Following the presented methodological pipeline, a comprehensive patient-specific knee joint model is available in less than 10 min, while avoiding additional manual interactions. However, with emerging applications in machine learning, the process of annotation and landmark identification can theoretically be performed real-time. The translation to the routine clinical practice by adopting these techniques will be the focus of future work. For example, accurate anatomical models enable generation of patient-specific instrumentation (PSI), recently introduced in total knee arthroplasty (TKA) (Watters et al., 2011; Reimann et al., 2019). Schotanus and colleagues demonstrated a superior outcome in terms of component alignment accuracy when relying on MRI-based PSI in comparing to CT- or X-ray-based PSI's. This was most possibly a result of considering the cartilage layer in PSI development (Schotanus et al., 2016). Avoiding manual cartilage segmentation, Van Dijck and colleagues developed a statistical shape modeling based tibiofemoral cartilage prediction tool. Based on the reported RMSE and inter-observer variability, they proved to outperform manual segmentation accuracy. As such, accurate soft tissue predictions enable to develop PSI's with an accuracy equaling MRI-based PSI's while avoiding time-consuming manual soft tissue segmentation and MRI related high costs (van Dijck et al., 2018).

Outside the clinical field of orthopaedics, computational modeling of patient-specific knee joint morphology can function as an input for Discrete Element Analysis (DEA). DEA can be used for non-invasive estimation of intra-articular joint contact stress (van Houcke et al., 2020a; Peiffer et al., 2022b). The cornerstone, however, remains accurate, and preferably individualized, inclusion of soft tissue and osseous morphometrics. The extraction of detailed morphometrics from MRI imaging relies on one of the three segmentation methods, namely, manual, semiautomatic and automatic. However, no numerical data are available comparing knee joint DEA modeling based on manual segmentation to (semi-) automatic segmentation. Previous research has proven the time consuming aspect and the possibly large variability related to manual segmentation. Furthermore, the robustness and reproducibility of (semi-)automatic segmentation enables a more efficient introduction of DEA modeling in clinics (Heye et al., 2013). Therefore, differences in DEA-based intra-articular stress predictions attributable to the type of underlying mesh are subject for future research.

4.2 Limitations

An important limitation is the inclusion of a homogeneous population of western European descent in our study. Extrapolation to other populations is not advised since the complex interaction between genes, culture and the environment results in a population-based variation of morphological features. Even more, our findings are based on a group of men, aged between 17 and 25 years with a total body length of 95% of the individuals ranging between 180.1–183.5 cm. However we do not question the validity of the model, more subjects should be included in future research to expand the range of total body length of the investigated population. Moreover, inclusion of additional subjects would allow to collect supplementary metadata, such as activity level and body mass index which are often discussed risk factors for cartilage loss, but were unfortunately not collected for the current dataset (Schneider et al., 2022).

Regarding meniscal inclusion, the menisci are solely statically modeled. Since MRI scanning was performed with the knee in fully extended position, uniquely validation of the meniscal position in a non-weight bearing, fully extended position was possible. As we hypothesized the menisci to adjust to the edges of the combined osseous–cartilage structure during stance, this concept could possibly be extrapolated to predict meniscal position during knee flexion. Improved insight in meniscal movement and validation of this concept requires currently lacking, additional MRI scanning in different degrees of knee flexion and should be subject to future research. However, modeling the menisci as an elastic tube from a fixed anterior to posterior root with varying height and subsequent allocation of a varying width allows for effortless translation towards meniscal modeling in different degrees of knee flexion.

Lastly, statistical modeling of soft tissue remains an approximation of reality and is based on a limited amount of samples to provide for the anatomical input in model development (n = 10). The aim is to find the optimal balance between including sufficient anatomical details on one hand and preserving computational efficiency on the other hand. As the reality is inevitably simplified, there is a definite need for validation tests to ensure that an adequate approximation is achieved. Furthermore, the pixel size of the used MR images influences the accuracy of anatomical landmark identification. Non-etheless, the described error range in this study is comparable to the relatively large inter- and intra-observer variability related to MRI-based manual soft tissue segmentations (Esfandiarpour et al., 2009; van der Merwe et al., 2019).

5 Conclusion

In conclusion, we present an innovative methodological workflow for personalized, static knee joint modelling. As soft tissue prediction is based on the underlying anatomy, we avoid laborious manual segmentation and allow for fast and personalized geometry predictions and maintain an accuracy comparable to manual soft tissue segmentation. Future research is necessary to implement an accurate morphometric knee joint model including the dynamic meniscus into clinical practice and thereby improve patient specific models of knee surgeries.

Data availability statement

The processed imaging data used for the model development in the manuscript are available upon request. Requests to access these datasets should be directed to emmanuel.audenaert@ugent.be. The original contributions presented in the study are publicly available. This data can be found here: https://www.mathworks.com/matlabcentral/fileexchange/124301-personalized-statistical-modeling-of-knee-soft-tissue.

Ethics statement

The studies involving human participants were reviewed and approved by Ethical Committee Ghent University Hospital. The patients/participants provided their written informed consent to participate in this study.

Author contributions

EA conceived of the presented idea. The concept was further thought through in cooperation with AB, GS, JV, AV, and EA designed the model and the computational framework. MP, KD, AC, and JG offered technical support during computational modeling. All authors discussed the results and contributed to the final manuscript.

Funding

This work was supported by an Aspirant Grant (#1122821N, FWO), a Mobility Research Grant (V424118, FWO) and a Senior Clinical Investigator Fellowship Grant (#1842619N, FWO), all originating from the Research Foundation–Flanders (FWO).

Conflict of interest

The authors declare that the research was conducted in the absence of any commercial or financial relationships that could be construed as a potential conflict of interest.

Publisher's note

References

Ariel de Lima, D., Helito, C. P., Lacerda de Lima, L., de Castro Silva, D., Costa Cavalcante, M. L., and Dias Leite, J. A. (2019). Anatomy of the anterolateral ligament of the knee: A systematic review. *Arthrosc. - J. Arthrosc. Relat. Surg.* 35 W.B. Saunders, 670–681.

Atkinson, P., Atkinson, T., Huang, C., and Doane, R. A. (2022). Comparison of the mechanical and dimensional properties of the human medial and lateral patellofemoral ligaments. *Orthop. Res. Soc.*

Audenaert, A., and Audenaert, E. (2008). Global optimization method for combined spherical-cylindrical wrapping in musculoskeletal upper limb modelling. *Comput. Methods Programs Biomed.* 92, 8–19. doi:10.1016/j.cmpb.2008.05.005

Audenaert, E. A., Khanduja, V., Bauwens, C., van Hoof, T., Pattyn, C., and Steenackers, G. (2019). A discrete element model to predict anatomy of the psoas muscle and path of the tendon: Design implications for total hip arthroplasty. *Clin. Biomech.* 70, 186–191. doi:10.1016/j.clinbiomech.2019.09.004

Audenaert, E. A., Mahieu, P., van Hoof, T., and Pattyn, C. (2009). Soft tissue structure modelling for use in orthopaedic applications and musculoskeletal biomechanics. *EURASIP J. Adv. Signal Process* 2010 (1), 389356. doi:10.1155/2010/389356

Audenaert, E. A., van Houcke, J., Almeida, D. F., Paelinck, L., Peiffer, M., Steenackers, G., et al. (2019). Cascaded statistical shape model based segmentation of the full lower limb in CT. *Comput. Methods Biomech. Biomed. Engin*. 22(6). 644–657. doi:10.1080/10255842.2019.1577828

Bae, K. T., Shim, H., Tao, C., Chang, S., Wang, J. H., Boudreau, R., et al. (2009). Intra- and inter-observer reproducibility of volume measurement of knee cartilage segmented from the OAI MR image set using a novel semi-automated segmentation method. *Osteoarthr. Cartil.* 17 (12), 1589–1597. doi:10.1016/j.joca.2009.06.003

Boer, C. G., Hatzikotoulas, K., Southam, L., Stefánsdóttir, L., Zhang, Y., Coutinho de Almeida, R., et al. (2021). Deciphering osteoarthritis genetics across 826,690 individuals from 9 populations. *Cell.* 184 (18), 6003–6005. doi:10.1016/j.cell.2021.11.003

Cohen, Z. A., McCarthy, D. M., Kwak, S. D., Legrand, P., Fogarasi, F., Ciaccio, E. J., et al. (1999). Knee cartilage topography, thickness, and contact areas from MRI: *In-vitro* calibration and *in-vivo* measurements. *Osteoarthr. Res. Soc.* 7, 95–109. doi:10.1053/joca.1998.0165

de Coninck, T., Vanrietvelde, F., Seynaeve, P., Verdonk, P., and Verstraete, K. (2017). MR imaging of the anatomy of the anterior horn of the medial meniscus. *Acta radiol.* 58 (4), 464–471. doi:10.1177/0284185116661880

de Roeck, J., van Houcke, J., Almeida, D., Galibarov, P., de Roeck, L., and Audenaert, E. A. (2020). Statistical modeling of lower limb kinetics during deep squat and forward lunge. *Front. Bioeng. Biotechnol.* 8, 233. doi:10.3389/fbioe.2020.00233

Dong, Y., Hu, G., Dong, Y., Hu, Y., and Xu, Q. (2014). The effect of meniscal tears and resultant partial meniscectomies on the knee contact stresses: A finite element analysis. *Comput. Methods Biomech. Biomed. Engin* 17 (13), 1452–1463. doi:10.1080/10255842.2012.753063

Esfandiarpour, F., Olyaei, G., Shakouri Rad, A., Farahmand, F., Talebian, S., Makhsous, M., et al. (2009). Reliability of determination of bony landmarks of the distal femur on MR images and MRI-based 3D models. *Article Iran. J. Radiology [Internet]* 6 (4), 225–230. Available from: https://www.researchgate.net/publication/224025984.

Hauser, R., Smoliński, J., and Gos, T. (2005). The estimation of stature on the basis of measurements of the femur. *Forensic Sci. Int.* 147 (2–3), 185–190. doi:10.1016/j.forsciint.2004.09.070

Haut, T. L., Hull, M. L., and Howell, S. M. (1998). A high-accuracy three-dimensional coordinate digitizing system for reconstructing the geometry of diarthrodial joints. *J. Biomech.* 31 (6), 571–577. doi:10.1016/s0021-9290(98)00049-9

Hedderwick, M., Stringer, M. D., McRedmond, L., Meikle, G. R., and Woodley, S. J. (2017). The oblique popliteal ligament: An anatomic and MRI investigation. *Surg. Radiologic Anat.* 39 (9), 1017–1027. doi:10.1007/s00276-017-1838-7

Heye, T., Merkle, E. M., Reiner, C. S., Davenport, M. S., Horvath, J. J., Feuerlein, S., et al. (2013). Reproducibility of dynamic contrast-enhanced MR imaging. Part II. Comparison of intra- and interobserver variability with manual region of interest placement versus semiautomatic lesion segmentation and histogram analysis. *Radiology* 266 (3), 812–821. doi:10.1148/radiol.12120255

Hunter, D. J., March, L., and Chew, M. (2020). Osteoarthritis in 2020 and beyond: A lancet commission. *Lancet [Internet]* 396, 1711–1712. doi:10.1016/s0140-6736(20)32230-3

James, E. W., LaPrade, C. M., and LaPrade, R. F. (2015). Anatomy and biomechanics of the lateral side of the knee and surgical implications. *Sports Med. Arthrosc. Rev.* 23 (1), 2–9. doi:10.1097/jsa.0000000000000040

Kang, K. T., Kim, S. H., Son, J., Lee, Y. H., and Chun, H. J. (2015). *In vivo* evaluation of the subject-specific finite element model for knee joint cartilage contact area. *Int. J. Precis. Eng. Manuf.* 16 (6), 1171–1177. doi:10.1007/s12541-015-0151-9

Kang, K. T., Kim, S. H., Son, J., Lee, Y. H., and Koh, Y. G. (2017). Validation of a computational knee joint model using an alignment method for the knee laxity test and computed tomography. *Biomed. Mater Eng.* 28 (4), 417–429. doi:10.3233/bme-171686

LaPrade, R. F., and Engebretsen, A. H. (2007). The anatomy of the medial part of the knee. *J. Bone Jt. Surg.* 89 (9), 2000–2010. doi:10.2106/jbjs.f.01176

Marra, M. A., Vanheule, V., Fluit, R., Koopman, B. H. F. J. M., Rasmussen, J., Verdonschot, N., et al. (2015). A subject-specific musculoskeletal modeling framework to predict *in vivo* mechanics of total knee arthroplasty. *J. Biomech. Eng.* 137, 020904. doi:10.1115/1.4029258

Mootanah, R., Imhauser, C. W., Reisse, F., Carpanen, D., Walker, R. W., Koff, M. F., et al. (2014). Development and validation of a computational model of the knee joint for the evaluation of surgical treatments for osteoarthritis. *Comput. Methods Biomech. Biomed. Engin* 17 (13), 1502–1517. doi:10.1080/10255842.2014.899588

Nauwelaers, N., Matthews, H., Fan, Y., Croquet, B., Hoskens, H., Mahdi, S., et al. (2021). Exploring palatal and dental shape variation with 3D shape analysis and geometric deep learning. *Orthod. Craniofac Res.* 24 (S2), 134–143. doi:10.1111/ocr.12521

Nomura, E., Inoue, M., and Osada, N. (2005). Anatomical analysis of the medial patellofemoral ligament of the knee, especially the femoral attachment. *Arthroscopy* 13 (7), 510–515. doi:10.1007/s00167-004-0607-4

Pascoletti, G., Aldieri, A., Terzini, M., Bhattacharya, P., Calì, M., and Zanetti, E. M. (2021). Stochastic PCA-based bone models from inverse transform sampling: Proof of concept for mandibles and proximal femurs. *Appl. Sci.* 11 (11), 5204. doi:10.3390/app11115204

Peiffer, M., Burssens, A., Duquesne, K., Last, M., de Mits, S., Victor, J., et al. (2022). Personalised statistical modelling of soft tissue structures in the ankle. *Comput. Methods Programs Biomed.* 218, 106701. doi:10.1016/j.cmpb.2022.106701

Peiffer, M., Burssens, A., Duquesne, K., Last, M., de Mits, S., Victor, J., et al. (2022). Personalised statistical modelling of soft tissue structures in the ankle. *Comput. Methods Programs Biomed.* 218, 106701. doi:10.1016/j.cmpb.2022.106701

Peña, E., Calvo, B., Martínez, M. A., and Doblaré, M. (2006). A three-dimensional finite element analysis of the combined behavior of ligaments and menisci in the healthy human knee joint. *J. Biomech.* 39 (9), 1686–1701. doi:10.1016/j.jbiomech.2005.04.030

Rachmat, H. H., Janssen, D., Zevenbergen, W. J., Verkerke, G. J., Diercks, R. L., and Verdonschot, N. (2014). Generating finite element models of the knee: How accurately can we determine ligament attachment sites from MRI scans? *Med. Eng. Phys.* 36 (6), 701–707. doi:10.1016/j.medengphy.2014.02.016

Reimann, P., Brucker, M., Arbab, D., and Lüring, C. (2019). Patient satisfaction - a comparison between patient-specific implants and conventional total knee arthroplasty. *J. Orthop.* 16 (3), 273–277. doi:10.1016/j.jor.2019.03.020

Rissech, C., Márquez-Grant, N., and Turbón, D. (2013). A collation of recently published western European formulae for age estimation of subadult skeletal remains: Recommendations for forensic anthropology and osteoarchaeology. *J. Forensic Sci.* 58, S163–S168. doi:10.1111/1556-4029.12011

Schneider, M. T. Y., Rooks, N., and Besier, T. (2022). Cartilage thickness and bone shape variations as a function of sex, height, body mass, and age in young adult knees. *Sci. Rep. [Internet]* 12 (1), 11707. Available at:https://www.nature.com/articles/s41598-022-15585-w. doi:10.1038/s41598-022-15585-w

Schotanus, M., Sollie, R., van Haaren, E., Hendrickx, R., Jansen, E., and Kort, N. (2016). A radiological analysis of the difference between MRI- and CT-based patient-specific matched guides for total knee arthroplasty from the same manufacturer: A randomised controlled trial. *J. Am. Coll. Radiol.* 98B (6), 786–792. doi:10.1302/0301-620x.98b6.36633

Seim, H., Kainmueller, D., Heller, M., Lamecker, H., Zachow, S., and Hege, H. C. (2008). Automatic segmentation of the pelvic bones from CT data based on a statistical shape model. Proceedings of the Eurographics Workshop on Visual Computing for Biomedicine, VCBM 2008, Delft, The Netherlands, 2008.

Sharma, L., Song, J., Dunlop, D., Felson, D., Lewis, C. E., Segal, N., et al. (2010). Varus and valgus alignment and incident and progressive knee osteoarthritis. *Ann. Rheum. Dis.* 69 (11), 1940–1945. doi:10.1136/ard.2010.129742

Tack, A., Mukhopadhyay, A., and Zachow, S. (2018). Knee menisci segmentation using convolutional neural networks: Data from the osteoarthritis initiative. *Osteoarthr. Cartil.* 26 (5), 680–688. doi:10.1016/j.joca.2018.02.907

Triantafyllidi, E., Paschos, N. K., Goussia, A., Barkoula, N. M., Exarchos, D. A., Matikas, T. E., et al. (2013). The shape and the thickness of the anterior cruciate ligament along its length in relation to the posterior cruciate ligament: A cadaveric study. *J. Arthrosc. Relat. Surg.* 29 (12), 1963–1973. doi:10.1016/j.arthro.2013.09.007

van der Merwe, J., van den Heever, D. J., and Erasmus, P. (2019). Variability, agreement and reliability of MRI. *knee Landmarks. J. Biomech.*, 95.

van Dijck, C., Wirix-Speetjens, R., and Jonkers, I. (2018). Statistical shape model-based prediction of tibiofemoral cartilage. *Comput. Methods Biomech. Biomed. Engin* 21 (9), 568–578. doi:10.1080/10255842.2018.1495711

van Haver, A., de Roo, K., de Beule, M., van Cauter, S., Audenaert, E., Claessens, T., et al. (2014). Semi-automated landmark-based 3D analysis reveals new morphometric characteristics in the trochlear dysplastic femur. *Arthroscopy* 22 (11), 2698–2708. doi:10.1007/s00167-013-2573-1

van Haver, A., Mahieu, P., Claessens, T., Li, H., Pattyn, C., Verdonk, P., et al. (2014). A statistical shape model of trochlear dysplasia of the knee. *Knee* 21 (2), 518–523. doi:10.1016/j.knee.2013.11.016

van Houcke, J., Audenaert, E. A., Atkins, P. R., AndersonCombined Geometric Morphometric, A. E. A., and Element, Discrete (2020). A combined geometric morphometric and discrete element modeling approach for hip cartilage contact mechanics. *Front. Bioeng. Biotechnol.* 8, 318. doi:10.3389/fbioe.2020.00318

van Houcke, J., Galibarov, P. E., van Acker, G., Fauconnier, S., Allaert, E., van Hoof, T., et al. (2020). Personalized hip joint kinetics during deep squatting in young, athletic adults. *Comput. Methods Biomech. Biomed. Engin* 23 (1), 23–32. doi:10.1080/10255842.2019.1699539

Vos, T., Flaxman, A. D., Naghavi, M., Lozano, R., Michaud, C., Ezzati, M., et al. (2012). Years lived with disability (YLDs) for 1160 sequelae of 289 diseases and injuries 1990–2010: A systematic analysis for the global burden of disease study 2010. *Lancet* 380 (9859), 2163–2196. doi:10.1016/S0140-6736(12)61729-2

Vrancken, A. C. T., Crijns, S. P. M., Ploegmakers, M. J. M., O'Kane, C., van Tienen, T. G., Janssen, D., et al. (2014). 3D geometry analysis of the medial meniscus - a statistical shape modeling approach. *J. Anat.* 225 (4), 395–402. doi:10.1111/joa.12223

Watters, T. S., Mather, R. C., Browne, J. A., and Berend, K. R. (2011). Analysis of procedure-related costs and proposed benefits of using patient-specific approach in total knee arthroplasty. *J. Surg. Orthop. Adv.* 20 (2), 112–116.

Wilson, W. T., Deakin, A. H., Payne, A. P., Picard, F., and Wearing, S. C. (2012). Comparative analysis of the structural properties of the collateral ligaments of the human knee. *J. Orthop. Sports Phys. Ther.* 42 (4), 345–351. doi:10.2519/jospt.2012.3919

Yoshida, N., Usui, M., and Kitajima, K. (2002). *Gaussian-Based free form deformation and its application to fashion design*. in *Initiatives of precision engineering at the beginning of a millennium*. Editor I. Inasaki (Boston, MA: Springer), 957–961.

Frontiers in
Bioengineering and Biotechnology

Accelerates the development of therapies, devices, and technologies to improve our lives

A multidisciplinary journal that accelerates the development of biological therapies, devices, processes and technologies to improve our lives by bridging the gap between discoveries and their application.

Discover the latest Research Topics

See more →

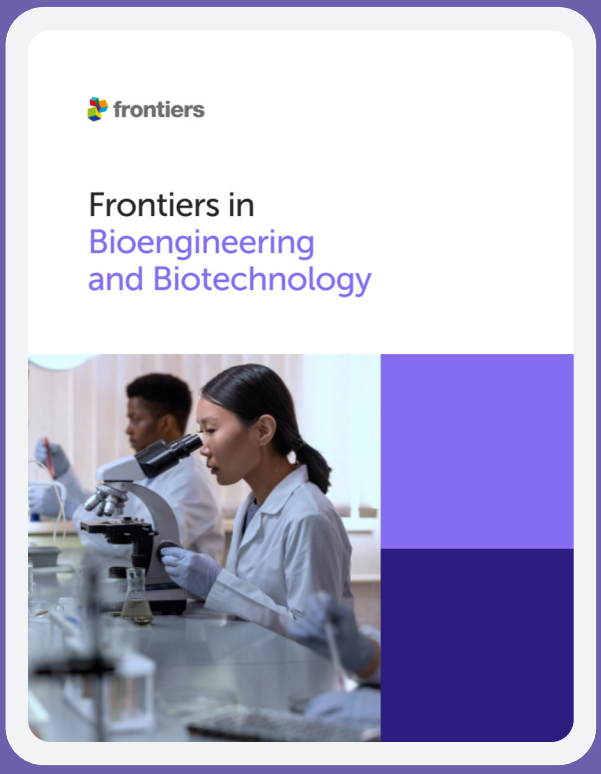

Frontiers

Avenue du Tribunal-Fédéral 34
1005 Lausanne, Switzerland
frontiersin.org

Contact us

+41 (0)21 510 17 00
frontiersin.org/about/contact